

OPERATION AND CONTROL OF MICROGRID IN ISLANDED AND GRID-CONNECTED MODES OF OPERATION

Thesis

Submitted in partial fulfillment of the requirements for the degree of
DOCTOR OF PHILOSOPHY

by

SHREERAM VISHWANATH KULKARNI



DEPARTMENT OF ELECTRICAL AND ELECTRONICS ENGINEERING
NATIONAL INSTITUTE OF TECHNOLOGY KARNATAKA
SURATHKAL, MANGALORE - 575025

2022

DECLARATION

by the Ph.D. Research Scholar

I hereby *declare* that the Research Thesis entitled **Operation and Control of Microgrid in Islanded and Grid-Connected Modes of Operation** which is being submitted to the National Institute of Technology Karnataka, Surathkal in partial fulfillment of the requirement for the award of the Degree of Doctor of Philosophy in Electrical and Electronics Engineering is a *bonafide report of the research work carried out by me*. The material contained in this Research Thesis has not been submitted to any University or Institution for the award of any degree.

Shreeram Vishwanath Kulkarni


.....
Shreeram Vishwanath Kulkarni, 177121EE504
Department of Electrical and Electronics Engineering


Place: NITK-Surathkal

Date: 08|04|2022

CERTIFICATE

This is to *certify* that the Research Thesis entitled **Operation and Control of Microgrid in Islanded and Grid-Connected Modes of Operation** submitted by Shreeram Vishwanath Kulkarni (Register Number: 177121EE504) as the record of the research work carried out by him, is *accepted as the Research Thesis submission* in partial fulfilment of the requirements for the award of degree of Doctor of Philosophy.


8/01/2022
Dr. Dattatraya N Gaonkar
(Research Guide)


11/1/22
(Chairman-DRPC, EEE Dept.)
PROFESSOR & HEAD
DEPARTMENT OF ELECTRICAL AND ELECTRONICS ENGINEERING
NATIONAL INSTITUTE OF TECHNOLOGY KARNATAKA
SRINIVASNAGAR, SURATHKAL, MANGALORE- 575025, INDIA

Acknowledgements

It gives me tremendous happiness and an extraordinary feeling of accomplishment to offer my genuine thanks to the individuals who made this dissertation feasible. First and foremost, I would like to offer my most profound thanks to my supervisor, Dr. Dattatraya N Gaonkar, Associate Professor, Department of Electrical and Electronics Engineering, for his perceptive direction, support, and showing trust in me constantly. He has been a consistent source of inspiration and support in this whole excursion.

I thank the National Institute of Technology Karnataka (NITK) for allowing me to pursue research. I might want to thank research progress assessment committee (RPAC) members Dr. A Karthikeyan and Dr. Udaya Kumar D, for their helpful input and direction. Likewise, I might want to express gratitude toward Dr. Shubhanga K N, Former Head of the Department of EEE, NITK, Surathkal, and Dr. Gururaj S Punekar, Head of the Department of EEE, NITK, Surathkal, for providing the necessary assets in the department to complete my research. I likewise wish to thank the non-teaching staff of the EEE department for providing fundamental support.

I would like to communicate my gratitude to every one of my colleagues and friends for making this journey significant.

I would like to offer my most profound thanks to my parents Late, Sri. Vishwanath Govindrao Kulkarni and Smt. Vijaya Vishwanath Kulkarni and my siblings for their unconditional love and patience. Their confidence and unrestricted love towards me are the justification for whatever I have accomplished in my life.

Shreeram Vishwanath Kulkarni

Abstract

A reliable energy source is important in daily life. Emerging concerns about primary energy availability, as well as the aging infrastructure of current electrical transmission and distribution systems, are placing greater emphasis on power supply sustainability, safety, and quality. To construct and upgrade existing infrastructures, large amounts of investments will be necessary, but perhaps the most appropriate technique to meet demands and expectations is to embrace creative concepts, technologies, and modern grid architecture. Future energy systems will have to keep up with technical advancements, societal standards, environmental concerns, and economic conditions. As a result, security mechanisms, operational safety, environmental protection, power quality, supply affordability, and energy efficiency must all be assessed in innovative ways to respond to new requirements. In this sense the control is decentralized and power flows bidirectionally, distribution grids are being converted from passive networks to active networks. This sort of network facilitates the integration of distributed generation (DG), renewable energy sources (RES), and energy storage systems (ESS), as well as the ability to integrate power generation and consumer demand in real-time. Because of the limitations of traditional power generated by fossil fuels, the role of power generation has always been critical. And this has been a source of concern due to environmental pollution and other issues. With the remarkable advancement of technology in past few years, several countries have directed their attention to how to successfully harness renewable energy to generate power. In this regard, microgrids are receiving an increasing amount of research and innovation due to their particular benefits in the implementation of renewable resources.

In the past few years, there has been significant growth in energy demand. It is a concern because of the large quantity of energy dissipated while transferring energy over long distances. The microgrid, which consists of distributed generation sources (DGs), is an excellent solution for reducing losses because it provides electricity close to the endpoint customers. Typically, the microgrid should be able to operate independently

(islanded) as well as in conjunction with the grid. Photovoltaic systems, wind farms, fuel cells, and micro-turbines are examples of DGs that are primarily classified as non-renewable and renewable energy resources. The recurrent nature of these sources causes significant stability difficulties in the power distribution network. Control and protection are required to sustain stable operation in the islanded mode of operation in terms of controlling the voltage and frequency enabling proportionate power-sharing. The voltage and frequency restoration must be maintained in an islanded AC microgrid to achieve proper power-sharing.

This thesis work summarises the architecture, classification, and characteristics of microgrid study in islanded and grid-connected operation modes. With a focus on PE-based DG inverters, control strategies for microgrids in both the operation modes are described and assessed. The output impedance of a PE-based DG has a significant impact on the parallel system and power distribution. Droop control is widely employed since multiple DGs operate simultaneously. However, power-sharing inefficiencies occur as a result of inconsistent line impedance, lowering the system's overall efficiency. To avoid being reliant on the DG inverter output line impedances, a control technique for accurate and proportional power-sharing with f/V restoration that pools an improved droop control with a virtual output impedance control with both the resistive and inductive output line impedances is designed. Then the entire microgrid system's state-space small-signal modeling and analysis are established. Meanwhile, the strategy's performance is enhanced in anticipation of a significant step-change in the operational power loads.

In the grid-connected operating mode, the effectiveness of a microgrid incorporating DGs would be improved in terms of power supply consistency for users. And among the most significant aspects of integrating a DG into the grid is islanding detection. Various islanding detection approaches have been developed over decades to improve the speed and accuracy of islanding detection. Furthermore, with new advancements such as micro smart grids on the horizon, there must be a compelling need for automatic islanding detection and mode switching to be included in the control. It's also critical that the islanding detection methods work well in unhealthy

grid environments. This work also proposes an islanding detection method based on Phase-Locked Loop (PLL) and a piezoelectric acoustic sensor. The PLL controller is one of the most often used fundamental concepts for grid synchronization solutions, and microgrid control includes PLL when integrated into the grid for synchronization. In islanded mode, it utilizes the phase angle generated through the droop controller, and in the grid-connected mode, it utilizes the angle by the PLL. This study focused on the three phase PLLs for grid synchronization and developed a PLL-based islanding detection method, as well as the design and dimensions of the piezoelectric acoustic sensor that was utilized for islanding detection. The islanding detection and automatic mode switching are efficiently achieved with the PLL and piezoelectric acoustic sensor.

According to virtual and real-time hardware in loop (HIL) simulation models, the proposed control techniques can provide voltage amplitude and frequency restoration, as well as proportional power-sharing in the islanded mode of operation. There is also quick and effective islanding detection and automatic mode switching in the grid-connected mode of operation. The Typhoon-402 hardware test-bed and the Typhoon HIL virtual system have been used to validate the proposed controller's performance.

Contents

Acknowledgements	i
Abstract	ii
List of figures	ix
List of tables	xvi
Nomenclature	xvii
1 INTRODUCTION	1
1.1 Introduction	1
1.2 Configuration of microgrid	2
1.3 Microgrid classification and control	4
1.3.1 Classification of microgrid	4
1.3.2 Control of microgrid	6
1.3.2.1 Communication based	9
1.3.2.2 Droop characteristic based	12
1.3.2.3 Virtual structure based	14
1.3.2.4 Construction and Compensation Based	14
1.3.2.5 Method Using a Combination of Droop and Signal Injection	17
1.4 Basic idea behind the conventional droop control	18
1.4.1 Droop control for parallel connected inverters	21
1.5 Islanding detection	24
1.5.1 Overview of Islanding Detection Methods	25
1.5.1.1 Passive Islanding Detection Methods	26
1.5.1.2 Active Islanding Detection Methods	29
1.5.1.3 Hybrid methods	31
1.6 Motivation	33

1.7	Contributions of this research work	34
1.8	Thesis organization	36
2	DROOP CONTROL STRATEGY FOR PE-BASED DGS IN THE ISLANDED OPERATION MODE	39
2.1	Introduction	39
2.2	Power Electronic (PE) inverter design	39
2.2.1	Selection of input DC voltage and DC-link capacitance	40
2.2.2	Selection of filter capacitance and inductance	41
2.2.3	Three phase inverter modeling	41
2.2.4	LCL filter and parallel RLC load	43
2.3	Control of PE-based DG systems	45
2.3.1	Power controller	46
2.3.2	Voltage controller	47
2.3.3	Current controller	48
2.4	Modeling and analysis of proposed droop controller	50
2.5	State-space and stability analysis of proposed droop control method	53
2.6	The complete Microgrid system model	60
2.6.1	Hardware in loop (HIL) simulation responses	64
2.6.2	Hardware in loop (HIL) real-time responses	70
2.7	Summary	74
3	SYNCHRONIZATION TECHNIQUES BASED ON PLL FOR PE-BASED DGS IN THE GRID-CONNECTED MODE	75
3.1	Introduction	75
3.2	Phase-locked loop for grid synchronization	77
3.3	Three-phase grid synchronization methods	81
3.3.1	Synchronous Reference Frame Phase-Locked Loop (SRF-PLL)	82
3.3.2	Active and Reactive Power Phase-Locked Loop (PQ-PLL)	82
3.3.3	Second Order Generalized Integrator-Phase-Locked Loop (SOGI-PLL)	83
3.3.4	Dual Second Order Generalized Integrator-Phase-Locked Loop (DSOGI-PLL)	84
3.3.5	Phase Transport Delay-Phase-Locked Loop ($T/4$ Delay-PLL)	86
3.3.6	Inverse Park Transform-Phase-Locked Loop (IPT-PLL)	87

3.3.7	Enhanced-Phase-Locked Loop (E-PLL)	89
3.4	Test system model description	90
3.5	HIL virtual and real-time responses	92
3.6	PLL based islanding detection for droop based microgrid	103
3.6.1	Microgrid's islanded mode of operation	103
3.6.2	Microgrid's grid-connected mode of operation	104
3.6.3	PLL and Islanding detection	106
3.7	Result and Discussion	109
3.8	Summary	120
4	ISLANDING DETECTION AND AUTOMATIC MODE SWITCH- ING BASED ON PSRF-PLL AND PIEZOELECTRIC ACOUSTIC SENSOR FOR GRID-CONNECTED DGS	121
4.1	Introduction	121
4.2	Control strategy for grid-connected and islanded operation modes . .	122
4.2.1	Grid-connected control mode	122
4.2.2	islanded control mode	124
4.3	Islanding detection and automatic mode switching with modified PLL	127
4.4	Experimental results and analysis	131
4.5	Islanding detection with piezoelectric acoustic sensor	140
4.6	Design and dimensions of proposed piezoelectric acoustic sensor . . .	143
4.7	Islanding detection with piezoelectric acoustic sensor	147
4.8	Simulation and Hardware In Loop Responses	148
4.8.1	COMSOL Multiphysics Simulation Responses	148
4.8.2	Hardware In the Loop-Virtual Responses	152
4.8.3	Hardware In the Loop-Real-time Responses	159
4.9	Summary	161
5	CONCLUSIONS AND SCOPE FOR FUTURE WORK	163
5.1	Conclusions	163
5.2	Scope for future work	165
	PUBLICATIONS	167
	Bibliography	168

List of Figures

1.1	Basic AC microgrid architecture.	3
1.2	Overall classification of microgrid.	4
1.3	Layers of the microgrid hierarchy (multi-agent controller).	6
1.4	Hierarchical AC microgrid control block diagram.	8
1.5	Overview of microgrid controls for islanded operation mode.	10
1.6	(a) Power flow, and (b) equivalent model's phasor diagram.	18
1.7	Control characteristics for frequency and voltage droop.	20
1.8	Comparing the droop characteristics of two different-rated inverters connected in parallel.	21
1.9	Islanding detection method.	25
1.10	Islanding detection methods (passive, active, and hybrid) flow diagram.	27
1.11	Organization of thesis.	36
2.1	The PE inverter with the output LC filter and RLC load.	40
2.2	d-equivalent circuit of three phase inverter.	42
2.3	q-equivalent circuit of three phase inverter.	42
2.4	Bode plots for LCL filter and parallel RLC load.	44
2.5	Parallel connected three-phase PE-based DGs in islanded mode.	46
2.6	Power controller scheme.	47
2.7	Overall control scheme for Microgrid in the islanded mode of operation.	49
2.8	Proposed controller block diagram for DGs.	52
2.9	Eigenvalue analysis of overall system with various frequency modes.	63
2.10	Typhoon-402 Hardware-in-loop experimental set-up.	64
2.11	Test microgrid system.	64
2.12	The Inverter output voltage (V).	65
2.13	The Inverter output current (A).	66

2.14	Frequency response (Hz).	67
2.15	The Inverter output d-axis voltage (V).	67
2.16	The active power response (kW).	68
2.17	The reactive power response (kVAr).	68
2.18	Output power of the DG (with 1.5 kW step change in load power at bus1) (a) Active power (b) Reactive power.	69
2.19	Output power of the DG (with 6 kW and 4 kVAr step change in load power at bus1) (a) Active power (b) Reactive power.	69
2.20	Output voltage and current of the DG with 1.5 kW step change in load power at bus1 (a) DG output voltages in Volts (b) DG output currents in Amperes.	70
2.21	Output power of the DG with 1.5 kW step change in load power at bus1 (a) Active power in kW(b) Reactive power in VAr.	71
2.22	Output power of the DG with 6 kW and 4 kVAr step change in load power at bus1 (a) Active power in kW (b) Reactive power in kVAr.	72
2.23	Output d-axis voltage and current of the DGs with 27 kW step change in load power at bus1 (a) DGs d-axis output voltages in Volts (b) DGs d-axis output currents in Amperes.	73
3.1	Basic structure of Phase Lock Loop (PLL).	77
3.2	Capture range of the phase-locked loop with f_0 and f_c	79
3.3	Functional diagram of capture range for the phase-locked loop with f_{min} and f_{max}	80
3.4	Input error voltage generation to the voltage controlled oscillator.	81
3.5	Control structure of Synchronous Reference Frame-Phase-locked Loop (SRF-PLL).	82
3.6	Instantaneous Active and Reactive Power phase-locked loop (PQ-PLL).	83
3.7	Control structure of Second Order Generalized Integrator-Phase-locked Loop (SOGI-PLL).	84
3.8	Control structure of Dual Second Order Generalized Integrator-Phase-locked Loop (DSOGI-PLL).	85
3.9	Detailed structure of a Quarter Phase Transport Delay or $T/4$ Delay -Phase-locked Loop ($T/4$ Delay-PLL).	87

3.10	Block diagram of the inverse park transform based phase-locked loop (IPT-PLL).	88
3.11	Block diagram of the enhanced phase-locked loop (E-PLL).	88
3.12	Control structure of a grid-connected Inverter based DG systems (test model).	90
3.13	Responses of SRF-PLL, SOGI-PLL, DSOGI-PLL, E-PLL, $T/4$ Delay-PLL, and IPT-PLL frequencies under grid voltage normal test condition.	92
3.14	Responses of SRF-PLL, SOGI-PLL, DSOGI-PLL, E-PLL, $T/4$ Delay-PLL, and IPT-PLL frequencies under grid voltage Sag test condition.	93
3.15	Responses of SRF-PLL, SOGI-PLL, DSOGI-PLL, E-PLL, $T/4$ Delay-PLL, and IPT-PLL frequencies under grid voltage Swell test condition.	94
3.16	Responses of SRF-PLL, SOGI-PLL, DSOGI-PLL, E-PLL, $T/4$ Delay-PLL, and IPT-PLL frequencies under grid voltage Unbalance test condition.	95
3.17	Responses of SRF-PLL, SOGI-PLL, DSOGI-PLL, E-PLL, $T/4$ Delay-PLL, and IPT-PLL frequencies under grid voltage Harmonics test condition.	96
3.18	Responses of the Grid, DG1, and DG2 frequencies and angle variations, and PCC voltage THD with DSOGI-PLL under various test cases: (a) grid voltage sag (b) grid voltage swell.	97
3.19	Responses of the Grid, DG1, and DG2 frequencies and angle variations, and PCC voltage THD with DSOGI-PLL under various test cases: (a) grid voltage unbalance (b) grid voltage harmonics.	98
3.20	Responses of the DSOGI-PLL frequency (Hz) under grid voltage normal, sag, swell, unbalance, and harmonics test conditions.	99
3.21	Responses of the DSOGI-PLL frequency (Hz), active power (kW), reactive power (kVAr) without step-change in the load.	99
3.22	Responses of the DSOGI-PLL frequency in Hz, active power in kW, reactive power in kVAr with step-change in the load.	101
3.23	DG1, DG2, Grid (SOGI-PLL and SRF-PLL) frequency responses (Hz) in the course of voltage sag condition at 0.3 s, to 0.75 s.	101
3.24	Responses of active power (kW) of DG1, DG2, Grid, and Load during the load change at 0.3 s to 0.8 s.	102

3.25	Responses of reactive power (kVAr) of DG1, DG2, Grid, and Load during the load change at 0.3 s to 0.8 s.	102
3.26	(a): Frequency droop (b): Voltage droop (c): islanded mode control.	105
3.27	Control scheme for grid connected mode.	106
3.28	Islanding detection flow diagram.	108
3.29	PLL control signals for islanding detection.	109
3.30	Grid-connected operation mode (a) load voltages in Volts (b) load currents in Amps.	110
3.31	Grid-connected operation mode (a) PLL (γ , θ , $\sin(\gamma - \theta)$) and PCC frequency (b) active power in kW.	111
3.32	islanded operation mode (a) load voltages in Volts (b) load currents in Amps.	113
3.33	islanded operation mode (a) PLL (γ , θ , $\sin(\gamma - \theta)$) and PCC frequency (b) active power in kW.	114
3.34	GC-SA-GC operation mode (a) load voltages in Volts (b) load currents in Amps.	115
3.35	GC-SA-GC operation mode (a) PLL (γ , θ , $\sin(\gamma - \theta)$) and PCC frequency (b) active power versus frequency plot.	116
3.36	GC-SA-GC operation mode (a) active power in kW (b) reactive power in kVAr.	117
4.1	Schematic diagram of (a) The microgrid system model, and (b) Hardware in loop implementation.	123
4.2	Control scheme for grid connected mode of operation.	124
4.3	Control scheme for islanded mode.	125
4.4	Detailed block diagram of the PSRF-PLL controller.	128
4.5	Phasor diagram (Reference Frame Transformation) of the PSRF-PLL controller.	128
4.6	PSRF-PLL controller-(a) bode plot, and (b) root locus.	130
4.7	Output frequency response of proposed PSRF-PLL and conventional PLL.	131
4.8	Grid and DG voltages and currents during transition.	132
4.9	Responses of the active powers of $DG_{1,2}$ v/s frequencies of $DG_{1,2}$ during transition.	133

4.10	Total harmonic distortion in PCC voltage for unbalance, harmonics, sag, swell, and faults.	133
4.11	PLL controller responses under full- load and no-load conditions. . . .	134
4.12	NDZ of proposed islanding detection method with other active and passive islanding detection methods.	136
4.13	Performance of microgrid system model in grid-connected to islanded and islanded to grid-connected mode transition: (a) Active powers of DGs, grid, and load, (b) Reactive powers of DGs, grid, and load. . . .	137
4.14	Performance of microgrid system model in grid-connected to islanded and islanded to grid-connected mode transition: Grid phase angle γ , DG phase angle θ , phase error Δe , and frequency at the PCC during transition.	138
4.15	Performance of microgrid system model in grid-connected to islanded and islanded to grid-connected mode transition: (a) Active powers of DGs, grid, and load, (b) Reactive powers of DGs, grid, and load. . . .	139
4.16	Grid-connected operation mode-PLL phase error and phase angle responses for the proposed PSRF-PLL and popular PLLs in the literature (Yang et al., 2015).	140
4.17	Grid-connected operation mode-PLL phase error and phase angle responses for the proposed PSRF-PLL and popular PLLs in the literature. For various case studies-(a) unbalance, (b) harmonics, (c) sag, (d) swell, and (e) faults.	141
4.18	Performance proposed islanding detection scheme under: (a) pole trip condition, (b) close in fault.	142
4.19	Proposed piezoelectric sensor design with requisite dimensions.	145
4.20	Equivalent circuit diagram of the lumped element model of acoustic sensor.	146
4.21	Diaphragm simulation of proposed piezoelectric sensor in COMSOL platform.	148
4.22	Piezoelectric acoustic sensor's diaphragm deflection at natural frequency.	149
4.23	Piezoelectric acoustic sensor's diaphragm deflection at four different modal frequencies.	150
4.24	Piezoelectric acoustic sensor's diaphragm simulation at fourth modal frequency.	150

4.25	Strain analysis of piezoelectric acoustic sensor diaphragm.	151
4.26	Strain analysis of piezoelectric acoustic sensor diaphragm.	151
4.27	Pressure and frequency responses of piezoelectric acoustic sensor under grid healthy condition.	153
4.28	Pressure and frequency responses of piezoelectric acoustic sensor under grid voltage Sag condition.	153
4.29	Pressure and frequency responses of piezoelectric acoustic sensor under grid voltage Swell condition.	154
4.30	Pressure and frequency responses of piezoelectric acoustic sensor under grid voltage Unbalance condition.	155
4.31	Pressure and frequency responses of piezoelectric acoustic sensor under grid voltage Harmonics condition.	156
4.32	Pressure and frequency responses with control commands of piezoelectric acoustic sensor for islanding detection for frequency <49 Hz. . . .	157
4.33	Pressure and frequency responses with control commands of piezoelectric acoustic sensor for islanding detection for frequency >51 Hz. . . .	157
4.34	Active power in kW and reactive power in kVAr responses with control commands of piezoelectric acoustic sensor during grid voltage sag condition.	158
4.35	NDZ comparison of proposed method with the other active and passive based islanding detection methods.	158
4.36	HIL real-time responses of PCC frequency in Hz, Sensor frequency in Hz and grid voltage in Volts during the grid frequency variation. . . .	159
4.37	HIL real-time responses of active powers of the load, grid, DG1 and DG2 in kW during the grid frequency variation.	160
4.38	HIL real-time responses of reactive powers of the load, grid, DG1 and DG2 in kVAr during the grid frequency variation.	160

List of Tables

1.1	Parameters for various kinds of networks	19
1.2	EN 50160 specification: The maximum fluctuation in grid frequency and voltage	25
1.3	Techniques for detecting passive islanding: a summary	29
1.4	Techniques for detecting active islanding: a summary	31
2.1	Initial conditions for eigenvalue spectrum analysis (Pogaku et al., 2007)	63
2.2	System frequency variation of control scheme	66
2.3	d-axis output voltage during the step change in the load of 27 kW . .	72
3.1	THE TEST SYSTEM PARAMETERS	91
3.2	PREFERENCE DIRECTION FOR PLL FOLLOWING DISTORTIONS	100
3.3	GC MODE	112
3.4	SA MODE	118
3.5	Test results for transition between GC-SA-GC modes.	118
3.6	PLL PHASE ERROR RESPONSES	119
4.1	Islanding detection time and NDZ with active and passive islanding detection methods	135
4.2	Test results for transition between grid-connected-islanded-grid-connected modes	136
4.3	DG controller and sensor parameters	147
4.4	DG controller and sensor parameters	152

Nomenclature

Abbreviations

Symbol	Meaning
ANSI	American National Standards Institute
SIA	Secretariat of Industrial Approvals
HV	High Voltage
MV	Medium Voltage
LV	Low Voltage
DG	Distributed Generation
DER	Distributed Energy Resources
SMG	Smart Micro Grid
HFAC	High Frequency AC
LFAC	Low Frequency AC
PE	Power Electronics
VSI	Voltage Source Inverter
CSI	Current Source Inverter
PWM	Pulse Width Modulation
DSP	Digital Signal Processor
SPC	Signal Processing Circuit
HIL	Hardware-In-Loop
CHP	Combined Heat and Power
PLL	Phase Locked Loop
THD	Total Harmonic Distortion
PCC	Point of Common Coupling
CB	Circuit Breaker
MGCC	Microgrid Central Controller
LC	Local Controller
CLC	Central Limit Control
MO	Market Operator
DNO	Distributed Network Operator
CLC	Central Limit Control
SCADA	Supervisory Control And Data Acquisition
PEV	Plug-in Electric Vehicle

ESS	Energy Storage Systems
VPD	Voltage Active Power Droop
FQB	Frequency Reactive Power Droop
NDZ	Non detection zone
OUF	Over/Under Frequency
OUV	Over/Under Voltage
PCC	Point of common coupling
PE	Power electronic
PIDM	Passive islanding detection method
PJD	Phase jump detection
PLL	Phase locked loop
PD	Phase Detector
LF	Low-pass Filter
VCO	Voltage Controlled Oscillator
PLCC	Power line carrier communication
ROCOF	Rate of change of Frequency
ROCOFOP	Rate of change of frequency over power
ROCONSV	Rate of change of negative sequence voltage
ROCOP	Rate of change of Power
ROCOV	Rate of change of voltage
FEM	Finite Element Modeling
LEM	Lumped Element Modeling
SA	Smart Appliance
CMOS	Complementary metal–oxide–semiconductor
MEMS	Micro Electro Mechanical Systems
DRIE	Deep Reactive Ion Etching
ANFIS	Adaptive Neuro-Fuzzy Inference System
SVM	Support Vector Machine
ML	Machine Learning
LV	Low Voltage
COMSOL	Multiphysics is a cross-platform finite element analysis
SPL	Sound Pressure Level
PZT	Lead Zirconate Titanate

Symbol	Meaning
$1 - \phi$	Single-Phase
$3 - \phi$	Three-Phase
V_d, V_q, I_d, I_q	Quadrature voltage and current quantities
V_{vd}, V_{vq}	d and q axis set-points of the virtual complex impedance
V_{odq}, i_{odq}	Inverter output d-axis voltage and currents
V_a, V_b, V_c	Three phase grid voltage quantities
V_{PCC}	Voltage at point of common coupling
V_n	Nominal system voltage in Volts
V_{ref}	Reference voltage
V_{DC}	DC side Voltage in Volts
I_g, I_{DG}	Output currents of grid and DG $\omega^*, V^*, \omega_n, V_{dn}$ Reference and nominal frequency and voltage
m_p, n_q	Frequency and voltage droop gains
ω_0	Grid nominal frequency
ω_g	Grid synchronization frequency
ω_c	Low pass filter cut-off frequency
ω_L, V_L	Lower limit of frequency and voltage in droop characteristics/curve
$\omega_{min}, \omega_{max}, V_{max}, V_{min}$	Minimum and maximum allowable frequency and voltage ranges
$P - \omega / P - f$	Frequency droop
$Q - V$	Voltage droop
S	Apparent power in VA
P	Active power in W
Q	Reactive power in VAR
$P1, P2, P_g, Q1, Q2, Q_g$	Real and reactive power output of DG _{1,2} and grid
P^*, Q^*	Reference active and reactive power ratings of DG _{1,2}
\hat{p}, \hat{q}	Instantaneous active and reactive power ratings of DG _{1,2}
P_{max}, Q_{max}	Maximum allowable power ratings of DG _{1,2}
P_{Load}, Q_{Load}	Real and reactive power demand of load
f_0	Resonance frequency
Q_f	Quality factor
F	Feed-forward gain

$k_{pv}, k_{iv}, k_{pi}, k_{ii}$	Proportional and integral gains of the PI controller
τ_v, τ_i	Time constants of voltage and current controller
d, q	Rotating reference frame quantities
α, β	Stationary orthogonal reference frame quantities
θ	Rotational angle
ϕ	Angle b/w voltage and current
δ	Power angle
γ, θ_{GC}	Grid and the DGs phase angles
$\Delta e / \sin(\gamma - \theta)$	PLL Phase error
$[T]$	Transformation matrix
Z	Line impedance in $\Omega/\text{unit length}$
R_V, L_V	Resistance and inductance of virtual impedance controller
R_i, R_g, L_i, L_g	Inverter and grid side resistance and inductance
C_{DC}	DC side capacitor in Farads
C_f	Filter capacitance
$R_{Load}, L_{Load}, C_{Load}$	Resistance, inductance, and capacitance of load
E	Young's Modulus of elasticity Charge coefficient of piezoelectric
dA	Space of the terminal electrodes in m^2
d_{33}	Charge coefficient of piezoelectric
ϵ	Strain applied
ν	Poisson's proportion
R_0	Radius of the diaphragm in m
ρ	Material density in kg per m^3
R_{ad}	Acoustic resistance in $Pa.s/m^3$
P_{in}	Inlet pressure applied to the diaphragm in Pa
P_d	Pressure at the diaphragm in Pa
M_{ad}	Acoustic mass in kg
C_{ad}	Acoustic compliance

Chapter 1

INTRODUCTION

1.1 Introduction

Coal and other fossil fuels constitute the principal conventional energy sources within the global traditional power system's network. A growing number of renewable energy sources, such as solar and wind energy, have now been used because of the exhaustion or depravity of existing energy sources as well as their impact on environmental damage. As conventional sources of energy such as coal and fossil fuels deteriorate and daily load demand rises, renewable energy sources and nonrenewables including such wind, solar, microturbines, and fuel cells, as well as storage technologies like supercapacitors and batteries, will become more important (Carreras et al., 2004, Nichols et al., 2006).

A microgrid is defined as a collection of these resources connected to supply the appropriate amount of load demand. Microgrids have recently drawn the interest of researchers, manufacturers, and businessmen due to their economic and environmental importance in terms of intrinsic advantages. Small-scale distributed generation systems (DGs) are a method of producing electricity near the load center or end customers. When used in conjunction with a power electronics (PE) interface, DGs can improve reliability and efficiency. To optimize performance or attain a good overall system capacity, inverters are frequently paralleled in power systems. When compared to a single centralized source, parallel operation of inverters provides improved reliability since if one of the inverters has failed, the remaining (n-1) inverters can provide the load with the power it requires. The growth of renewable energy sources has aided this (Mohd et al., 2010).

On the distribution and transmission networks at load centers, DGs can provide power ranging from a fraction of a kW to around 100 MW. A distributed system, on the other hand, cannot be given a standard definition of power rating because the rating is strongly dependent on the system's development and implementation (Ackermann et al., 2001).

In (Dragicevic et al., 2017), Various microgrid control decentralized and distributed technologies are described. When compared to conventional generators, the PE interface between DGs and the utility grid is more flexible and efficient in terms of control (Pouresmaeil et al., 2013) (Vijay et al., 2017). However, for the isolated functioning of a microgrid with several PE-based DGs, there are technical concerns such as proportionate load power-sharing, voltages, total harmonic distortion, frequencies level maintenance, and so on. As a result, control of PE-based DGs is critical, and many control approaches have been developed to improve their stable functioning. The IEEE standard 1547 specifies the technical requirements for connecting DG units to the electrical grid.

1.2 Configuration of microgrid

A microgrid is a grid on a small scale. To meet the required amount of load demand, a group or cluster of DGs, combining renewable and nonrenewable energy sources includes small hydropower, biomass energy, wind energy, solar energy, and geothermal energy, fuel cells, microturbine, IC engines, energy storage, and integrated CHP, are connected. The Microgrids can be grid-connected or island-based and it acts as a distinct controlled unit capable of delivering enough power toward its local area. Figure 1.1 depicts the fundamentals of AC microgrid construction.

The design comprises of three radial feeders which have been linked to the grid utility via an isolating switch at the common coupling point (PCC). The voltage, current, and frequency of the DGs are all controlled by a microgrid central controller (MGCC) and The PCC's frequency and voltage variations are controlled by the MGCC. The circuit breakers provided at each feeder start location allow critical feeders (such as DGs and critical loads) to serve loads autonomously from the main grid. Most of the other local loads and DGs are controlled by local controllers (LCs). Setpoints originate from the MGCC, however, choices are made at the local level instead of the

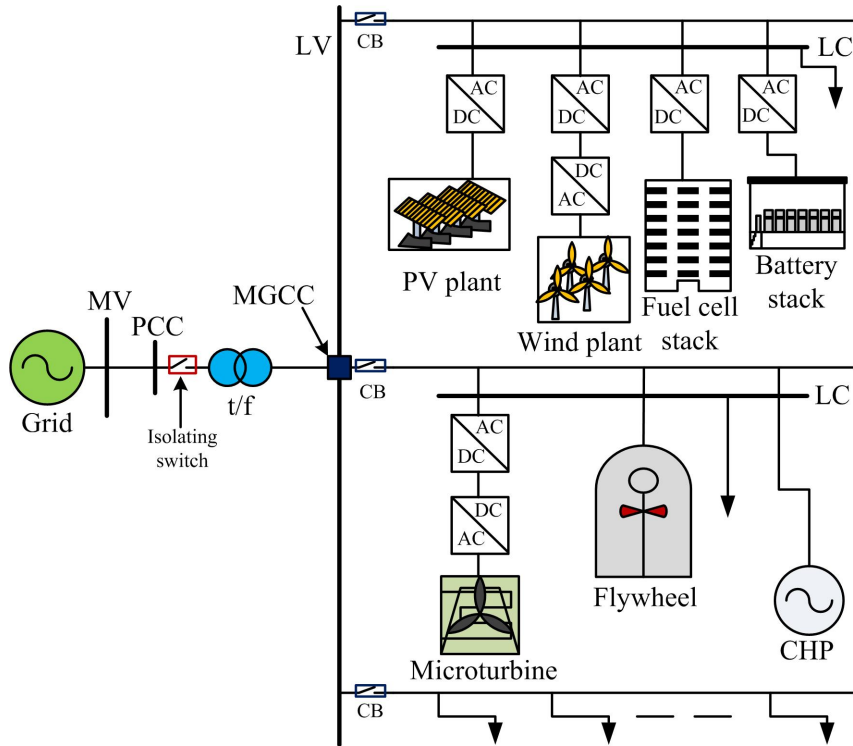


Figure 1.1: Basic AC microgrid architecture.

centralized level.

As a basic steady-state analyzer for any electrical network, power flow analysis is crucial for the implementation and management of microgrids since it provides an overall perspective of the system. It could be used for microgrid network service asset and configuration optimization during the basic stages of the microgrid. It could potentially be utilized for congestion management and real-time power regulation while in operation. In a power system network, power flow analysis can be utilized to perform security and protection coordination. It can also be used to get started with system dynamics and small-signal analysis. Power flow analysis could be included as part of a comprehensive energy management system (Lasseter, 2002).

1.3 Microgrid classification and control

1.3.1 Classification of microgrid

Microgrids can be $1-\phi$ or $3-\phi$ systems, and they can indeed be coupled to low-voltage (LV) or medium-voltage (MV) systems in either islanded or grid-connected operation modes. Both types of operation have their own set of controls and specifications perspectives (Wang et al., 2012, Eid et al., 2016). Figure 1.2 summarises the overall categorization of a microgrid.

There are several ways to categorize microgrids, including the following:

- When it comes to power sources, whether AC or DC.
 - DC microgrids.
 - High-frequency AC (HFAC) microgrids: Reduces the influence of variations in renewable-based DGs in the microgrid and resolves issues with power quality induced by the usage of many converters.

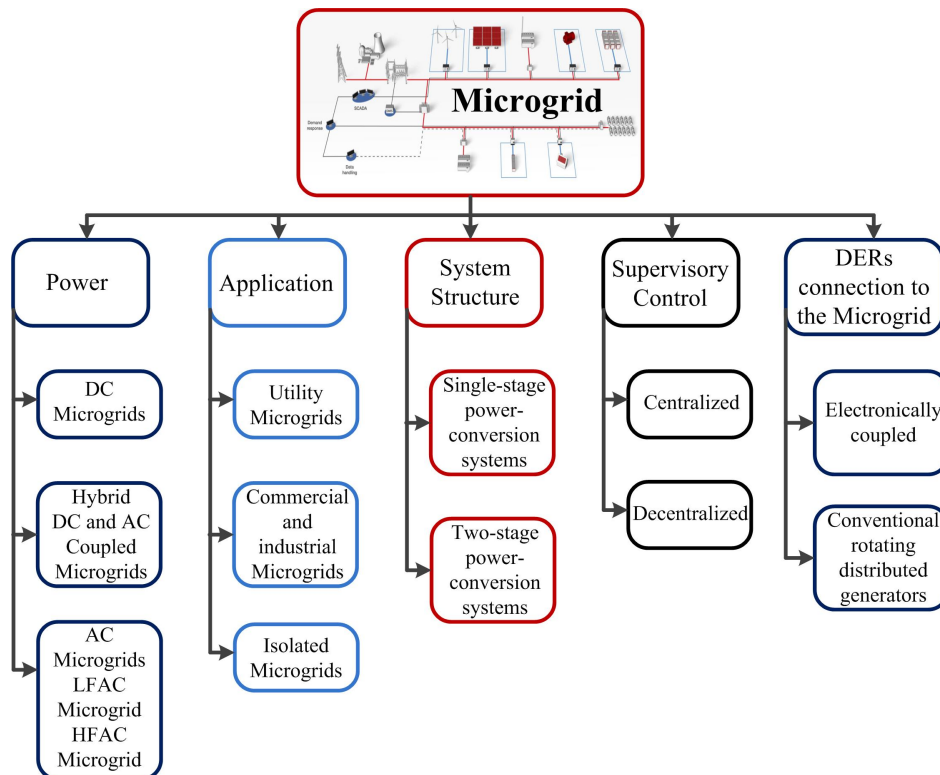


Figure 1.2: Overall classification of microgrid.

- Since the initial proposal of the microgrid, line-frequency alternating current (LFAC) has received the most attention.
- Microgrids that are both AC and DC linked.
- They can be grouped into three groups based on the application they are used for.
 - Utility microgrids: A microgrid is a small part of town.
 - Microgrids for industrial and commercial applications (commercial and industrial).
 - islanded microgrids.
- They fall into two categories in terms of system structure, it could depend on how many stages there are in the power processing.
 - Power-conversion systems with only one stage of conversion (AC-DC or DC-AC).
 - The most typical configuration for any electronically connected DG with a power conversion system has two stages (AC-DC-AC or DC-AC-DC).
- They can be either centralized or decentralized in terms of supervisory control.
 - Centralized control: A microgrid's central controller delivers the appropriate set points over a two-way communication system, sends set points to the LC channel, although the method is inefficient and redundant.
 - decentralized control: Technique is a multi-agent system that allows for system flexibility and communication between two agents via communication languages.
- In terms of the microgrid's connectivity to the DGs.
 - Electronically interconnected.
 - Rotating distributed generators in the conventional insight.

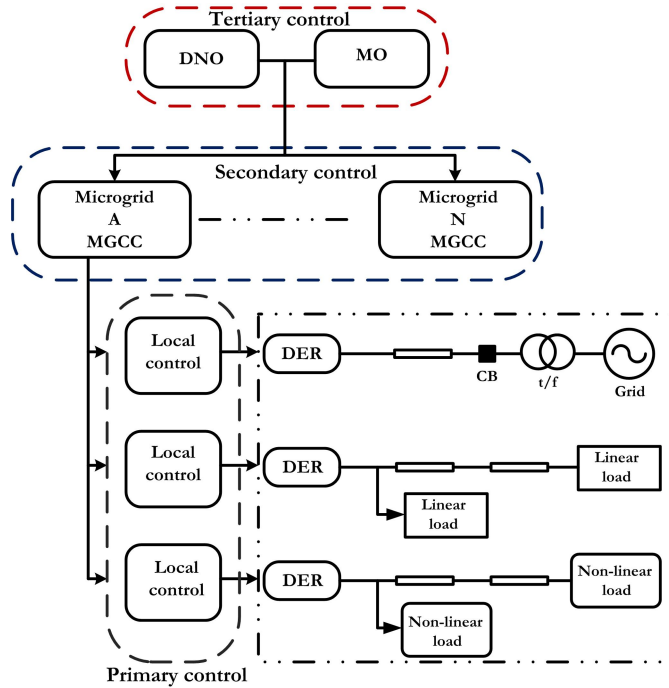


Figure 1.3: Layers of the microgrid hierarchy (multi-agent controller).

1.3.2 Control of microgrid

To serve in both grid-connected and standalone modes, the microgrid system should always be structured as a complete in terms of control levels. IEEE 1547-2003 specifies how the microgrid connects to the grid. Grid disruptions can be smoothed considerably by using the appropriate control measures while switching from grid-connected to autonomous mode. The microgrid ought to be self-sufficient, with frequency and voltage operating inside of acceptable boundaries. A schematic of the microgrid's control layers can be found in Figure 1.3 (Eid et al., 2016), which shows the distribution network operators and market operators as well as the microgrid's control center MGCC and the load controller (LC), that further could either be the source regulator or a small micro load regulator, as secondary controls.

The hierarchical control levels can be used to fulfill microgrid control objectives. The International Society of Automation's ANSI/ISA-95 is a global standard for establishing an automatic interconnection among enterprise and control mechanisms. This standard was created with global producers in mind. It was created to be used in a variety of industries and processes, including process types including batch, continuous, and repeated. ISA-95's objectives are to give the following: standard

vocabulary as a framework as a basis for establishing an automation framework and how data would have to be used, standardized data models, and uniform operational models for vendor and producer interactions (Guerrero et al., 2011). The following are the zero to three levels that can be used to adjust ISA-95 toward the operation of an MG:

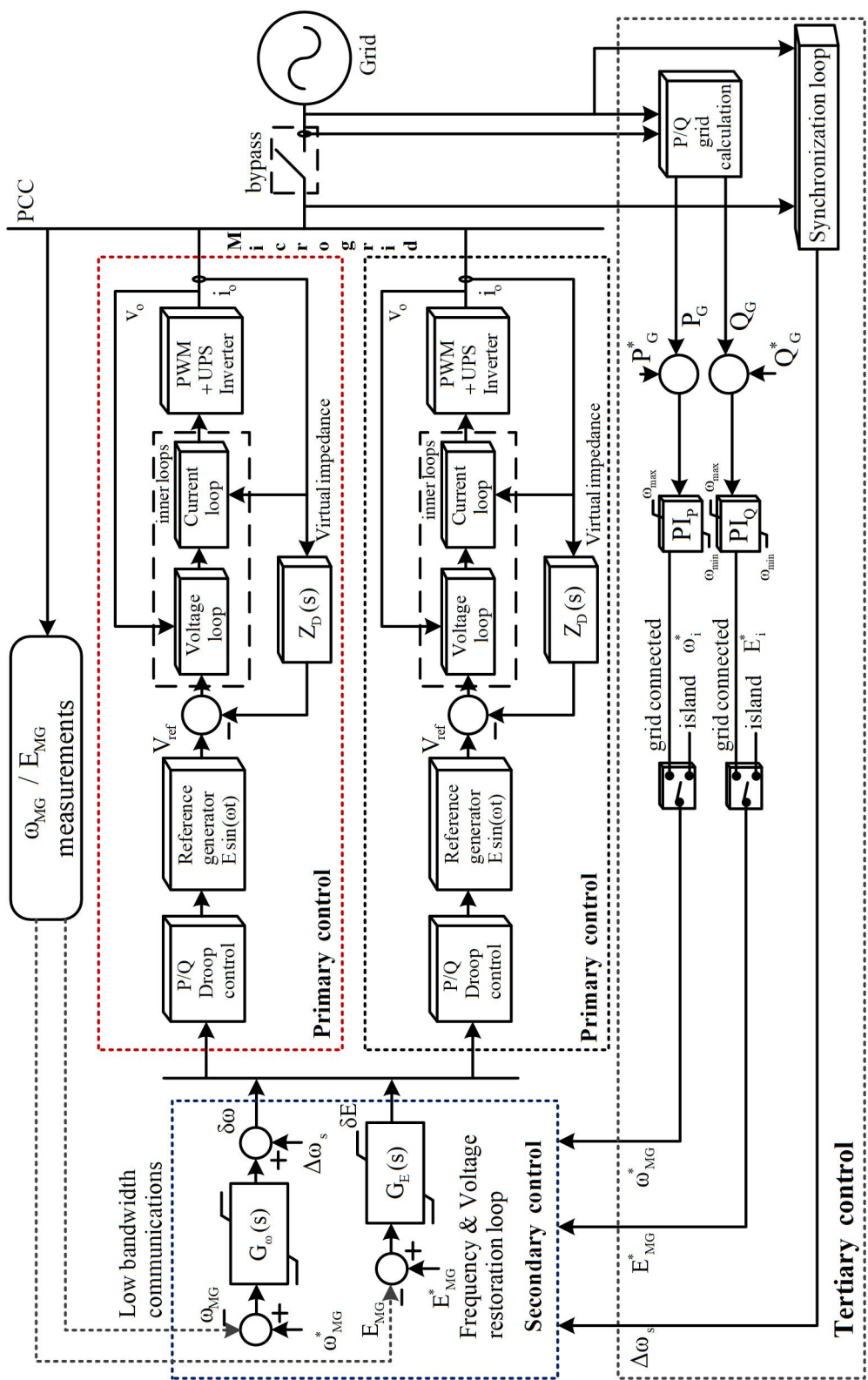


Figure 1.4: Hierarchical AC microgrid control block diagram.

- Tertiary control: The transmission of energy among the MG and the grid is controlled by this energy-production level.
- Secondary control: Ascertains about the electrical parameters are in MG are in acceptable limits. It may also feature a synchronization control loop that allows the MG to be seamlessly connected to or disconnected from the distribution system.
- Primary control: At this level, droop-based control is commonly employed to approximate physical mechanisms that make the system more reliable and attenuated. To replicate the behavior of physical output impedance, the controller incorporates a virtual impedance loop.
- Inner control loops: Each module's regulatory difficulties are incorporated into this level. To modulate the output current and voltage while maintaining the system balanced, there are several strategies available, including voltage and current feedback, feedforward control, and linear/nonlinear controllers.

Figure 1.4 shows a schematic of the control hierarchy of an AC microgrid. where G_ω and G_E are the frequency and amplitude restoration controllers when the grid is not present, $\Delta\omega_s$ is a synchronization term that stays at zero. For the droop approach and the virtual complex impedance control loop, the primary control relies solely on the local output measurements (voltage and current) to evaluate active (P) and reactive (Q). The deviations caused by the first control will be corrected by the secondary control. To link from a microgrid to the main grid, we must first identify the grid's voltage and frequency, it will serve as a basis of reference to the secondary control loop. The synchronization control loop depicted in 1.4 will synchronize the phase between the grid and the MG.

The following sections provide an in-depth insight into control methodologies for microgrid operating autonomously.

1.3.2.1 Communication based

Because of the necessity of microgrids, many control mechanisms have been devised to ensure that the microgrid operates in a stable state (Arunan et al., 2017). Communication-based control techniques necessitate communication links between

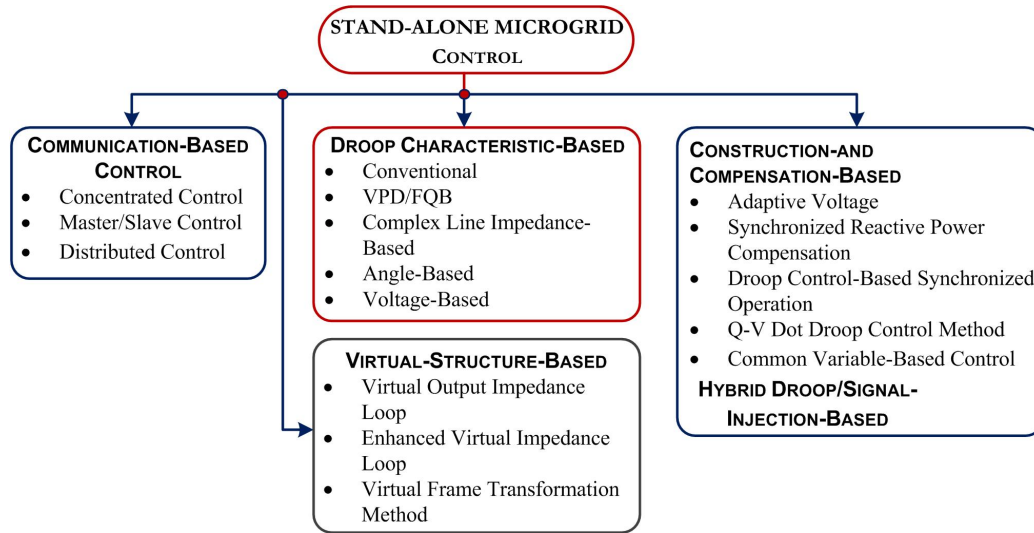


Figure 1.5: Overview of microgrid controls for islanded operation mode.

modules, which raises the system’s cost. Long-distance communication links will be more susceptible to interference, lowering system dependability, and limiting system expansion. As a result, communication lines are frequently avoided, particularly when large distances and substantial investment costs are involved. It is commonly required to operate without communication connectivity to connect remote inverters. It can aid in the redundancy and reliability needs of a supervisory system while avoiding complexity and high costs. Furthermore, because the modules are plug-and-play, a system like this is simple to expand because it is necessary to replace one module instead of actually bringing the overall system to a standstill. Different approaches of control are depicted in Figure 1.5 (Malik et al., 2017)(Han et al., 2016).

- **Concentrated control:**

(Shanxu et al., 1999, Abdelaziz et al., 2014) presents the concentrated/central control method. The control technique necessitates the use of common synchronization signals and units which share current. The Phase-Locked Loop (PLL) within every unit guarantees that the output voltage and synchronization signal have the same frequency and phase. Also, there is a total load detector in place for the current sharing units, which generates a current reference point for every unit. (Abdelaziz et al., 2014) and (Wu et al., 1994) explain the supervision of the central limit method. To ensure equitable distribution of current in CLC mode, all units should indeed be configured the same way and each unit should

monitor the average current.

Reference (Abdelaziz et al., 2014) presents a multistage centralized control strategy for plug-in electric vehicles with a high penetration rate (PEVs). The coordination makes it possible for PEVs to contribute significantly to the efficient and effective operation of the islands' microgrids. The benefit of using a concentrated strategy is that it keeps current sharing constant even when the load changes. Therefore, this method of surveillance necessitates the use of a centralized controller, which makes system expansion difficult and diminishes redundancy. Furthermore, to achieve synchronization among the units, current reference must be provided to all converters via high-bandwidth communication lines. A single-point failure can put the security of communications systems at risk.

- **Master/Slave control:**

On individual inverters, control of the master/slave technique is employed to achieve parallel control unit operation. The primary parallel module, which is equipped with the appropriate control, performs the function of a master inverter, which is in charge of paralleled control, via a mode-selecting switching configuration, while the rest act as slave inverters (Siri et al., 1992, Pei et al., 2004). To facilitate plug-and-play integration, the master-slave control strategy leverages the grid link as the master control at the common between grid and DG and ensures effective and reliable microgrid function under all operational conditions (Caldognetto and Tenti, 2014).

- **Distributed control:**

Parallel converters frequently use distributed control (Prodanovic et al., 2000, Mahmud et al., 2014, 2019). The distribution of momentary average current seems to be a popular distributed control for parallel converters. In this type of control, each inverter has its own control circuit, so there is no need for a central controller. Furthermore, average current sharing necessitates the voltage reference synchronization and utilization of a current sharing bus. The current sharing bus provides an additional current control loop so every converter is usually required to follow the same reference current. When a module fails, it can effortlessly separate from the microgrid while the rest of the modules con-

tinue to function regularly in parallel. For frequency restoration and economic dispatch, reference (Xin et al., 2015) employs a completely distributed control mechanism. The most significant benefit of using DGs is that they will always share loads based on their incremental costs.

In (Mahmud et al., 2014), The distribution of active and reactive power is handled by a robust distributed controller. It achieves robustness by utilizing partial feedback linearization and taking structured uncertainty into account. The basic power-sharing and voltage regulation are both well-managed. But, interconnections between inverters are still required as a result system’s flexibility and redundancy is reduced. (Vrdoljak et al., 2010) present a methodological approach for a discrete-time sliding mode-based load frequency regulator for power systems.

1.3.2.2 Droop characteristic based

To connect remote inverters, it is often necessary to operate without communication links. It can help a supervisory system’s redundancy and reliability requirements while avoiding complexity and expensive costs.

- **Conventional:**

To enable power-sharing in parallel inverters without communication, the classic frequency and voltage droop control is provided. The basic idea behind the conventional droop control is explained in section 1.4.

- **VPD/FQB:**

As a result, the features to note that ”voltage active power droop (VPD) and frequency reactive power boost (FQB)” alternately studied (Guerrero et al., 2005, 2007), as equations (1.1) and (1.2).

$$\omega_i = \omega_{rated} + m_Q * Q_i \tag{1.1}$$

$$E_i = E_{rated} - n_P * P_i \tag{1.2}$$

Using an extremely resistive transmission system to control low-voltage ac microgrid is easier with this type of control. The VPD/FQB approach, on the

other hand, is highly dependent on system factors, which severely limits its applicability. It's also unable to effectively distribute the burden of active current.

- **Complex line impedance-based:**

In (Moawwad et al., 2013), a PQV-droop approach is being provided to help control and manage the voltage at the common point while simultaneously powers are controlled and regulated. The elimination of sharing errors improves the accuracy of sharing, which is initiated by reduced frequency synchronization signals. The process of error elimination, on the other hand, will reduce the output voltage amplitude (Han et al., 2016). The voltage magnitude is affected by both active and reactive powers in electric systems with complex impedance. In addition, to compensate for line impedance issues and enable effective power-sharing, additional loops such as impedance voltage drop estimator (Li and Kao, 2009), grid parameters estimator (Vasquez et al., 2009), and reactive current loop (Hanaoka et al., 2003) have indeed been incorporated into the standard droop control system.

- **Angle-based:**

In (Majumder et al., 2009, 2010) recommends controlling voltage drop by altering the phase angle for distributed source voltages with relation to a common time reference for the entire system. Then using an angle droop allows for effective DG load distribution without degrading the system's frequency in an undesired way, and it also has the advantage of not restricting the selection of droop gain like typical frequency droop regulation entails. There's no need for DGs to communicate with each other, as well. Because of this, unless the local control systems are not even in synchronization, a defect in the inverters' crystal clocks allows their frequencies to vary significantly, causing phase limits to be breached over a certain period and leading to system instability. It's been hypothesized that DGs might be synchronized using the controller network infrastructure bus/system. A further investigation into the loss synchronizing signal in certain DG units is required.

- **Voltage-based:**

The output voltage's permissible range is fully utilized by the voltage-based control strategy. DGs are dispatched appropriately in this range because they

are operating at their highest power tracking point. This is especially beneficial for DGs, as it allows them to utilize their energy more efficiently.

1.3.2.3 Virtual structure based

First, the AC microgrid needs to be linked to the DG, then a virtual impedance can be carefully adjusted to prevent current spikes.

- **Virtual output impedance loop:**

The virtual complex output impedance technique has been utilized for avoiding the coupling of active-reactive power (P and Q) (Guerrero et al., 2005, 2013). The quick control loops of the droop strategy are used to build this control approach. As a result, it is possible to alter the predicted voltage. Considering the time-variant virtual output impedance can help with soft starting.

- **Enhanced virtual impedance loop:**

For good reactive and harmonic power exchange, the upgraded virtual impedance control technology is implemented. The controller reduces the DG unit's equivalent harmonic impedance rather than extracting the fundamental and harmonic components. As a result, the DG's equivalent harmonic impedance is reduced. It does, however, demand a working knowledge of line impedance considerations and low-bandwidth communications (He et al., 2013).

- **Virtual frame transformation method:**

The virtual frame transformation (De Brabandere et al., 2007, Lee et al., 2009) is another way based on a virtual structure. Both of the output line's reactance (X) and resistance (R) should be addressed in general.

1.3.2.4 Construction and Compensation Based

Control approaches based on construction and compensation principles have recently been developed by several academics.

- **Adaptive voltage droop control:**

In (Rokrok and Golshan, 2010), it provides a new adaptable voltage droop methodology enabling parallel operation of DGs in islanded AC microgrid. This reactive power control (Q - V) adds two additional terms as follows:

1. The voltage loss across transmission lines
2. Term to maintain system stability while increasing reactive power-sharing during high load situations

To improve system disturbance-rejection capabilities and power-sharing efficiency, (Zhang et al., 2016) created a sliding-mode direct voltage loop as well as upgraded droop-power loop technologies with virtual $-ve$ impedance.

- **A synchronized method of compensating reactive power:**

The accuracy of sharing reactive power can be increased by including a disturbance in the real power which is triggered by low-frequency synch signals from the central unit and calculates the actual reactive power control error (He and Li, 2011, 2012). The standard reactive power droop control has been given a delayed integration period to address the concerns with sharing reactive power. The synchronized reactive power compensation technique induces a coupling term (real-reactive power) to discover difficulties in sharing reactive power and enhance the consistency of sharing. A central controller's synchronization signals are essential to ensure proper functioning. It can be compared to an event-triggered universal system with a common basis.

- **Droop control-based synchronized operation:**

The approach primarily consists of two key operations. (Han et al., 2015)

- Operation to reduce errors
- Operation to restore voltage

The synchronization signals with a narrow bandwidth activate the error minimization mechanism in sharing, thereby increasing sharing effectiveness. The process of reducing errors, on the other hand, will reduce the output voltage amplitude. As a result, to compensate for the decrease, the voltage recovery procedure is proposed. This method requires relatively little communication, and plug-and-play is avoided.

- **Droop Control Method $Q-\dot{V}$:**

To increase the sharing of reactive power (Lee et al., 2013a,b), this technique creates relationships between reactive power and at which the rate of DG voltage changes \dot{V} . The droop controller Q- \dot{V} is written as (1.3)

$$\begin{aligned} \dot{V}_x &= \dot{V}_{0x} - n_x(Q_{0x} - Q_x) \\ \dot{V}_x &= \dot{V}_{0x} + \int_{\mathbf{t}} \dot{V}_x dx \end{aligned} \quad (1.3)$$

The control outcome in the proposed control technique is linked to the voltage change rate's beginning condition. Stable-state solutions may not exist, despite the system's stability. Furthermore, Power-sharing approaches are not necessarily preferable to traditional methods in terms of performance. The integral in equation (1.3) tries to maintain voltage with a localized control loop for whom the response is based on the integrator's initial conditions, resulting in an unstable system. As a result, these controllers would be inappropriate for microgrid practical applications.

- **Method of control based on Common variable:**

The sharing of both active power and reactive power requires a variable-based approach. The sharing of reactive power is particularly challenging to establish due to the imbalance seen between DG and the microgrid. output interface inductors. A reactive power-sharing approach that can be adjusted has been proposed by several researchers, similar to active power regulation, in which an inbuilt controller regulates the common bus voltage V_{com} (Sao and Lehn, 2008)-(Zhong, 2013b).

$$E_i = k_q \int (V_{ref} - V_{com} dt) \quad (1.4)$$

where, k_q is the integer gain and V_{ref} is given by equation (1.5).

$$V_{ref} = E^* - D_Q Q_i \quad (1.5)$$

Each DG's V_{com} and V_{ref} are equivalent in steady-state condition. Furthermore, the steady-state reactive power is estimated using the equation (1.6).

$$Q = \frac{E^* - V_{com}}{D_Q} \quad (1.6)$$

It is known from the equation (1.6) that every DG's reactive power is equivalent. The reactive power regulation will then be unaffected by microgrid operation settings. In conclusion, the control technique based on a shared variable may accomplish precise proportionate load power-sharing between parallel DGs while being robust to changes in system parameters. Nevertheless, these approaches have the drawback as a result of the requirement for load voltage information being hard to monitor when the DG and the common bus are separated by a large distance. Furthermore, when the establishment of an AC microgrid is complicated, the common voltage may not exist in a distributed real system with dispersed loads. In (Rezaei and Soltani, 2015), an adaptive sliding mode control in voltage controller is presented to compel the master DG unit's voltage and frequency to follow predetermined directions.

1.3.2.5 Method Using a Combination of Droop and Signal Injection

With the signal injection technique, reactive power-sharing being adequately managed and line impedance fluctuations are not an issue (Tuladhar et al., 2000, Perreault et al., 1998). It's capable of dealing with both the loads (linear and nonlinear), depending on circumstances. Two separate control variables make it simple to share actual and reactive powers amongst the DGs:

- Power angle
- Voltage amplitude

Adding external communication, on the other hand, is not wanted. Because power balancing and system sustainability are dependent on each of these signals, such communications add complexity and impair reliability. Voltage control is not guaranteed. The method's intricacy and the requirement for measuring and creating high-frequency components are other drawbacks. Furthermore, the signal injection approach can degrade power quality, increasing transmission line losses due to the harmonic current generated by the process. In addition, the injected signal may cause inter harmonics and resonance. This strategy may reduce system stability by

adjusting the voltage droop bandwidth. Harmonic virtual impedance is presented as an option in (He et al., 2013). The research provides a virtual impedance control technique for distributed generation (DG) units. At fundamental and a few selected harmonic frequencies, the suggested approach can achieve accurate adjustment of DG unit corresponding impedance.

1.4 Basic idea behind the conventional droop control

Because of its inherent advantages for parallel-connected DG systems, the droop control technique in the primary control layer is the most commonly employed control strategy. Initially, the traditional P - ω (frequency droop control) is presented to enable power-sharing in parallel inverters without communication (Chandorkar et al., 1993, De Brabandere et al., 2007). The primary idea behind this method is to replicate the behavior of synchronous generators (Pogaku et al., 2007, D'Arco and Suul, 2014). Droop control is notable for avoiding the use of control signals to communicate across inverters and instead relying solely on the measurement of local feedback variables. Figure 1.6 and equations (1.7) and (1.8) depicts the flow of power at point A (Weedy et al., 2012).

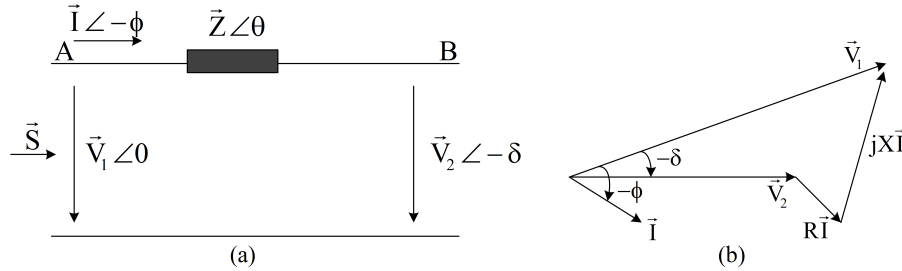


Figure 1.6: (a) Power flow, and (b) equivalent model's phasor diagram.

$$\vec{S} = \vec{V}_1 \vec{I}^* = \vec{V}_1 \left(\frac{\vec{V}_1 - \vec{V}_2}{\vec{Z}} \right)^* \quad (1.7)$$

$$\vec{S} = V_1 \left(\frac{V_1 - V_2 e^{j\delta}}{Z e^{-j\theta}} \right) = \frac{V_1^2}{Z} e^{j\theta} - \frac{V_1 V_2}{Z} e^{(\theta+\delta)} \quad (1.8)$$

The active and reactive power flow are expressed by the equations (1.9) to (1.12).

Table 1.1: Parameters for various kinds of networks

Network	Line re- sistance ($R_g\Omega/km$)	Line re- actance ($X_g\Omega/km$)	Ratio (R_g/X_g)
Low Voltage	0.642	0.083	7.7
Medium Volt- age	0.611	0.190	0.85
High Voltage	0.060	0.191	0.31

$$P = \frac{V_1^2}{Z} \cos\theta - \frac{V_1 V_2}{Z} \cos(\theta + \delta) \quad (1.9)$$

$$Q = \frac{V_1^2}{Z} \sin\theta - \frac{V_1 V_2}{Z} \sin(\theta + \delta) \quad (1.10)$$

$$P = \frac{V_1}{R^2 + X^2} [R(V_1 - V_2 \cos\delta) + X V_2 \sin\delta] \quad (1.11)$$

$$Q = \frac{V_1}{R^2 + X^2} [-R V_2 \sin\delta + X(V_1 - V_2 \cos\delta)] \quad (1.12)$$

The simplified equations (1.11) and (1.12) can be rewritten as equations (1.13) and (1.14).

$$V_2 \sin\delta = \frac{XP - RQ}{V_1} \quad (1.13)$$

$$V_1 - V_2 \cos\delta = \frac{RP + XQ}{V_1} \quad (1.14)$$

Line impedances in medium and high-voltage networks are mostly inductive, with $X \gg R$, which implies R can indeed be neglected. When power angle (δ) is quite low, then $\sin\delta$ is equal to δ and then $\cos\delta$ becomes 1. The equations (1.13) and (1.14) will then be rewritten as equations (1.15) and (1.16), respectively. The typical line parameters for low voltage (LV), medium voltage (MV) and high voltage (HV) lines are depicted in Table 1.1 (Laaksonen et al., 2005).

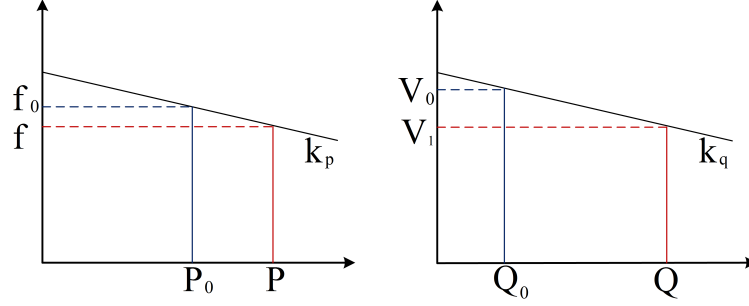


Figure 1.7: Control characteristics for frequency and voltage droop.

$$\delta \cong \frac{XP}{V_1 V_2} \quad (1.15)$$

$$V_1 - V_2 \cong \frac{XQ}{V_1} \quad (1.16)$$

Equations (1.15) and (1.16) demonstrates that now the δ is dominated by P , and the voltage difference is dominated by Q for a small δ , and a voltage difference $V_1 - V_2$ for $X \gg R$. To put it another way, the angle δ could indeed be managed while controlling P , whereas the voltage of inverter V_1 may be regulated by regulating Q . As a result, the P and Q are dynamically controlled through frequency and voltage control respectively.

Through varying P and Q separately, the amplitude of the grid voltage and frequency can be controlled. These observations serve as the basis for the equations (1.17) and (1.18).

$$f - f_0 = -k_p * (P - P_0) \quad (1.17)$$

$$V_1 - V_0 = -k_q * (Q - Q_0) \quad (1.18)$$

The rated frequency and grid voltages are f_0 and V_0 , respectively, and the (momentary) inverter's active and reactive power setpoints are P_0 and Q_0 , respectively. A visual representation of frequency droop and voltage droop characteristics may be seen in Figure 1.7.

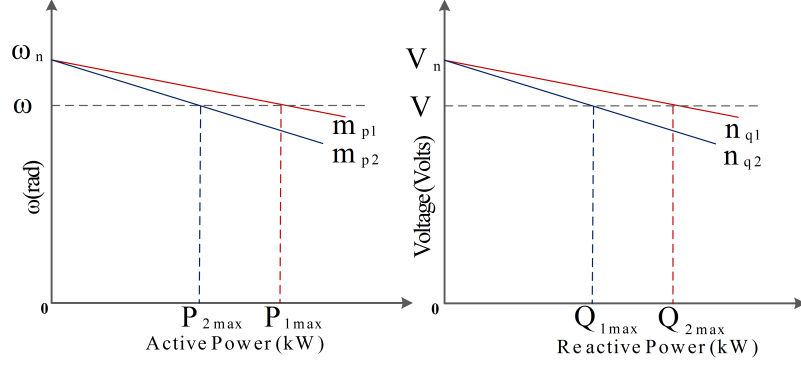


Figure 1.8: Comparing the droop characteristics of two different-rated inverters connected in parallel.

1.4.1 Droop control for parallel connected inverters

A single inverter module will be unable to meet the load demand requirements. Two or more inverters must be linked in parallel in such instances. The open-circuit frequency and voltage of the inverter are both unique. As a result, if they were simply paralleled without any extra regulation, huge circulating currents would emerge. To solve these problems an artificial droop in inverter frequency and voltage are introduced as shown in equations (1.19) and (1.20).

$$\omega^* = \omega_{ni} - m_{pi}P_i \quad (1.19)$$

$$V^* = V_{ni} - n_{qi}Q_i \quad (1.20)$$

ω_n and V_n are the nominal operating frequency and system voltage respectively. And m_p and n_q are the frequency and voltage droop coefficients. While the active and reactive powers of the i^{th} inverter are P_i and Q_i respectively. The first inverter is represented by replacing i with 1, while the second inverter is represented by $i=2$.

In (Bush, 2014) the slope % indicates the slope coefficients. That is the proportion or a ratio of the measured quantity variation that causes a 100% change in the controlled quantity. For a % increase in m_p , a % decrease in frequency will result in a 100 percent increase in active power output, and a % increase n_q will result in a 100 percent increase in reactive power output. Figure 1.8 (Pogaku et al., 2007) shows the droop features coefficients of two different rated inverters (m_p and n_q) are computed using equation (1.16) for the specified frequency and voltage.

$$m_{pi} = \frac{f_{max} - f_{min}}{P_{i_{max}}} \quad (1.21)$$

$$n_{qi} = \frac{V_{0dmax} - V_{0dmin}}{Q_{i_{max}}} \quad (1.22)$$

In (He and Li, 2012), an improved technique for proportional load-sharing in a meshed parallel inverters system with complex impedance is proposed. In (Saha et al., 2008), a full modeling and performance study of the microgrid in grid-connected and islanded mode with a microturbine-based distributed generation system is described. In (He et al., 2013), the detailed modeling microgrid system for tiny signal stability analysis is described, along with experimental verification results. In an isolated microgrid, hierarchical control strategies are utilized in addition to conventional droop control and virtual impedance schemes to accomplish proportionate power-sharing.

The proportionate power-sharing between inverters is determined from the values of drop coefficients for distinct inverters. Throughout many systems, the P - ω characteristics are inflexible, and the frequency variation from no load to full load is incredibly small (Chandorkar et al., 1993). If the value of m_{p2} becomes bigger than the value of m_{p1} , ω_2 would begin to drift below ω_1 . As a consequence, the vector V_2 will lag behind the vector V_1 , increasing the power flow between Inverter 1 and Inverter 2. As an outcome, Inverter 1 would be in responsible of considerably higher percentage of the load. The maximum frequency and voltage variations, and also the inverter rated power, determine m_p and n_q . For instance, in a microgrid of n DGs, the associated m_p and n_q must fulfil the minimum constraints (Rokrok and Golshan, 2010), as following equations (1.23), (1.24):

$$m_{p1}P_{n1} = m_{p2}P_{n2} = \dots = m_{pn}P_{nN} = \Delta\omega_{max} \quad (1.23)$$

$$n_{q1}Q_{n1} = n_{q2}Q_{n2} = \dots = n_{qn}Q_{nN} = \Delta V_{max} \quad (1.24)$$

A combined power-frequency curve could be constructed for the entire system's inverters. Similarly t the integrated load curve is also specified. For a stable operation, the inverters must output an amount of power equal to that of the loads. The steady-state network frequency will change as the change in the load due to the combined power-frequency curve's rigidity. A slower outer loop can then even regain the ability to restore nominal values. For the inverters, equations (1.17) and

(1.18) must be adjusted to restore the frequency and voltage of P_{ni} and Q_{ni} . This is the same as vertically changing the power-frequency curve. A master controller can restore frequency in a gradual, coordinated manner by employing a slow communication channel between the inverters (Chandorkar et al., 1993). Furthermore, a higher droop gain value enhances power-sharing accuracy while increasing frequency/voltage deviation from normal values, resulting in a trade-off among both voltage-frequency and precision in sharing the load for droop technique (Guerrero et al., 2011).

The droop control have been applied to parallel connected inverters based DGs to avoid communication means while obtaining good power sharing. However, although this technique achieves high reliability and flexibility, it has several drawbacks that limit its application. Some of them are listed below: :

- Since there is only one control variable for each droop characteristic, e.g., m_p for frequency droop characteristic, it is impossible to satisfy more than one control objectives. As an example, a design trade-off needs to be considered between the time constant of the control system and the voltage and frequency regulation.
- The conventional droop method is developed assuming highly inductive effective impedance between the converter and the AC bus. However, this assumption is challenged in microgrid applications since low-voltage transmission lines are mainly resistive. Thus, equation (1.11) is not valid for microgrid applications (Sao and Lehn, 2005)(Sao and Lehn, 2008)(Vijay et al., 2021).
- As like the frequency, the voltage is not a global quantity in the microgrid. Thus, the reactive power control in equation (1.11) may adversely affect the voltage regulation for critical loads (Diaz et al., 2010).
- In case of non-linear loads, the conventional droop method is unable to distinguish the load current harmonics from the circulating current. Moreover, the current harmonics distorts the DG output voltage (Zhong, 2013a).

To overcome these shortages, modification of conventional droop control scheme is introduced in Chapter 2.

1.5 Islanding detection

DGs, which contain both conventional and renewable technologies, are becoming more prevalent in the energy system, resulting in changes to the way it looks. Active grids are becoming increasingly popular. These grids can incorporate a large number of storage units, function as islands, and be linked by flexible transmission networks. This convoluted environment would impose several requirements on DG units, depending upon the size and degree of integration with the power system. As a result, grid monitoring will remain a key function of DG units at all levels. A potential island situation in a power system with a lot of DG has always been important to detect.

As a result, except for low-power DGs, islanding detection is really not required. Because, as previously mentioned, the power system is evolving, a micro and smart grid (MSG) may be a feature of the future scenario. An MSG is typically associated to a distribution grid but can operate autonomously if the main grid encounters problems. Since the degree of interconnectivity and dependability of information flow among some of the numerous participants in this prospective situation cannot be predicted, islanding identification could be regarded an important characteristic, essential, and preferable in some situations. This islanding situation is impossible to forecast due to the extent of connectivity and dependency on information sharing. In certain cases, islanding detection is a necessary feature, while in many others, it is an option.

Grid control methods are distinct from traditional DG inverter control methods since they rely on grid to DG inverter communication. A circuit breaker (CB) was installed at the PCC to protect the DGs from unhealthy events such as grid voltage sag, swell, unbalance, harmonics, and errors, indicated in Figure 1.9. The grid's transmitter (T) generates a control signal to identify islanding when there are the disturbances, and the PCC's receiver (R) receives that signal. The control command will then be transmitted to the CB to isolate the DG (Langella and Testa, 2010).

During grid faults, communication between the DG and CB might be from a variety of island detection mechanisms. communication systems (CS) penetration in LV distribution grid is restricted to the smart metering technology (Code, 2006). However, the high installation costs have prevented these CS approaches from being widely adopted commercially. With numerous inverters acting in parallel, they may be the best methods for detecting an islanding. The following sections will provide

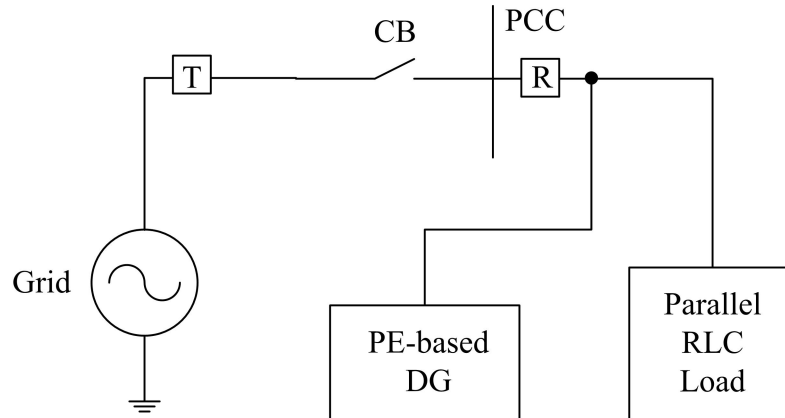


Figure 1.9: Islanding detection method.

Table 1.2: EN 50160 specification: The maximum fluctuation in grid frequency and voltage

Parameter	Minimal	Maximal
Frequency (Hz)	49 Hz	51 Hz
Voltage (p.u.)	0.9 p.u.	1.1 p.u.

an overview on islanding detection strategies for the grid-connected DG systems.

1.5.1 Overview of Islanding Detection Methods

The major purpose of the grid-connected operation is to achieve optimal and cost-effective performance. Islanding might be planned or unplanned. Even if the grid is cut off, microgrids continue to provide power to the locally connected loads. Unplanned islanding, on the other hand, is a chaotic process that should be avoided at all costs. It could happen for a variety of causes, including line trip, error by human, or equipment failure. Unplanned islanding can endanger the safety of system operators and have a significant impact on the microgrid's operation. Islanding must be identified in the event of intentional islanding, and the DGs must either be disconnected or the mode of operation changed from grid-connected to islanded. Several alternative islanding detection approaches have been proposed throughout the decades to detect islanding events that meet international requirements during grid disturbances.

The identification of islanding is largely dependent on the controller's implementation within the DG inverter control platform, which can include the following meth-

ods.

- **Passive Islanding Detection Methods:**

In the passive approaches, a change in voltage amplitude, frequency, or phase following a disconnection is detected. The NDZ for passive approaches is not zero, which is why active approaches are usually used to improve their effectiveness.

- **Active Islanding Detection Methods:**

Active techniques induce fluctuations in amplitude, frequency, and phase attributes of the PCC, which may be quantified by passive approaches. Using active techniques, the NDZ can be reduced significantly. When a significant number of inverters are connected in parallel, however, the power quality suffers, resulting in grid instability.

- **Hybrid Islanding Detection Methods:**

It is possible to detect islanding by employing passive as well as active detection techniques.

1.5.1.1 Passive Islanding Detection Methods

Passive islanding detection approaches, as the title implies, passively measure electrical parameters at the PCC to see if values are well below a pre-defined threshold. When the recorded electrical characteristics exceed a certain threshold, islanding occurs, as shown in Figure 1.10, which is most likely to occur during grid disturbances. Passive techniques rely on the monitoring of grid variables, which tend to vary when an island is present. Detection approaches for passive islanding are discussed in detail in the subsequent sections. It's worth noting that some conventional methods are provided a broader view, while newer approaches are explained in significant detail. Table 1.3 provides an overview of these strategies.

- **OUF–OUV Detection:**

Over and Under Frequency (OUF) and Over and Under Voltage (OUV) safety methods are necessary for all grid-connected DGs, allowing them to disconnect for providing power to the electrical grid if such PCC parameters exceed the

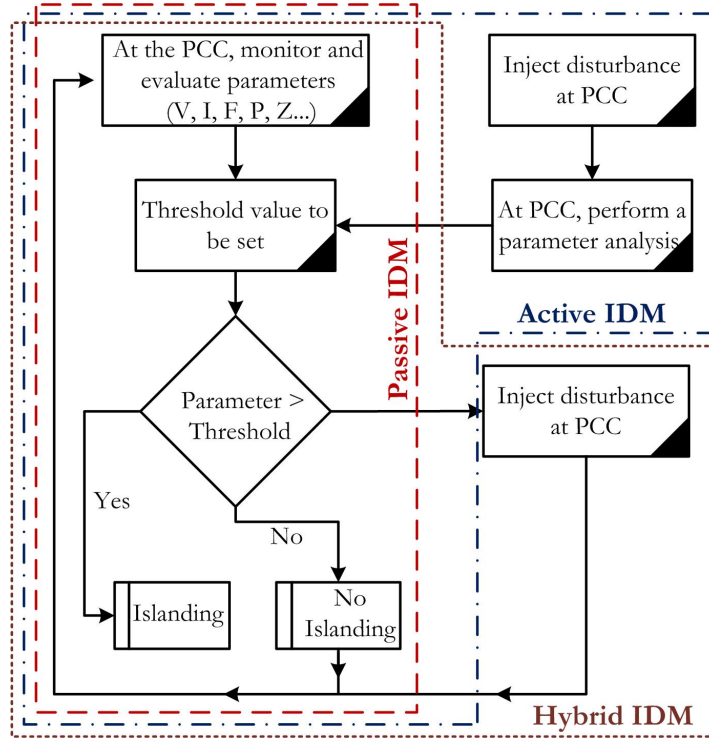


Figure 1.10: Islanding detection methods (passive, active, and hybrid) flow diagram.

specified boundaries. According to IEEE 1547 standards, the usual limitations for the voltage operating range is $\pm 10\text{-}15\%$ p.u. in voltage and ± 1 Hz for frequency at the reference value. It is common to utilize voltage and frequency monitoring to trigger the DG inverter to identify islanding if there is an OUV or an OUF. This should not detect islanding even though voltage and frequency fluctuations are often very small to trigger OUF/OUV except if the amount of power mismatches at the PCC due to islanding is relatively low. Given that perhaps the powers (active and reactive) are still equal, perhaps there should be no changes in amplitude or frequency, but the worst scenario for islanding detection is given by $\Delta P = 0$ and $\Delta Q = 0$.

It is possible to identify the NDZ effectively, however in most cases, this method is categorized as unsatisfactory for enabling anti-islanding protection that satisfies the requirements (Basso et al., 2015).

- **Phase Jump Detection (PJD):**

During islanding, a reactive power mismatch creates a phase shift seen between

both the voltage and current of the DG inverter terminal, that is detected by using this approach. In contrary towards the OUF approach, the phase can vary even more quickly than the frequency, so it is conceivably able to detect islands even more quickly. The zero-cross detection synchronization approaches should conveniently have been used to implement this technique, in which the phase of a current being corrected about once the voltage zero-crosses and therefore the eventual phase jumps can be identified.

High speed PLLs, but from the other hand, were already commonly used in more robust synchronisation, thereby the phase jump is even less significant that's because the PLL drives the current to re-synchronize with the voltage after islanding to minimize the phase jump. Therefore, selecting the most appropriate thresholds for achieving a consistent islanding detection is still challenging because of switching reactive loads. To be used with non-unity power factor (PF) systems, such as wind turbines, this strategy could result in inconvenient trips as well.

As no power mismatch exists while islanding, the voltage phase does not alter, and hence the NDZ becomes insignificant as zero. This cannot happen for any passive techniques (Singam and Hui, 2006).

- **Harmonic Detection (HD):**

There will still be harmonics produced even when the DG inverter is set to function ideally due to the switching of higher-order harmonics (i.e., voltage drop or ripple due to odd harmonics), harmonics, and dead-time. These harmonics are kept to a minimum to fulfil industry requirements (Std: IEEE 1574 THD < 5%) utilizing passive and software parts (typically filters and compensatory control methods). Grid impedance controls how much voltage harmonics they produce, even though they produce just a little amount. Because grid impedance is restricted, voltage harmonics are hard to identify.

The load impedance has taken the position of the grid impedance in islanding mode, and the load impedance is generally substantially bigger than the grid impedance, therefore the harmonics concentration in the voltage would be significantly enhanced, which might be used as a criterion for island detection. (Jang and Kim, 2004).

Table 1.3: Techniques for detecting passive islanding: a summary

Islanding technique	NDZ	Power quality impact	Detection time	Error detection rate
OUV/OUF	Large	None	4 ms–2 s	Low
PJD	Large	None	10–20 ms	Low
HD	Large for high Q	None	45 ms	High
ROCOP and RO-COF	Small	None	24–26 ms	High

- **The Rate of Change of Power (ROCOP) and The Rate of Change of Frequency (ROCOF):**

It is possible to detect an islanding occurrence by keeping track of how much the targeted DG's power output varies due to an islanding event. (Redfern et al., 1993)

When the DGs are in islanding mode, the frequency of the DGs fluctuates due to the power mismatch. So, monitoring the amount of frequency change over a few cycles and comparing it to the threshold value can be used to identify an islanding occurrence (Redfern et al., 1993, Freitas et al., 2005).

The ROCOF approach has trouble detecting islanding events since both the load and the islanded DG have a slight power imbalance. To resolve this concern, an approach that is based on df/dP has been proposed to identify islanding even in the presence of a slight power mismatch (Pai and Huang, 2001).

1.5.1.2 Active Islanding Detection Methods

Active techniques work on the principle of introducing minor perturbations to the output of the DG inverter, resulting in slight variations in frequency, phase, harmonics, and power. The Figure 1.10 shows how active islanding detection constantly changes the PCC parameter settings while evaluating how they react. Islanding oc-

curs when the values of one or more parameters exceed a predetermined cut off point. The targeted actions are as follows:

- OUF protection will be activated when the frequency drifts enough.
- OUV protection will be activated when the voltage varies enough.
- Estimation of grid impedance and, as a result, indirect detection of islanding.
- Estimation based on the PLL.
- Detection of a negative sequence.

As described by IEEE 1574 or VDE 0126-1-2006, active approaches, when paired with passive methods, result in islanding without NDZ. A full examination of the most generally used techniques are listed in (Bower and Ropp, 2002, De Mango et al., 2006, Petrone et al., 2008). The following section summarises the major elements of the most efficient active islanding detection approaches and these methods are summarised in the Table 1.4.

- **Frequency Drift Methods:**

To reduce grid frequency deviations, these methods use positive feedback to change the frequency reference. While the frequency cannot drift while the grid is in existence, once the grid is removed, the disturbances will have the ability to change the frequency till it is detected by the OUF (Petrone et al., 2008, Li et al., 2014, Ropp et al., 1999).

- **Voltage Drift Methods:**

These strategies use either positive feedback of the current or changing the reactive power to target grid voltage variation. With the grid, the voltage could have been well regulated. If the grid is disconnected, however, the disruption will then be capable of changing the voltage until it reaches OUV detection (Petrone et al., 2008, Li et al., 2014, Liu et al., 2010, Lopes and Sun, 2006).

- **Estimation of Grid Impedance:**

The concept is to use a perturbation, which including harmonic insertion or PQ fluctuations, to estimate grid impedance based on the grid responses (Ahmad et al., 2013, O’kane and Fox, 1997).

Table 1.4: Techniques for detecting active islanding: a summary

Islanding technique	NDZ	Power quality impact	Detection time	Error detection rate
FJ	Small	Degrades	75 ms	Low
SVS	Smallest	Slightly degrades	0.5 s	Low
Impedance measurement	Small	Degrades	0.77–0.95 s	Low
Phase PLL perturbation	Smallest	Negligible	120 ms	Low

- **PLL-Based Islanding Detention:**

To synchronize the output current of a DG inverter well with grid voltage, this approach uses the same basic PLL structure. And it's reliant on a conscious modification in the inverter current, resulting in an angle of θ_{PLL} (Ciobotaru et al., 2010, Velasco et al., 2010). In Chapters 3 and 4, the essential concept of the PLL-based islanding detection approach is explained in detail.

1.5.1.3 Hybrid methods

In comparison to passive and active islanding detection approaches, active approach have a lower NDZ, increasing detection accuracy. Adding a disturbance signal, On either side, it complicates the system and degrade the power quality. For example, in Figure 1.10, a hybrid detection strategy employs passive detection in conjunction with an active detection method as a secondary detection method to prevent the need to continuously inject disruption signals. Hybrid tactics describe strategies that incorporate both passive and active elements. The selection from the extensive scholarly literature on hybrid approaches are listed below.

- **Method of voltage imbalance and frequency set point:**

A hybrid islanding detection methodology blends an active method known as positive feedback with a passive method known as voltage unbalancing (VU).

The voltages at the DG’s output terminal are constantly monitored and the voltage unbalance is detected. In detection, voltage unbalance is used because of its higher sensitivity. The frequency setpoint is lowered to distinguish between islanding occurrences and other disturbances when voltage unbalance reaches the threshold value (Menon and Nehrir, 2007).

- **Shifts in voltage and actual power:**

The average rate of voltage change is computed for five cycles when a $\frac{dV}{dt} \neq 0$ is detected to inspect for islanding. If the voltage is greater than the setpoint, then it can be considered an islanding event, and if it is less than minimum setpoint, then islanding is not suspected. As of this moment, the system’s islanding status is determined by using real power shift (Mahat et al., 2009).

- **Injection of voltage fluctuation:**

The hybrid islanding detection methodology incorporates two methods that rely on passive detection methods, particularly ROCOF and ROCOV, as well as one factor, the correlation factor (CF), which establishes the effect of changes in the DG source’s voltage level and the voltage disruption. Detection is based on passive islanding as the primary method, and secondary detection is provided by active detection (Chang, 2010).

- **SFS and Q-f methods combined in a hybrid design:**

Passive Q—f droop is paired with active SFS in this hybrid technique. SFS instabilities is combated and the NDZ is reduced using the Bacterial Foraging optimization algorithm. To enhancing hybrid islanding detection, overall performance of Q—f curve technique is introduced in the above approach in (Vahedi et al., 2010).

The following summarises the discussions on droop control and islanding detection methods.

- Since every droop feature has a single control variable, like m_p for frequency droop, it is difficult to meet multiple control objectives. For instance, a design balance between the controller’s time constant and the controller’s speed and regulation of voltage and frequency must be taken into account.

- The conventional droop method implies that the converter and the AC network have a high inductive effective impedance. In microgrid implementations, nonetheless, this idea is called a serious challenge because low-voltage transmission lines are generally resistive. As a result, 1.11 is no longer valid for microgrids.
- The voltage, unlike the frequency, is not a universal variable in the microgrid. As a result, the regulation of reactive power in 1.12 and 1.13 may have a negative impact on voltage regulation for important loads (Diaz et al., 2010).
- In the context of nonlinear loads, the conventional droop technique must identify current harmonics from circulating current. Because of the current harmonics, the overall DG output voltage is also influenced. By altering the conventional droop technique, total harmonic distortion (THD) in output voltages could be decreased (Borup et al., 2001, Zhong, 2013a).
- Passive techniques rely on the monitoring of grid variables, which tend to vary when an island is present. Even though it is essential to recognize the NDZ, this technology is generally inappropriate for anti-islanding protection in most cases.
- Modest disturbances to the output of the DG inverter result in minor fluctuations in PCC parameters. Adding a disturbance signal, and on the other hand, causes the system to become more complicated and affects the power quality.
- Islanding happens with no or minimal NDZ when active methods are combined with passive methods.
- To avoid the need to continuously inject disruption signals, a hybrid detection strategy uses passive detection in conjunction with an active detection method as a secondary detection method.

1.6 Motivation

As in the preceding discussion, in an islanded microgrid the system frequency restoration and system voltage limits must be maintained to achieve more accurate power sharing. The conventional droop control approach, on the other hand, will depend

on the network's output impedance attributes. To accomplish these objectives, a reliable control approach for precise power-sharing with f/V restoration should always be evaluated, and also the significance of network output line impedances.

When the microgrid's grid-connected functioning is disrupted, the distributed generators (DGs) should indeed instantaneously disconnect from the grid to ensure safe operation. The system will revert to a stable operating range with adequate modeling and consistent islanding detection technique behavior. In the instance of a grid breakdown, it is required to investigate and implement enhanced islanding detection with a smaller NDZ.

The following research contributions are made as a result of the foregoing observations in this work.

1.7 Contributions of this research work

In the proposed research work, an improved droop control technique and modified islanding detection and automatic mode switching in islanded and grid-connected operation modes are developed respectively. In the proposed research work, the following contributions have been made.

1. Design of a droop control strategy using a virtual complex impedance in a standalone microgrid.
 - In the power controller outer loop, a conventional droop control approach is implemented.
 - Virtual complex impedance control in the voltage controller inner loop is implemented.
 - Testing the proportional load sharing efficacy of the implemented controllers.
2. In the islanded microgrid, development of a improved droop control technique for parallel connected PE-based DGs.
 - Developing a improved control technique for power-sharing with f/V restoration using state-space small-signal modeling, pooling an improved droop with a virtual output impedance control-based droop control.

- Implementation of proposed improved droop control technique for parallel-connected PE-based DGs.
 - Develop and analyze a suggested droop control technique's entire microgrid system state-space small-signal modeling.
 - Escalating the robustness of the proposed strategy for step change in the system power loads.
3. Development of an islanding detection and automatic switching approach employing a phase-locked loop (PLL) controller.
- In grid-connected operating mode, investigate and analyse phase-locked loop controllers.
 - The behavior of PLLs has been performed for their effectiveness under diverse power quality variations.
 - PLL phase error is used to identify islanding and switch the operating modes (grid-connected and islanded) automatically.
 - Grid disturbances in terms of faults have been used to test the effectiveness of detection of islanding and automatic transition to a different mode.
 - The PLL phase error responses for all forms of faults in the system are listed, as well as the behavior of responses with PLL detection time.
4. Development of modified Park synchronous reference frame based phase-locked loop (PSRF-PLL) and Piezoelectric Acoustic Sensor for islanding detection.
- Implementation of PSRF-PLL based islanding detection and automatic mode switching for parallel-connected multi-DG systems.
 - Comparison of the PLL phase error and phase angle responses for the proposed PSRF-PLL and popular PLLs in the popular literature for power quality issues.
 - Using a lumped equivalent network model, investigate and analyze the behavior of a piezoelectric acoustic sensor.
 - Piezoelectric acoustic sensor modeling for specialized applications like islanding detection.
 - The proposed islanding detection strategy's effectiveness will be tested in both healthy and unhealthy grid environments.

1.8 Thesis organization

As illustrated in Figure 1.11, the complete thesis is divided into six chapters. The following are concise summaries of each chapter:

Chapter 1: In islanded and grid-connected operation modes, a basic overview of microgrid control and classification is presented. The concept of a droop control approach in a microgrid for parallel-connected PE-based DG systems is described in the islanded mode of operation. Following that, the significance on islanding detection is discussed. The state-of-the-art literature on droop control tactics and islanding detection approaches is reviewed in this chapter.

Chapter 2: In a islanded microgrid, the performance of a droop-controlled PE-based parallel-connected distributed generating source is described. The state-

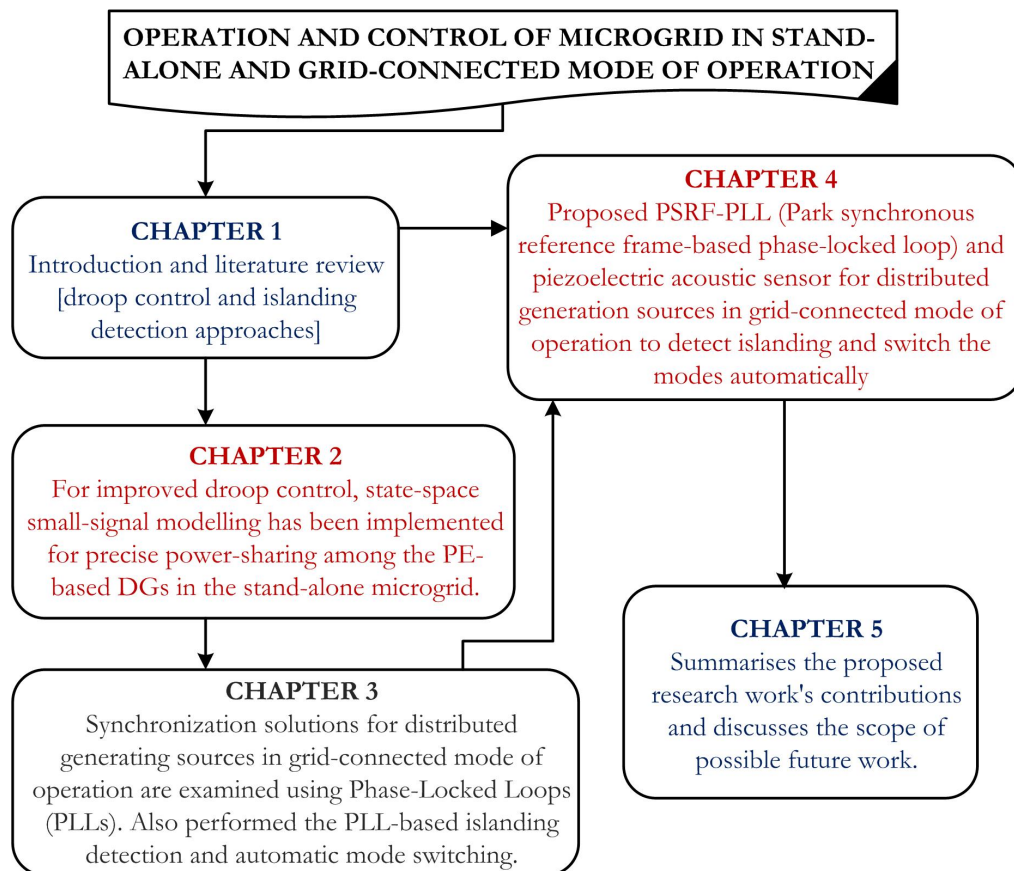


Figure 1.11: Organization of thesis.

space small-signal modeling has been implemented for accurate power-sharing across the PE-based DGs in the microgrid for improved droop control. Using the real-time hardware in the loop (HIL) platform, the proposed droop control is evaluated and validated. This chapter compares the responses of the proposed droop control with those of alternative droop-based control systems.

Chapter 3: This chapter covers the Phase-Locked Loops (PLLs) synchronization strategies for grid-connected distributed generation. For various power quality fluctuations, the significance of various three-phase PLLs is investigated. Then PLL-based islanding detection and automatic mode switching for droop-based microgrid is presented with HIL responses.

Chapter 4: The modified Park synchronous reference frame-based phase-locked loop (PSRF-PLL) for DGs in the grid-connected operation mode is covered in this chapter. The islanding detection and automatic mode switching with the proposed PLL with the proposed droop control for parallel-connected PE-based DGs are discussed with HIL responses. Then, the PLL phase error and phase angle responses for the proposed PSRF-PLL and popular PLLs are also listed. and an islanding detection technique based on piezoelectric acoustic sensor is also discussed in this chapter. The suggested piezoelectric acoustic sensor diaphragm's design as well as COMSOL simulation responses for proposed sensor dimensions, are listed. Meanwhile, the sensor characteristics' deflection, stress, strain distribution, and dynamic performance are examined using Finite Element Modeling (FEM). The suggested islanding detection HIL responses are then escalated.

Chapter 5: This chapter summarises the proposed research's contributions and discusses the scope of possible future work.

Chapter 2

DROOP CONTROL STRATEGY FOR PE-BASED DGS IN THE ISLANDED OPERATION MODE

2.1 Introduction

This chapter focuses on the modeling and control of parallel-connected power electronics-based distributed generating sources in the islanded mode of operation. The frequency and voltage restoration must be kept constant in an AC microgrid to achieve precise power-sharing. In this context, a reliable control technique for power-sharing with f/V restoration is presented, which pools an improved droop with a virtual impedance control-based droop control. State-space small-signal modeling and an examination for the entire microgrid system are discussed in this chapter.

Figure 2.1 illustrates a three-phase power electronic inverter with LC filter feeding an RLC load. In the diagram, the intrinsic series resistances of the inductor and capacitor are indicated.

2.2 Power Electronic (PE) inverter design

The design and modeling of islanded AC PE system include three 10 kVA, 50 Hz voltage source inverters (VSIs), which are used as interface of renewable energy resources and energy storage units to a distribution grid. A pulse-width modulation

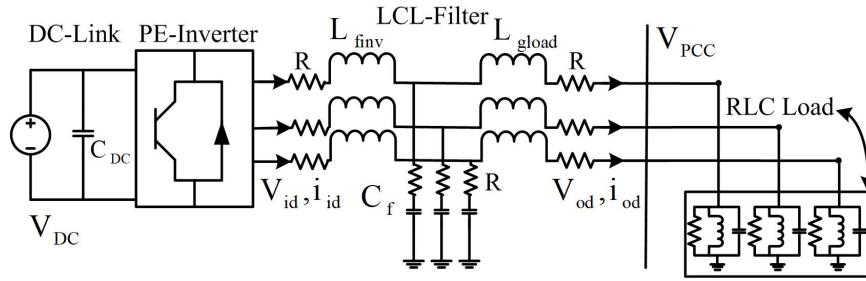


Figure 2.1: The PE inverter with the output LC filter and RLC load.

(PWM) scheme. with a triangular carrier of 10 kHz. has been employed. The most suitable power gates for such application are the Insulated Gate Bipolar Transistors (IGBTs). A second order passive LCL low pass filter is designed for attenuating switching harmonics and the design of parallel RLC load is discussed. For regulating the voltage at the output of the LCL filter, across the capacitor, a dq vector control scheme employing a simple PI-type controller is used. The performance of the inverter is verified through virtual and real-time responses in Typhoon HIL-402. The following assumptions have been made to facilitate easy modelling of the system:

1. All the switches are ideal with low internal resistance and infinite snubber capacitance values.
2. The switching frequency of the inverter is much higher than the operating frequency.
3. The filter inductance is linear and parasitic inductances and resistances are ignored.

2.2.1 Selection of input DC voltage and DC-link capacitance

The input DC voltage is chosen such that the amplitude of the basic element of the inverter's voltage level can be adjusted by $\pm 10\%$ while operating with linear PWM. In this case, the modulation index (m_a), which controls the amplitude of the inverter voltage, is even less than or nearly equal to 1 under this situation. The m_a can be calculated using equation (2.1).

$$m_a = \frac{V_{DC} * \pi}{4 * V_{DC}} \approx 0.8 \quad (2.1)$$

The relationship between the DC bus voltage and the fundamental component of the line-to-line voltage in the output of the a PWM controlled inverter V_{L-L} is given by (2.2):

$$V_{DC} = \frac{V_{L-L,rms}}{m_a * 0.612} \quad (2.2)$$

With V_{L-L} as 398.37 V \approx 400 V the V_{DC} considering the switching losses in the inverter is nearly equal to 800 V. The 0.612 factor comes from $\frac{10\sqrt{3}}{9\pi}$.

The calculation of DC link capacitor is given as equation (2.3)

$$C_{DC} = \frac{I_{rated} * T}{V_{rated}} \quad (2.3)$$

With $I_{rated}=15.15$ A and $V_{rated}=400$ V, the value of the capacitor 795.2 μ F. The calculation of I_{rated} will be given by the following equations (2.4) and (2.5).

$$KVA = \frac{V_{rated} * I_{rated} * \sqrt{3}}{1000} \quad (2.4)$$

$$I_{rated} = \frac{KVA * 1000}{V_{rated} * \sqrt{3}} \quad (2.5)$$

2.2.2 Selection of filter capacitance and inductance

Now, with $P_{base}=8$ kW, $V_{DC}=800$ V, $\omega=2*\pi*50$ Hz, and $\omega_{SW}=2*\pi*10$ kHz, $Z_b = \frac{V_{ph}^2}{P_{base}}$, and $C_b = \frac{1}{\omega*Z_b}$, the filter capacitance C_f and filter inductance L_f can be calculated as equations (2.6) and (2.7)

$$C_f = 0.5 * C_b \quad (2.6)$$

$$L_f = \frac{\sqrt{1/k_a + 1}}{C_f * \omega_{SW}^2} \quad (2.7)$$

2.2.3 Three phase inverter modeling

The dq-equivalent circuits of a three-phase inverter are shown in Figure 2.2 and Figure 2.3, it turns out to be a simple RLC circuit due to the filter inductance and capacitance and hence the following well-know equations can be framed as (2.8) to (2.11):

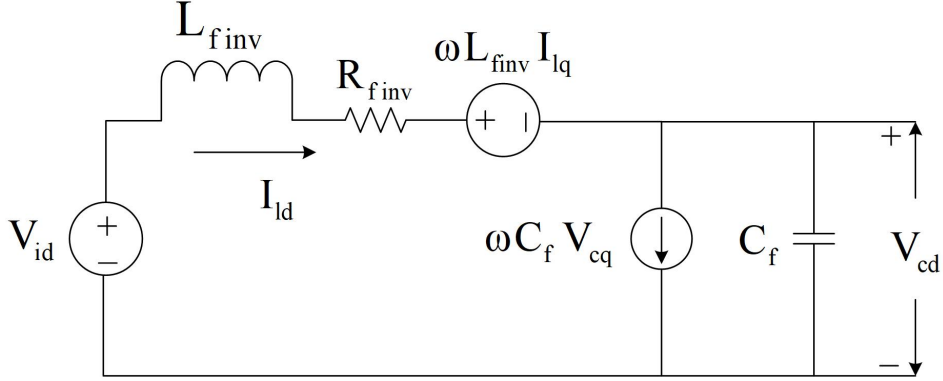


Figure 2.2: d-equivalent circuit of three phase inverter.

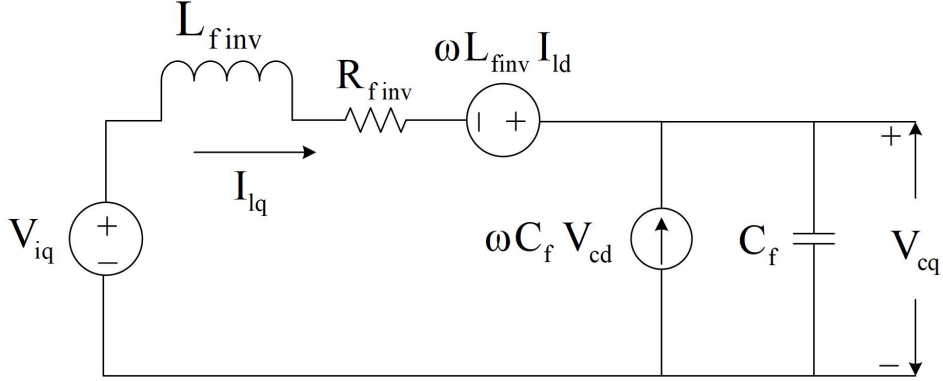


Figure 2.3: q-equivalent circuit of three phase inverter.

$$\frac{di_{ld}}{dt} = \frac{-R_f}{L_f} * i_{ld} + \omega_0 i_{lq} + \frac{v_{id}}{L_f} - \frac{v_{0d}}{L_f} \quad (2.8)$$

$$\frac{di_{lq}}{dt} = \frac{-R_f}{L_f} * i_{lq} + \omega_0 i_{ld} + \frac{v_{iq}}{L_f} - \frac{v_{0q}}{L_f} \quad (2.9)$$

$$\frac{dv_{0d}}{dt} = \omega_0 * v_{0q} + \frac{1}{C_f} * (i_{ld} - i_{0d}) \quad (2.10)$$

$$\frac{dv_{0q}}{dt} = -\omega_0 * v_{0d} + \frac{1}{C_f} * (i_{lq} - i_{0q}) \quad (2.11)$$

The equations (2.8) and (2.9) represents the R-L part and the equations (2.10) and (2.11) represents the capacitance part. The output coupling inductance has been included in the equations (2.12) and (2.13).

$$\frac{di_{0d}}{dt} = \frac{-R_c}{L_c} * i_{0d} + \omega_0 i_{0q} + \frac{v_{0d}}{L_c} - \frac{v_{bd}}{L_c} \quad (2.12)$$

$$\frac{di_{0q}}{dt} = \frac{-R_c}{L_c} * i_{0q} + \omega_0 i_{0d} + \frac{v_{0q}}{L_c} - \frac{v_{bq}}{L_c} \quad (2.13)$$

Combining all these equations gives the overall inverter model (2.14).

$$\begin{bmatrix} \dot{\Delta i_{ld}} \\ \dot{\Delta i_{lq}} \\ \text{dot}\Delta v_{od} \\ \text{dot}\Delta v_{oq} \\ \text{dot}\Delta i_{od} \\ \text{dot}\Delta i_{oq} \end{bmatrix} = \begin{bmatrix} \frac{-R_f}{L_f} & \omega_0 & \frac{-1}{L_f} & 0 & 0 & 0 \\ \omega_0 & \frac{-R_f}{L_f} & 0 & \frac{-1}{L_f} & 0 & 0 \\ \frac{1}{C_f} & 0 & 0 & \omega_0 & \frac{-1}{C_f} & 0 \\ 0 & \frac{1}{C_f} & \omega_0 & 0 & 0 & \frac{-1}{C_f} \\ 0 & 0 & \frac{1}{L_c} & 0 & \frac{-r_c}{L_c} & \omega_0 \\ 0 & 0 & 0 & \frac{1}{L_c} & \omega_0 & \frac{-r_c}{L_c} \end{bmatrix} \begin{bmatrix} \Delta i_{ld} \\ \Delta i_{lq} \\ \Delta v_{od} \\ \Delta v_{oq} \\ \Delta i_{od} \\ \Delta i_{oq} \end{bmatrix} + \begin{bmatrix} \frac{1}{L_f} & 0 \\ 0 & \frac{1}{L_f} \\ 0 & 0 \\ 0 & 0 \\ 0 & 0 \\ 0 & 0 \end{bmatrix} \begin{bmatrix} \Delta v_{id} \\ \Delta v_{iq} \\ 0 \\ 0 \\ 0 \\ 0 \end{bmatrix} + \begin{bmatrix} 0 & 0 \\ 0 & 0 \\ 0 & 0 \\ 0 & 0 \\ \frac{-1}{L_c} & 0 \\ 0 & \frac{-1}{L_c} \end{bmatrix} \begin{bmatrix} \Delta v_{bd} \\ \Delta v_{bq} \\ 0 \\ 0 \\ 0 \\ 0 \end{bmatrix} + \begin{bmatrix} -I_{ld} \\ I_{lq} \\ -V_{0d} \\ V_0 \\ -I_{0d} \\ I_{0q} \end{bmatrix} \Delta\omega \quad (2.14)$$

After performing Park's transformation, all of these equations have been framed in the dq frame. This allows the user to use DC values as input to the PI controller rather than AC values.

2.2.4 LCL filter and parallel RLC load

The LCL filter design and parallel RLC load modeling for inverter-based DGs are depicted in this section. The base impedance and base capacitance of the microgrid system is given by equation (2.15).

$$Z_{base} = \frac{V_{ph}^2}{P}; \quad C_{base} = \frac{1}{\omega_n * Z_{base}} \quad (2.15)$$

where, Z_{base} is base impedance in Ω and C_{base} is base capacitance in F, V_{ph} is the phase voltage in V, P is the rated active power in kW, and ω_n is the nominal angular frequency in radians. The value of the filter capacitor is selected based on the base capacitance of the microgrid system and is given in (2.16).

$$C_f = \frac{C_{base}}{2} \quad (2.16)$$

The filter inductance is designed on the basis of the maximum current ripple of the inverters. Here we considered a maximum current ripple of 10% and is given by

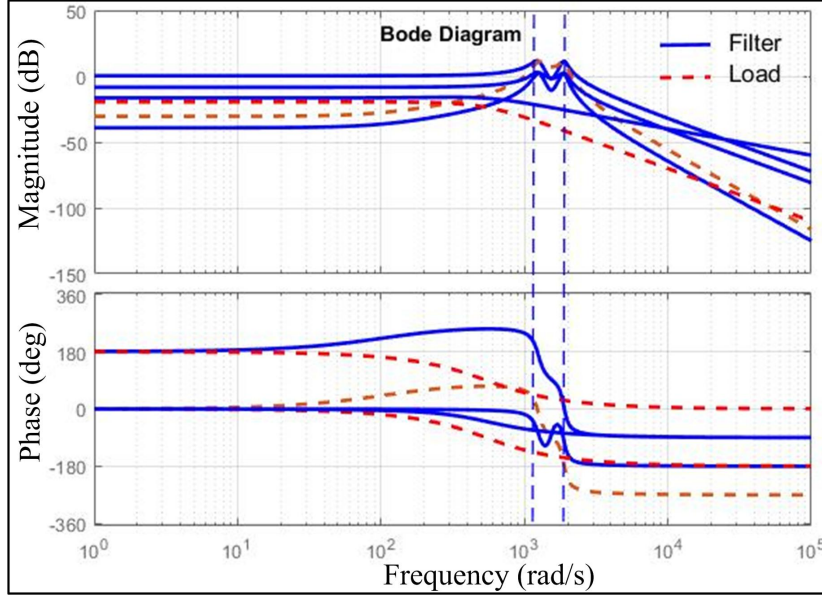


Figure 2.4: Bode plots for LCL filter and parallel RLC load.

equation (2.17).

$$\Delta I_{max} = 0.1 * I_{max} \quad (2.17)$$

Where I_{max} is given in equation (2.18)

$$I_{max} = \frac{P_{rated} * \sqrt{2}}{3 * V_{ph}} \quad (2.18)$$

The filter inductances L_{inv} and L_g are given in equation (2.19).

$$L_{inv} = \frac{V_{DC}}{6 * f_{sw} * \Delta I_{max}}; \quad L_g = 0.5 * L_{inv} \quad (2.19)$$

Where L_{inv} is inverter side filter inductance in H, L_g is grid side filter inductance in H, f_{sw} is inverter switching frequency in Hz, and V_{DC} is DC-link voltage in V. The parallel RLC load is considered as a general structure of the local load. According to the IEEE 1547.1 test setup a parallel RLC load is connected in between the inverter-based DGs and the grid. The modeling of the parallel RLC load includes The active power P_{load} in kW, reactive power Q_{load} in kVAR, resonance frequency f_o in Hz and quality factor Q_f . The modelling equations are given in equations (2.20) and (2.21).

$$P_{Load} = \frac{V_{PCC}^2}{R}; \quad Q_{Load} = V_{PCC}^2 \left(\frac{1}{\omega L} - \omega C \right) \quad (2.20)$$

$$f_o = \frac{1}{2\pi\sqrt{LC}}; \quad Q_f = R\sqrt{\frac{C}{L}} \quad (2.21)$$

Where the $V_{PCC}=V_{grid}$ in GC operation mode and $V_{PCC}=V_{DG}$ in SA operation mode. And L is load inductance in Henry, C is load capacitance in Farad and ω is the angular frequency of the microgrid system. The bode plots of the LCL filter and parallel RLC load are shown in Figure 2.4. A peak response is seen at 11.7dB magnitude and the high frequency is around 1.24e3 depicts the good system dynamics.

The state-space analysis including the Eigenvalue spectrum of the complete microgrid system, especially when considering the second-order LCL filter, the RL-modeled line, and the load model, is being shown. Finally, the proposed droop control strategy is tested and verified on the real-time Hardware in the Loop platform (HIL). Along with an analysis that compares the responses of the proposed droop-based control strategies to those of the existing droop-based control strategies.

2.3 Control of PE-based DG systems

The control structure of PE-based DS systems in the islanded mode of operation includes

- Power controller
- Voltage controller
- Current controller

The overall control scheme is shown in Figure 2.5. In addition to the above controllers, a virtual complex impedance is further added to reduce the circulating currents and to improve the reactive power-sharing among the parallel-connected PE-based DGs in the microgrid. The voltage and currents controllers are designed to eliminate high-frequency disturbances and resonance caused due to the passive filters, and the frequency and phase are set by the outer power control loop. The controller design for the inner control loop is designed to be faster than the outer control loop. The following sections describe the modeling of the controllers in a synchronous reference

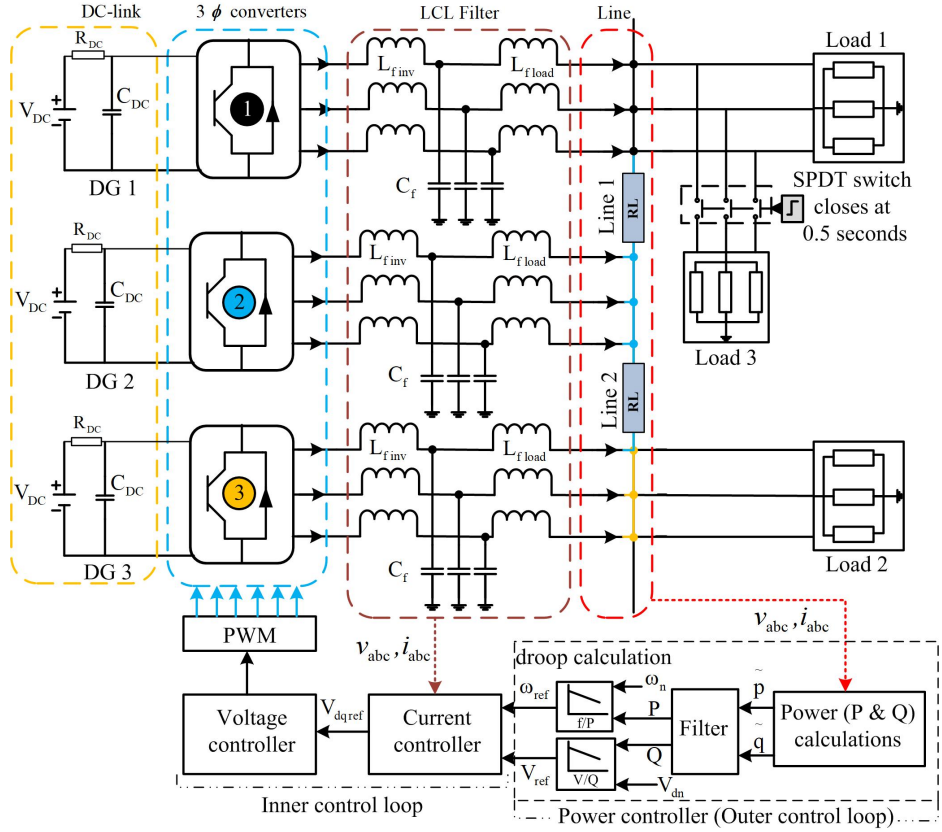


Figure 2.5: Parallel connected three-phase PE-based DGs in islanded mode.

frame for power, current, voltage, and impedance controller (Pogaku et al., 2007, Guerrero et al., 2004).

2.3.1 Power controller

The power controller is implemented in the outer control loop as shown in Figure 2.6. In this control, the frequency and phase references are set by the droop strategy implemented for the inverter-based distributed generation sources. The controller is responsible for regulating the output active power in accordance with the frequency deviation and the reactive power depending on the voltage deviation. wherein the instantaneous active and reactive power is calculated with inverter output $d - axis$ voltage and currents, which is given by (2.22).

$$\hat{p} = V_{od}i_{od} + V_{oq}i_{oq} ; \hat{q} = V_{od}i_{oq} - V_{oq}i_{od} \quad (2.22)$$

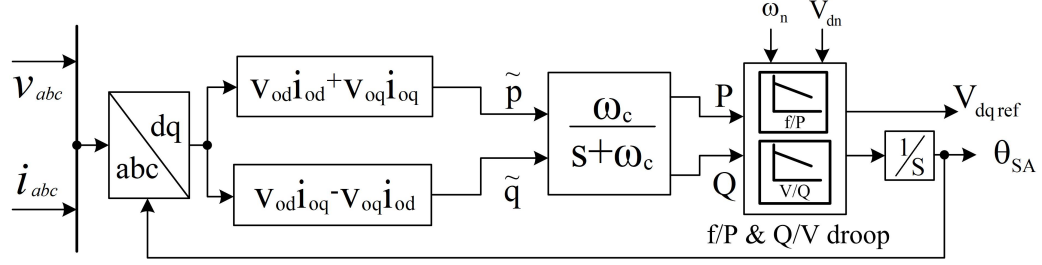


Figure 2.6: Power controller scheme.

After filtering out the instantaneous components, the fundamental power components are obtained as (2.23).

$$P = \frac{\omega_c}{s + \omega_c} \hat{p} ; Q = \frac{\omega_c}{s + \omega_c} \hat{q} \quad (2.23)$$

Where ω_c is the low pass filter cut-off frequency. After obtaining the fundamental power components, an artificial droop is introduced in the power controller, and the droop equations are given as (2.24).

$$\omega^* = \omega_n - m_p P ; V^* = V_{dn} - n_q Q \quad (2.24)$$

Where, ω^* and V^* are the reference frequency and voltage of the droop controller, and P and Q are the output active and reactive powers of the inverters.

2.3.2 Voltage controller

The Voltage Controller for the inverter implemented in the inner loop employs a standard PI controller and all the gains such as feed-forward, feedback, proportional and integral, are included in the following state-space and state equations. The state equations for voltage controller are given by the equations (2.25) and (2.26).

$$\frac{d\phi_d}{dt} = V_{od}^* - V_{od} \quad (2.25)$$

$$\frac{d\phi_q}{dt} = V_{oq}^* - V_{oq} \quad (2.26)$$

And the algebraic equations including the virtual impedance and the small-signal state-space form are shown in equations (2.27) and (2.28).

$$i_{id}^* = Fi_{od} - \omega_n C_f V_{oq} + k_{pv}(V_{od}^* - V_{od} - V_{vd}) + k_{iv} \frac{d\phi_d}{dt} \quad (2.27)$$

$$i_{iq}^* = Fi_{oq} - \omega_n C_f V_{od} + k_{pv}(V_{oq}^* - V_{oq} - V_{vq}) + k_{iv} \frac{d\phi_q}{dt} \quad (2.28)$$

2.3.3 Current controller

The Current Controller for the inverter is also implemented in the inner loop, which employs a standard PI controller. The proportional and integral gains are included in the following state equations. The state equations for controller are given in (2.29) and (2.30).

$$\frac{d\gamma_d}{dt} = i_{id}^* - i_{id} \quad (2.29)$$

$$\frac{d\gamma_q}{dt} = i_{iq}^* - i_{iq} \quad (2.30)$$

And the algebraic equations and small signal state-space form are given in equations (2.31) and (2.32).

$$V_d^* = k_{pi}(i_{id}^* - i_{id}) + k_{ii} - \omega_n L_i i_{iq} \quad (2.31)$$

$$V_q^* = k_{pi}(i_{iq}^* - i_{iq}) + k_{ii} + \omega_n L_i i_{id} \quad (2.32)$$

The voltages and currents are regulated using the standard PI controllers, and decoupling is implemented in the control structure due to the LCL filters in the system.

In chapter 1.4, in equation (1.11)-(1.14) considering medium and high-voltage network, the resistance in the line impedances are neglected. But the problems are raised due to neglecting the resistance in the output impedance are being solved to achieve proportional load sharing. In a real practical scenario, it is not possible to have all the network and control parameters the same for all the inverters operating in parallel. To overcome these problems the droop control scheme including the virtual

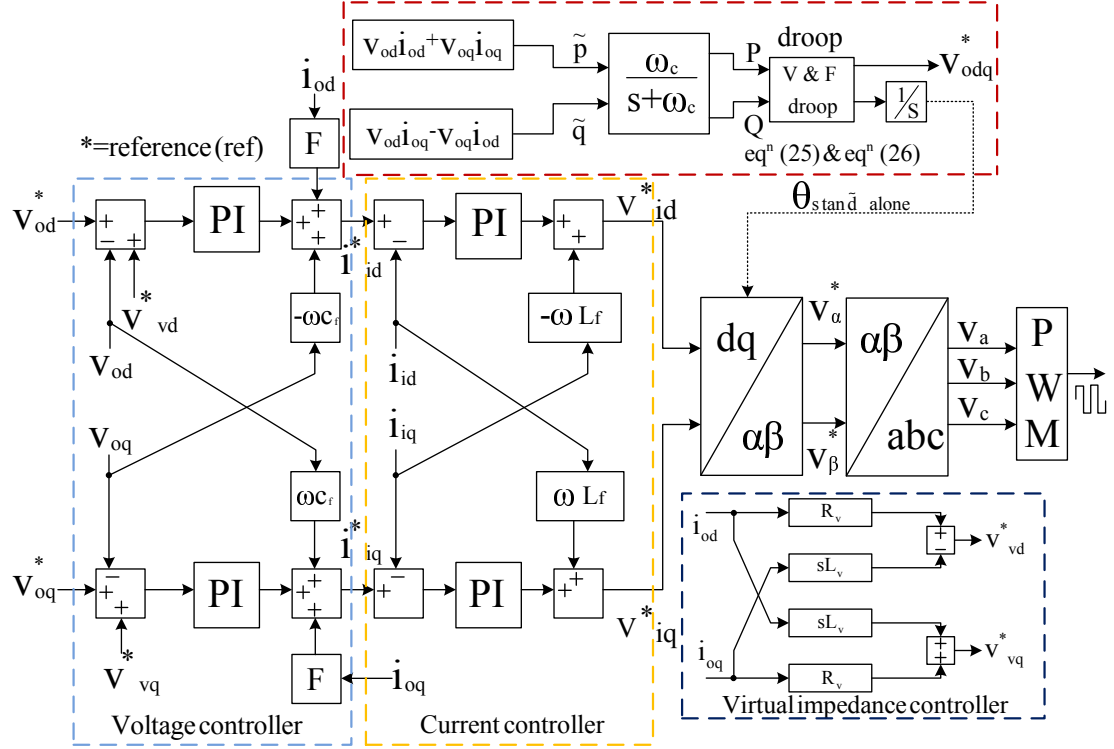


Figure 2.7: Overall control scheme for Microgrid in the islanded mode of operation.

control loop is implemented for parallel-connected inverters. The virtual impedance has a great impact in balancing the output impedance characteristic (Guerrero et al., 2004). The block diagram for virtual complex impedance to be added in the outer loop is shown in Figure 2.7. The state equations for virtual impedance V_{vd} and V_{vq} are included in the voltage controller loop are given in (2.33) and (2.34).

$$V_{vd}^* = I_{id} * R_v - \frac{dI_{iq}}{dt} * L_v \quad (2.33)$$

$$V_{vq}^* = I_{iq} * R_v - \frac{dI_{id}}{dt} * L_v \quad (2.34)$$

The overall control scheme is shown in Figure 2.7, it can be shown that the characteristic of the output impedance is modified by the new term, which includes inductive and resistive components in the virtual complex impedance (Wang et al., 2015).

2.4 Modeling and analysis of proposed droop controller

Conventional droop control works properly only for inductive line impedance and if any disturbance made the line impedance resistive, the conventional control goes into an unstable region. To avoid this type of dependency on the output line impedance, we need to consider the controller performance for both the resistive as well as the inductive line impedances in the control scheme to operate in the stable region. Here we considered a dual impedance controller, one with inner control loop that is power controller and another one with the outer control loop that is voltage controller. The power controller additional control equations are given in (2.35) and (2.36).

$$\omega^{ref} = \omega_n - m_p P + N_q Q \quad (2.35)$$

$$V^{ref} = V_n - n_q Q + M_p P \quad (2.36)$$

N_q and M_p are the terms used to reduce the circulating currents and to improve the power-sharing accuracy among the parallel-connected PE-based DGs. The equations for N_q and M_p are derived as follows. Considering voltage of equal magnitude and phase angle $V_e = V_{1,2}$, the partial derivative of the equations 1.11 and 1.12 with respect to δ and V_e are given as equations (2.37)-(2.42).

$$P = \frac{V_e^2}{Z} [\cos(\theta) - \cos(\theta + \delta)] \quad (2.37)$$

$$Q = \frac{V_e^2}{Z} [\sin(\theta) - \sin(\theta + \delta)] \quad (2.38)$$

$$\frac{\partial P}{\partial \delta} = \frac{V_e^2}{Z} [\sin(\theta + \delta)] \quad (2.39)$$

$$\frac{\partial P}{\partial V_e} = \frac{2V_e}{Z} [\cos(\theta) - \cos(\theta + \delta)] \quad (2.40)$$

$$\frac{\partial Q}{\partial \delta} = \frac{-V_e^2}{Z} [\cos(\theta + \delta)] \quad (2.41)$$

$$\frac{\partial Q}{\partial V_e} = \frac{2V_e}{Z} [\sin(\theta) - \sin(\theta + \delta)] \quad (2.42)$$

Dividing the equations (2.39) and (2.40), we get (2.43)

$$\frac{\partial P/\partial \delta}{\partial P/\partial V_e} = \frac{-V_e}{2} \left[\frac{\sin(\delta + \theta)}{\cos(\theta) - \cos(\theta + \delta)} \right] \quad (2.43)$$

By solving the above equation, we get M_p as equation (2.44)

$$M_p = \frac{\partial P}{\partial \delta} = \frac{-V_e}{2} \cot(\delta) \left(\frac{\partial P}{\partial V_e} \right) = \frac{-V_e n_q}{2} \cot(\delta) \quad (2.44)$$

Where M_p is the additional frequency droop coefficient in equation (2.36) given as $\frac{\partial P}{\partial \delta}$. In similar analytical procedure we can solve for N_q , we get equations (2.45)-(2.47)

$$\frac{\partial Q/\partial V_e}{\partial Q/\partial \delta} = \frac{-2}{V_e} \left[\frac{\sin(\theta) - \sin(\theta + \delta)}{\cos(\theta + \delta)} \right] = \frac{-2}{V_e} \left[\frac{[1 - \cos(\delta)]}{\sin(\delta)} \right] \quad (2.45)$$

$$\frac{\partial Q/\partial V_e}{\partial Q/\partial \delta} = \frac{-2}{V_e} \left[\frac{[2 \sin^2(\delta/2)]}{\sin(\delta)} \right] \quad (2.46)$$

$$N_q = \frac{\partial Q}{\partial V_e} = \frac{-2}{V_e} \tan(\delta/2) \left(\frac{\partial Q}{\partial \delta} \right) = \frac{-2m_p}{V_e} [\tan(\delta/2)] \quad (2.47)$$

Where N_q is the additional voltage droop coefficient in equation 2.35 given as $\frac{\partial Q}{\partial V_e}$. From the well-known impedance triangle we can write the equations for $\cot(\delta)$ and $\tan(\delta/2)$ as equations (2.48) and (2.49)

$$\cot(\delta) = \frac{R}{X} \quad (2.48)$$

$$\tan(\delta/2) = \pm \sqrt{\frac{1 - \cos(\delta)}{1 + \cos(\delta)}} \quad (2.49)$$

Involving the equations (2.44), (2.47), (2.48), and (2.49) in equations (2.35) and (2.36) the modified droop equations then becomes as equations (2.50) and (2.51)

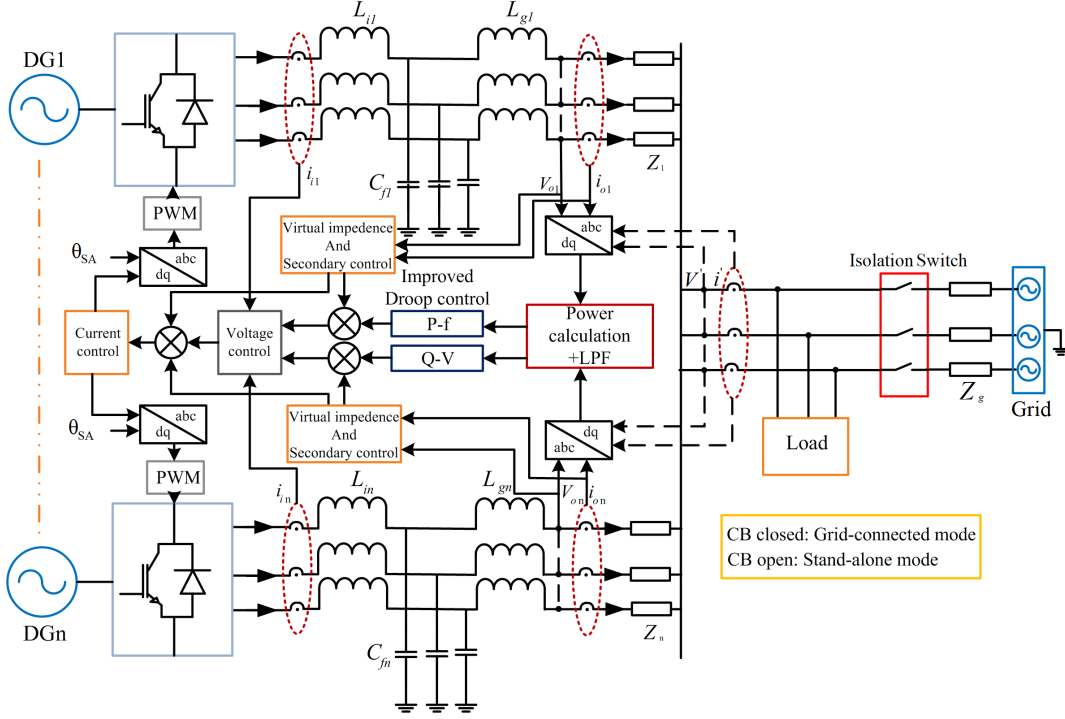


Figure 2.8: Proposed controller block diagram for DGs.

$$\omega^{ref} = \omega_n - m_p P - \frac{2n_q}{V_e} \left[\sqrt{\frac{1 - R/X}{1 + R/X}} \right] \quad (2.50)$$

$$V^{ref} = V_n - n_q Q - \frac{V_{com} m_p}{2} \left[\frac{R}{X} \right] \quad (2.51)$$

Where ω_n , ω^{ref} , are the nominal and reference frequencies and V_n , and V^{ref} are d-axis nominal and reference voltages sequentially. P and Q are the ascertained output real and output reactive powers of the DGs. The m_p and n_q are droop coefficients and are conferred in equations (2.52) and (2.53).

$$m_p = \frac{\omega_{max} - \omega_{min}}{P_{max}} \quad (2.52)$$

$$n_q = \frac{V_{odmax} - V_{odmin}}{Q_{max}} \quad (2.53)$$

Where, ω_{max} and ω_{min} are the maximum and minimum system frequencies, and V_{odmax} and V_{odmin} are the maximum and minimum DG output voltage limits. The

P_{max} and Q_{max} are the maximal real and reactive output powers of the system.

2.5 State-space and stability analysis of proposed droop control method

The control part of the PE-based DG is as shown in Figure 2.8, which includes a Power controller with droop control, voltage controller with virtual impedance control (VIC), current controller with PWM controller. The VIC is included to lessen the circulating current and to enhance the reactive power allocation with the parallel associated DGs. The DG controlling part is divided into two primary parts, for example, (i) Inner control loop and (ii) Outer control loop. The accompanying sections demonstrate the modeling of the controllers in a synchronous reference frame.

i) Inner control loop:

Inner control loop includes power controller, the frequency and the phase operations are carried out in this loop (i.e., droop control of parallel-connected DGs). In this control, the frequency and phase references are set by the droop strategy actualized for the PE-based DGs. The controller is responsible for controlling the output active power as per the frequency deviation and the reactive power contingent upon the voltage deviation. The voltage and current are derived from DQ axis components and are written in the vector form as equation (2.54)

$$v_{odq} = \begin{bmatrix} v_{od} & v_{oq} \end{bmatrix}^T ; \quad i_{odq} = \begin{bmatrix} i_{od} & i_{oq} \end{bmatrix}^T ; \quad i_{ldq} = \begin{bmatrix} i_{ld} & i_{lq} \end{bmatrix}^T \quad (2.54)$$

The instantaneous active power and reactive power are determined from the inverter d-axis output voltage and currents, as conferred in equations (2.55) and (2.56).

$$p = v_{od}i_{od} + v(oq)i_{oq} \quad (2.55)$$

$$q = v_{od}i_{oq} - v(oq)i_{od} \quad (2.56)$$

To get the fundamental active and reactive power components the instantaneous components are filtered out by the low pass filter as equations (2.57) and (2.58).

$$P = \frac{\omega_c}{S + \omega_c} p \quad (2.57)$$

$$Q = \frac{\omega_c}{S + \omega_c} q \quad (2.58)$$

The term $\omega/S + \omega_c$ characterizes the low-pass filter where ω_c is filter cut-off frequency of 31.42 radians. At that point, the modeled droop equations are acquainted in the control loop to accomplish equivalent sharing of real and reactive powers, refer equations (2.50) and (2.51).

Now, the small signal state space inner control loop with active power (P), reactive power (Q), voltage (V), current (I), and reference frequency (ω) can be dictated as equations (2.59)-(2.64).

$$\begin{bmatrix} \Delta \dot{\delta} & \Delta P & \Delta Q \end{bmatrix}^T = A \begin{bmatrix} \Delta \delta & \Delta P & \Delta Q \end{bmatrix}^T + B \begin{bmatrix} \Delta \dot{i}_{ldq} & \Delta v_{odq} & \Delta i_{odq} \end{bmatrix}^T \quad (2.59)$$

$$\begin{bmatrix} \Delta \omega & \Delta v_{odq}^{ref} \end{bmatrix}^T = \begin{bmatrix} C_\omega & C_v \end{bmatrix}^T \begin{bmatrix} \Delta \delta & \Delta P & \Delta Q \end{bmatrix}^T \quad (2.60)$$

$$A = \begin{bmatrix} 0 & -m_p & 0 \\ 0 & -\omega_c & 0 \\ 0 & 0 & -\omega_c \end{bmatrix} \quad (2.61)$$

$$B = \begin{bmatrix} 0 & 0 & 0 & 0 & 0 & 0 \\ 0 & 0 & \omega_c I_{od} & \omega_c I_{oq} & \omega_c V_{od} & \omega_c V_{oq} \\ 0 & 0 & \omega_c I_{oq} & -\omega_c I_{od} & -\omega_c V_{oq} & \omega_c V_{od} \end{bmatrix} \quad (2.62)$$

$$C_\omega = \begin{bmatrix} 0 & -m_p & 0 \end{bmatrix} \quad (2.63)$$

$$C_v = \begin{bmatrix} 0 & 0 & -n_q \\ 0 & 0 & 0 \end{bmatrix} \quad (2.64)$$

ii) Outer control loop:

The outer control loop incorporates the current controller and the voltage controller, which are intended to eliminate the high-frequency disturbances and the resonance

brought about by the passive filters (He et al., 2013). The outer control loop aims to be faster than the inner control loop.

A) Voltage Controller

The Voltage Controller implemented in the outer loop utilizes a PI controller and the gains like, "feed-forward gain, feedback gain, proportional and integral gains, are included in the following state-space equations (Kulkarni and Gaonkar, 2017). The state equations for voltage controller are given by the equations" (2.65) and (2.66).

$$\frac{d\phi_d}{dt} = V_{od}^{ref} - V_{od} - V_{vd}^{ref} \quad (2.65)$$

$$\frac{d\phi_q}{dt} = V_{oq}^{ref} - V_{oq} - V_{vq}^{ref} \quad (2.66)$$

And the mathematical equations inclusive of the VIC and small signal state-space form are given in equations (2.67) and (2.68).

$$i_{ld}^{ref} = Fi_{od} - \omega_n C_f (V_{oq} - V_{vq}^{ref}) + k_{pv} (V_{od}^{ref} - V_{od} - V_{vd}^{ref}) + k_{iv} \phi(d) \quad (2.67)$$

$$i_{lq}^{ref} = Fi_{oq} - \omega_n C_f (V_{od} - V_{vd}^{ref}) + k_{pv} (V_{oq}^{ref} - V_{oq} - V_{vq}^{ref}) + k_{iv} \phi(q) \quad (2.68)$$

The small signal state-space form of the voltage controller includes equation (2.69) to equation (2.77):

i) The reference input

$$[\Delta \dot{\phi}_{dq}] = [0][\Delta \phi_{dq}] + B_{V1} \begin{bmatrix} \Delta V_{odq}^{ref} & \Delta V_{vdq}^{ref} \end{bmatrix}^T + B_{V2} \begin{bmatrix} \Delta i_{ldq} & \Delta V_{odq} & \Delta i_{odq} & \Delta V_{vdq} \end{bmatrix}^T \quad (2.69)$$

where $\Delta \phi_{dq} = [\Delta \phi_d \quad \Delta \phi_q]^T$

And the terms B_{V1} and B_{V2} in matrix form are

$$B_{V1} = \begin{bmatrix} 1 & 0 & 1 & 0 \\ 0 & 1 & 0 & 1 \end{bmatrix} \quad (2.70)$$

$$B_{V2} = \begin{bmatrix} 0 & 0 & -1 & 0 & 0 & 0 & -1 & 0 \\ 0 & 0 & 0 & -1 & 0 & 0 & 0 & -1 \end{bmatrix} \quad (2.71)$$

ii) The feedback input

$$[\Delta i_{ldq}^{ref}] = C_v [\Delta \phi_{dq}] + D_{V1} \begin{bmatrix} \Delta V_{odq}^{ref} & \Delta V_{vdq}^{ref} \end{bmatrix}^T + D_{V2} \begin{bmatrix} \Delta i_{ldq} & \Delta V_{odq} & \Delta i_{odq} & \Delta V_{vdq} \end{bmatrix}^T \quad (2.72)$$

Where Δi_{ldq}^{ref} represents the feedback input and ΔV_{vdq}^{ref} represents the VIC reference. The state equations for VIC are included in the voltage controller loop as in equations (2.73) and (2.75).

$$V_{vd}^{ref} = I_{ld} * R_v - \frac{dI_{lq}}{dt} * L_v \quad (2.73)$$

$$V_{vq}^{ref} = I_{lq} * R_v + \frac{dI_{ld}}{dt} * L_v \quad (2.74)$$

And the analogous state-space equations for the voltage controller including VIC are as follows:

$$C_V = \begin{bmatrix} k_{iv} & 0 \\ 0 & k_{iv} \end{bmatrix} \quad (2.75)$$

$$D_{V1} = \begin{bmatrix} k_{pv} & 0 & 1 & 0 \\ 0 & k_{pv} & 0 & 1 \end{bmatrix} \quad (2.76)$$

$$B_{V2} = \begin{bmatrix} 0 & 0 & -k_{pv} & -\omega_n C_f & F & 0 & -k_{pv} & 0 \\ 0 & 0 & \omega_n C_f & -k_{pv} & 0 & F & 0 & -k_{pv} \end{bmatrix} \quad (2.77)$$

Where, k_{pv} (proportional gain) and k_{iv} (integral gain) are attributed to the voltage controller.

B) Current controller

The Current Controller for the inverter is additionally executed in the inner control loop, which utilizes the PI controller. The corresponding proportional and integral gains are included in the state equations. The controller state equations are given in (2.78) and (2.79).

$$\frac{d\gamma_d}{dt} = i_{ld}^{ref} - i_{ld} \quad (2.78)$$

$$\frac{d\gamma_q}{dt} = i_{lq}^{ref} - i_{lq} \quad (2.79)$$

And the mathematical equations and small signal state-space form are given in equations (2.80) and (2.81)

$$V_{id}^{ref} = -\omega_n L_f i_{lq} + k_{pi}(i_{ld}^{ref} - i_{ld}) + k_{ii}\gamma(d) \quad (2.80)$$

$$V_{iq}^{ref} = -\omega_n L_f i_{ld} + k_{pi}(i_{lq}^{ref} - i_{lq}) + k_{ii}\gamma(q) \quad (2.81)$$

The current controller reference and feed-back inputs in the small signal state-space form are given in equations (2.82)-(2.88):

i) The reference input

$$[\Delta\gamma_{dq}] = [0][\Delta\gamma_{dq}] + B_{C1}[\Delta i_{ldq}^{ref}] + B_{C2} \begin{bmatrix} \Delta i_{ldq} & \Delta V_{odq} & \Delta i_{odq} \end{bmatrix}^T \quad (2.82)$$

where $\Delta\gamma_{dq} = [\Delta\gamma_d \quad \Delta\gamma_q]^T$

$$B_{C1} = \begin{bmatrix} 1 & 0 \\ 0 & 1 \end{bmatrix} \quad (2.83)$$

$$B_{C2} = \begin{bmatrix} -1 & 0 & 0 & 0 & 0 & 0 \\ 0 & -1 & 0 & 0 & 0 & 0 \end{bmatrix} \quad (2.84)$$

ii) The feedback input

$$[\Delta V_{idq}^{ref}] = C_c[\Delta \gamma_{dq}] + D_{C1}[\Delta i_{ldq}^{ref}] + D_{C2} \begin{bmatrix} \Delta i_{ldq} & \Delta V_{odq} & \Delta i_{odq} \end{bmatrix}^T \quad (2.85)$$

$$C_c = \begin{bmatrix} k_{ii} & 0 \\ 0 & k_{ii} \end{bmatrix} \quad (2.86)$$

$$D_{C1} = \begin{bmatrix} k_{pi} & 0 \\ 0 & k_{pi} \end{bmatrix} \quad (2.87)$$

$$D_{C2} = \begin{bmatrix} -k_{pi} & -\omega_n L_f & 0 & 0 & 0 & 0 \\ \omega_n L_f & -k_{pi} & 0 & 0 & 0 & 0 \end{bmatrix} \quad (2.88)$$

The following state equations (2.89)-(2.104) are included in the islanded microgrid state-space modeling.

$$\Delta \dot{i}_{ldq} = \left(\frac{1}{L_f} \right) \Delta v_{dq} - \left(\frac{r_f}{L_f} \right) \Delta i_{ldq} - \omega \Delta i_{ldq} - \Delta v_{odq} \quad (2.89)$$

$$\Delta \dot{v}_{odq} = \left(\frac{1}{C_f} \right) \Delta i_{ldq} - \left(\frac{1}{C_f} \right) \Delta i_{odq} - \omega \Delta v_{odq} \quad (2.90)$$

$$\begin{bmatrix} \Delta \dot{i}_{ldq} & \Delta \dot{v}_{odq} \end{bmatrix}^T = A \begin{bmatrix} \Delta i_{ldq} & \Delta v_{odq} \end{bmatrix}^T + B \begin{bmatrix} \Delta v_{dq} & \Delta i_{Ldq} \end{bmatrix}^T \quad (2.91)$$

$$\begin{bmatrix} \Delta \dot{v}_{odq} \end{bmatrix} = C \begin{bmatrix} \Delta i_{ldq} & \Delta v_{odq} \end{bmatrix}^T + D \begin{bmatrix} \Delta v_{dq} & \Delta i_{Ldq} \end{bmatrix}^T \quad (2.92)$$

$$A = \begin{bmatrix} -\frac{r_f}{L_f} & -\omega & -\frac{1}{L_f} & 0 \\ +\omega & \frac{r_f}{L_f} & 0 & -\frac{1}{L_f} \\ \frac{1}{C_f} & 0 & 0 & -\omega \\ 0 & \frac{1}{C_f} & \omega & 0 \end{bmatrix} \quad (2.93)$$

$$B = \begin{bmatrix} -\frac{1}{L_f} & 0 & 0 & 0 \\ 0 & \frac{1}{L_f} & 0 & 0 \\ 0 & 0 & -\frac{1}{C_f} & 0 \\ 0 & 0 & 0 & -\frac{1}{C_f} \end{bmatrix} \quad (2.94)$$

$$C = \begin{bmatrix} -\frac{r_f}{L_f} & -\omega & -\frac{1}{L_f} & 0 \\ +\omega & \frac{r_f}{L_f} & 0 & -\frac{1}{L_f} \\ \frac{1}{C_f} & 0 & 0 & -\omega \\ 0 & \frac{1}{C_f} & \omega & 0 \end{bmatrix} \quad (2.95)$$

$$D = [0] \quad (2.96)$$

$$\frac{di_{linedq}}{dt} = \left(\frac{1}{L_{line}} \right) v_{odq} - \omega i_{linedq} - \left(\frac{R_{line}}{L_{line}} \right) i_{linedq} \quad (2.97)$$

$$\Delta \dot{i}_{linedq} = \left(\frac{1}{L_{line}} \right) \Delta v_{odq} - \omega i_{linedq} - \left(\frac{r_{line}}{L_{line}} \right) \Delta i_{linedq} \quad (2.98)$$

$$\begin{bmatrix} \Delta \dot{i}_{linedq} & \Delta \dot{v}_{odq} \end{bmatrix}^T = A \begin{bmatrix} \Delta i_{linedq} & \Delta v_{odq} \end{bmatrix}^T + B \begin{bmatrix} \Delta v_{odq} \end{bmatrix} \quad (2.99)$$

$$\begin{bmatrix} \Delta \dot{i}_{linedq} & \Delta \dot{v}_{odq} \end{bmatrix}^T = C \begin{bmatrix} \Delta i_{linedq} & \Delta v_{odq} \end{bmatrix}^T + D \begin{bmatrix} \Delta v_{odq} \end{bmatrix} \quad (2.100)$$

$$A = \begin{bmatrix} -\frac{R_{line}}{L_{line}} & -\omega & 0 & 0 \\ +\omega & \frac{R_{line}}{L_{line}} & 0 & 0 \\ 0 & 0 & \frac{1}{L_{line}} & 0 \\ 0 & 0 & 0 & \frac{1}{L_{line}} \end{bmatrix}; \quad B = \begin{bmatrix} -\frac{1}{L_{line}} & 0 & 0 & 0 \\ 0 & -\frac{1}{L_{line}} & 0 & 0 \\ 0 & 0 & \frac{1}{C_f} & 0 \\ 0 & 0 & 0 & \frac{1}{C_f} \end{bmatrix} \quad (2.101)$$

$$C = \begin{bmatrix} 1 & 0 & 0 & 0 \\ 0 & 1 & 0 & 0 \\ 0 & 0 & 1 & 0 \\ 0 & 0 & 0 & 1 \end{bmatrix} \quad D = [0]$$

$$B = \begin{bmatrix} -\frac{1}{L_{line}} & 0 & 0 & 0 \\ 0 & -\frac{1}{L_{line}} & 0 & 0 \\ 0 & 0 & \frac{1}{C_f} & 0 \\ 0 & 0 & 0 & \frac{1}{C_f} \end{bmatrix} \quad (2.102)$$

$$C = \begin{bmatrix} 1 & 0 & 0 & 0 \\ 0 & 1 & 0 & 0 \\ 0 & 0 & 1 & 0 \\ 0 & 0 & 0 & 1 \end{bmatrix} \quad (2.103)$$

$$D = [0] \quad (2.104)$$

Where, the equations (2.89)-(2.104) are the state equations for LCL filter, output line impedance and load models.

2.6 The complete Microgrid system model

The complete small-signal state-space model can be acquired by consolidating all the state-space models of the inner control loop and the outer control loop, given by equations (2.105)-(2.107).

$$\begin{aligned} & \left[\Delta \dot{\delta} \quad \Delta \dot{P} \quad \Delta \dot{Q} \quad \Delta \dot{\phi}_{dq} \quad \Delta \dot{\gamma}_{dq} \quad \Delta \dot{i}_{ldq} \quad \Delta \dot{v}_{odq} \quad \Delta \dot{v}_{vdq} \quad \Delta \dot{i}_{odq} \right]^T \\ = & A \left[\Delta \delta \quad \Delta P \quad \Delta Q \quad \Delta \phi_{dq} \quad \Delta \gamma_{dq} \quad \Delta i_{ldq} \quad \Delta v_{odq} \quad \Delta v_{vdq} \quad \Delta i_{odq} \right]^T + B \left[\Delta v_{0dq} \quad \Delta v_{vdq} \right]^T \end{aligned} \quad (2.105)$$

$$\begin{bmatrix} \Delta \omega \\ \Delta i_{odq} \end{bmatrix} = \begin{bmatrix} C_\omega \\ C_i \end{bmatrix} \left[\Delta \delta \quad \Delta P \quad \Delta Q \quad \Delta \phi_{dq} \quad \Delta \gamma_{dq} \quad \Delta i_{ldq} \quad \Delta v_{odq} \quad \Delta v_{vdq} \quad \Delta i_{odq} \right]^T \quad (2.106)$$

There are a total of 17 states, 4 outputs, and two outputs from every single parallel-connected DG. The overall system spectrum including the inner controller, the outer controller, filter, load, and RL line model is given as A_{System} (A_{Sys}).

$$[A_{Sys}] = \begin{bmatrix} A_{11} \\ A_{12} \end{bmatrix} + \begin{bmatrix} A_{21} \\ A_{22} \end{bmatrix} + \begin{bmatrix} A_{31} \\ A_{32} \end{bmatrix} \quad (2.107)$$

$$A_{11} = \begin{bmatrix} 0 & -m_p & 0 & 0 & 0 & 0 & 0 \\ 0 & -\omega_c & 0 & 0 & 0 & 0 & 0 \\ 0 & 0 & -\omega_c & 0 & 0 & 0 & 0 \\ 0 & -m_p & 0 & 0 & 0 & 0 & 0 \\ 0 & 0 & -n_q & 0 & 0 & 0 & 0 \\ 0 & 0 & 0 & k_{iw} & 0 & k_{ic} & 0 \\ 0 & 0 & 0 & 0 & k_{iw} & 0 & k_{ic} \\ 0 & 0 & 0 & 0 & 0 & 0 & 0 \\ 0 & 0 & 0 & 0 & 0 & 0 & 0 \end{bmatrix} \quad (2.108)$$

$$A_{12} = \begin{bmatrix} 0 & 0 & 0 & 0 & 0 & 0 & 0 \\ 0 & 0 & 0 & 0 & 0 & 0 & 0 \\ 0 & 0 & 0 & 0 & 0 & 0 & 0 \\ 0 & 0 & 0 & 0 & 0 & 0 & 0 \\ 0 & 0 & 0 & 0 & 0 & 0 & 0 \\ 0 & 0 & 0 & 0 & 0 & 0 & 0 \\ 0 & 0 & 0 & 0 & 0 & 0 & 0 \\ 0 & -m_p & 0 & 0 & 0 & 0 & 0 \\ 0 & -m_p & 0 & 0 & 0 & 0 & 0 \end{bmatrix} \quad (2.109)$$

$$A_{21} = \begin{bmatrix} 0 & 0 & 0 & 0 & 0 \\ 0 & 0 & 0 & 0 & -A1 \\ 0 & 0 & 0 & 0 & A2 \\ 1 & 0 & 1 & 0 & -1 \\ 0 & 1 & 0 & 1 & 0 \\ k_{pc} & 0 & k_{pv} & 0 & -k_{pc} \\ 0 & k_{pc} & 0 & k_{pv} & -A7 \\ -A9 & \omega & -A10 & 0 & 0 \\ -\omega & -A9 & 0 & -A10 & 0 \end{bmatrix} \quad (2.110)$$

$$A_{22} = \begin{bmatrix} A11 & 0 & 0 & \omega & 0 \\ 0 & A11 & -\omega & 0 & 0 \\ 0 & 0 & A12 & 0 & -A13 \\ 0 & 0 & 0 & A12 & -\omega \\ 0 & 0 & -A15 & 0 & 1 \\ 0 & 0 & 0 & -A15 & 0 \\ 0 & 0 & 0 & 0 & 0 \\ 0 & 0 & 0 & 0 & 0 \end{bmatrix} \quad (2.111)$$

$$A_{31} = \begin{bmatrix} 0 & 0 & 0 & 0 & 0 \\ A2 & A3 & A4 & 0 & 0 \\ -A1 & -A4 & A3 & 0 & 0 \\ 0 & -1 & 0 & -A5 & A6 \\ -1 & 0 & -1 & A6 & A5 \\ A7 & -k_{pv} & -A8 & -k_{pv} & -A8 \\ -k_{pc} & A8 & -k_{pv} & A8 & -k_{pv} \\ 0 & 0 & 0 & 0 & 0 \\ 0 & 0 & 0 & 0 & 0 \end{bmatrix} \quad (2.112)$$

$$A_{32} = \begin{bmatrix} 0 & 0 & 0 & 0 & 0 \\ 0 & 0 & 0 & 0 & 0 \\ \omega & A14 & \omega & 0 & 0 \\ -A13 & \omega & A14 & 0 & 0 \\ 0 & 1 & 0 & 0 & 0 \\ 1 & 0 & 1 & 0 & 0 \\ 0 & 0 & 0 & -A16 & A17 \\ 0 & 0 & 0 & A17 & -A16 \end{bmatrix} \quad (2.113)$$

Where, $A1 = \omega_c i_{od}$, $A2 = \omega_c i_{oq}$, $A3 = \omega_c v_{od}$, $A4 = \omega_c v_{oq}$, $A5 = \frac{R_v}{L_v}$, $A6 = \omega L_v$, $A7 = \omega_n L_f$, $A8 = \omega_n C_f$, $A9 = \frac{R_f}{C_f}$, $A10 = \frac{1}{L_{ff}}$, $A11 = \frac{1}{C_f}$, $A12 = \frac{1}{L_{load}}$, $A13 = \frac{R_{load}}{L_{load}}$, $A14 = \frac{R_{line}}{L_{line}}$, $A15 = \frac{1}{L_{line}}$, $A16 = R_v$, and $A17 = \omega L_v$.

After modeling the complete microgrid system, the steady-state operating regions

Table 2.1: Initial conditions for eigenvalue spectrum analysis (Pogaku et al., 2007)

Parameter	Value	Parameter	Value
v_{od}	400	$i_{od} = i_{ld}$	20
v_{oq}	0	$i_{oq} = i_{lq}$	5
ω	314.2	ω_c	31.42

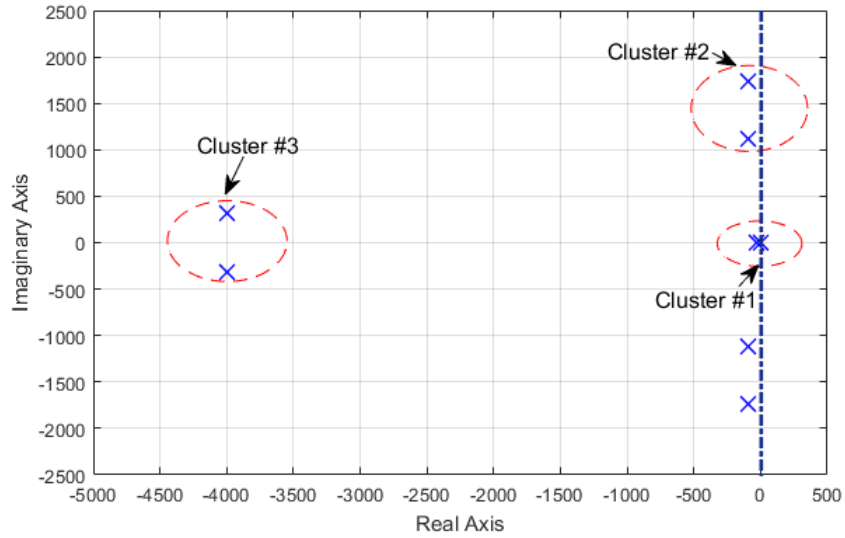


Figure 2.9: Eigenvalue analysis of overall system with various frequency modes.

of the modeled microgrid system were obtained from $[A_{Sys}]$. The eigenvalue analysis of the overall system for various frequency modes is shown in Figure 2.9. The initial conditions to obtain the eigenvalue spectrum are given in Table 2.1.

There are three operating regions and these regions can be obtained with these eigenvalues. The analysis of the state of these eigenvalues shows that the regions are categorized into three frequency ranges (high, medium, and low frequency).

- *High-cluster-3:* Conscious of the state variables of load with LCL filter and the output impedance currents.
- *Medium-cluster-2:* Conscious of the state variables of an outer control loop.
- *Low-cluster-1:* Conscious to the state variables of an inner control loop.

In the next following section, the analysis of the modeled droop controller for various

test cases is presented.

2.6.1 Hardware in loop (HIL) simulation responses

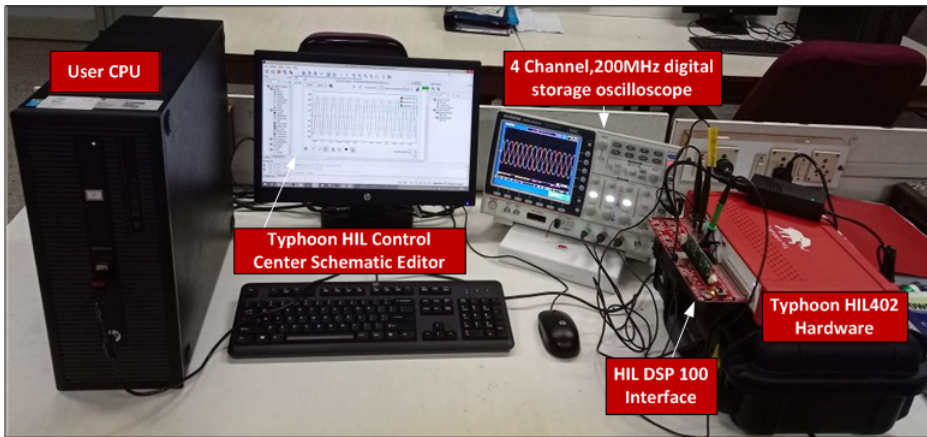


Figure 2.10: Typhoon-402 Hardware-in-loop experimental set-up.

To investigate the completion of the proposed scheme, it has been executed in the Typhoon hardware-in-loop (HIL)-402 as shown in Figure 2.10. The stand-alone microgrid configuration considered for this study is shown in Figure 2.11 and the parameters considered are listed in Appendix 5.2. The presented microgrid consists

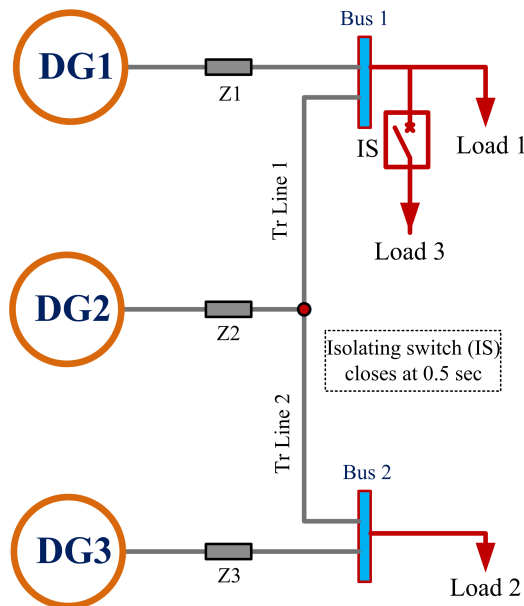


Figure 2.11: Test microgrid system.

of three PE-based DGs of each 10 KVA capacity and all the DGs are connected at the different locations in the distribution network. The converters are supplied with the DC voltage source, thereby the DC bus dynamics are avoided. But this is not a problem since the main interest is the investigation of the stability of the microgrid system and the behaviour of the controllers in regulating the active and reactive power flows. In this figure only islanled mode is considered hence isolation switch used to transfer between the grid-connected mode and islanded modes is not shown. Once the isolation switch is opened the microgrid is responsible for feeding all critical loads while maintaining the system frequency and voltages in prescribed limits. The resistive and inductive loads are used to test the proposed improved droop control (IDC) scheme. The responses for conventional droop control (CDC), virtual impedance control (VIC) with CDC (VIC-CDC), IDC, and VIC with IDC are presented.

Figure 2.12 and 2.13 shows the response of the DG output voltage, and current for the CDC, CDC+VIC (or simply VIC), IDC, and IDC+VIC schemes. It is found that the proposed IDC scheme shows a steady response with a slight magnitude difference from the other schemes.

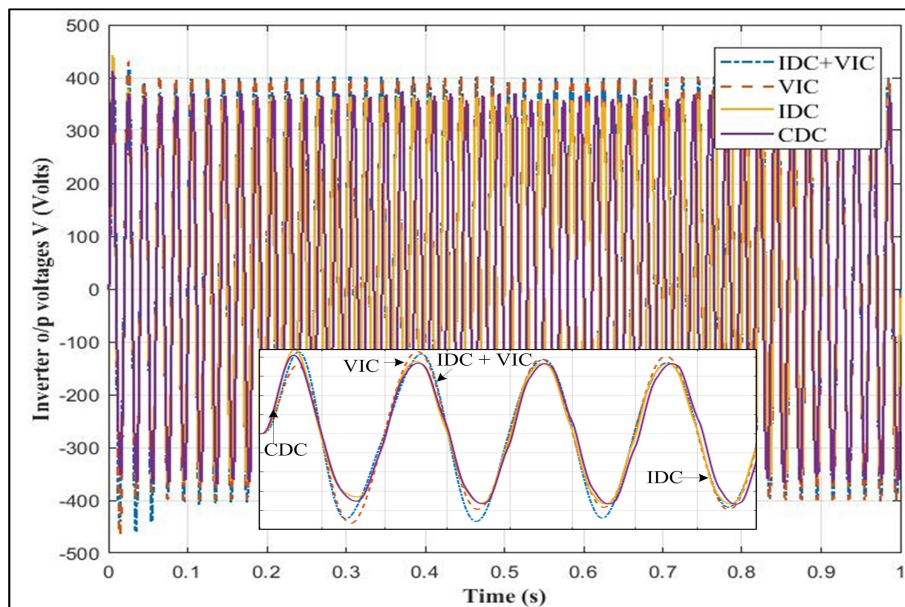


Figure 2.12: The Inverter output voltage (V).

In Figure 2.14 the variation of system frequency for all the four control schemes are presented. We can see the variation in the system frequency with the step load

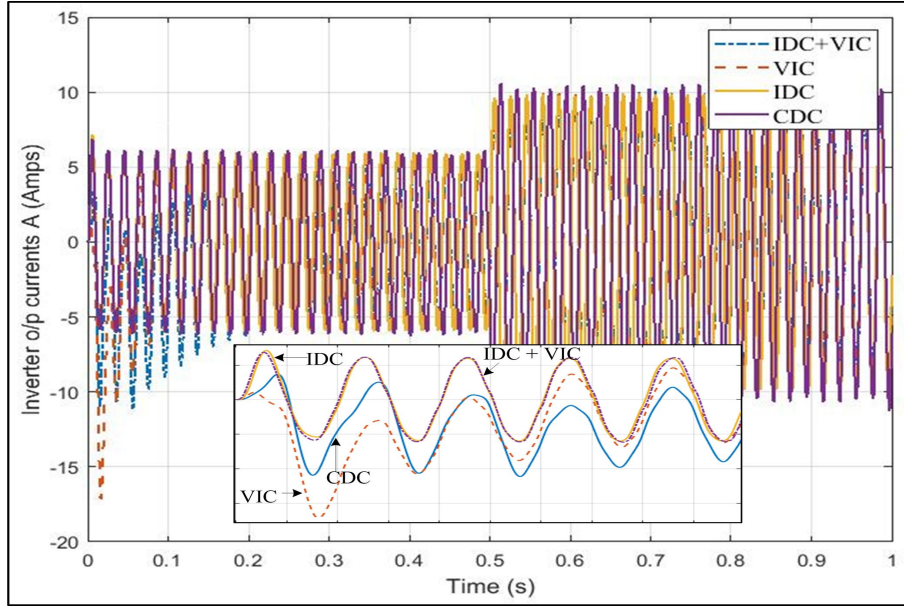


Figure 2.13: The Inverter output current (A).

Table 2.2: System frequency variation of control scheme

Control scheme	Frequency variation in (Hz)
CDC	50 Hz < f > 48.52 Hz
VIC	50 Hz < f > 49.96 Hz
IDC	50 Hz < f > 49.99 Hz
IDC+VIC	50 Hz < f > 49.97 Hz

at 0.5 s. The change in frequency variation following the active power output of the DGs can be noticed is shown in Figure 2.16. In the proposed IDC scheme, the frequency variations are accurate and the variations with other control schemes are still acceptable, the variations of frequencies for the control schemes are listed in Table 2.2.

Figure 2.15 shows the inverter d-axis output voltage response for the CDC, VIC+CDC, IDC, and VIC+IDC schemes with load step at 0.5 s. It can be observed that at 0.5 seconds due to the step load, a dip can be found in the inverter d-axis output voltage for less than 1 ms.

In Figure 2.16 and 2.17, the active and reactive power responses in kW and kVAR for the CDC, VIC+CDC, IDC, and VIC+IDC schemes with load step of 1.5 kW at

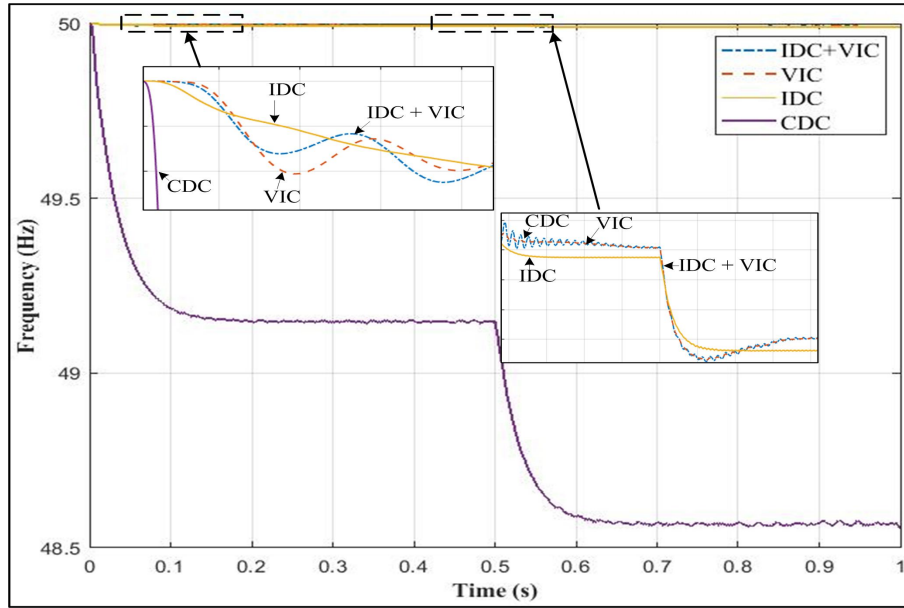


Figure 2.14: Frequency response (Hz).

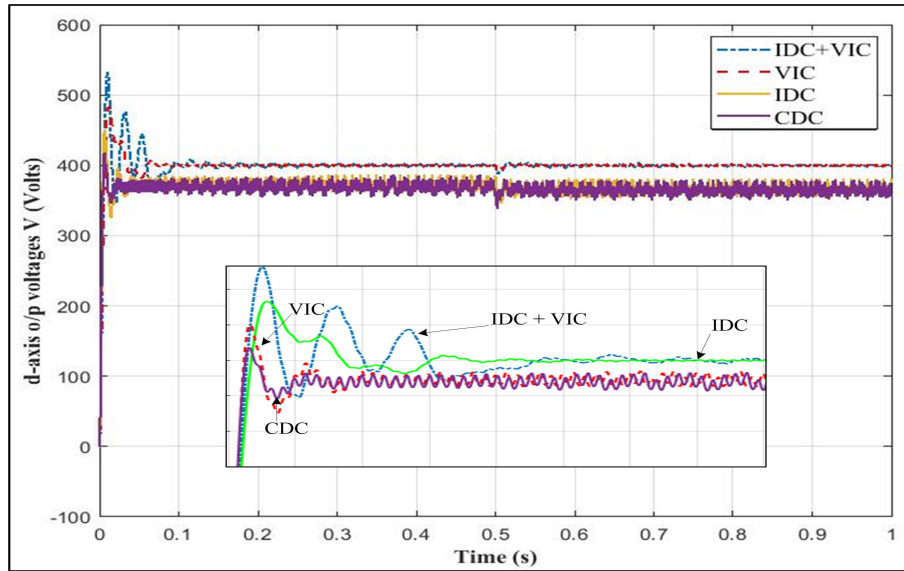


Figure 2.15: The Inverter output d-axis voltage (V).

0.5 s is shown respectively. It is demonstrated that with the proposed IDC scheme the accuracy in sharing the load without oscillations and the proportional sharing is properly achieved.

The active power and reactive power responses of all three parallel-connected DGs are shown in Figure 2.18 and Figure 2.19.

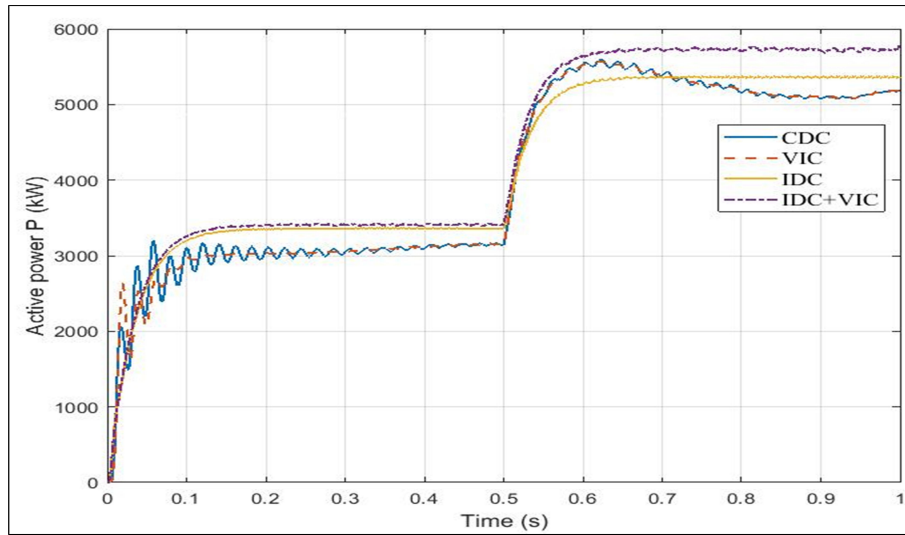


Figure 2.16: The active power response (kW).

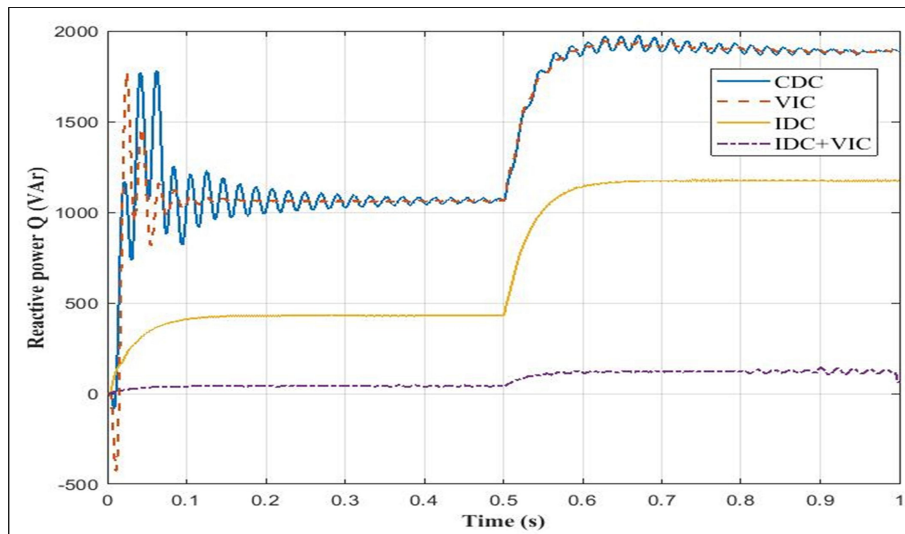


Figure 2.17: The reactive power response (kVAr).

Figure 2.18 shows the active and reactive power responses of DGs for 1.5 kW step change in the R-load at bus1. The active power proportional load sharing can be seen in Figure 2.18 (a) and Figure 2.18 (b) shows the reactive power exchange between the DGs even though the step changes in the real power, this is due to the resistive component in the lines. The condition from no-load to full-load is carried out to see the responses of DGs for low-frequency mode. Figure 2.19 (a) and (b) shows the active and reactive power responses of DGs from no-load to 6 kW and 4 kVAr step

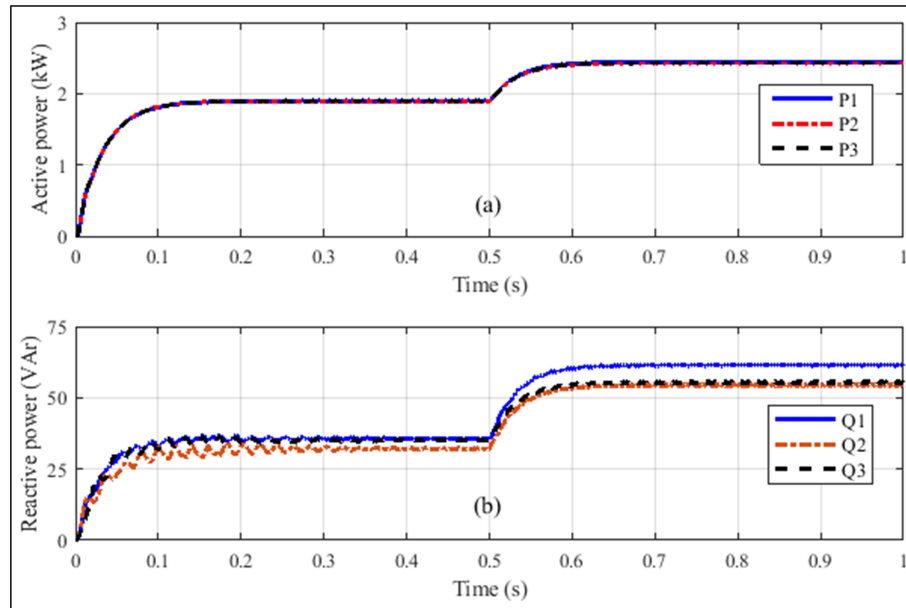


Figure 2.18: Output power of the DG (with 1.5 kW step change in load power at bus1) (a) Active power (b) Reactive power.

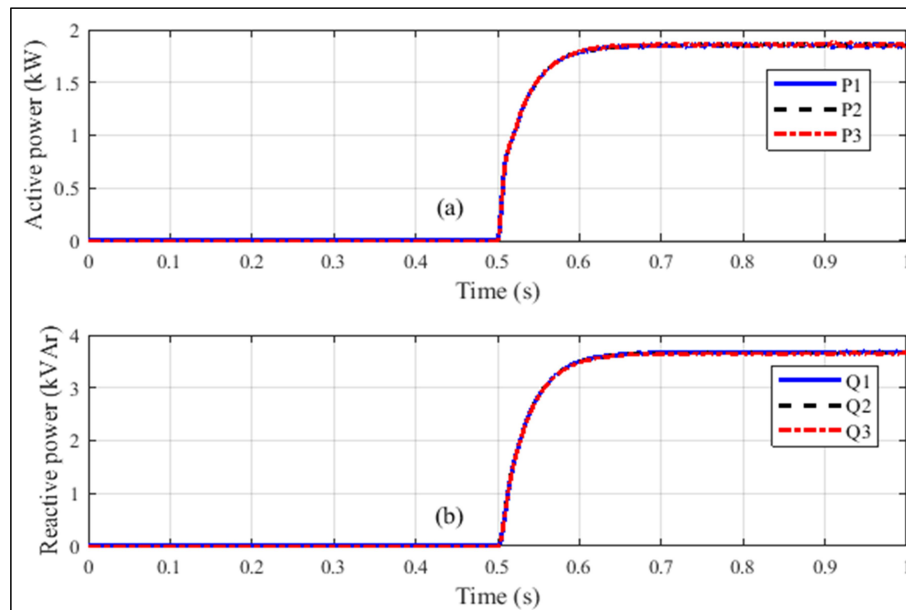


Figure 2.19: Output power of the DG (with 6 kW and 4 kVAr step change in load power at bus1) (a) Active power (b) Reactive power.

change in the RL-load and the proportional load sharing of active and reactive powers are achieved.

2.6.2 Hardware in loop (HIL) real-time responses

Figure 2.20 shows the variation in the output voltage and current of the inverter-based DG1 at 0.5 sec are attributed to the step change of 4kW of load at bus1.

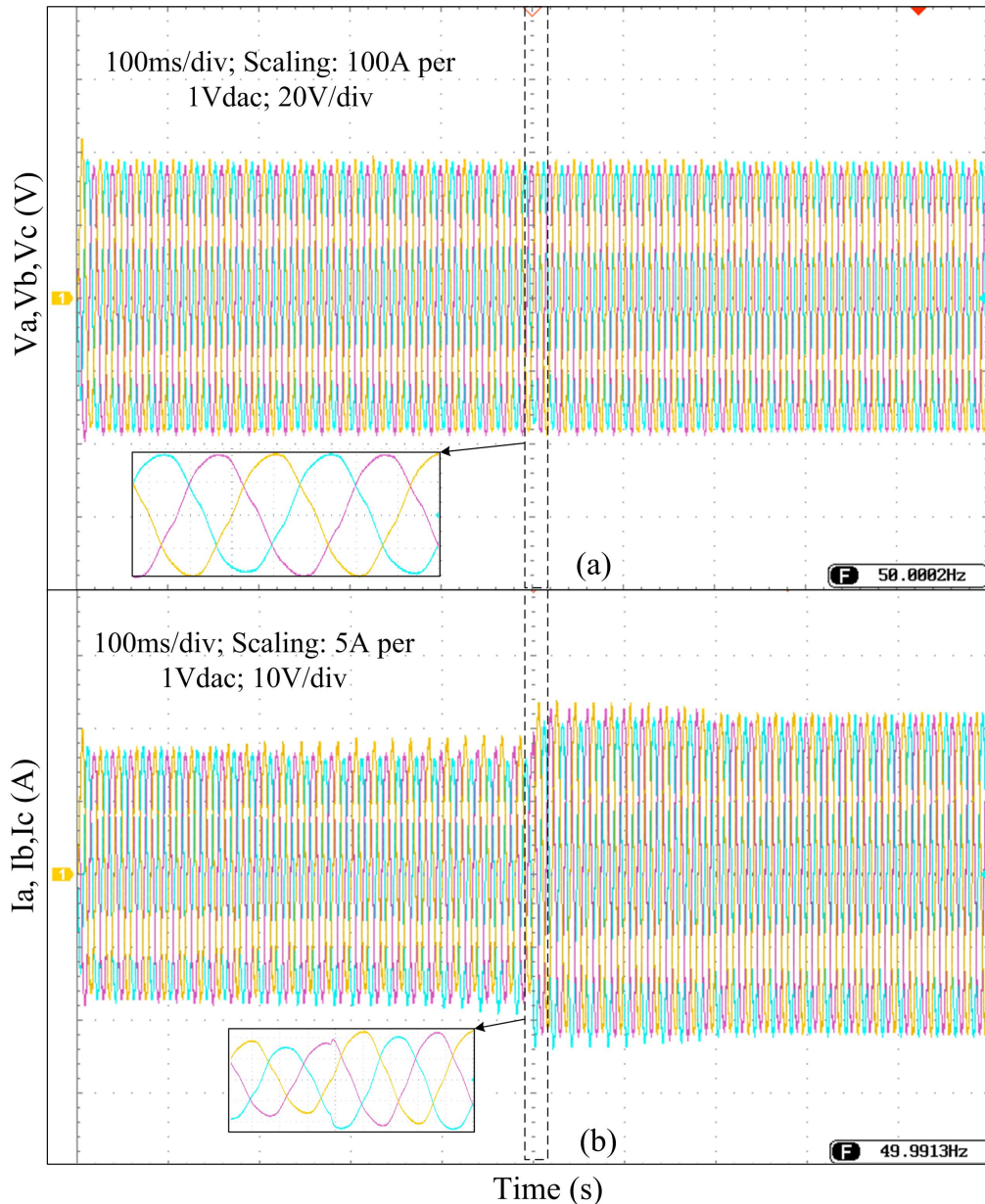


Figure 2.20: Output voltage and current of the DG with 1.5 kW step change in load power at bus1 (a) DG output voltages in Volts (b) DG output currents in Amperes.

In Figure 2.22 it can be seen that the DG which is nearer to the step changed load takes the major part of the transients, while other DGs respond slowly. This

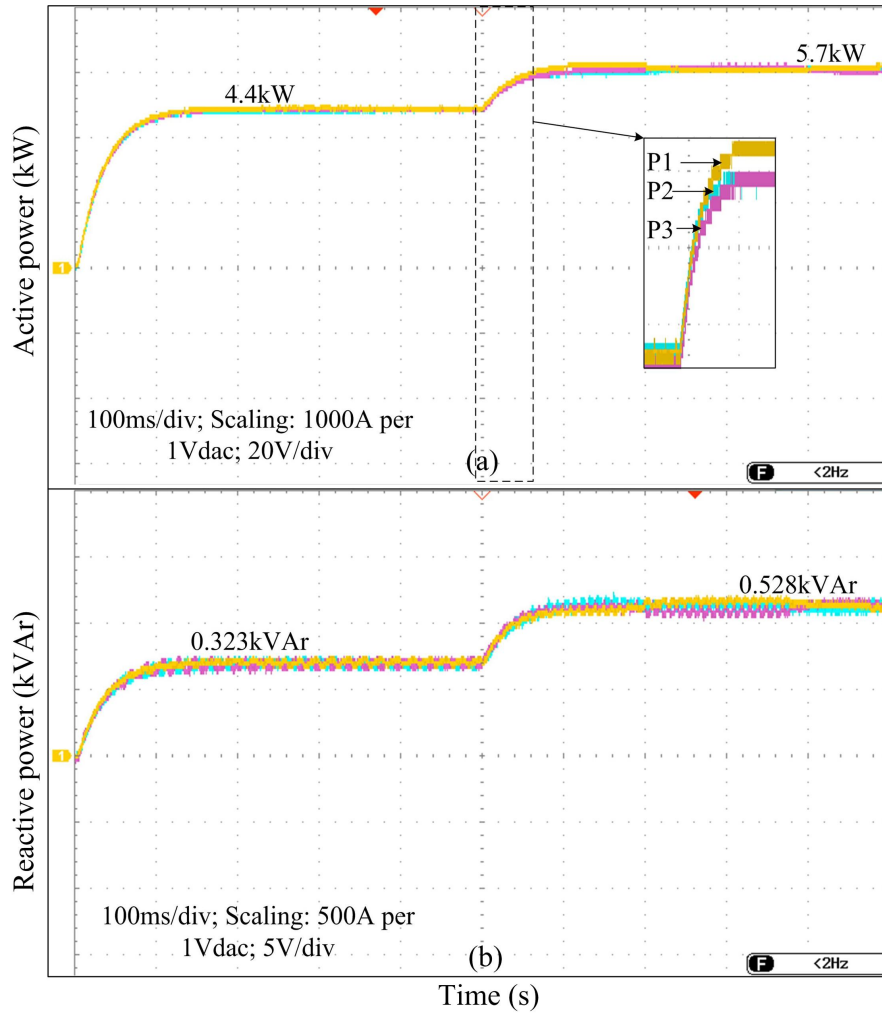


Figure 2.21: Output power of the DG with 1.5 kW step change in load power at bus1 (a) Active power in kW(b) Reactive power in VAR.

is because the inverter output impedance for that DG saw from the load point is considerably low. And the reactive power exchange between the DGs even though the step changes in the real power (R-load) of 1.5 kW at bus1. This is due to the resistive component in the lines. An increase in voltage droop can nullify this effect but it will deteriorate the voltage quality.

In Figure 2.22 a step-change in RL load is introduced to study the low-frequency mode response. Figure 2.22 (a) and 2.22 (b) shows the responses of active power and reactive power responses when the step changes in RL load of 6 kW and 4 kVAr occurred from the no-load condition.

Figure 2.23 (a) and (b) shows the responses of d-axis voltage and current with

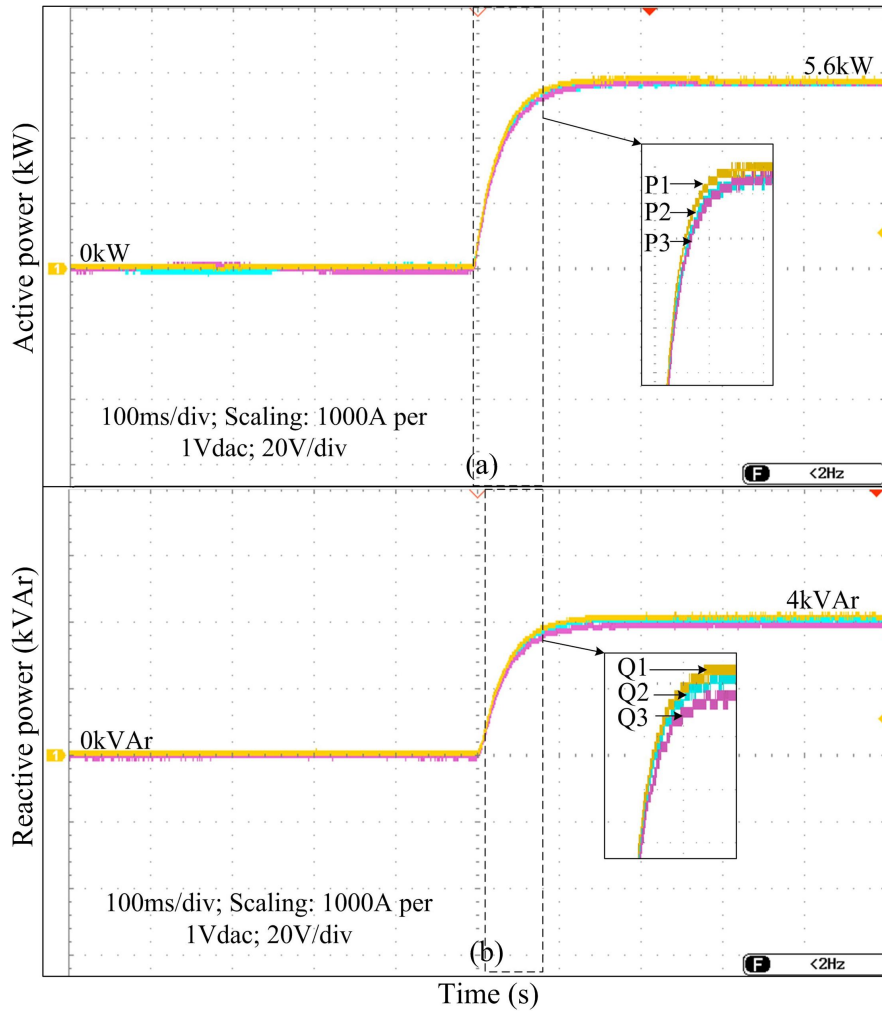


Figure 2.22: Output power of the DG with 6 kW and 4 kVAr step change in load power at bus1 (a) Active power in kW (b) Reactive power in kVAr.

Table 2.3: d-axis output voltage during the step change in the load of 27 kW

Time (s)	d-axis output voltage (V)
0.0-0.5 sec	400 Volts
0.5-0.51 sec	320 Volts
0.51-1.0 sec	380 Volts

the step-change in load to 27 kW at the bus1. The notch in the output d-axis voltage and a disturbance in the d-axis current can be seen at the step change in load at 0.5 s. Figure 2.23 (a) for a 27-kW load change, shows the output voltage

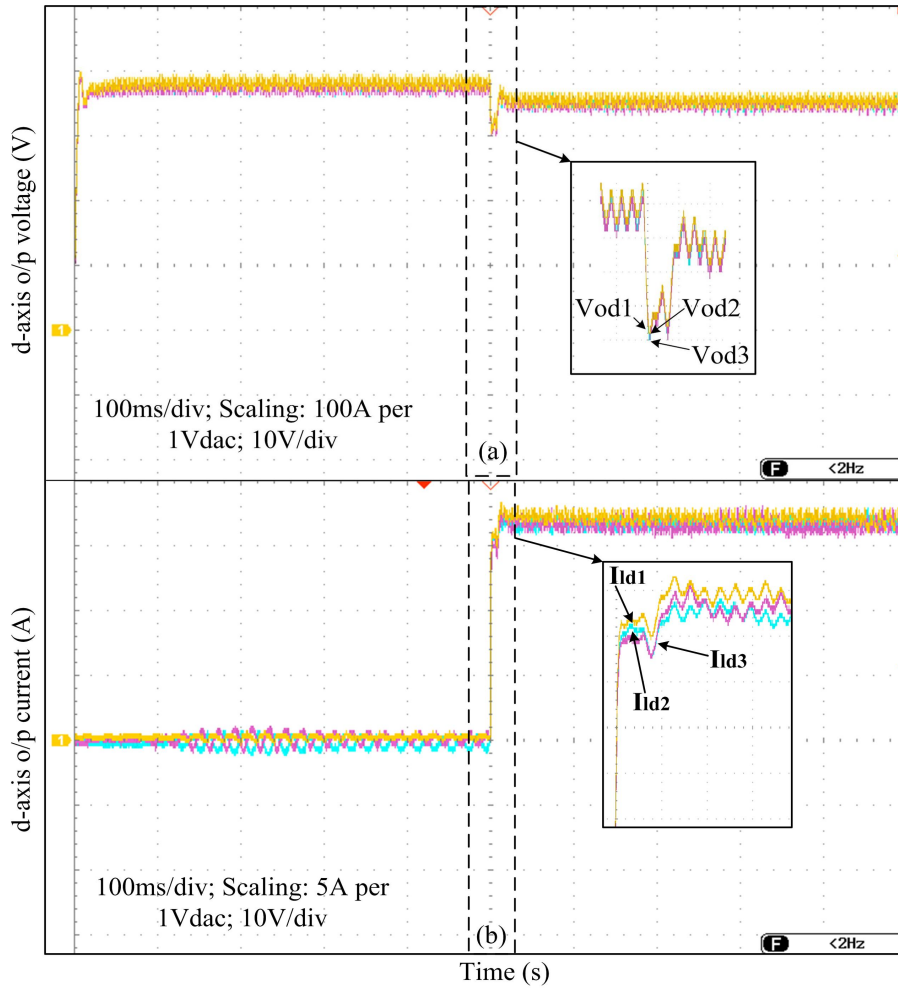


Figure 2.23: Output d-axis voltage and current of the DGs with 27 kW step change in load power at bus1 (a) DGs d-axis output voltages in Volts (b) DGs d-axis output currents in Amperes.

behaviour of all three inverter-based DGs. The output voltage of inverter-based DGs has a notch of 20% for less than 1 ms. The oscillations in the response are within the acceptable range ($\pm 10\%$) and are listed in Table 2.3. Figure 2.23 (b) shows the inverter inductor current responses of all the three inverter-based DGs. Cluster "3" in Figure 2.9 shows a response with high-frequency modes at an approximate frequency of 800 Hz. According to the results, the damping of these modes is largely dependent on the system load level.

2.7 Summary

An islanded microgrid state-space small-signal model is discussed. The modeling includes low-frequency inverter dynamics, high-frequency inverter dynamics, network dynamics, and load dynamics. Each of the microgrid's sub-modules was examined separately before being integrated to create the final microgrid model. The eigenvalues of the model and its sensitivity to various operating modes were investigated. The power-sharing controller of the micro sources' network architecture and parameters were found to be extremely sensitive to the prevailing low-frequency modes. In high-frequency modes, the inverter inner control loop, network dynamics, and load dynamics are all relevant. The improved droop control to proportional load sharing for both resistive and inductive output line impedances is presented here as an improvement to the existing droop control schemes. In the power controller's internal control loop, modeling of resistive output line impedance is being used. In the second step, the virtual complex output impedance in the outer control loop continuously addresses the voltage regulation needs. Using a real-time hardware-in-loop simulator, the entire microgrid model is implemented and validated with a step-change in load power. A successful droop control strategy has been implemented and executed as shown by the responses.

Chapter 3

SYNCHRONIZATION TECHNIQUES BASED ON PLL FOR PE-BASED DGS IN THE GRID-CONNECTED MODE

3.1 Introduction

The decentralized Generation systems (DGs) have gained attention due to the limitations of central power plants. Including these DGs, distributed loads, and storage units, we can framework a microgrid. The concept of micro-grid can increase reliability as well as the efficiency concerning power quality. The microgrid can be operated in a grid-integrated mode and an islanded mode. Grid-integrated distributed generation systems are often used to enlarge power capacity in areas where a stable power supply is not guaranteed. The control of the power flow and the known power factor are the main important methods in the assimilation of the distribution network. To assure an endless supply of power without limiting the flow of energy generated. The premise is that the phase angle of the grid voltage must be determined to control the power factor and power flow in the grid. PLL can be considered a primary structure to integrate the DG into the grid network (Dragicevic et al., 2017). In the AC micro-grid, bi-directional current can be achieved in coordination with the grid, and for grid-connected DGs in the micro-grid, bi-directional current can be achieved

and optimized continuously. More flexible microgrids provide additional incentives by reducing the demand obtained by the grid. Intended or unintended inversion can occur with microgrids that are interfaced with the network through the PLL controller. It is also possible to smoothly switch between grid-connected and standalone modes with these PLLs. The IEEE 1547 guideline standards deal with related networking (Pouresmaeil et al., 2012). PLL controllers are being used as a conventional approach for acquiring phase and frequency data in electrical system networks (Lin et al., 2016), (Kulkarni and Gaonkar, 2020). In power electronics and electrical systems, the PLL method has been applied to the synchronization of DG networks based on power converters (Gaonkar, 2010). With the power conversion system utility, this can also be used to produce synchronized references. Detecting the zeroth sequence of the line voltage is a straightforward approach to obtain information on phase. Since there is only a crossover point that can be detected every half-cycle of the operating frequency. Another option is to use the quadrature-phase of a 90-degree shift in the input waveform as a technique (Kulkarni and Gaonkar, 2021), (Han et al., 2016).

Synchronous Reference Frame Phase-Locked Loop (SRF-PLL) is extensively utilized in three-phase systems. These PLLs can even be used in case of network voltage distortion with high-order harmonics by reducing the bandwidth of the PLL. In (Guo et al., 2011), a powerful digital synchronous PLL is introduced, depending on the theory of instantaneous real and virtual power (PQ-PLL) to sustain synchronization presence of the existence of harmonics. This PLL has the same structural characteristics as the SRF-PLL and in addition, we obtain a +ve sequence voltage. Quadrant phase transport delay or $T/4$ Delay Phase-Locked Loop ($T/4$ Delay-PLL) design is another alternative for phase detection (Rolim et al., 2006). In $T/4$ Delay the grid voltage frequency f_0 dependency will make the $T/4$ Delay-PLL is unsuitable in grid voltage frequency fluctuations. Furthermore, the frequency distortions directly disseminate to the low-pass filter once the input voltage is deferred by $T/4$ Delay. The Inverse Park Transform is another construction to detect the phase error and it is based on the $dq \rightarrow \alpha\beta$ (Yang et al., 2015). The grid voltage distortions are not disseminating to the low-pass filter which gives a good harmonic rejection but the design parameter k_{pit} (proportional and integral PI gain parameters) in the IPT-PLL arrangement should be accurate and precise. The Enhanced Phase-Locked Loop (E-PLL) will detect the phase error without any transformations given in (Teodorescu et al., 2011). By checking the latency induced by the low frequencies, E-PLL exhibits

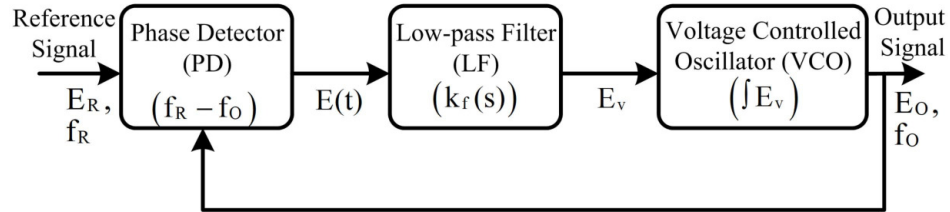


Figure 3.1: Basic structure of Phase Lock Loop (PLL).

slow dynamics, so not a good explication for purposes that require fast response. In (Karimi-Ghartemani and Iravani, 2002) the Park synchronous reference frame PLL (SRF-PLL) has been proposed to operate during grid disturbances and brings the system to the stable region. Most of the PLL algorithms are very sensitive to faults and result in sudden phase angle changes during fault conditions. During unplanned events of power quality variations like sag, swell, harmonics, unbalances, and faults, it is necessary to develop appropriate control strategies. An appropriate modeling and consistent behaviour of the control strategy will bring back the system into a stable operating region.

3.2 Phase-locked loop for grid synchronization

Starting from the computer to communicate the phase lock loop is widely used in many applications. Such as synchronization, clock recovery, tone generation, noise reduction, jitter reduction, microprocessor, frequency synthesizer, frequency shift, and also used in frequency modulation demodulation circuits (Ndjountche, 2018). Multiple output frequencies of an input signal can be generated, and as the name suggests, PLL is a control system that keeps the identical phase among the input and output signals, thereby synchronizing the phase and frequency concerning the output with the input (Golestan et al., 2019).

We can get a constant or zero phases difference when the output frequency exactly matches the input frequency, the loop can be said to be in a locked state. Mathematically, we can express the lock condition as equations (3.1) and (3.2).

$$f_0 = f_R \quad (3.1)$$

$$\Delta\phi_0 = 0 \quad (3.2)$$

The Figure 3.1 shows the PLLs fundamental construction. The phase detector (PD) compares the reference frequency (f_R) with voltage controlled oscillator (VCO) frequency (f_0) and based on that it generates the error signal($E(t)$). And now this $E(t)$ goes through the low pass filter (LF) and produces an error voltage (E_v). With the error signal, the VCO increases or decreases the oscillator frequency up till the VCO's oscillator frequency locks to the input frequency ($f_R = f_0$). And in the locked state, there can be zero phase difference between the reference signals. output signal (E_R and E_0).

The PD is accomplished with a simple multiplier term, the LF with a PI controller, and the VCO with a sinusoidal function provided by a linear integrator. The system's input signal is given by equation (3.3)

$$v = V \sin(\theta) + V(\omega t + \phi) \quad (3.3)$$

and the VCO's generated signal is provided by equation (3.4)

$$v' = \cos \theta' = \cos(\omega' t + \phi') \quad (3.4)$$

The multiplier PD output phase error signal can be expressed as equations (3.5) and (3.6)

$$\epsilon_{pd} = V k_{pd} \sin(\omega t + \phi) + \cos(\omega' t + \phi') \quad (3.5)$$

$$\epsilon_{pd} = \frac{V k_{pd}}{2} \left[\sin((\omega - \omega')t + (\phi - \phi')) + \sin((\omega + \omega')t + (\phi + \phi')) \right] \quad (3.6)$$

Because the LF cancels out the high-frequency components of the PD error signal, only the low-frequency term will be evaluated from now on. As a result, in this analysis, the PD error signal to be evaluated is as

$$\bar{\epsilon}_{pd} = \frac{V k_{pd}}{2} \sin((\omega - \omega')t + (\phi - \phi')) \quad (3.7)$$

The DC term of the phase error signal is provided if the VCO is considered to be properly tuned to the input frequency, i.e., with $\omega \approx \omega'$.

$$\bar{\epsilon}_{pd} = \frac{V k_{pd}}{2} \sin(\phi - \phi') \quad (3.8)$$

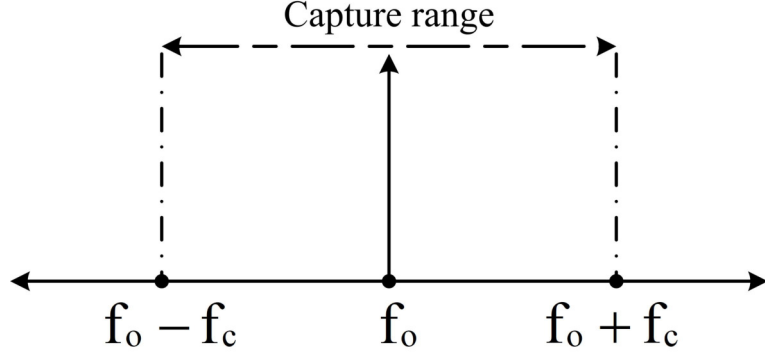


Figure 3.2: Capture range of the phase-locked loop with f_0 and f_c .

Because of the sinusoidal function, it can be shown that the multiplier PD produces nonlinear phase detection. When the phase error is moderate, i.e. when $\phi \approx \phi'$, the output of the multiplier PD can be linearized in the proximity of such an operating point because $\sin(\phi - \phi') \approx \sin(\theta - \theta') \approx (\theta - \theta')$. As a result, once the PLL is locked, the phase error signal's relevant term is given as equation (3.9)

$$\bar{\omega}' = (\omega_c + \Delta\bar{\omega}') = (\omega_c + k_{vco}v_{lf}) \quad (3.9)$$

where ω_c is the VCO's center frequency and is fed into the PLL as a feed-forward parameter based on the frequency range to be detected. As a result, slight signal variations in VCO frequency are produced as equation (3.10)

$$\bar{\omega}' = k_{vco}v_{lf} \quad (3.10)$$

and the phase-angle variations sensed by the PLL can be written as equation (3.11)

$$\theta'(t) = \int \bar{\omega}' dt + \int k_{vco}v_{lf} dt \quad (3.11)$$

A small-signal linearized model of the multiplier PD can be implemented using this equation. This model demonstrates a zero-order unit where the gain is proportional to the input signal amplitude in its locked state.

Figure 3.2 shows the capture range of PLL. Now with no lock, the PLL can only be locked if the input signal is within range of capturing the PLL ($f_0 - f_c < f < f_0 + f_c$). This means that whenever the input signal is within the capture range, the VCO

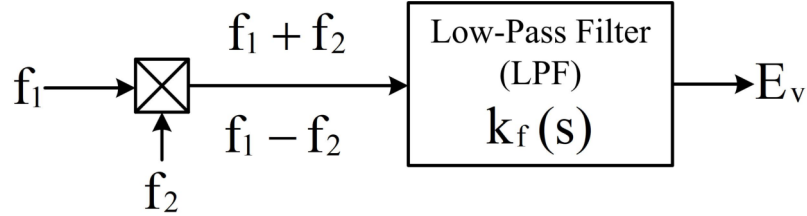


Figure 3.4: Input error voltage generation to the voltage controlled oscillator.

of utilizing a low pass filter (LPF). Therefore, simply multiplying two signals, can make a difference between the two. In frequency domain analysis when we multiply two frequency signals (f_1 and f_2), we get two terms, one is the summation of the frequencies ($f_1 + f_2$) and another one is the difference between the two frequencies ($f_1 - f_2$). So there high-frequency components ($f_1 + f_2$) can be eliminated by the LPF, while ($f_1 - f_2$) will tell us the phase difference. When ($f_1 - f_2$) passing through the LPF, it provides the required error voltage (E_v) for the VCO. So using this error it is possible to lock the VCO frequency to the input frequency as shown in Figure 3.4.

The error voltage E_v from the LPF is fed into the VCO as a controlled voltage and we want a pure frequency at the output of the VCO. The VCO can be a harmonic or relaxation oscillator but we cannot endure any phase noise, we need the VCO output frequency to be agile and precise (Zhou et al., 2014).

3.3 Three-phase grid synchronization methods

PLL technology is used to synchronize the distributed source with the grid, and it plays an important part in grid synchronization. Various PLL-based synchronization approaches are discussed in this section. Phase-Locked Loop with Synchronous Frames (SRF-PLL). The Phase-Locked Loop (PQ-PLL), Quarter Phase Transport Delay or $T/4$ Delay Phase-Locked Loop ($T/4$ Delay-PLL), Inverse Park Transformation Phase-Locked Loop (IPT-PLL), Enhanced Phase-Locked Loop (E-PLL), and Park synchronous reference frame Phase-Locked Loop (SRF-PLL) are all described and analyzed.

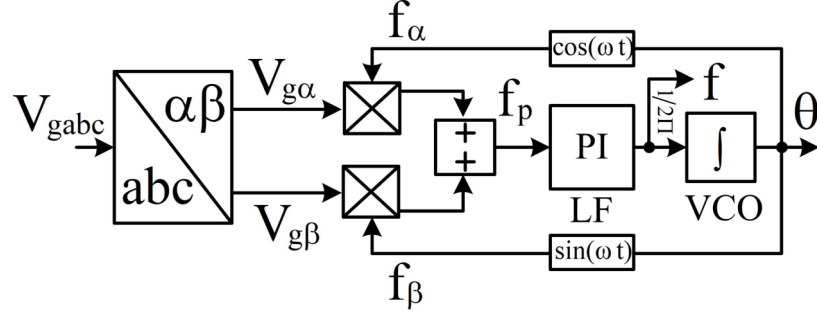


Figure 3.6: Instantaneous Active and Reactive Power phase-locked loop (PQ-PLL).

vigorous digital synchronizing PLL, which is based on the instantaneous (PQ) power theory. This can be used in presence of $-ve$ sequence unbalances and sub-harmonics (Rolim et al., 2006). From Figure 3.5 and Figure 3.6, we can see that it has an alike structure as conventional SRF-PLL, however it can be quickly followed by the power theory. Additionally, we can get $+ve$ sequence voltages as a by-product.

3.3.3 Second Order Generalized Integrator-Phase-Locked Loop (SOGI-PLL)

To further enhance completion in terms of the performance of the PLL, a 2 stage adaptive filter (notch filter) having 2-adaptive gains have been added, which acts as a generalized sine integrator. The block diagram of the second-order "generalized integrator" (SOGI-PLL) is depicted in Figure 3.7. The frequency of the grid ω from the feedback will be from sinusoidal and cosine blocks detected by a generalized sinusoidal integrator (Yang et al., 2015).

Subsequently, SOGI-PLL's orthogonal system based on Figure (3.7) can defined as:

$$v_{g\alpha\beta}(s) = \begin{bmatrix} v_{g\alpha}(s) \\ v_{g\beta}(s) \end{bmatrix} = \begin{bmatrix} \frac{k\omega s}{s^2+k\omega s+\omega^2} \\ \frac{k\omega^2}{s^2+k\omega s+\omega^2} \end{bmatrix} \quad (3.14)$$

The k is the control parameter of the SOGI-based PD system proposed in (3.14). If we set the value of k to $\sqrt{2}$, then we can obtain a good connection linking overshoot and settling time. Moreover, according to Mathematical Equation (3.14), the SOGI-PLL PD system operates with a bandpass filter. With ω from filtering and θ from Park transformation as the feedback from the SOSI PD system which makes complicated

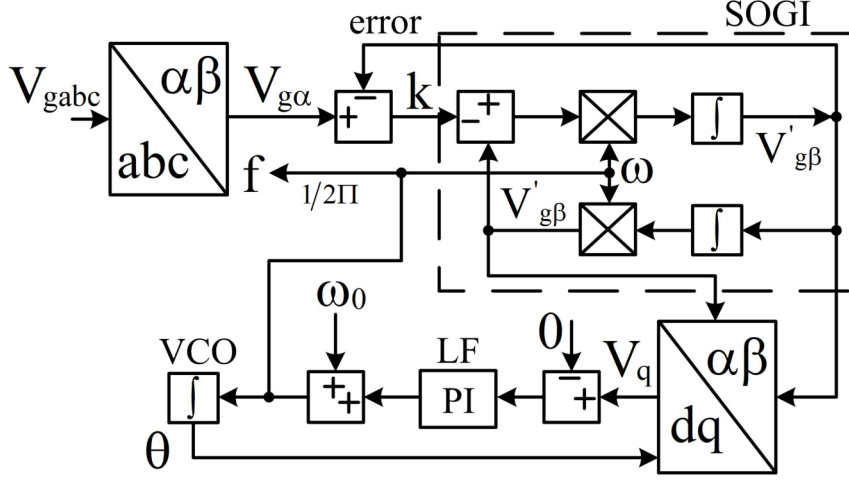


Figure 3.7: Control structure of Second Order Generalized Integrator-Phase-locked Loop (SOGI-PLL).

construction of SOGI-PLL. Hence, this PLL is further intricate in the structure other than the other PLLs. Though, we can use SOGI-PLL to suppress the harmonics feature in single-phase applications.

3.3.4 Dual Second Order Generalized Integrator-Phase-Locked Loop (DSOGI-PLL)

A double quadratic generalized integrator DSOGI-PLL extracts a fundamental positive sequence to SRF-PLL. However, we employ a generalized two-second integrator to perform a quadrature signal generator, shown in Figure 3.8 The three-phase grid voltage vector is presented as equations (3.15) to (4.15).

$$v_{gabc} = \begin{bmatrix} v_{ga} & v_{gb} & v_{gc} \end{bmatrix}^T \quad (3.15)$$

Then, the *+*ve-sequence component of the grid voltage component is obtained as follows.

$$v_{gabc}^+ = \begin{bmatrix} v_{ga}^+ & v_{gb}^+ & v_{gc}^+ \end{bmatrix}^T \quad (3.16)$$

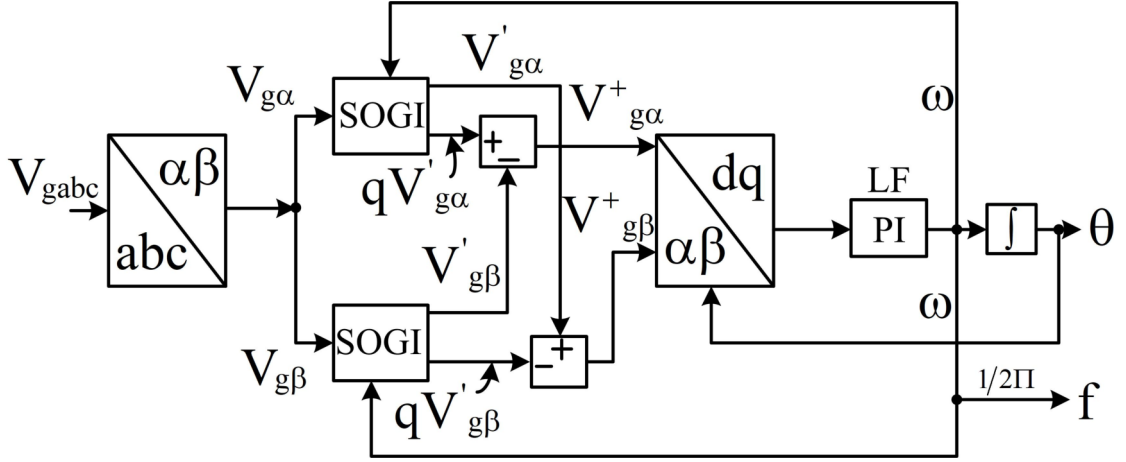


Figure 3.8: Control structure of Dual Second Order Generalized Integrator-Phase-locked Loop (DSOGI-PLL).

$$[T] = \frac{1}{3} \begin{bmatrix} 1 & a^2 & a \\ a & 1 & a^2 \\ a^2 & a & 1 \end{bmatrix} \quad (3.17)$$

Where, $a = e^{-j\frac{2\pi}{3}}$ and the +ve sequence component of the grid voltage can be given as

$$v_{g\alpha\beta}^+ = \frac{2}{3} \begin{bmatrix} 1 & \frac{-1}{2} & \frac{-1}{2} \\ 0 & \frac{\sqrt{3}}{2} & \frac{-\sqrt{3}}{2} \end{bmatrix} \quad (3.18)$$

$$v_{g\alpha\beta}^+ = \frac{2}{9} \begin{bmatrix} 1 & \frac{-1}{2} & \frac{-1}{2} \\ 0 & \frac{\sqrt{3}}{2} & \frac{-\sqrt{3}}{2} \end{bmatrix} \begin{bmatrix} 1 & a^2 & a \\ a & 1 & a^2 \\ a^2 & a & 1 \end{bmatrix} v_{gabc} \quad (3.19)$$

$$v_{g\alpha\beta}^+ = \frac{2}{3} \begin{bmatrix} 1 & \frac{-1}{2} & \frac{-1}{2} \\ 0 & \frac{\sqrt{3}}{2} & \frac{-\sqrt{3}}{2} \end{bmatrix} \begin{bmatrix} 1 & \frac{-1}{2} & \frac{-1}{2} \\ 0 & \frac{\sqrt{3}}{2} & \frac{-\sqrt{3}}{2} \end{bmatrix} v_{g\alpha\beta} \quad (3.20)$$

$$v_{g\alpha\beta}^+ = \frac{1}{2} \begin{bmatrix} 1 & -b \\ b & 1 \end{bmatrix} v_{g\alpha\beta} \quad (3.21)$$

Similarly, the -ve sequence component of the grid voltage vector is given in equation (4.16).

$$v_{g\alpha\beta}^- = \frac{1}{2} \begin{bmatrix} 1 & -b \\ b & 1 \end{bmatrix} v_{g\alpha\beta} \quad (3.22)$$

where, $b = e^{-j\frac{\pi}{2}}$. Therefore, the exact extraction of the sequence component here requires a 90 degree phase shift of $v_{g\alpha}$ and $v_{g\beta}$. The purpose of this is, the transmit delay buffer means and another the full pass filter system. But, since this method is not frequency-adapted, the estimation of positive sequences can be error-prone.

A compound of a lowpass filter (LPF) and a bandpass filter (BPF) is appropriated to prevent the harmonics of the input signal. The BPF in (4.17) grants only the harmonic filter, while the LPF in (4.19) provides the harmonic filter and a 90⁰ phase shift. Additionally, the filter parameter ω for frequency arrangement is updated in the PLL. The block diagram, shown in Figure 3.8.

$$BPF(s) = \frac{v'}{v} = \frac{ks^2 + k\omega s + \omega^2}{s^2 + k\omega s + \omega^2} \quad (3.23)$$

$$LPF(s) = \frac{qv'}{v} = \frac{ks^2 + k\omega s + \omega^2}{s^2 + k\omega s + \omega^2} \quad (3.24)$$

The standard of DSOGI-PLL is to extort the basic +ve sequence and usual SRF-LL. Consequently, it provides accurate +ve sequence knowledge for the system synchronization that too in a situation like network outages. The 90⁰ phase shift information can also be obtained from this PLL. So, DSOGI-PLL can extend for single-phase purposes (Rodriguez et al., 2011).

3.3.5 Phase Transport Delay-Phase-Locked Loop ($T/4$ Delay-PLL)

$T/4$ delay-PLL is shown in Figure 3.9. In this, the Park transformation $\alpha\beta \rightarrow dq$, is used for the phase detection. A grid voltage v_{gabc} with α variable and a virtual β variable are to be in-quadrature and required in single-phase as well as in three-phase applications. In Figure 3.9, we can see that a $T/4$ delay of input grid voltage β variable is being assimilated, where $[T]$ is the input grid voltage v_{abc} fundamental period.

Precisely, on a presumption that the grid voltage v_{gabc} is pure sinusoidal, given as (4.20)

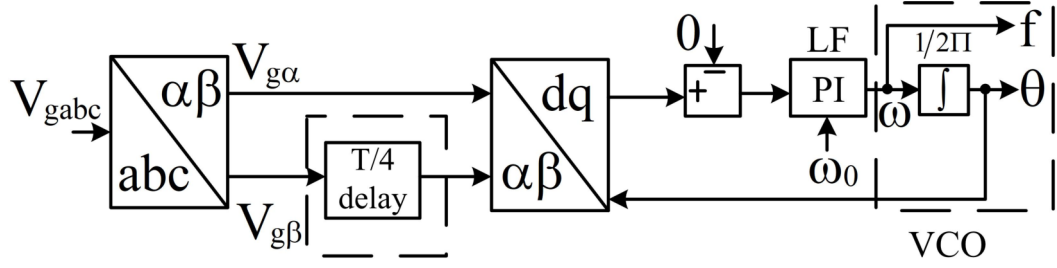


Figure 3.9: Detailed structure of a Quarter Phase Transport Delay or $T/4$ Delay -Phase-locked Loop ($T/4$ Delay-PLL).

$$v_g(t) = v_g \cos(\theta) = v_g \cos(\omega t + \phi_0) \quad (3.25)$$

Where, ω will be an angular frequency of the grid and ϕ_0 is the initial grid voltage phase angle. After the Park transformation to the above equation yields to (4.21)

$$v_{dq} = [T_p]v_{\alpha\beta} \approx v_g \begin{bmatrix} 1 \\ \epsilon \end{bmatrix} \quad (3.26)$$

Where T_p is the Park transform matrix. The ϵ is the phase error detected and regulated by PI-controller. After error regulation, the nominal grid angular frequency ω_0 is feed-forwarded then the grid voltage vector phase θ will be locked. Meanwhile, grid voltage amplitude $v_q = v_d$ and frequency $f = \frac{\omega}{2\pi}$ can also be obtained. The accomplishment of $T/4$ Delay-PLL employing a quarter ($T/4 = \frac{1}{4f_0}$) with f_0 being the grid nominal frequency is usually used.

3.3.6 Inverse Park Transform-Phase-Locked Loop (IPT-PLL)

Inverse Park Transform is one more option to detect phase error ϵ and it is based on the $dq \rightarrow \alpha\beta$. Figure 3.10 shows the block diagram of the IPT-PLL system. In comparison with the $T/4$ Delay PLL, we can see an extra LPF in the IPT-PLL.

$$v_{gdq}(s) = T(s) \begin{bmatrix} v_g(s) \\ v_\beta(s) \end{bmatrix} \quad (3.27)$$

$$v'_{gdq}(s) = T(s) \begin{bmatrix} v_\alpha(s) \\ v_\beta(s) \end{bmatrix} \quad (3.28)$$

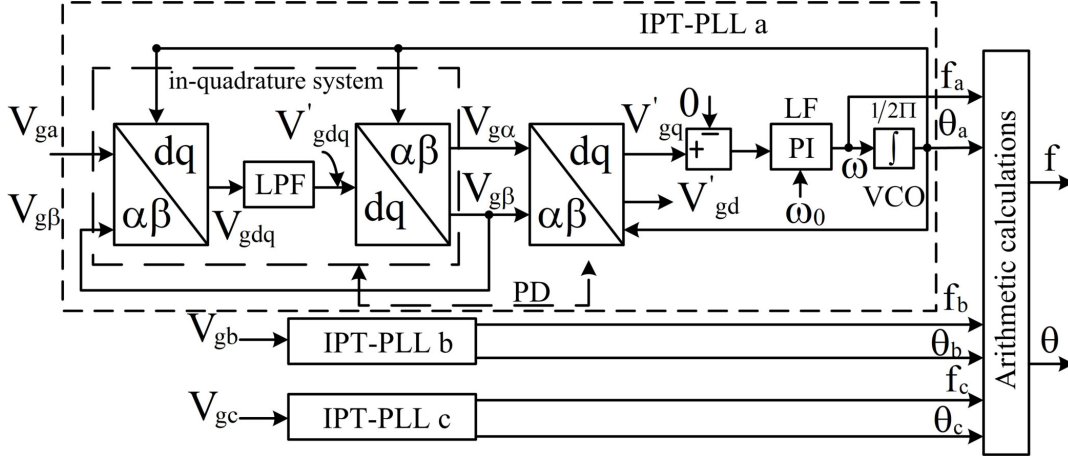


Figure 3.10: Block diagram of the inverse park transform based phase-locked loop (IPT-PLL).

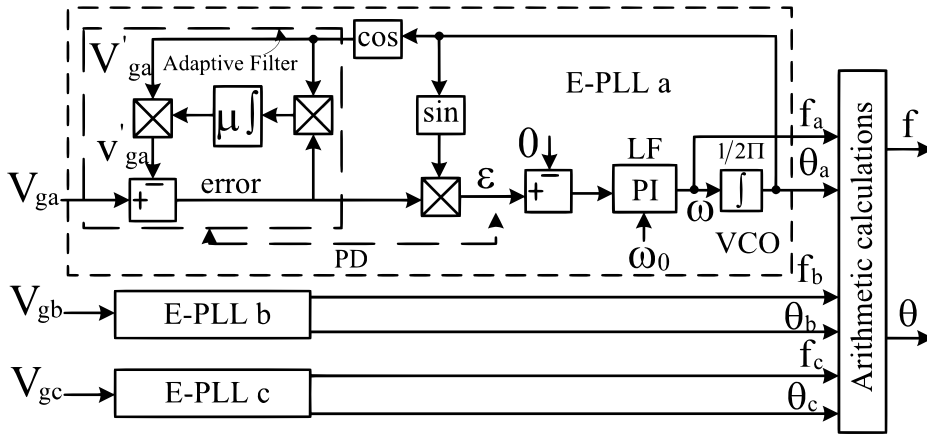


Figure 3.11: Block diagram of the enhanced phase-locked loop (E-PLL).

$$v'_{gdq}(s) = G_{LPF}(s)v_{dq}(s) = \frac{\omega_c}{s + \omega_c}v_{dq}(s) \quad (3.29)$$

Where $T(s)$ the Laplace is form of T shown in Figure Figure 3.10 and $G_{LPF}(s)$ is LPFs transfer function, and ω_c is the cut-off frequency. Next, utilizing the Euler's-formula and the Laplace-property as the frequency shifting provides (3.30),

$$v_{g\alpha\beta}(s) = \begin{bmatrix} v_\alpha(s) \\ v_\beta(s) \end{bmatrix} = \begin{bmatrix} \frac{\omega_c s}{s^2 + \omega_c + \omega^2} \\ \frac{\omega_c \omega}{s^2 + \omega_c + \omega^2} \end{bmatrix} v_g(s) \quad (3.30)$$

Now, with this we can state that the attainment of IPT-PLL depends on the LPFs, $G_{LPF}(s)$. The design of the IPT-PLL composition can be defined as $k_{ipt} =$

$\frac{\omega_c}{\omega}$. According to 3.30, $V_g(s) \rightarrow V_{g\alpha}(s)$ (2nd order bandpass filter) and $V_g(s) \rightarrow V_{g\beta}(s)$ (2nd order lowpass filter). Hence, the design parameter k_{pit} is the same as $\sqrt{2}$ so that the optimum attenuation of the second-order filter can be confirmed and the cutoff frequency ω_c of the LPF can be determined accordingly. On the other hand, the parameter value of k_{pit} needs to be adjusted in accordance with the delay. However, with orthogonal system ($v_{g\alpha\beta}$) procurement the IPT-PLL PD system can also guarantee harmonic filters for the system voltage.

3.3.7 Enhanced-Phase-Locked Loop (E-PLL)

Since $T/4$ Delay-PLL and IPT-PLL correspond to quadrature systems, it is probable to detect phase errors ϵ in the Park transform. The enhanced Phase-Locked Loop (E-PLL) will detect the phase error without any transformations, but it enables an adaptive filtering technique for phase detection. The input to an adaptive filter is the reference signal and error signal by which the filter can automatically adjust the parameters (Karimi-Ghartemani et al., 2011). The Enhanced PLL (E-PLL) uses the adaptive filtering technique with a nonlinear adaptive notch filter which was the same as introduced in (Khajehoddin et al., 2012). The composition of E-PLL is as shown in Figure 3.11. The detection of phase can be achieved by an adaptive filter (AF) and a sine multiplier, so compared with a PLL based on a sine multiplier, E-PLL can improve performance (Pawar and Mane, 2017). More specifically, the estimation of grid input voltage v_q is performed by AF. With phase error ϵ and locked-phase θ , one can minimize the objective function $\frac{(v_g - v'_g)^2}{2}$. Therefore, we can obtain the non-oscillation phase and non-oscillation frequency of E-PLL.

From Figure 3.11 we can clearly see that the grid voltage amplitude v_q can lock the phase θ of input voltage. And the measured grid voltage amplitude v'_g can be expressed as (3.31),

$$v'_g = \mu * error * \cos(\theta) \quad (3.31)$$

Where, μ is the control parameter which decides AF filtering speed and the error will be $V_g - V'_g$. Simply linearizing (3.31) yields in (3.32),

$$\frac{v'_g(s)}{v_g(s)} = \frac{1}{\tau s + 1} \quad (3.32)$$

which represents a simple low-pass filter having time constant as $\tau = \frac{2}{\tau t}$. In (Kivimäki et al., 2017) the approximated settling time for AF is given as $4\tau = \frac{8}{\mu}$.

3.4 Test system model description

Two parallel-connected inverter-based DGs integrated into the Grid at PCC are shown in Figure 3.12. As a severe consequence of the protection means specified in 3.5, standard parallel RLC loads are taken into account (Kulkarni et al., 2021). Where L_i the DG side is filter inductance, and L_g is the grid side filter inductance, and C_F is the capacitance of the filter. The parameters of the test system are listed in Table 3.1. The controller part includes a droop controller as well as a standard current controller in the primary level of the control architecture. And the synchronization controller (PLL) is embedded in the secondary level of the control architecture. All the listed and studied PLLs will come under the secondary control level.

Now, the active and reactive power (instantaneous) calculation for droop controller with DGs output DQ-axis voltage, and current are given as (3.33) and (3.34)

$$\tilde{p} = V_{od}i_{od} + V_{oq}i_{oq} \quad (3.33)$$

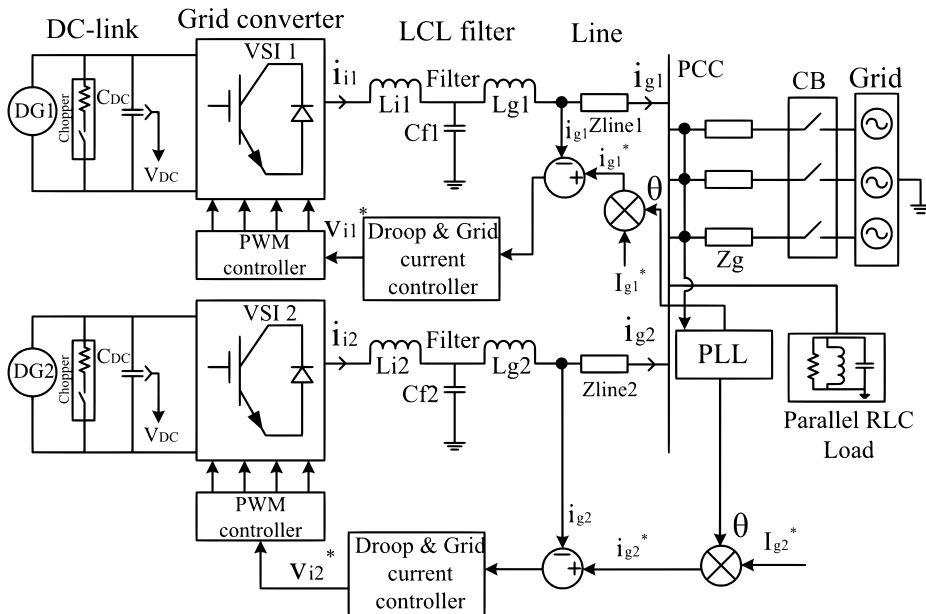


Figure 3.12: Control structure of a grid-connected Inverter based DG systems (test model).

Table 3.1: THE TEST SYSTEM PARAMETERS

Parameter	Value	Parameter	Value
V_{DC}	700 V	C_{DC}	0.06 mF
R_{DC}	0.02 Ω	L_{fi}	0.01 H
L_g	0.013 H	C_f	5
V_g	230 V	R_g	0.15 Ω
ω	314	ω_c	31.42

$$\tilde{q} = V_{od}i_{oq} - V_{oq}i_{od} \quad (3.34)$$

where \tilde{p} and \tilde{q} are the instantaneous active power in kW and reactive power in kVAR respectively. V_{odq} and i_{odq} are the d-axis and q-axis output voltages in Volts and currents in Amperes respectively.

Equations (3.35) and (3.36) show the fundamental components of active and reactive powers and ω_c is the cut-off frequency of lowpass filter.

$$P = \frac{\omega_c}{S + \omega_c} \tilde{p} \quad (3.35)$$

$$Q = \frac{\omega_c}{S + \omega_c} \tilde{q} \quad (3.36)$$

In (3.35) and (3.36) the term $(\frac{\omega_c}{s+\omega_c})$ gives the low-pass filter where $\omega_c=31.42$ radians. Then, as shown in (3.37) and (3.38), artificial droops (frequency droop (m_p) and voltage droop (n_q)) of control loops are introduced.

$$m_p = \omega_n \left(1 - \frac{P f_{droop}}{P_{max}} \right) \quad (3.37)$$

$$n_q = V_{dn} \left(1 - \frac{Q V_{droop}}{Q_{max}} \right) \quad (3.38)$$

Among them, ω_n and V_{dn} are the nominal angular frequency in radians and d-axis reference voltage in volts respectively. The measured active and reactive powers will be P and Q, and m_p and n_q are the droop slope coefficients.

3.5 HIL virtual and real-time responses

The studied six PLL controllers (SRF-PLL, SOGI-PLL, DSOGI-PLL, E-PLL, $T/4$ Delay-PLL, and IPT-PLL) were implemented in Typhoon HIL-402. The performance analysis and verification of the PLL controllers under various power quality issues are listed.

In Figure 3.13 the responses of all the studied PLLs concerning the grid voltage are listed. Under the grid voltage normal test condition we can see that the DSOGI-PLL shows a better performance in comparison with all other PLLs. The maximum variations can be seen with the SRF-PLL and in the $T/4$ Delay-PLL as the oscillations persist in the frequency. This can be overcome by increasing the proportional and differential gain with the compromise in its overall frequency bandwidth. And the E-PLL and IPT-PLL will show almost similar responses in their frequency variations as subject to the normal grid voltage test condition.

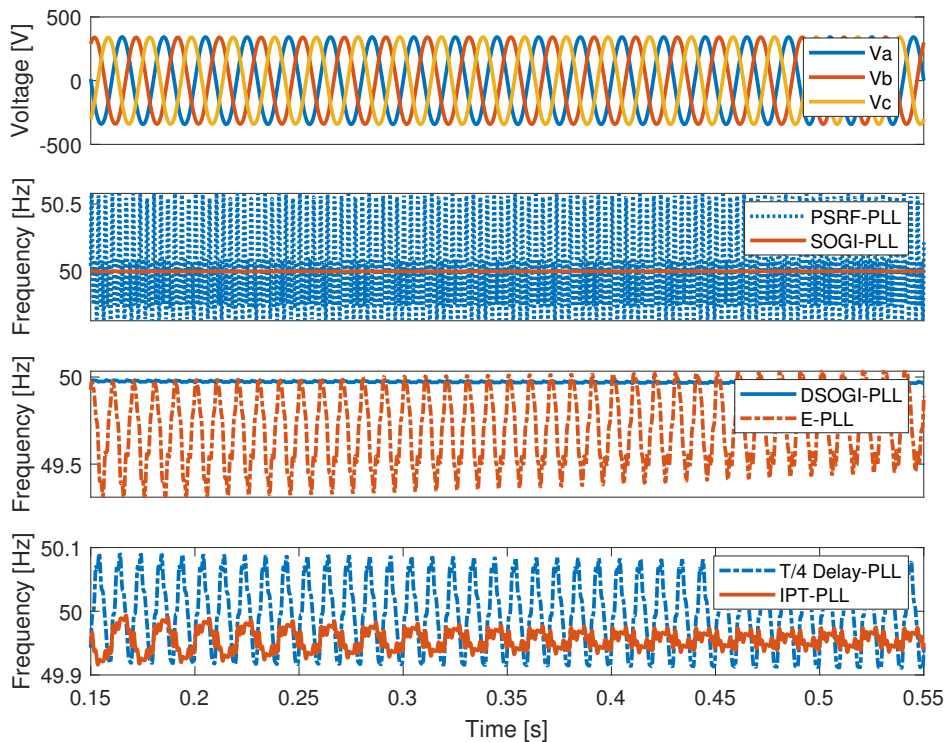


Figure 3.13: Responses of SRF-PLL, SOGI-PLL, DSOGI-PLL, E-PLL, $T/4$ Delay-PLL, and IPT-PLL frequencies under grid voltage normal test condition.

In Figure 3.14 the grid is subjected to 5% of voltage sag at 0.2 s to 0.4 s. The frequency responses of the PLLs show a promising result at the time of insertion of sag and removal of sag. The promising response for all the other PLLs is seen with the SOGI-PLL and the DSOGI-PLL. The fluctuations in the $T/4$ Delay-PLL will be more following the SRF-PLL. But we can see the frequency variations as subject to grid voltage sag at 0.2 s and 0.4 s in all the other PLLs except SOGI-PLL and DSOGI-PLL.

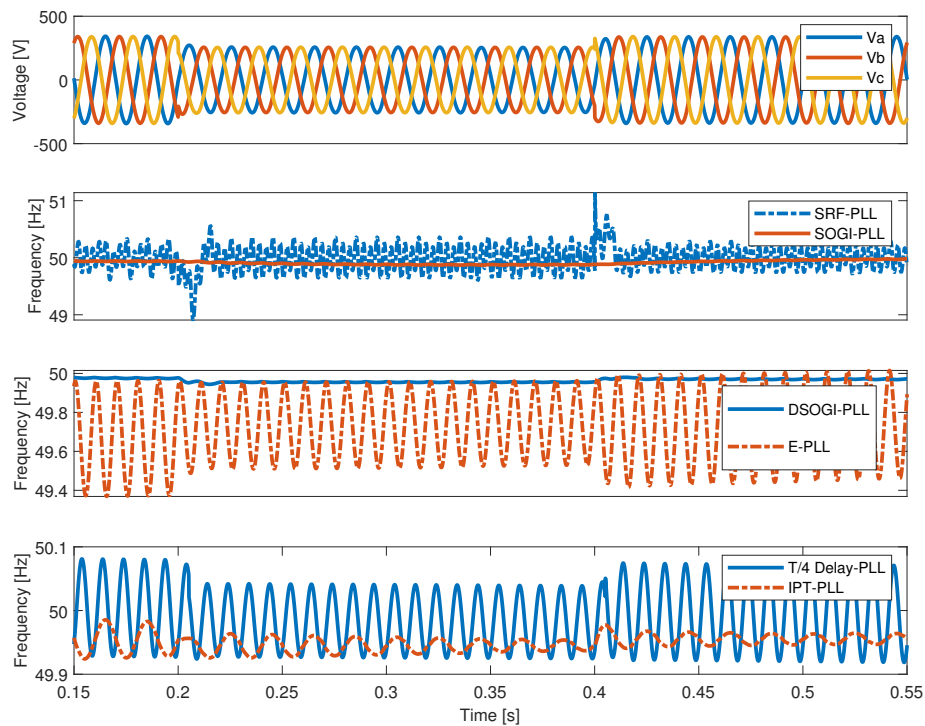


Figure 3.14: Responses of SRF-PLL, SOGI-PLL, DSOGI-PLL, E-PLL, $T/4$ Delay-PLL, and IPT-PLL frequencies under grid voltage Sag test condition.

Under the unbalance, the grid voltage sag, and grid voltage swell conditions produced similar responses. The Figure 3.15 and Figure 3.16 the grid is subjected to 5% of voltage swell and 5% in A-phase, 10% in B-phase, and 2% in C-Phase of the grid voltage unbalance is created at 0.2 s to 0.4 s. The frequency response variations can be seen at the time of insertion of swell and removal of swell. The SOGI-PLL and DSOGI-PLL frequency variations are negligible. But the SRF-PLL and $T/4$ Delay-PLL show the dip and notch in their frequencies, these PLLs can be used

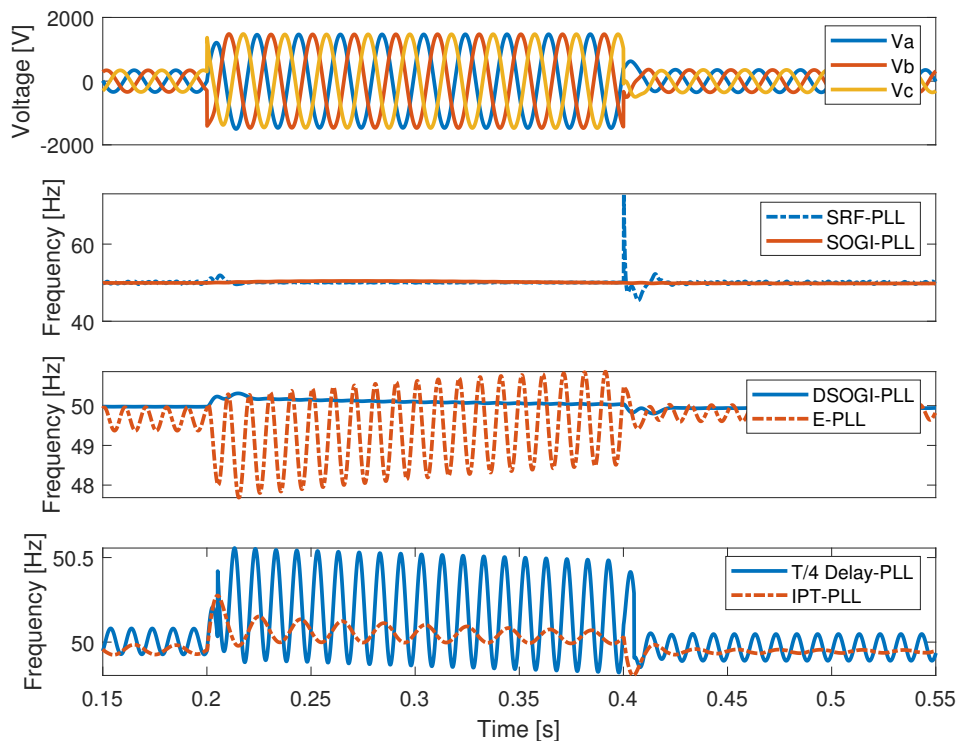


Figure 3.15: Responses of SRF-PLL, SOGI-PLL, DSOGI-PLL, E-PLL, $T/4$ Delay-PLL, and IPT-PLL frequencies under grid voltage Swell test condition.

in anti-islanding schemes for better performance in the islanding detection but as compared to E-PLL and IPT-PLL these PLLs are not enough to work in the grid-connected mode, where the grid voltage sag and swell are well within the prescribed ranges.

In Figure 3.17 the responses of all the studied PLLs concerning the grid harmonics are depicted. Under the grid voltage harmonic test condition, the DSOGI-PLL frequency again will not be subject to major variations but these kinds of responses were good when the grid voltages were affected for a short period but not for the long-lasting grid disturbances. In this case, one can go for SRF-PLL, and $T/4$ Delay-PLL to disconnect the grid and DGs. The E-PLL and IPT-PLL are subjected to the harmonics but not much like the SRF-PLL and $T/4$ Delay-PLL.

Figure 3.18 shows the responses of the Grid, DG1, and DG2 frequencies and angle (θ) variations, and PCC voltage THD with DSOGI-PLL under grid voltage swell, grid voltage sag, grid voltage unbalance, and grid voltage harmonics. Figure 3.18 (a) and

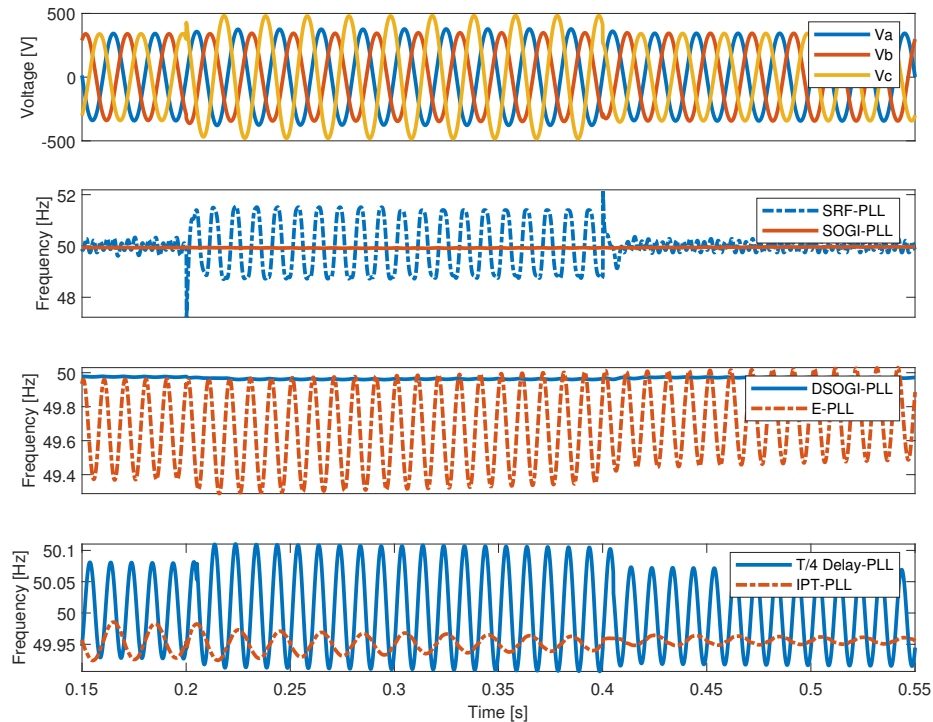


Figure 3.16: Responses of SRF-PLL, SOGI-PLL, DSOGI-PLL, E-PLL, $T/4$ Delay-PLL, and IPT-PLL frequencies under grid voltage Unbalance test condition.

3.18 (b), the grid is subjected to 5% of voltage sag and 10% of voltage swell at 0.2 s to 0.4 s respectively. The frequency responses of the PLLs show a promising result at the time of insertion of sag and removal of sag. The grid is subjected to 5% of voltage sag at 0.2 s to 0.4 s. The frequency responses of the PLLs show a promising result at the time of insertion of sag and removal of sag. The promising response for all the other PLLs is seen with the SOGI-PLL and the DSOGI-PLL.

Figure 3.19 (a) grid is subjected to 5% of voltage swell and 5% in A-phase, 10% in B-phase, and 2% in C-Phase of the grid voltage unbalance is created at 0.2 s to 0.4 s. The frequency response variations can be seen at the time of insertion of swell and removal of swell. The SOGI-PLL and DSOGI-PLL frequency variations are negligible. Figure 3.19 (b) the responses of all the studied PLLs concerning the grid harmonics are depicted. Under the grid voltage harmonic test condition, the DSOGI-PLL frequency again will not be subject to major variations but these kinds of responses were good when the grid voltages were affected for a short period but

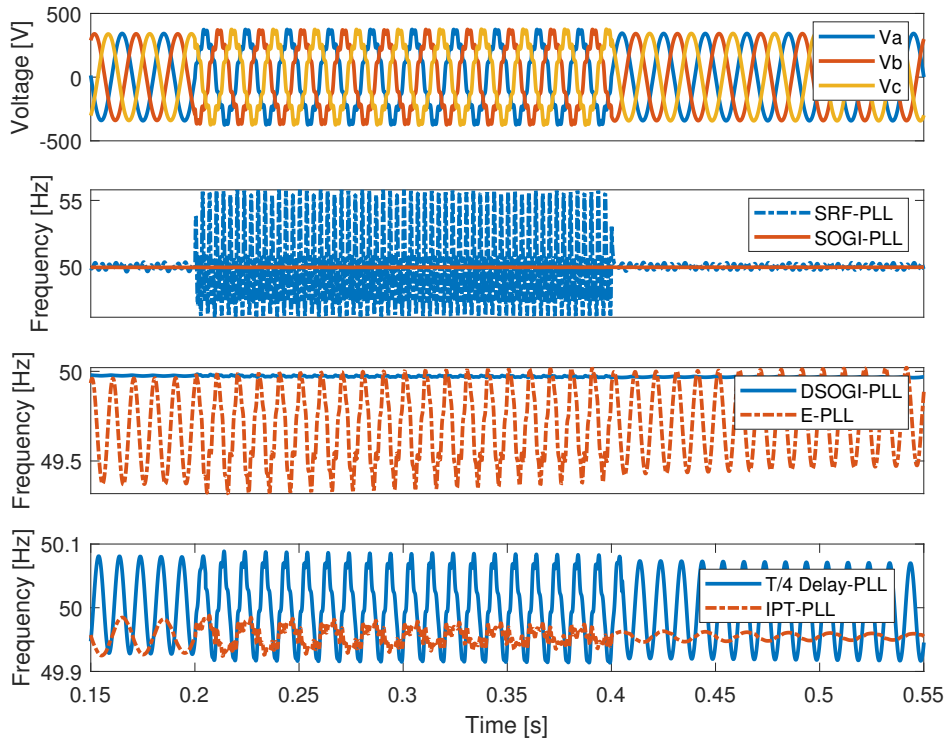


Figure 3.17: Responses of SRF-PLL, SOGI-PLL, DSOGI-PLL, E-PLL, $T/4$ Delay-PLL, and IPT-PLL frequencies under grid voltage Harmonics test condition.

not for the long-lasting grid disturbances.

Table 3.2, gives the reference direction for PLL following distortions. After reviewing the responses from various test cases to make it easier to select PLLs for various requirements, the selection guide is purely based on the responses of the power quality test cases listed in this article.

In Figure 3.20 the frequency responses of the DSOGI-PLL under various test conditions are shown. As we can see the frequency variation at 0.2 s to 0.4 s are well within the IEEE standard limit.

The variations of frequencies are under the IEEE 1547 standard limits. We cannot see the variations in the DG frequencies, as the frequencies vary between 50.001 Hz to 49.99 Hz, the changes are very minute with DSOGI-PLL in the DGs grid-connected mode. But we can see the disparity in the grid frequency as it is subject to the different test cases. The power quality variations are created at 0.2 s to 0.4 s, so the maximum variation will be seen at 0.2 s to 0.4 s. But the differences in the standard

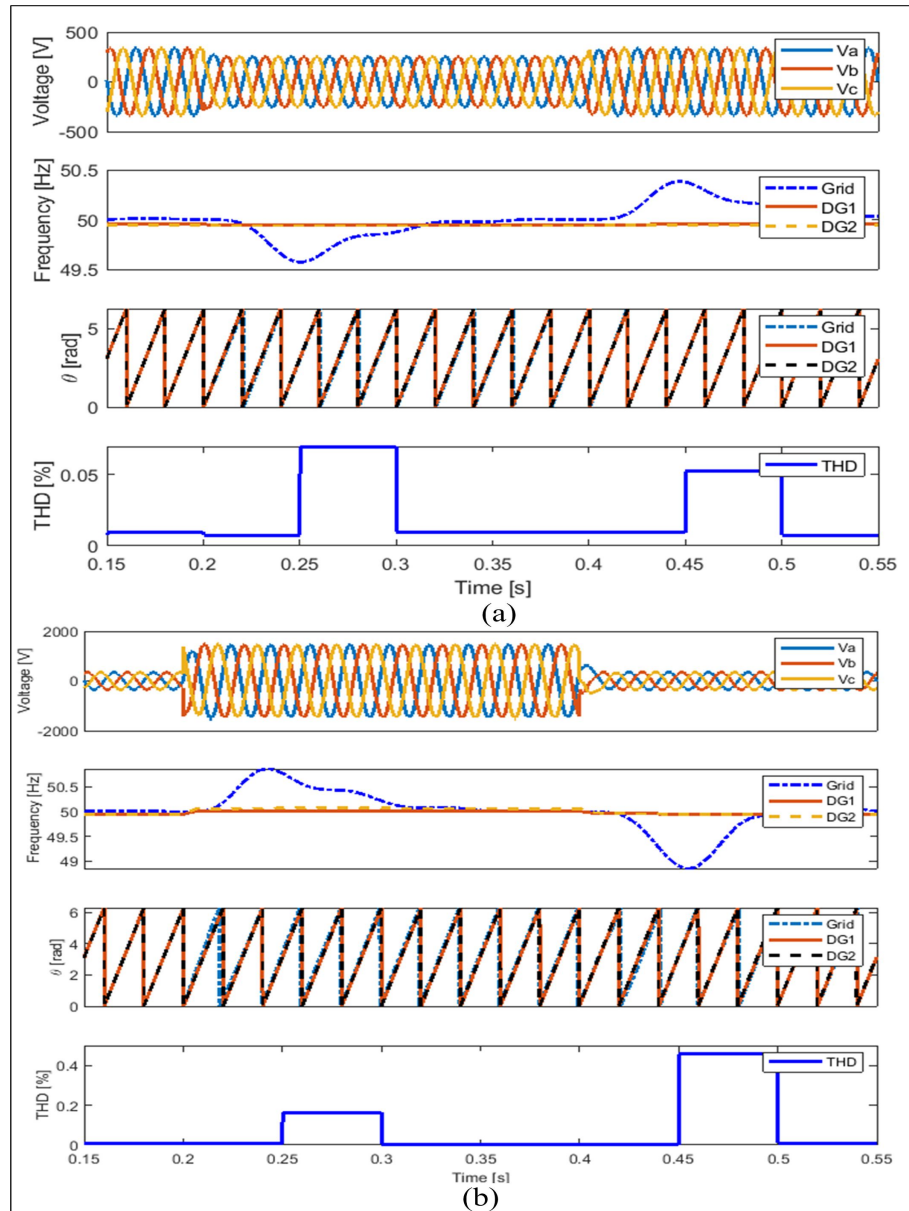


Figure 3.18: Responses of the Grid, DG1, and DG2 frequencies and angle variations, and PCC voltage THD with DSOGI-PLL under various test cases: (a) grid voltage sag (b) grid voltage swell.

prescribed value concerning frequency, angle, and the % THD are well within the limits.

This PLL is suitable for the grid-connected DG systems when the disturbance period is very limited. In a healthy grid environment, these PLLs show very much optimistic and reliable performance. As we can see in Figure 3.21 and Figure 3.22.

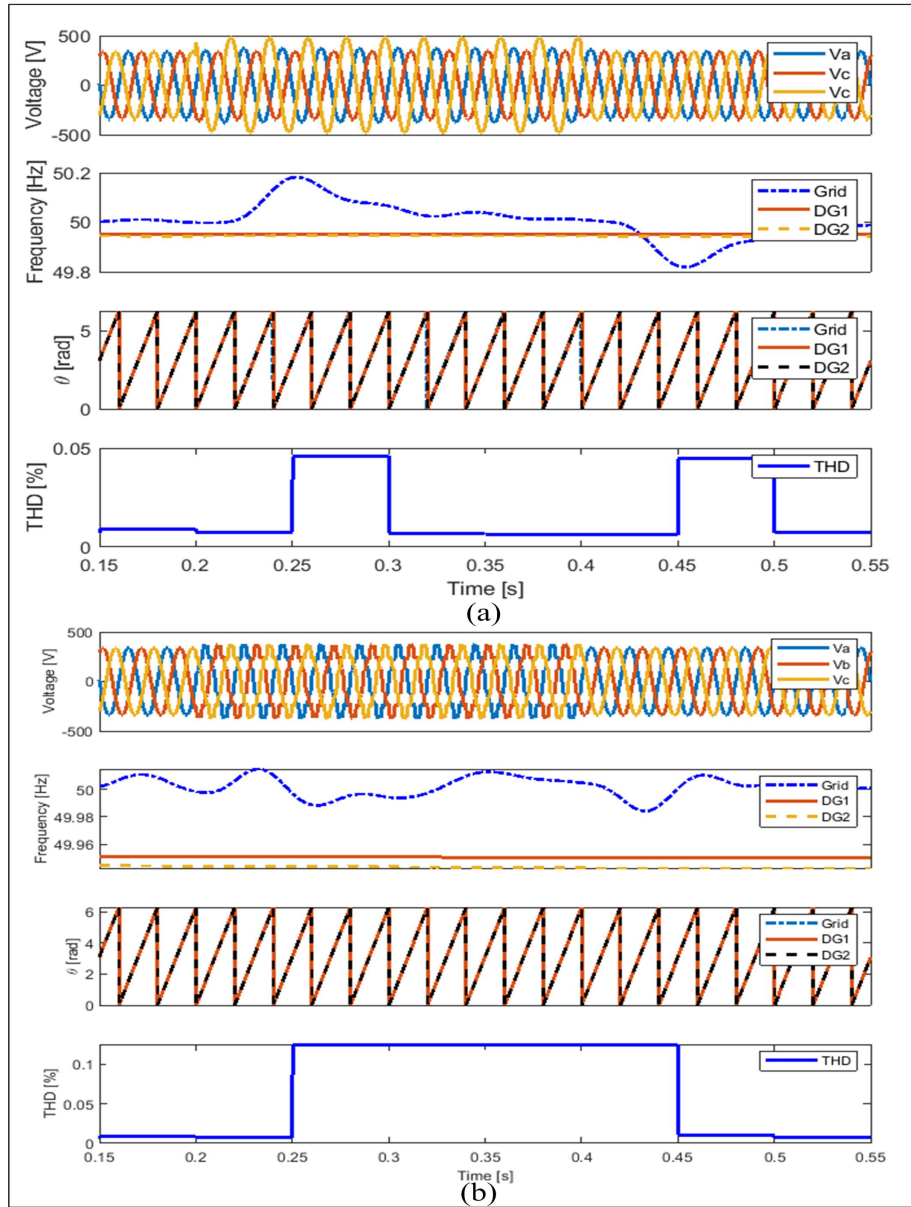


Figure 3.19: Responses of the Grid, DG1, and DG2 frequencies and angle variations, and PCC voltage THD with DSOGI-PLL under various test cases: (a) grid voltage unbalance (b) grid voltage harmonics.

the active power and reactive power responses were plotted for Grid and DGs with DSOGI-PLL.

The proportional sharing of the power for the load demand and the DGs capacities can be realized. In Figure 3.2 the 10 KVA DG1 can take maximum sharing concerning the 5 KVA DG2. The excess power generated by both the DGs is being

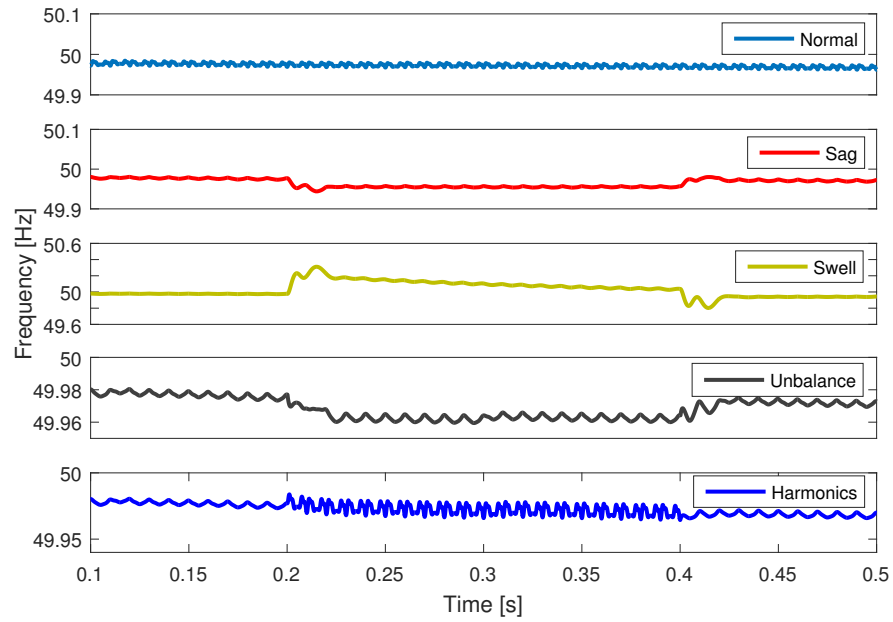


Figure 3.20: Responses of the DSOGI-PLL frequency (Hz) under grid voltage normal, sag, swell, unbalance, and harmonics test conditions.

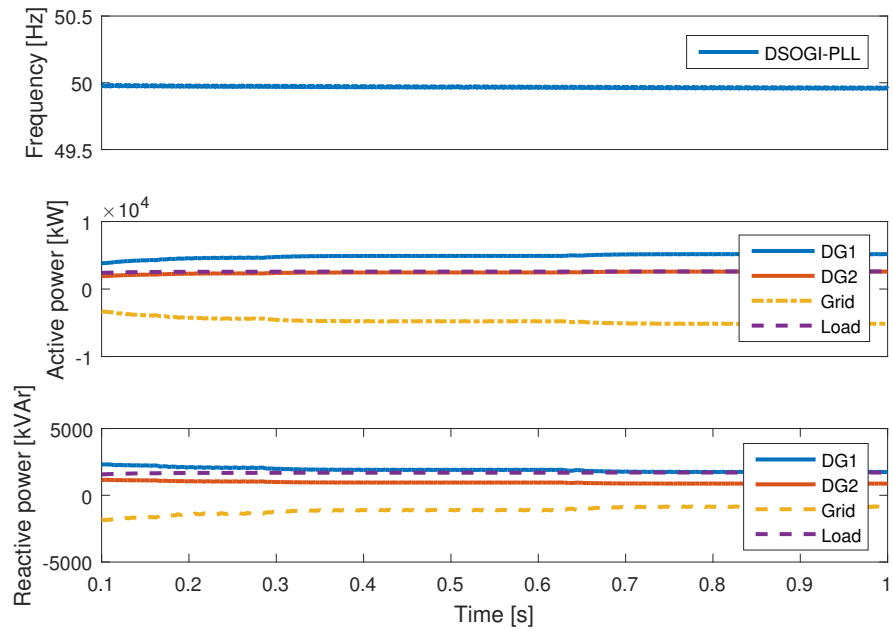


Figure 3.21: Responses of the DSOGI-PLL frequency (Hz), active power (kW), reactive power (kVAr) without step-change in the load.

Table 3.2: PREFERENCE DIRECTION FOR PLL FOLLOWING DISTORTIONS

Phase-Locked Loop	Construction	Synchronization efficiency	Distortion handling
SRF-PLL	Simplest	Modest	Sparse
PQ-PLL	Simplest	Modest	Sparse
SOGI-PLL	Modest	Modest	Modest
DSOGI-PLL	Complex	Good	Good
$T/4$ Delay-PLL	Simplest	Sparse	Sparse
IPT-PLL	Complex	Modest	Modest
E-PLL	Complex	Modest	Modest
SRF-PLL	Complex	Good	Good

sent to the grid, and to test the frequency sustainability or synchronizing capability of DSOGI-PLL is tested for step-change in the load demand at 0.2 s, 0.4 s, and at 0.6 s. The subsequent switching of the load during grid-connected operation mode can prove the capability and flexibility of the DSOGI-PLL performance. The DSOGI-PLL shows a reliable performance under the grid-connected mode of operation. So, the experimental verification under test the cases like case1: Grid voltage sag, and case2: Frequent changes in the load power are performed and the responses are recorded.

Figure 3.23 to Figure 3.25 shows the experimental responses for the grid-connected DG systems with DSOGI-PLL controller. In Figure 3.23 the DG1, DG2, SOGI-PLL, and SRF-PLL frequency responses in presence of grid-voltage sag test cases are presented. The frequency variation in DGs can be negligible due to they have synchronized to the grid by DSOGI-PLL. And the response for SRF-PLL is also shown in Figure 3.23, where the variation at 0.3 s and 0.75 s can be seen clearly.

The oscillations present during the start and end of the disturbance can be overcome by the DSOGI-PLL. With the help of the SRF-PLL, we can able to detect the islanding at the time of 0.3 s due to the nature of the response and we can re-synchronize after 0.75 s.

In Figure 3.24 and Figure 3.25 the responses of the active powers and the reactive powers of DG1, DG2, Grid, and Load with DSOGI-PLL for the grid-connected operation mode are shown. In the grid-connected mode with DSOGI-PLL, to test the power-sharing the capability of DGs (10 KVA and 5 KVA), the load change at 0.3 s (from 15 kW, 1 kVAR to 10 kW, 0.5 kVAR) and 0.8 s (from 10 kW, 0.5 kVAR to 15 kW, 1 kVAR) are carried out. The responses recorded for both the active and reactive

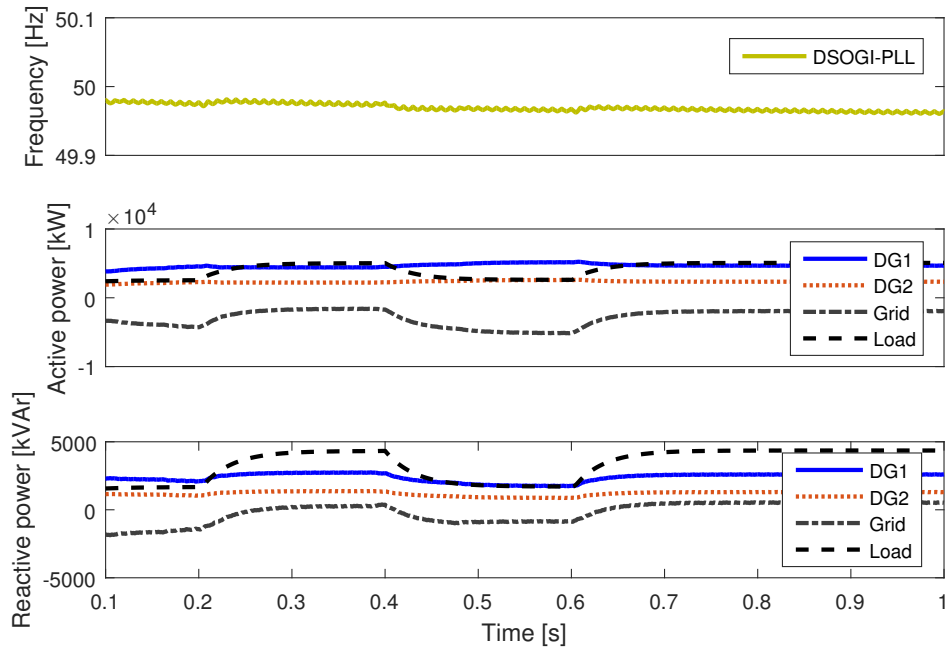


Figure 3.22: Responses of the DSOGI-PLL frequency in Hz, active power in kW, reactive power in kVAr with step-change in the load.

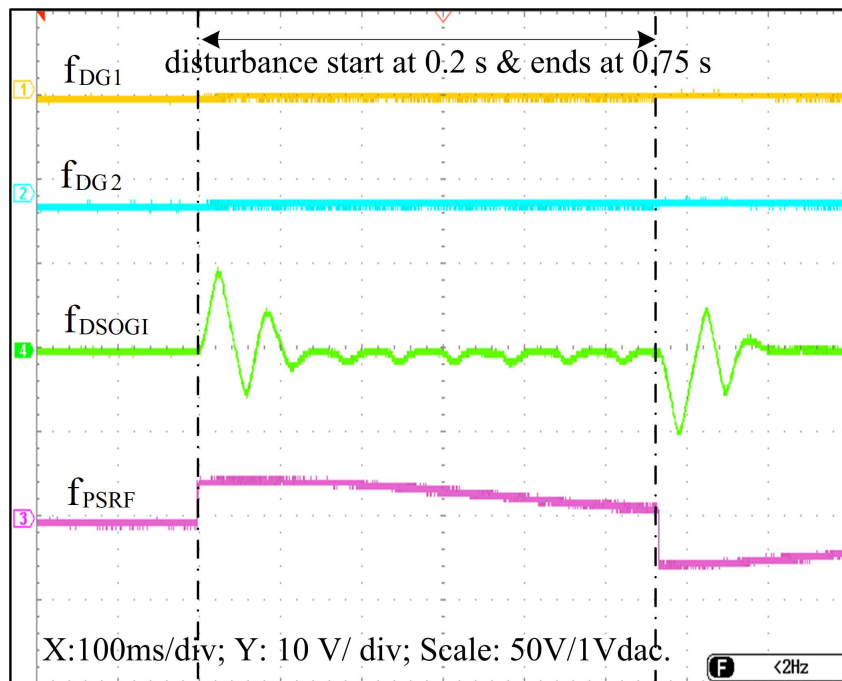


Figure 3.23: DG1, DG2, Grid (SOGI-PLL and SRF-PLL) frequency responses (Hz) in the course of voltage sag condition at 0.3 s, to 0.75 s.

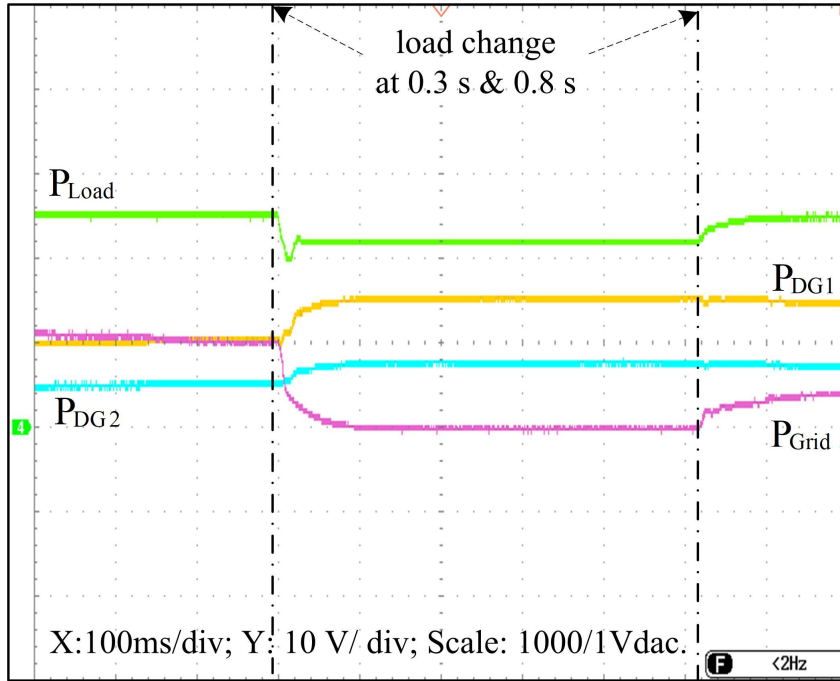


Figure 3.24: Responses of active power (kW) of DG1, DG2, Grid, and Load during the load change at 0.3 s to 0.8 s.

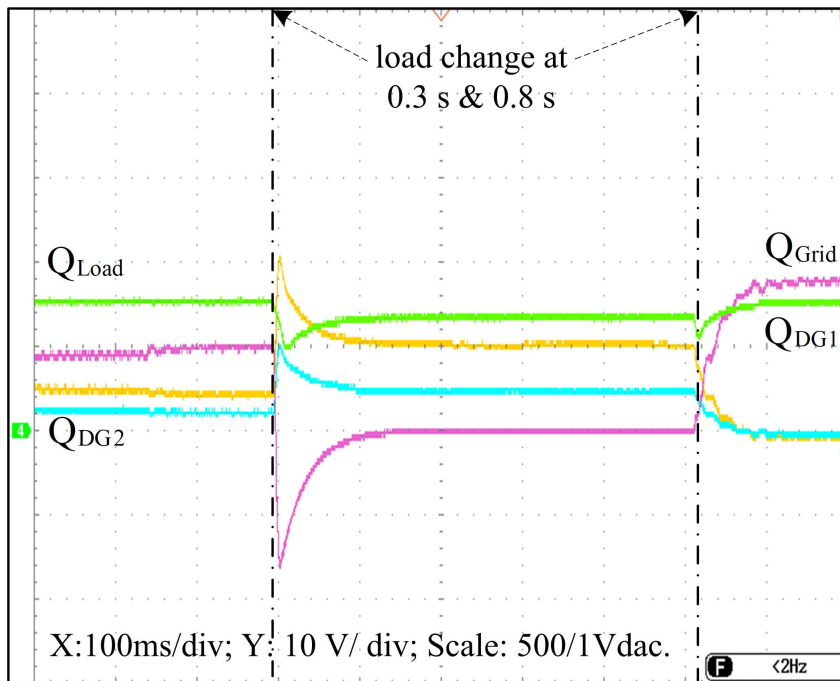


Figure 3.25: Responses of reactive power (kVAr) of DG1, DG2, Grid, and Load during the load change at 0.3 s to 0.8 s.

powers shows good sharing capability under the mentioned test case. The DG1 and DG2 share the load proportionally according to their power ratings, and the excess power will be sent to the grid.

Concerning the responses of SRF-PLL, SOGI-PLL, DSOGI-PLL, E-PLL, and IPT-PLL subjects to all the test cases, the choice of the PLLs under various power quality issues can be drawn attention. In this regard, the researchers and industrialists may choose the PLLs suitable for them according to the grid environment in which they are working.

3.6 PLL based islanding detection for droop based microgrid

In grid-connected operation mode constant current control and the phase-locked loop (PLL) generator are incorporated in the control scheme Bifaretti (2013) Dong et al. (2014). In the grid-connected operation mode, frequency and voltage are maintained by the grid itself. Generally, PLL is used to track the frequency and phase angle of the grid for synchronization and resynchronization. The PLL is responsible for a smooth transition between the grid-connected mode and islanded operation mode. The grid failure detection for a wind turbine with a linear balanced load of 11kW is presented in Teodorescu and Blaabjerg (2004). The conventional droop control technique will rely on the output impedance characteristics of the network. In order to overcome this problem the virtual complex impedance scheme is accomplished in the outer voltage controller loop Wang et al. (2015) Guerrero et al. (2008) Tang et al. (2016).

3.6.1 Microgrid's islanded mode of operation

In SA operation mode there is no impact of the grid on the inverter-based DGs. The PCC voltages are equal to the inverter front-end voltages. And all the critical loads are supplied by the DGs themselves while maintaining the voltage and frequency in the prescribed limits. The voltage, active power, and reactive power equations are shown in (3.39).

$$\begin{aligned} V_{PCC} &= V_{DG} \\ P_{load} &= P_{DG}; \quad Q_{load} = Q_{DG} \end{aligned} \quad (3.39)$$

If connected microgrid system load is greater than DGs generated power then the system will go into the unstable region, which is given by (3.40).

$$P_{load} > P_{DG}; \quad Q_{load} > Q_{DG} \quad (3.40)$$

In this scenario, a proper control technique has to be implemented to ensure a stable SA operation mode. The load shifting, load cutting, and hike in the DGs generated powers are some general techniques to be adopted. The active power versus frequency and reactive power versus voltage droop slopes for both the DGs are shown in Figure 3.26.

The droop coefficients for parallel inverter-based DGs having equal power ratings to share the load proportionally are given in (3.41).

$$m_{p1} = m_{p2}; \quad n_{q1} = n_{q2} \quad (3.41)$$

In this system the DG1 has a maximum power rating of 10kVA, the droop slopes of active power and frequency curve is higher than that of other DG2 having a power rating of 5kVA, and droop coefficients are given by (3.42).

$$m_{p1} = 2 * m_{p2}; \quad n_{q1} = 2 * n_{q2} \quad (3.42)$$

The SA mode control technique for inverter-based DGs is shown in Figure3.26. The droop control is implemented in the power loop for the inverter-based DGs. Frequency and voltages are regulated following the active power and reactive power variations respectively.

3.6.2 Microgrid's grid-connected mode of operation

In GC operation mode the power generated by the inverter-based DGs is transferred to the microgrid system load and excess generated power is being transferred to the grid. If microgrid system load demand is more than the power generated by DGs, then the grid takes up the excess load. In GC mode of operation, it is easy to conclude that the total microgrid system load demand is being supplied by both the inverter-based

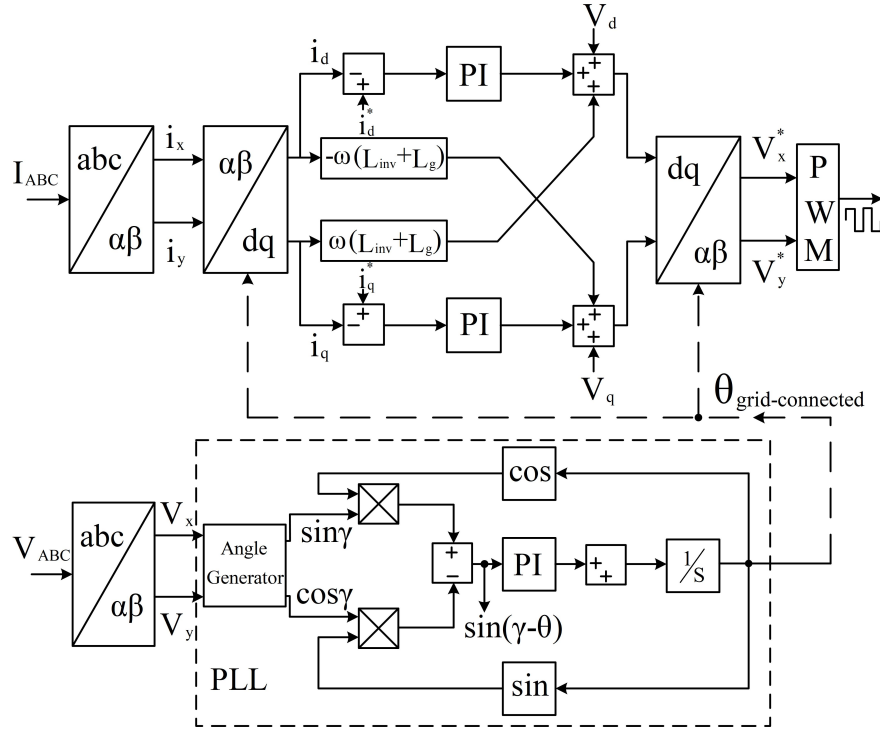


Figure 3.27: Control scheme for grid connected mode.

The GC control scheme is shown in Figure 3.27. The grid currents and voltages are being regulated by standard PI controllers in inner and outer control loops respectively. The q -axis reference current is set to zero to achieve the zero phase angle difference between the voltage and current. A decoupling of cross-coupling is implemented in the outer control loop to compensate for the coupling due to the LCL filters in the microgrid system model. The control signals for the inverter-based DGs are being generated by the standard PWM technique. The PLL for GC mode of operation is explained in the next subsection.

3.6.3 PLL and Islanding detection

A phase-locked loop (PLL) is a closed-loop device in which an internal oscillator is regulated by a feedback loop to maintain the time of an external periodic signal. PLL techniques are widely employed in a variety of fields, including communications, computers, and modern electronics. They can generate synchronized frequencies with external periodic occurrences, retrieve significant signals from distorted sources, and distribute clock-timing pulses in complex control systems. Because it should work

in harmony with the grid, a grid-connected power converter perfectly reflects the PLL philosophy. It should phase-lock its internal oscillator to a specific grid power signal to provide amplitude and phase-coherent internal signal that may be used by numerous control system blocks. Furthermore, the PLL gives constant information about the phase-angle and amplitude of the magnitude of interest, which is usually the fundamental grid voltage, allowing space vector-based controllers and modulators to be constructed even with single-phase signals.

The basic SRF-PLL is modified with cosine and sine multiplier for islanding detection as shown in Figure 3.27, which is essentially used in three-phase inverters based DGs for grid synchronization and fault detection. Here stationary frame grid voltages V_α , V_β are the input signals to the PLL and these are fed to the angle generator. The output signals of angle generator are $\sin\gamma$ and $\cos\gamma$, given in (3.48) and (3.49). The sinusoidal phase angle difference between the grid and the DG is formulated as given below.

$$V_{abc} = [T]V_{\alpha\beta} \quad (3.45)$$

where, V_{abc} are the measured three phase voltages of the grid and T is the Clark transformation matrix, given as $[T]=0.8165^* \begin{bmatrix} 1 & 0 \\ -0.5 & 0.866 \\ -0.5 & -0.866 \end{bmatrix}$. And $V_{\alpha\beta}$ are the Clark transformed grid voltages and are given by (3.46) and (3.47).

$$V_\alpha = V_a - 0.5 * V_b - 0.5 * V_c \quad (3.46)$$

$$V_\beta = 0.866 * V_b - 0.866 * V_c \quad (3.47)$$

The phase angle between these two grid voltage components can be calculated as (3.48) and (3.49).

$$\sin(\gamma) = \frac{V_\alpha}{\sqrt{(V_\alpha^2 + V_\beta^2)}} \quad (3.48)$$

$$\cos(\gamma) = \frac{V_\beta}{\sqrt{(V_\alpha^2 + V_\beta^2)}} \quad (3.49)$$

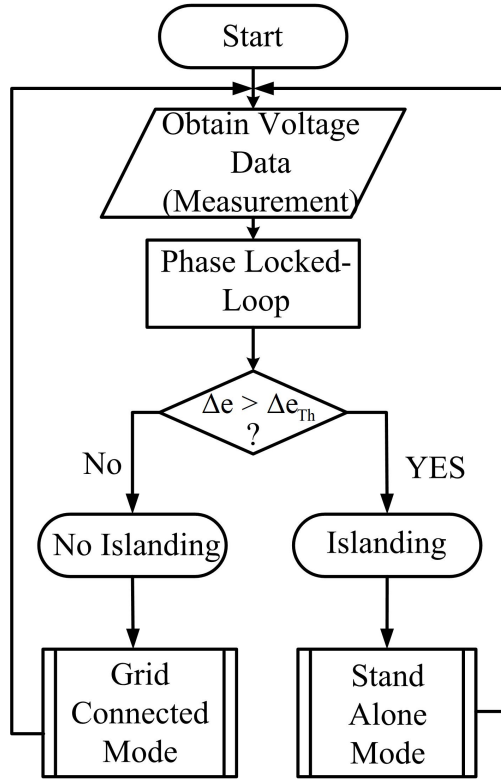


Figure 3.28: Islanding detection flow diagram.

With the help of $\sin \gamma$ and $\cos \gamma$ we can calculate the DGs phase angle in the grid-connected mode of operation $\theta_{grid-connected}$. Then the phase-locking between the DGs and the grid will be decided.

The phase difference between $\sin \gamma$ and $\cos \gamma$ quantities and the DGs phase angle θ is the the PLL phase error signal $\sin(\gamma - \theta)$ as shown in Figure 3.27. The phase error signal $\sin(\gamma - \theta)$ is used to detect the islanding and also used to switch the corresponding modes of operation. During the grid connect-mode due to faults/disturbances in one or more lines, the PLL generated phase error will exceed the threshold value. And this error exceeding the set threshold is considered as the grid failure and consequently, the SA control mode is switched. The islanding detection and mode switching operations are based on the SRF-PLL controller phase error $\Delta e / \sin(\gamma - \theta)$, the detailed islanding detection flow diagram is shown in Figure 3.28 and PLL control signals are shown in Figure 3.29.

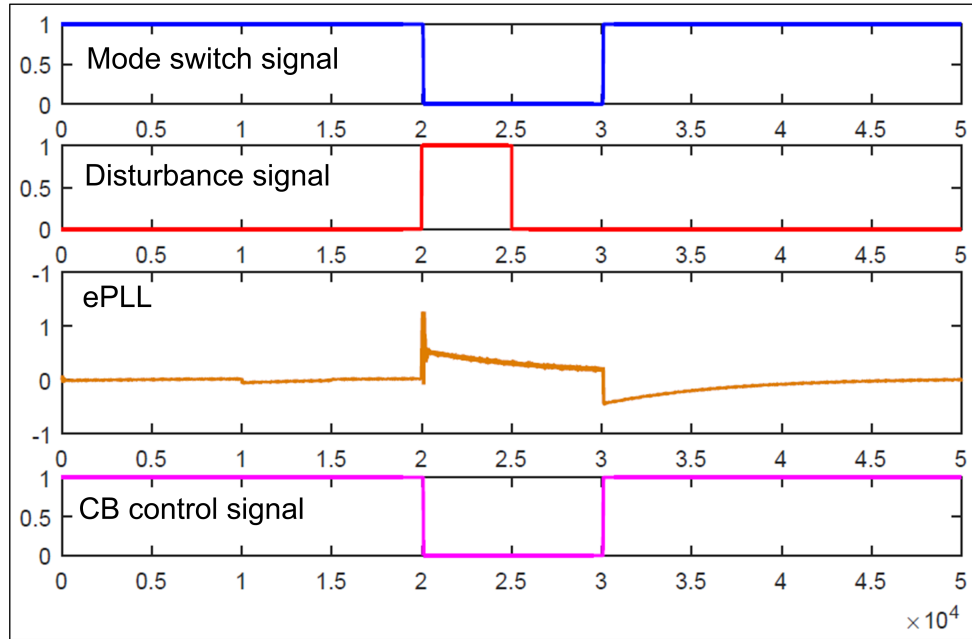


Figure 3.29: PLL control signals for islanding detection.

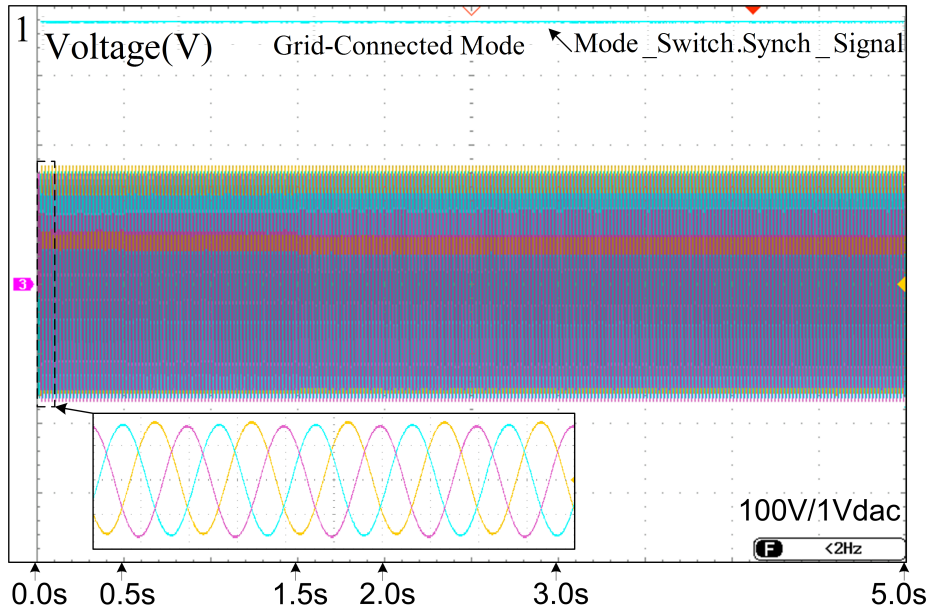
3.7 Result and Discussion

The islanded (SA) and grid-connected (GC) control schemes for microgrid system model is shown in Figure 3.26 and 3.27 respectively. The mode switch block switches the GC operation mode and SA operation mode depending on required set points 1 (Grid-connected mode) or 0 (islanded mode) received from the PLL. A fault is created at 2.0 sec and is sustained up to 2.5 sec. The responses are plotted for three cases as follows:

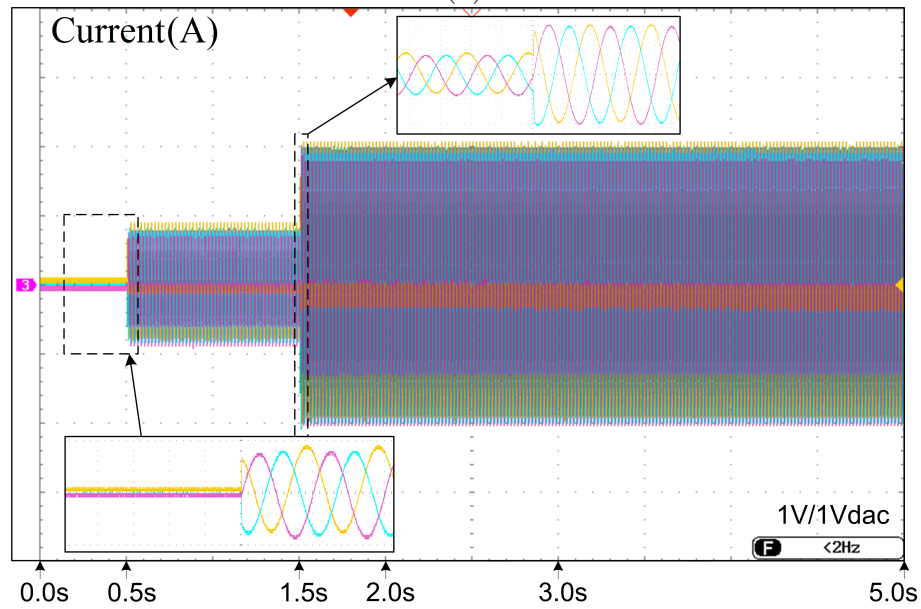
1. GC: Grid-connected mode of operation.
2. SA: islanded mode of operation.
3. GC-SA-GC: Transition between grid-connected mode and islanded mode.

Case1 GC: Grid-connected mode

Figure 3.27 shows the grid-connected mode of operation, where the mode switch block receives setpoint signal 1 from PLL thus the GC operation mode will be switched. Three-phase load voltages and currents are shown in Figure 3.30 (a) and (b). We can see the load currents variations in terms of load changes as: 0.0 sec-0.5 sec and 0.5 sec-1.5 sec.



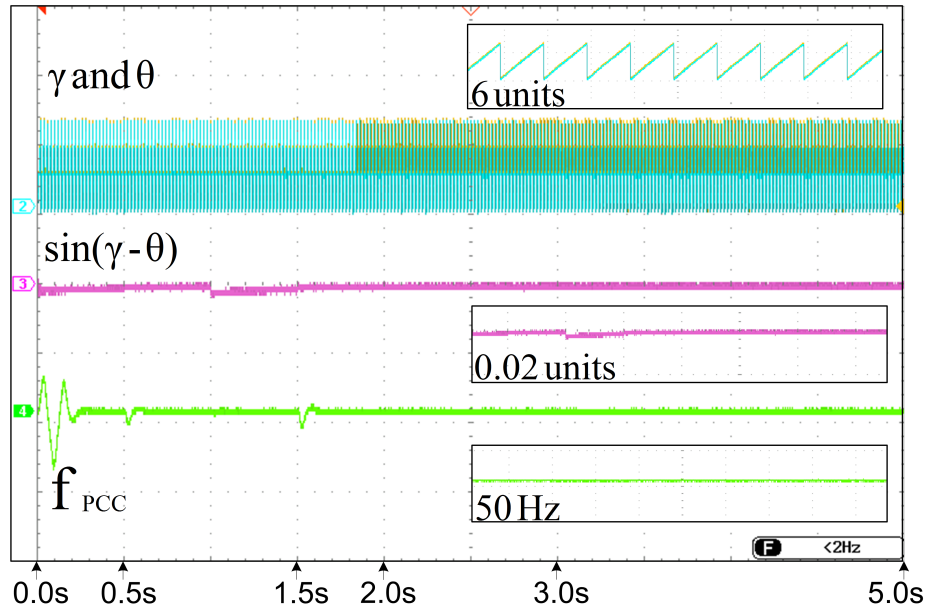
(a)



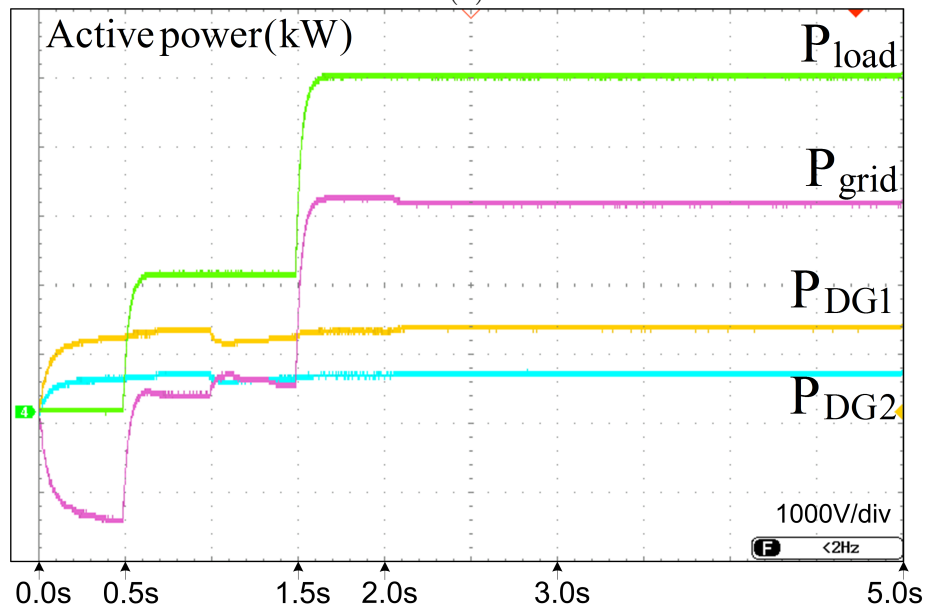
(b)

Figure 3.30: Grid-connected operation mode (a) load voltages in Volts (b) load currents in Amps.

In Figure 3.31(a) PLL γ , θ , $\sin(\gamma - \theta)$ and frequency at point of common coupling are shown. The zero-crossing is not affected and PLL maximum phase error response reaches a value of 0.04 and then settles to 0.02. PCC frequency will oper-



(a)



(b)

Figure 3.31: Grid-connected operation mode (a) PLL (γ , θ , $\sin(\gamma - \theta)$) and PCC frequency (b) active power in kW.

ate at 50 Hz. The 3.31(b) shows active powers P_{load} , P_{grid} , P_{DG1} and P_{DG2} . At no load the generated power is being exported to the grid and when the load switches at 0.5sec the load demand is supplied by the DGs and the grid, summarised in Table 3.3.

Case2 SA: islanded mode

The results for islanded operation mode are shown in Figure 3.26. The mode switch block receives setpoint signal 0 from PLL $\sin(\gamma - \theta)$, the operation mode will be switched to the islanded mode. Three-phase load voltages and currents are shown in 3.32 (a) and (b). We can see the load voltages and currents variations in terms of load changes as: 0.0 sec-0.5 sec and 0.5 sec-1.5.

In 3.33(a) PLL γ , θ , $\sin(\gamma - \theta)$ and frequency at point of common coupling are shown. There is no impact of the grid on the DGs, we can see small variations in PLL γ , θ but the zero crossing is not effected and PLL maximum phase error $\sin(\gamma - \theta)$ response is seen to be 0.8 and then settles to 0.15. Maximum 50.21 Hz and minimum 49.59 Hz variations are seen in the PCC frequency. The variations are in standard limits and 1.5 sec onwards it continues to operate at 50Hz. In 3.33(b) active powers P_{load} , P_{grid} , P_{DG1} and P_{DG2} . As there is no grid, power generated by DGs is being supplied to the load demand in SA mode, shown in Table 3.4.

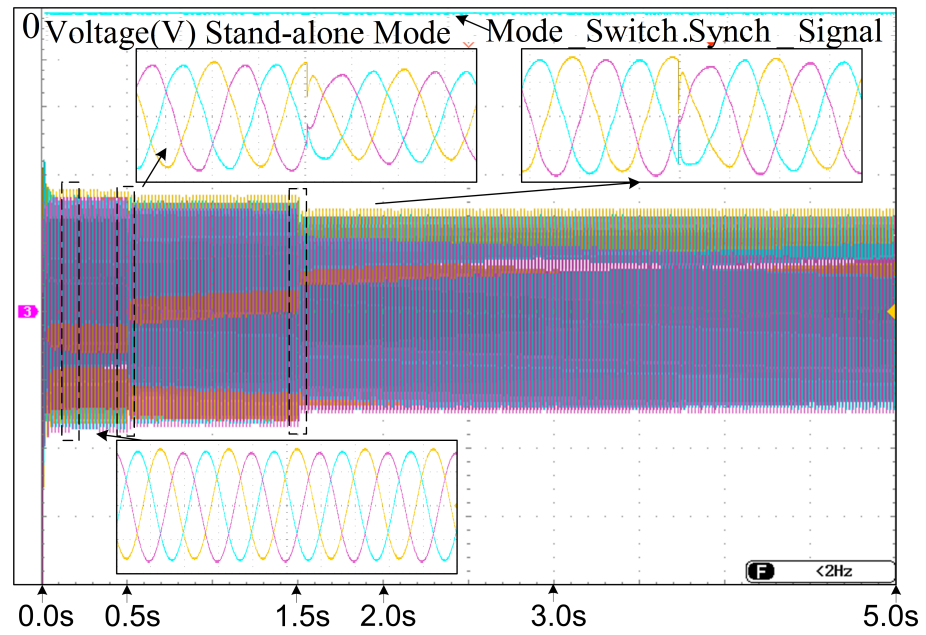
Case3 GC-SA-GC: Transition between grid-connected and islanded mode

In Figure 3.29 The set point 1 is for GC mode and 0 for SA mode. Three phase load voltages and currents are shown in 3.34 (a) and (b). Grid disturbance is introduced at 2.0 sec and 3.004 sec we can see the voltage and current spikes due to the mode switching operation. The mode will switch automatically to the respective operation mode. In 3.35 (a) PLL γ , θ , $\sin(\gamma - \theta)$ and frequency at point of common coupling are shown.

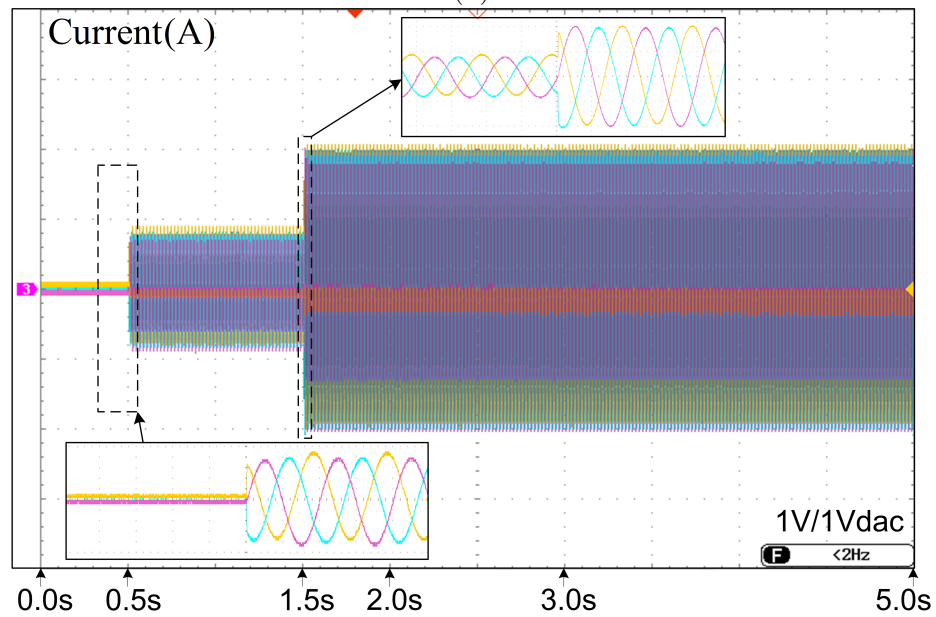
The γ , θ can be seen during the switching, and the signal $\sin(\gamma - \theta)$ is used to detect islanding and automatic mode switching. Initially, the system is operating in the GC mode, when the disturbance occurs the $\sin(\gamma - \theta)$ will exceed the threshold value and within 10.4ms the PLL will detect islanding and switches to SA operation

Table 3.3: GC MODE

Power	0.0-0.5 sec		0.5-1.5 sec		1.5-5.0 sec	
	P (kW)	Q (kVAr)	P (kW)	Q (kVAr)	P (kW)	Q (kVAr)
Load	-	-	8.0	0.2	20.0	0.07
Grid	-6.0	-0.75	1.0	-0.02	12.5	-0.3
DG1	4.0	0.5	4.6	0.15	5.0	0.25
DG2	2.0	0.25	2.3	0.07	2.5	0.12



(a)

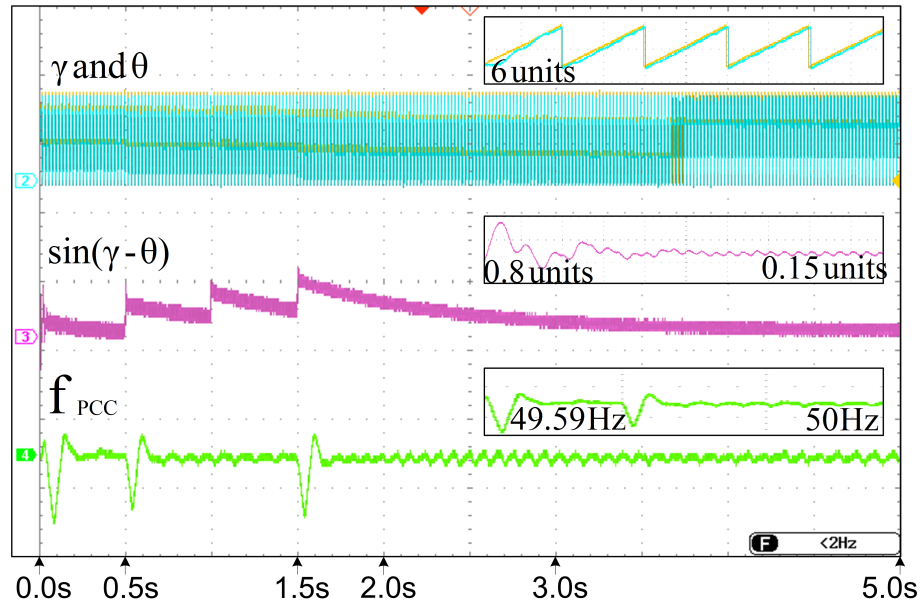


(b)

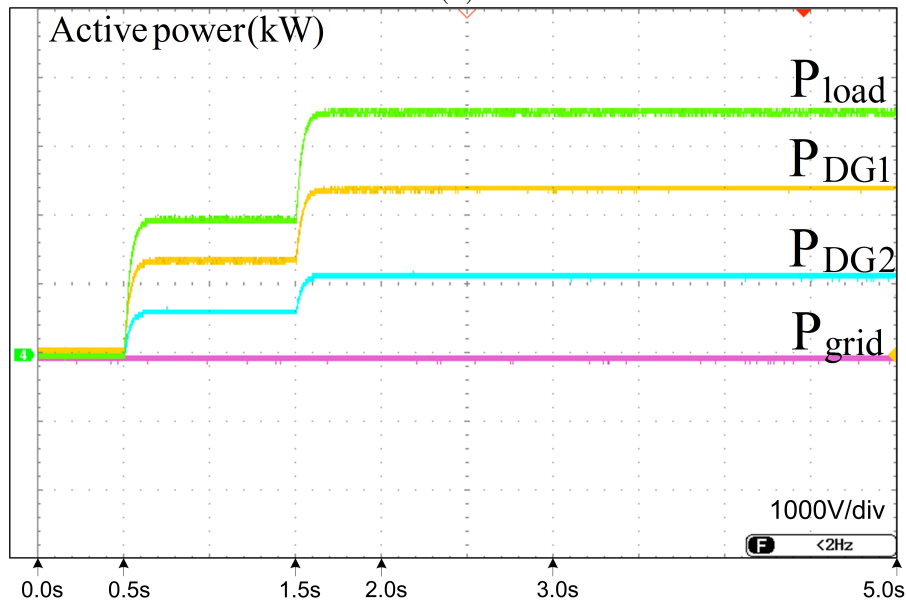
Figure 3.32: islanded operation mode (a) load voltages in Volts (b) load currents in Amps.

mode. The fault is introduced at 2.0 sec to 2.5 sec but the system will continue in the SA operation mode up to 3.004 sec after fault clearance.

At 3.004 sec the grid voltage settles down to a normal value and the mode switch block switches the operation mode to GC operation mode. We can see the variations



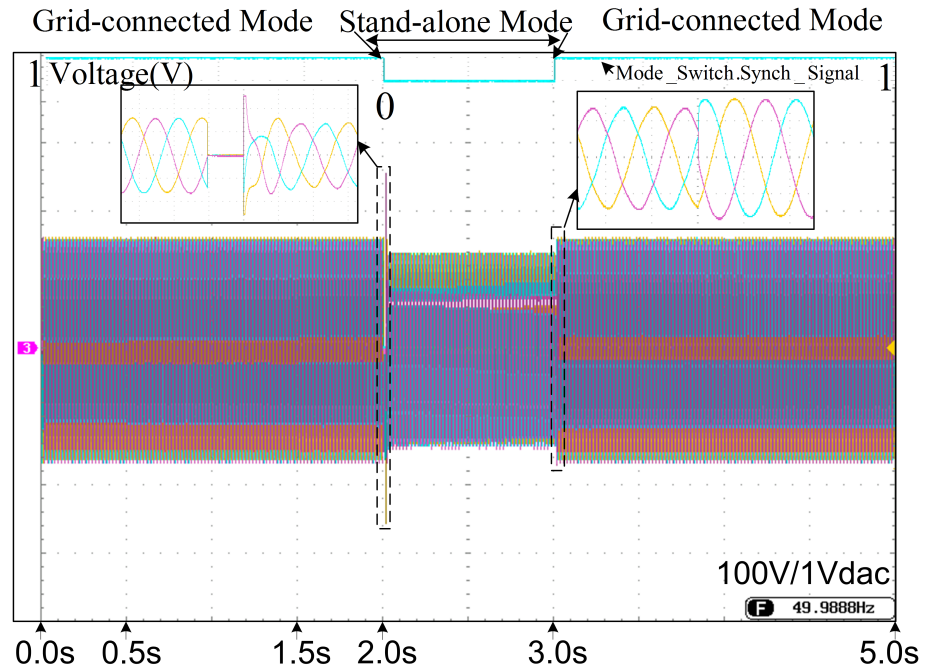
(a)



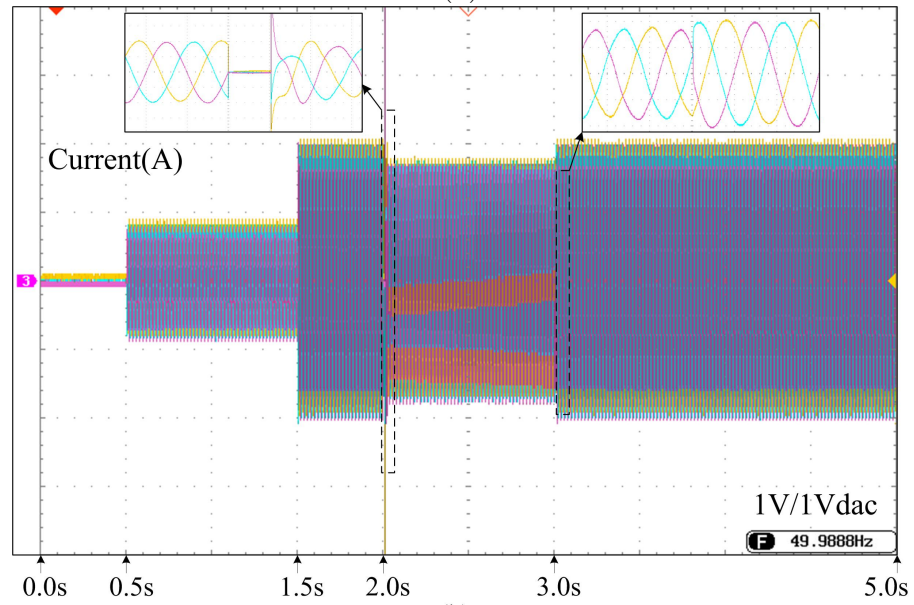
(b)

Figure 3.33: islanded operation mode (a) PLL (γ , θ , $\sin(\gamma - \theta)$) and PCC frequency (b) active power in kW.

of the PCC frequency (50.4Hz to 49.6Hz) during GC and SA mode switching. In 3.35 (b) the responses of active power versus frequency of both the DGs are shown. The droop-controlled inverters will share the load proportionally depending on their power ratings. In Figure3.36 (a) and (b) shows active powers P_{load} , P_{grid} , P_{DG1} and P_{DG2}



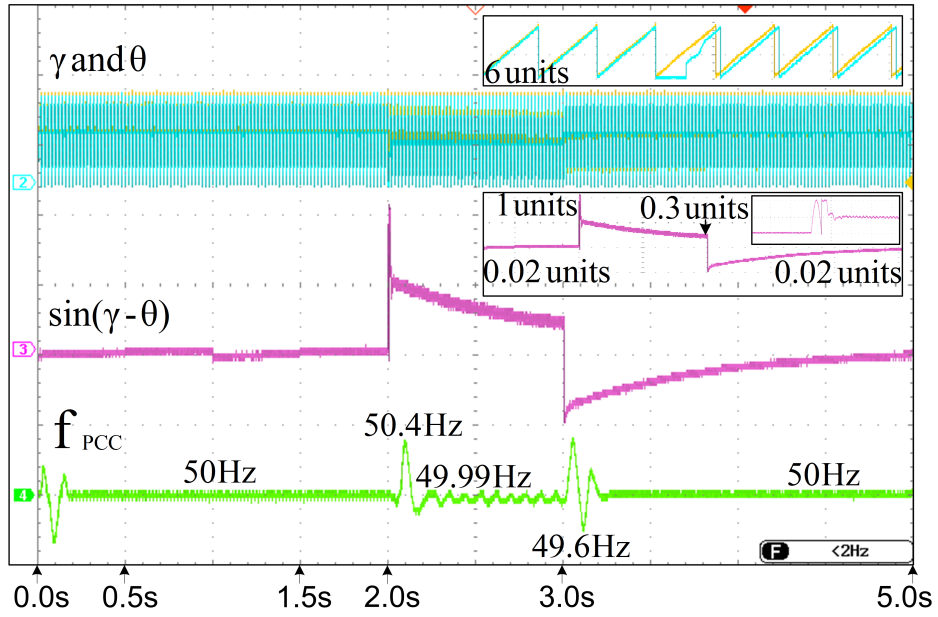
(a)



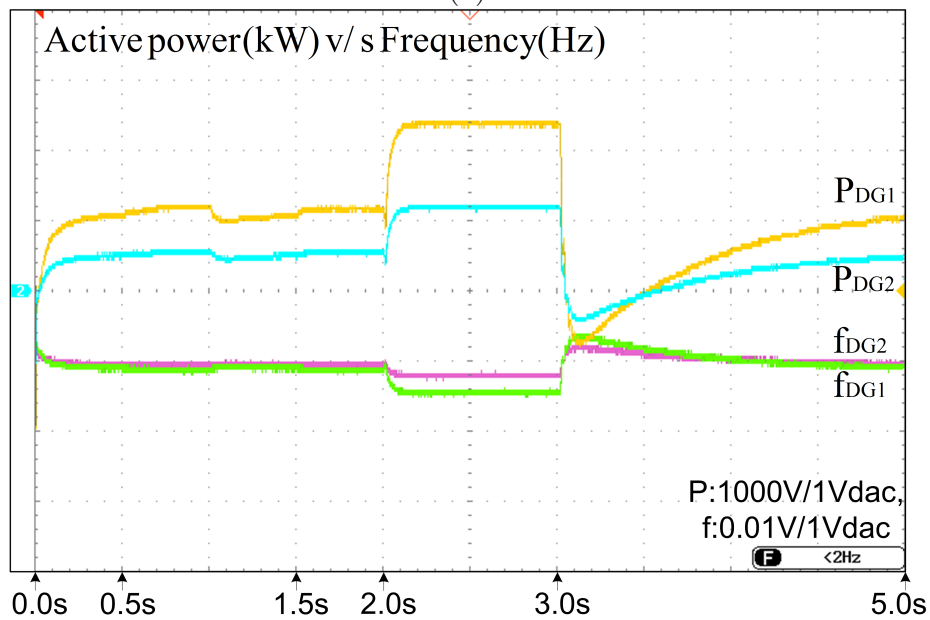
(b)

(b)

Figure 3.34: GC-SA-GC operation mode (a) load voltages in Volts (b) load currents in Amps.

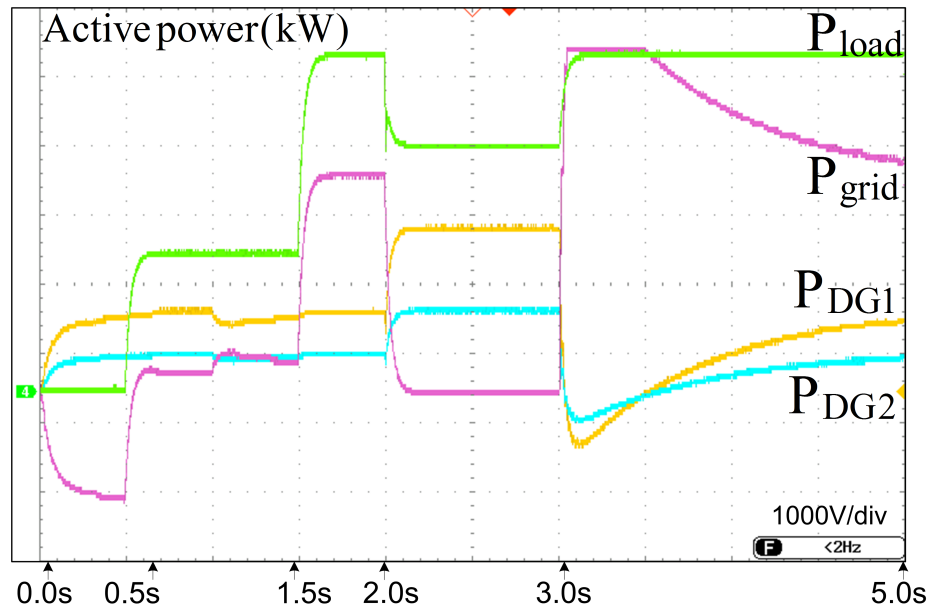


(a)

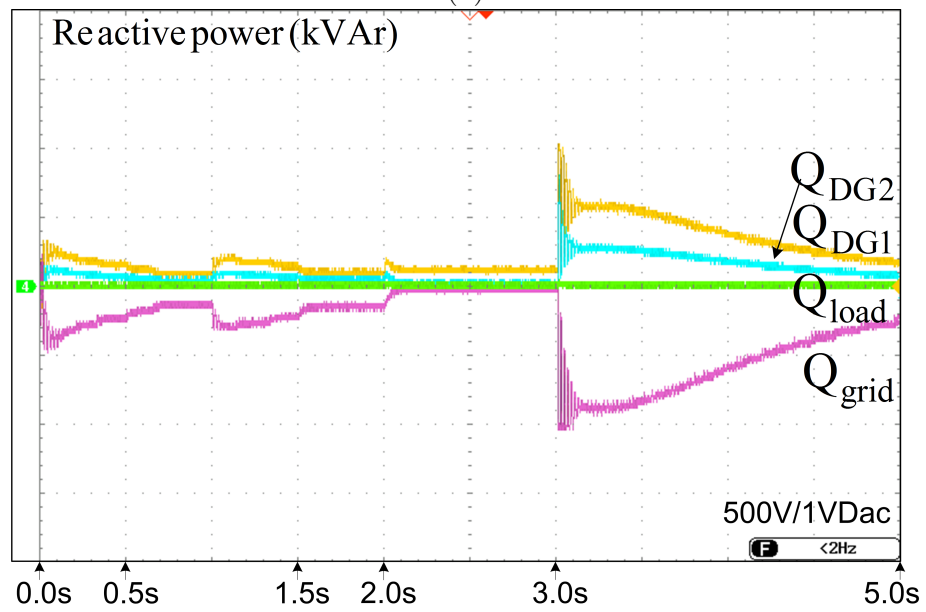


(b)

Figure 3.35: GC-SA-GC operation mode (a) PLL (γ , θ , $\sin(\gamma - \theta)$) and PCC frequency (b) active power versus frequency plot.



(a)



(b)

Figure 3.36: GC-SA-GC operation mode (a) active power in kW (b) reactive power in kVAr.

Table 3.4: SA MODE







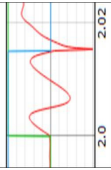
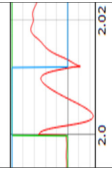
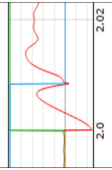
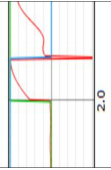
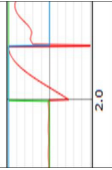
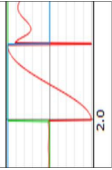
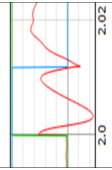
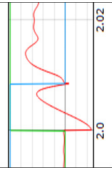
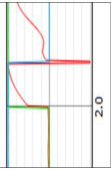
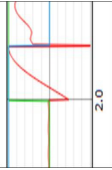
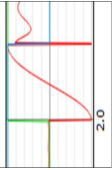
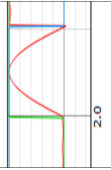
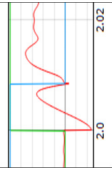
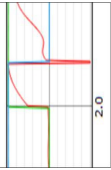
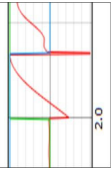
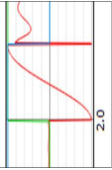
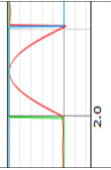
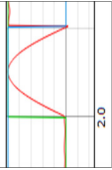
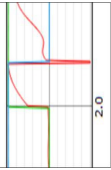
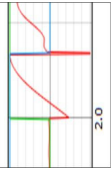
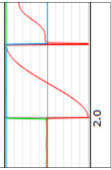
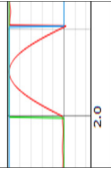
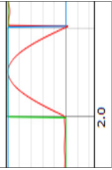

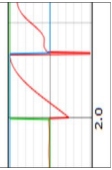
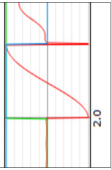

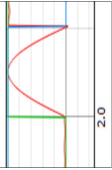


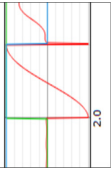


Power	0.0-0.5 sec		0.5-1.5 sec		1.5-5.0 sec	
	P (kW)	Q (kVAr)	P (kW)	Q (kVAr)	P (kW)	Q (kVAr)
Load	-	-	8.0	-	15.0	-
Grid	-	-	-	-	-	-
DG1	-	-	5.2	0.16	9.5	0.3
DG2	-	-	2.6	0.07	5.5	0.12

Table 3.5: Test results for transition between GC-SA-GC modes.

Power	0.0-0.5 sec		0.5-1.5 sec		1.5-5.0 sec		1.5-5.0 sec		1.5-5.0 sec	
	P (kW)	Q (kVAr)	P (kW)	Q (kVAr)	P (kW)	Q (kVAr)	P (kW)	Q (kVAr)	P (kW)	Q (kVAr)
Load	-	-	8.0	0.2	20.0	0.7	15.0	-	20.0	0.7
Grid	-6.0	-	1.0	-	12.5	-0.3	-	-	12.5	-0.3
		0.75		0.02						
DG1	4.0	0.5	4.6	0.15	5.0	0.25	9.5	0.3	5.0	0.25
DG2	2.0	0.25	2.3	0.07	2.5	0.12	5.3	0.12	2.5	0.12

and reactive powers Q_{load} , Q_{grid} , Q_{DG1} and Q_{DG2} . At no load the generated power is being exported to the grid and when the load switches at 0.5 sec the load demand is supplied by the DGs and the grid. At 2.0104 sec mode will switch to SA mode and power generated by DGs is being supplied to load demand. Again the mode will switch to GC mode at 3.004 sec after the fault clearing. The power exchange by the DGs, grid, and load are summarized in Table 3.5. And Table 3.6. shows the PLL phase error responses for all types of faults in the system, the behavior of responses with detection time by the PLL is also listed.

Table 3.6: PLL PHASE ERROR RESPONSES

Nature of faults	PLL Phase error ($\sin(\gamma-\theta)$)			Nature of faults	PLL Phase error ($\sin(\gamma-\theta)$)		
	 $\sin(\gamma-\theta)$	 Mode switch signal	 Disturbance fault signal		 $\sin(\gamma-\theta)$	 Mode switch signal	 Disturbance fault signal
A-GND				A-B-GND			
B-GND				A-C-GND			
C-GND				B-C-GND			
A-B				A-B-C			
A-C				A-B-C-GND			
B-C							

3.8 Summary

The performance and behavior of SRF-PLL, SOGI-PLL, DSOGI-PLL, E-PLL, and IPT-PLL in a healthy and unhealthy grid environment were investigated in this chapter. The extensive examination of all the PLL under various test situations reveals that the SOGI-PLL and DSOGI-PLL can be used for grid-connected LV systems, but the $T/4$ Delay-PLL can be used for long-lasting disturbances. The DSOGI-PLL is ideal for grid-connected DG systems that operate in a healthy grid environment. The E-PLL comes into play when one wants to avoid using a complex network and instead use adaptive filtering to simplify the structure. When the grid is subjected to frequent harmonic changes, we can use IPT-PLL to restructure the PLL for a more sturdy design and improved performance with the inverse park transform.

The islanded operation mode control system was implemented using both droop control and a virtual impedance loop, and it was evaluated for two different power rating DGs. The test results indicate that in a multi-DG scenario, control schemes for decentralized DGs performed better in terms of power-sharing. A typical current controller with PLL was used to implement the control scheme for grid-connected operation mode. The PLL phase error measurement ($\sin(\gamma - \theta)$), which provided a quick reaction and was capable of providing both synchronization and re-synchronization successfully, was used to identify islanding and switch modes automatically. The experimental responses for a three-phase fault were recorded, and it was discovered that PLL can detect islanding within 0.0104 seconds and switch to the next mode automatically. According to IEEE standards, the PCC frequency variation was also within the permissible limitations (± 1).

Chapter 4

ISLANDING DETECTION AND AUTOMATIC MODE SWITCHING BASED ON PSRF-PLL AND PIEZOELECTRIC ACOUSTIC SENSOR FOR GRID-CONNECTED DGs

4.1 Introduction

In islanded mode, the DGs have to produce constant voltage and frequency and in the grid-integrated operation mode, the DGs are required to operate with active and reactive power control mode. This necessitates two control strategies for the grid-integrated and islanded modes. Additionally, efficient islanding detection is expected between both operation modes. Meantime, in the grid-integrated operation mode of the DG system, the PLL controller is used for effective synchronization with the grid (Ray et al., 2017), (Xiang et al., 2021). If the disturbances occur in the grid-integrated mode, then the DGs must disconnect automatically from the grid to ensure

secure operation. The IEEE 1574 standards address the standardized interconnection of the DGs to the grid (Basso, 2014). Most of the PLL algorithms are very sensitive to faults and result in sudden phase angle changes during fault conditions. During unplanned events of power quality variations such as sag, swell, harmonics, unbalance, and faults, a proper control strategy needs to be developed for seamless and automatic mode transition. An appropriate modeling and consistent behavior of the control strategy will bring back the system into a stable operating region. In this regard, the Park synchronous reference frame PLL (PSRF-PLL) and piezoelectric acoustic sensor have been proposed to detect the islanding effectively with very less detection time during grid disturbances and to switch the modes of operation of the microgrid. In the islanded mode of operation, a droop control technique has been implemented for parallel-connected inverter-based DGs.

The microgrid system model considered for the present study implemented in the HIL tool is shown in Figure 4.1. This model is able to operate both in the grid-connected and in the islanded modes of operation. In this microgrid model two three-phase voltage source inverters, (VSIs) based DGs are connected to a balanced 230 V 50 Hz grid supply with constant DC voltage source, a braking chopper, LCL filter, distribution lines, parallel RLC load, circuit breaker (CB). The microgrid system model is connected to a balanced grid at the point of common coupling (PCC) through the LCL filters and the R-L modeled distribution lines.

The parallel RLC load is considered as a general structure of the local load. According to the IEEE 1547.1 test set-up, a parallel RLC load is connected between the inverter-based DGs and the grid for anti-islanding detection (Kulkarni et al., 2021).

4.2 Control strategy for grid-connected and islanded operation modes

4.2.1 Grid-connected control mode

In the grid-connected mode of operation, the microgrid system operates with a constant current control strategy, and the controller is designed in the $d - q$ reference frame. The grid-connected mode control scheme is shown in Figure 4.2. The equations pertaining to the rotating reference frame are given in (4.1) and (4.2).

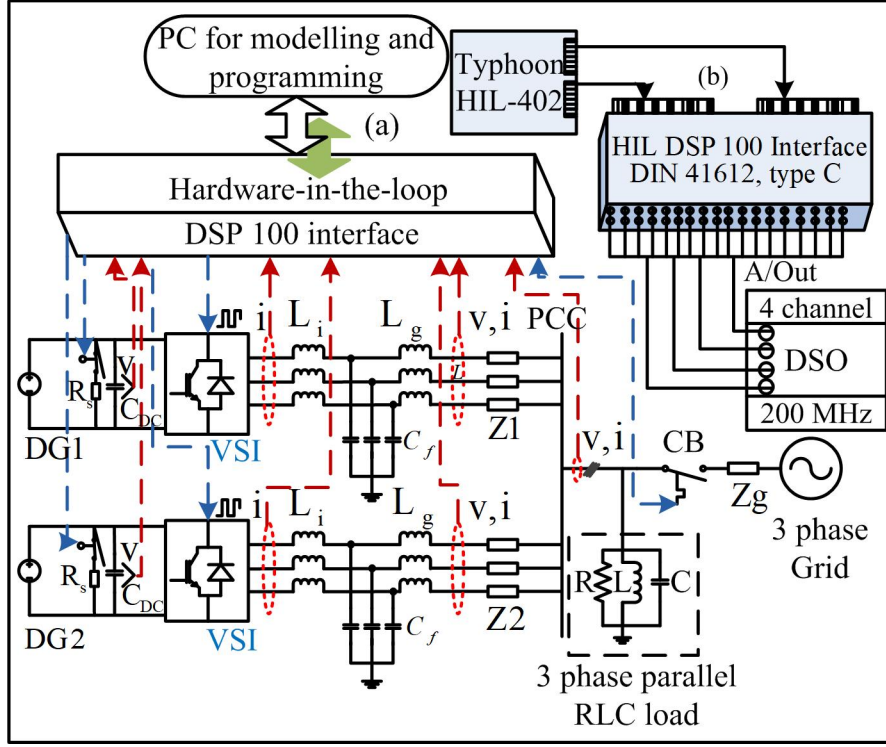


Figure 4.1: Schematic diagram of (a) The microgrid system model, and (b) Hardware in loop implementation.

$$V_{gd} = V_{id} - \left([L_i + L_g] \frac{di_d}{dt} + [R_i + R_g i_d] + \omega L_i i_q \right) \quad (4.1)$$

$$V_{gq} = V_{iq} - \left([L_i + L_g] \frac{di_q}{dt} + [R_i + R_g i_q] - \omega L_i i_d \right) \quad (4.2)$$

To avoid coupling between both the d and q current components, $\omega(L_i + L_g)$ is included in the control structure. Thus, independent control of the current components is achieved. The grid currents and voltages are regulated using standard PI controllers in the inner and outer control loops, respectively. The q -axis reference current is set to zero to achieve a zero phase angle difference between the voltage and the current in the inner current control loop. Moreover, to compensate for the coupling due to the LCL filters in the system, decoupling is implemented in the outer control loop. Then, the control signals for the inverters are generated by using the standard PWM technique. The generated θ_{GC} from the PLL is used to synchronize between the DGs and the grid.

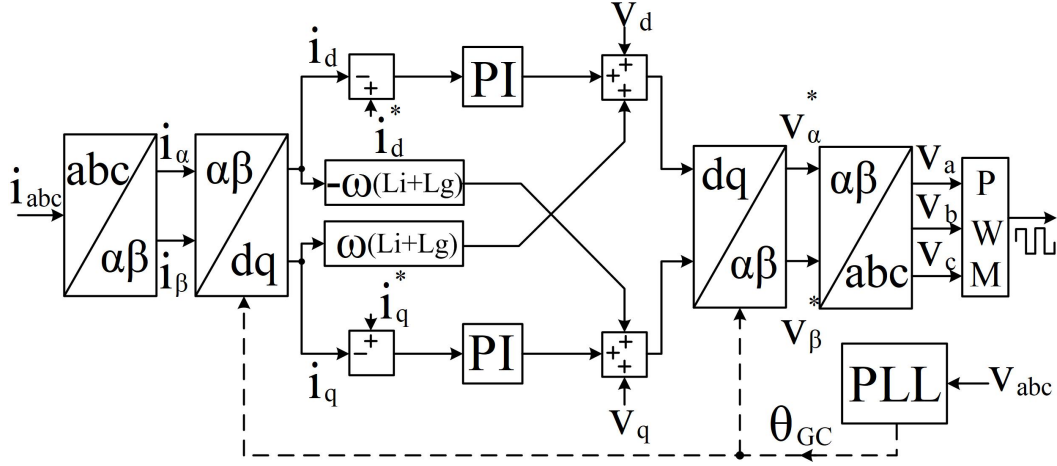


Figure 4.2: Control scheme for grid connected mode of operation.

4.2.2 islanded control mode

The islanded mode of operation includes a power controller, a voltage controller, and a current controller. In addition to the above controllers, a virtual complex impedance is further added to reduce the circulating currents and to improve the reactive power-sharing among the parallel-connected inverter-based DGs in the microgrid. The voltage and currents controllers are designed to eliminate high-frequency disturbances and resonance caused due to the passive filters. The frequency and the phase are set by the droop controller in the outer power control loop. The overall control scheme is shown in Figure 4.3, wherein the instantaneous active and reactive power is calculated with inverter output d -axis voltage and currents, which is given by (4.3).

$$\hat{p} = V_{od}i_{od} + V_{oq}i_{oq} ; \hat{q} = V_{od}i_{oq} - V_{oq}i_{od} \quad (4.3)$$

After filtering out the instantaneous components, the fundamental power components are obtained as (4.4).

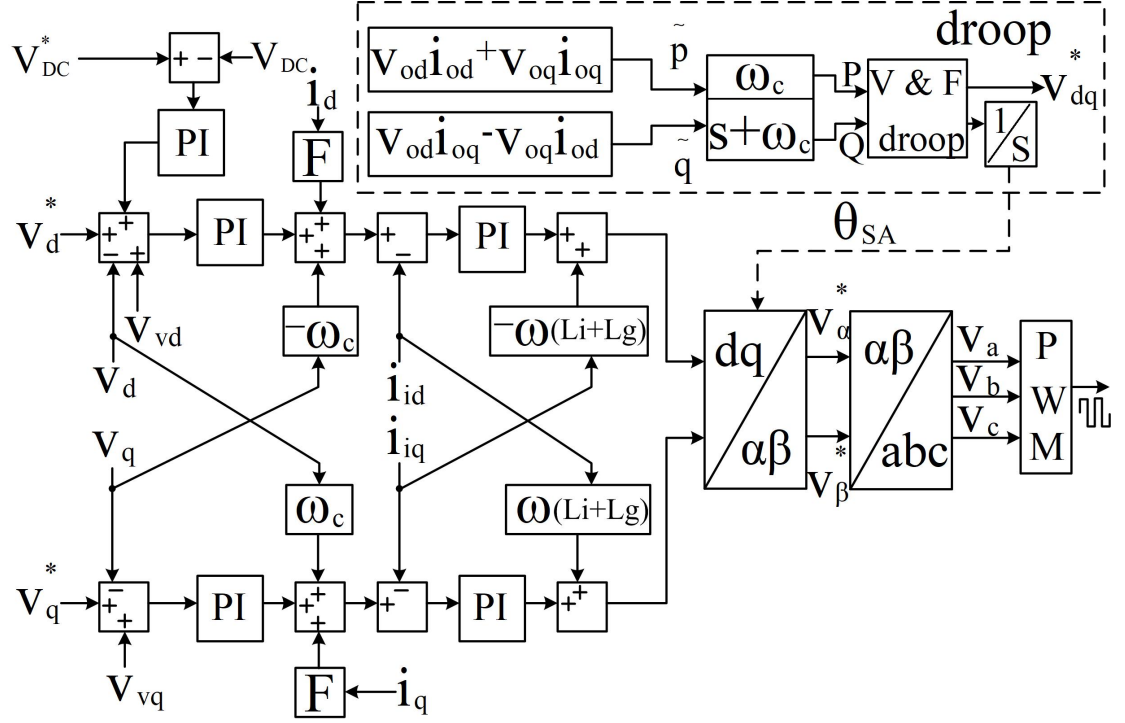


Figure 4.3: Control scheme for islanded mode.

$$P = \frac{\omega_c}{s + \omega_c} \hat{p} ; Q = \frac{\omega_c}{s + \omega_c} \hat{q} \quad (4.4)$$

Where ω_c is the low pass filter cut-off frequency.

After obtaining the fundamental power components, an artificial droop is introduced in the power controller, and the droop equations are given as (4.5).

$$\omega^* = \omega_n - m_p P ; V^* = V_{dn} - n_q Q \quad (4.5)$$

Where, ω^* and V^* are the reference frequency and voltage of the droop controller, and P and Q are the output active and reactive powers of the inverters.

For a given range of frequency, voltage, and power magnitude, the droop gains m_p , and n_q are calculated as (4.6):

$$m_p = \frac{\omega_{max} - \omega_{min}}{P_{max}} ; n_q = \frac{V_{max} - V_{min}}{Q_{max}} \quad (4.6)$$

Where, ω_{min} , ω_{max} , V_{min} , and V_{max} are the minimum and maximum allowable range of variations in the frequency and voltage. Equation (4.14) shows the droop coefficients for equal power ratings of the inverter-based DGs.

$$m_{p1} = m_{p2} ; n_{q1} = n_{q2} \quad (4.7)$$

Where, m_{p1} and n_{q1} are for inverter 1 and m_{p2} and n_{q2} are for inverter 2. The microgrid system model is shown in Figure 4.1, wherein DG_1 has maximum power rating of 10kVA and DG_2 of 5kVA. The droop coefficients for both the DGs are given in (4.16) and (4.17).

$$m_{p1} = 2 * m_{p2} \quad (4.8)$$

$$n_{q1} = 2 * n_{q2} \quad (4.9)$$

The $d - q$ reference frame islanded voltage controller equations are written as (4.10) and (4.11).

$$i_{id}^* = Fi_{od} - \omega_n C_f V_{oq} + k_{pv}(V_{od}^* - V_{od} - V_{vd}) + k_{pv} \frac{d(V_{od}^* - V_{od} - V_{vd})}{dt} \quad (4.10)$$

$$i_{iq}^* = Fi_{oq} - \omega_n C_f V_{od} + k_{pv}(V_{oq}^* - V_{oq} - V_{vq}) + k_{pv} \frac{d(V_{oq}^* - V_{oq} - V_{vq})}{dt} \quad (4.11)$$

Where, F is the feed-forward gain, k_{pv} and k_{iv} are the proportional and integral gains of the PI controller, respectively, and V_{vd} and V_{vq} are the d and q axis set-points of the virtual complex impedances. The equations for V_{vd} and V_{vq} are given in (4.12).

$$\begin{aligned}
V_{vd}^* &= I_{id} * R_v - \frac{dI_{iq}}{dt} * L_v \\
V_{vq}^* &= I_{iq} * R_v - \frac{dI_{id}}{dt} * L_v
\end{aligned} \tag{4.12}$$

The islanded current controller equations are written as (4.13).

$$\begin{aligned}
V_d^* &= k_{pi}(i_{id}^* - i_{id}) + k_{ii} - \omega_n L_i i_{iq} \\
V_q^* &= k_{pi}(i_{iq}^* - i_{iq}) + k_{ii} + \omega_n L_i i_{id}
\end{aligned} \tag{4.13}$$

The voltages and currents are regulated using the standard PI controllers, and decoupling is implemented in the control structure due to the LCL filters in the system. The output DC-link voltage control is activated only when the reference voltage is more than the DC-link voltage. The operation of this control is to maintain the reference voltage to its standard reference. Then the control signals for the inverter are generated using the PWM technique.

4.3 Islanding detection and automatic mode switching with modified PLL

The inverter-based DGs are synchronized with the grid by the PLL. In the present paper, a modified Park synchronous reference frame phase-locked loop (PSRF-PLL) based islanding detection and automatic mode switching have been proposed for parallel-connected multi-DG systems.

Figure 4.4. shows a detailed structure of the PSRF-PLL, where the input voltages to the PLL are the grid side voltage quantities (V_a , V_b , and V_c). In Figure 4.5, the PSRF-PLL phasor diagram is shown, where a , b , and c are the three-phase quantities with 120° phase shift between each phase, d and q are the rotating reference frame quantities with θ as the rotational angle, α and β are the stationary orthogonal reference frame quantities, and the formulation of the proposed PSRF-PLL is:

$$V_\alpha = V_a \tag{4.14}$$

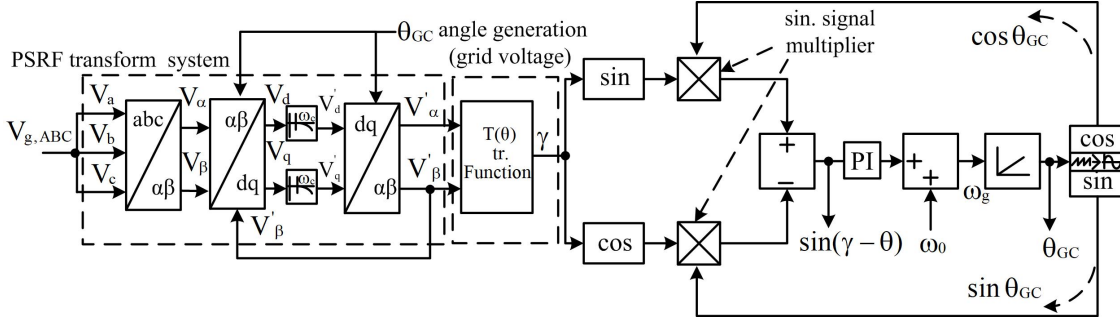


Figure 4.4: Detailed block diagram of the PSRF-PLL controller.

$$V_\beta = \frac{1}{\sqrt{3}}(V_a + 2V_b) \quad (4.15)$$

Where, V_α is superimposed with V_a and $V_a + V_b + V_c = 0$, and V_β' is the output obtained from the filtered dq quadrature signals after the Park transformation.

The V_d and V_q quadrature signal equations are:

$$V_d = V_\alpha \cos \theta + V_\beta \sin \theta \quad (4.16)$$

$$V_q = V_\beta \cos \theta - V_\alpha \sin \theta \quad (4.17)$$

The equations are written in the matrix form as:

$$\begin{bmatrix} V_d \\ V_q \end{bmatrix} = \begin{bmatrix} \cos \theta & \sin \theta \\ \sin \theta & -\cos \theta \end{bmatrix} \begin{bmatrix} V_\alpha \\ V_\beta \end{bmatrix} \quad (4.18)$$

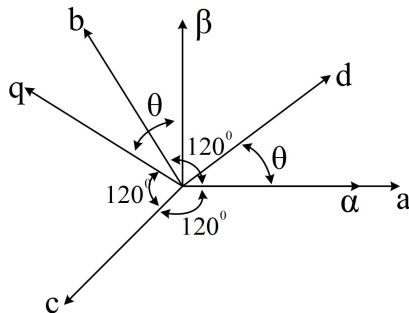


Figure 4.5: Phasor diagram (Reference Frame Transformation) of the PSRF-PLL controller.

Where, $\begin{bmatrix} \cos \theta & \sin \theta \\ \cos \theta & -\sin \theta \end{bmatrix}$ is the transformation matrix $[T]$.

The equation is re-written as:

$$[V_{dq}] = [T][V_{\alpha\beta}] \quad (4.19)$$

$$[V_{\alpha\beta}] = [T]^{-1}[V_{dq}] \quad (4.20)$$

Then, the equations for $V'_{\alpha\beta}$ are as follows:

$$[V'_{\alpha\beta}] = \left[\frac{\omega_c}{s + \omega_c} \right] * [T]^{-1} * [T][V_{\alpha\beta}] \quad (4.21)$$

Where, the 1st term in (4.21) is first order low pass filter (LPF) with ω_c as the cut-off frequency. Equation (4.21) is re-written as:

$$[V'_{\alpha\beta}] = [T]^{-1}[V'_{dq}] \quad (4.22)$$

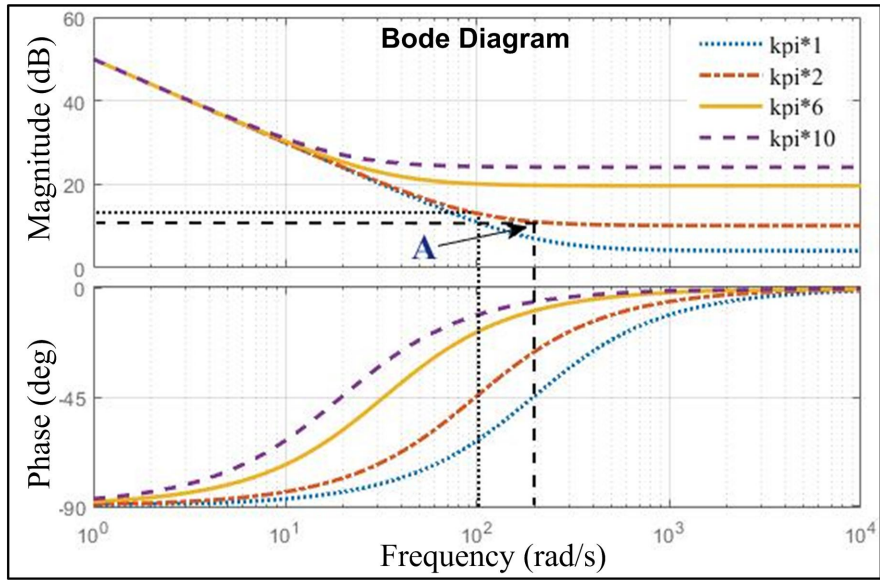
Where, V'_α and V'_β are:

$$[V'_\alpha] = [V'_d \cos \theta - V'_q \sin \theta] \quad (4.23)$$

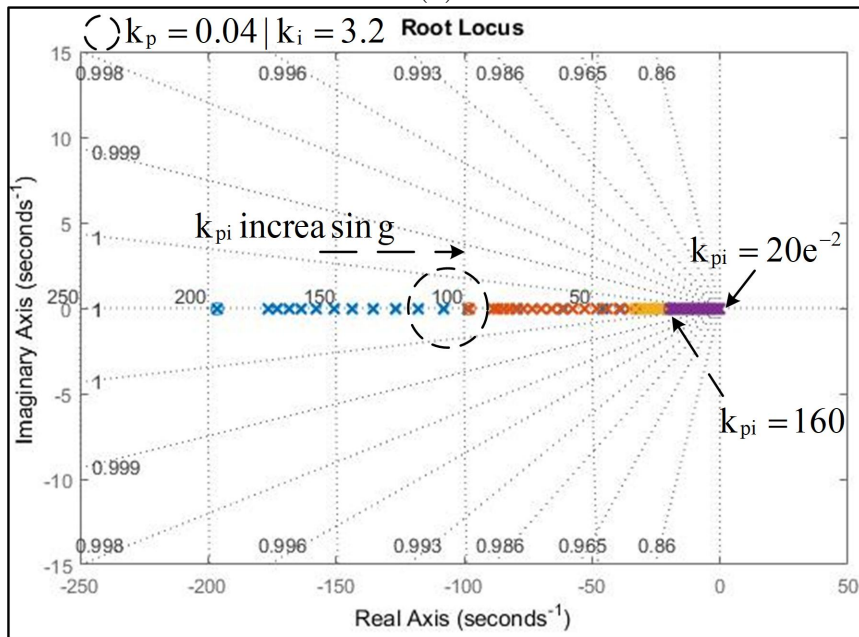
$$[V'_\beta] = [V'_q \cos \theta + V'_d \sin \theta] \quad (4.24)$$

Where γ and θ_{GC} are the grid and the DGs' phase angles. The orthogonal stationary frame grid voltages are input to the angle generator. The angle γ and θ_{GC} must be interlocked, thereby reducing the PLL phase error (Δe) to zero. Then, the Δe is passed through the PI controller to get the frequency of the DGs. To improve the starting dynamic response and to reduce the control effort, the grid nominal frequency of ω_0 is feed-forwarded, and thus, the phase tracking is accomplished more quickly. Then, the signal ω_g is integrated to generate the measured angle of the DG voltages. Thus, the proposed PSRF-PLL is simple to implement with less computational burden and shows reliable performance under various grid disturbance conditions.

To design and select appropriate gains for the proposed PSRF-PLL controller, the bode plot and root locus study were carried out. Figure 4.6 shows the Bode plot and root locus of the proposed PSRF-PLL controller. The bandwidth of the



(a)



(b)

Figure 4.6: PSRF-PLL controller-(a) bode plot, and (b) root locus.

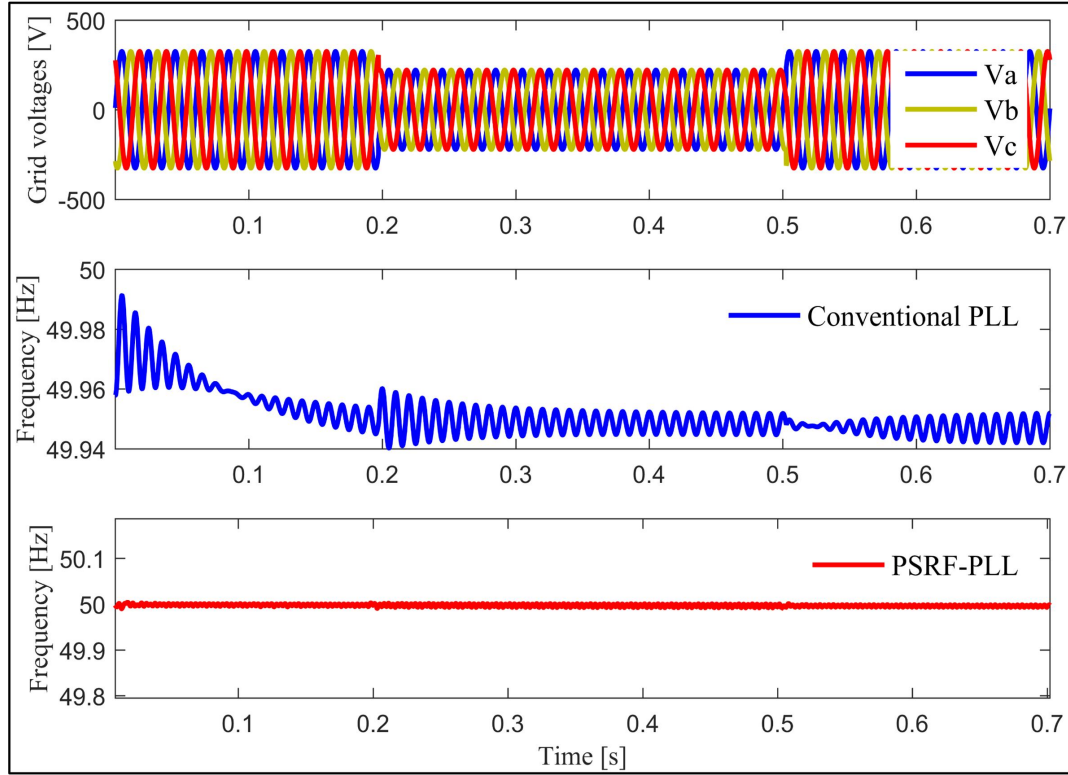


Figure 4.7: Output frequency response of proposed PSRF-PLL and conventional PLL.

controller must be within 120 Hz, so it was designed for bandwidth of 110 Hz and 28.1° phase. It was observed from the root locus plot that with increasing gain values beyond $k_p=0.2$ and $k_i=160$, the controller falls into the unstable region and may lead to a false islanding detection during the disturbances of the microgrid system in the grid-connected mode of operation. The circle indicates the appropriate values to be chosen while designing the proposed PSRF-PLL controller. The results of the test (voltage sag) are shown in Figure 4.7. As shown, the response of the proposed PSRF-PLL is able to generate a steady response comparatively with the conventional PLL. The islanding detection and mode switching operations are based on the PSRF-PLL controller phase error $\Delta e/\sin(\gamma - \theta)$.

4.4 Experimental results and analysis

The microgrid system model is tested experimentally on the real-time hardware in the loop (HIL) platform. Figure 4.1 (a) and (b) shows the schematic diagram of the

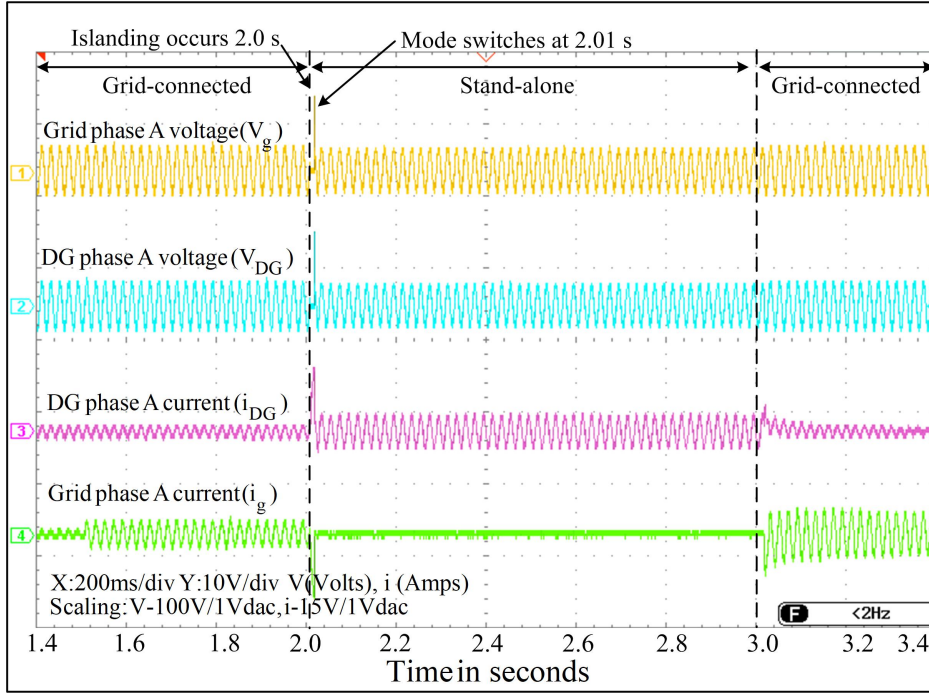


Figure 4.8: Grid and DG voltages and currents during transition.

set-up and general connection diagram of the HIL implementation, where Typhoon 402 and HIL DSP 100 are used, and all the responses are captured in the 4 channel 200 MHz DSO. The proposed control schemes were analyzed in detail in the present section for islanded mode, grid-connected mode, islanding detection, and also for automatic mode switching under grid disturbances.

Figure 4.8 shows the grid and DG phase A voltages and currents. A fault is introduced at 2.0 s, and the PLL responds immediately and switches to the islanded mode at 2.01 s. The voltage and current variation due to the mode switching operation can be observed. After mode switches to the islanded mode, the grid currents i_g becomes zero, and the i_{DG} continues to supply the microgrid critical loads. After the fault clearance at 3.004 sec, the proposed PSRF-PLL again switches to the grid-connected mode of operation.

In Figure 4.9, the responses of the active power versus frequency of both the DGs are shown; the frequency of the DGs predominately depends on its active powers.

Figure 4.10 shows the total harmonic distortion (THD) in phase A voltage at the PCC. The THD for all the five test cases under normal conditions in the grid-connected mode of operation for the proposed PSRF-PLL is shown. From the THD of

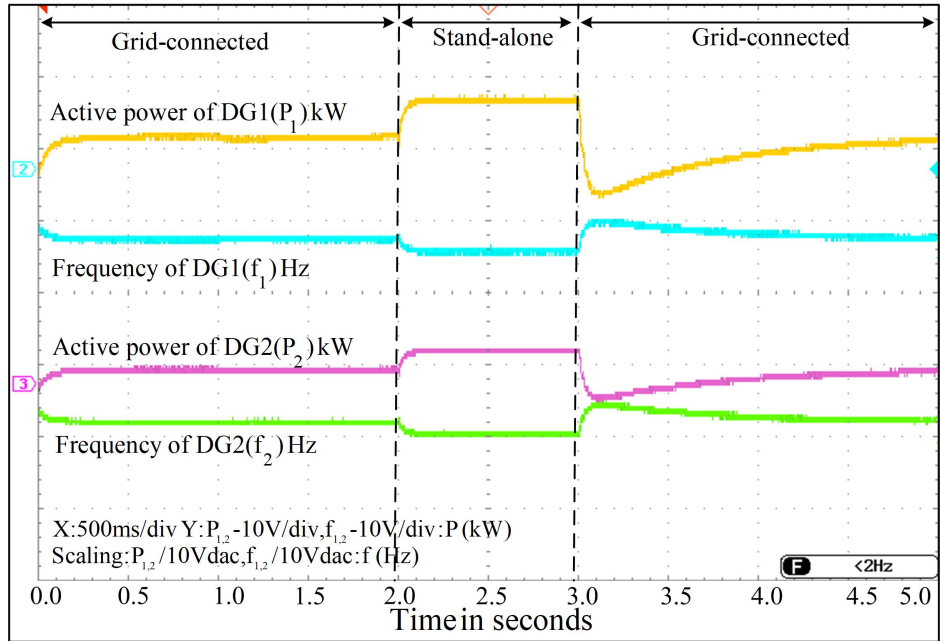


Figure 4.9: Responses of the active powers of $DG_{1,2}$ v/s frequencies of $DG_{1,2}$ during transition.

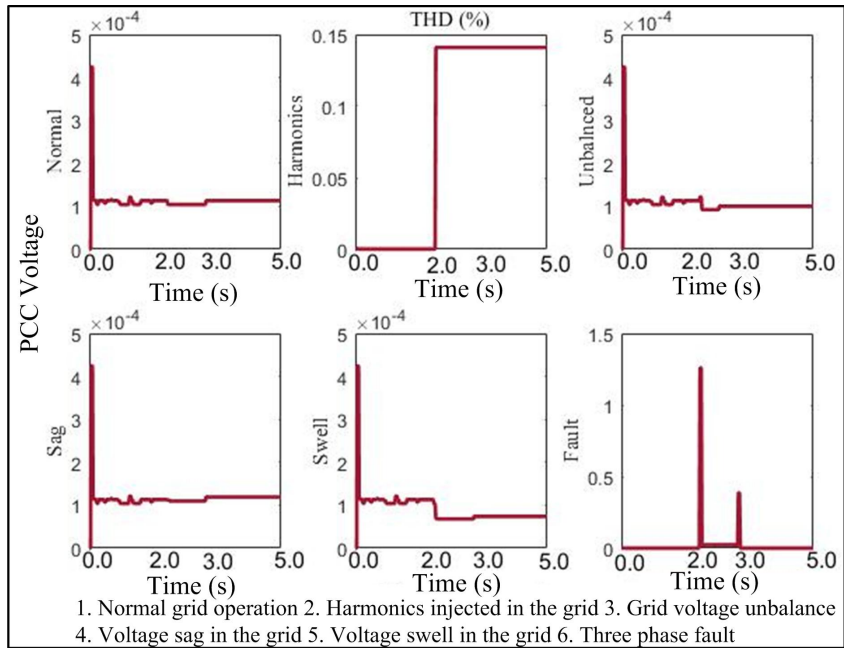


Figure 4.10: Total harmonic distortion in PCC voltage for unbalance, harmonics, sag, swell, and faults.

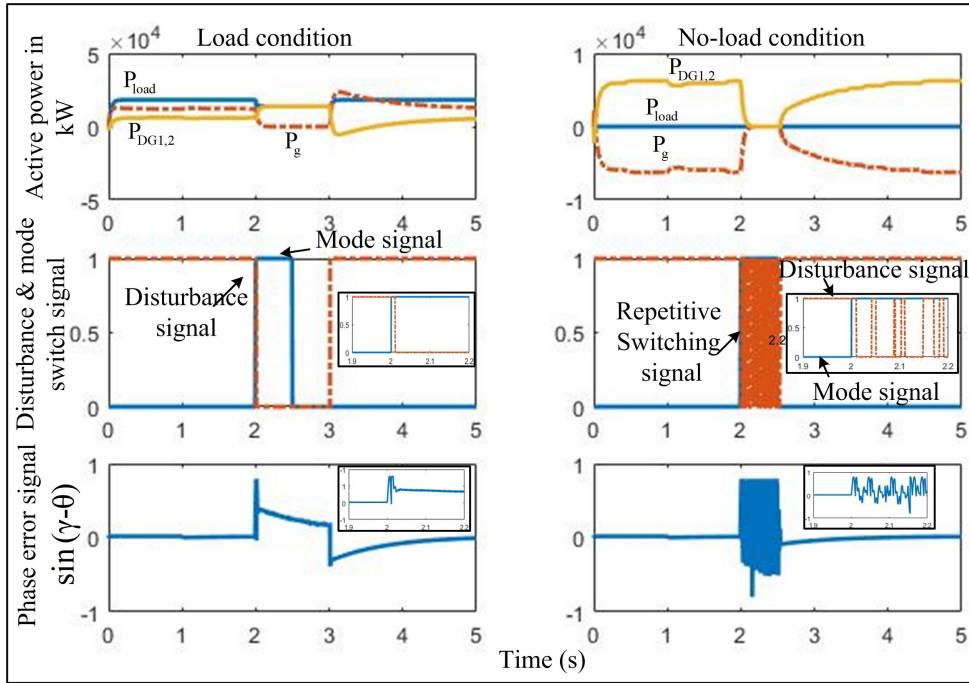


Figure 4.11: PLL controller responses under full- load and no-load conditions.

phase A, it can be observed that there is minimum TDH value and not much voltage distortion in the waveform due to unbalance, sag, and swell. But the distortion due to grid voltage harmonics and three-phase to ground fault is about 0.2% to 2%. According to the IEEE-1547 series of standards, total THD should not exceed 5% of the fundamental frequency. It can be observed from Figure 4.10 that PCC voltage THD is less than 2% for all the test cases.

To evaluate the effectiveness of the proposed PSRF-PLL method with power mismatch conditions, the microgrid system with PLL controller for islanding detection and automatic mode switching was tested and the responses were plotted. Figure 4.11 shows the responses for load and no-load conditions. At 2.0 s, the disturbance was introduced and removed after 2.5 s. For all the load conditions, the controller worked perfectly, but for the no-load condition with disturbance, it showed repetitive variation (oscillatory behavior). For the no-load condition, the mode switch signal repeatedly switches between grid-connected and islanded modes. The no-load condition does not come into the picture, and during the disturbance, the controller detects the islanding and switches the respective modes as per the load conditions. From Figure 4.11, it can be concluded that there is no NDZ for loaded conditions using the

Table 4.1: Islanding detection time and NDZ with active and passive islanding detection methods

Reference	Method	NDZ	Detection time
(De Mango et al., 2006)	OUV/OUF	large	4 ms-2 s
(Singam and Hui, 2006)	phase jump detection	large	10-20 ms
(Li et al., 2014)	frequency jump	small	75 ms
(O’kane and Fox, 1997)	impedance measurement	small	0.77-0.95 s
(Dong et al., 2014)	frequency positive feedback	negligible	0.252 s
(Sun et al., 2003)	phase PLL perturbation	smallest	120 ms
Proposed (Kulkarni et al., 2021)	PLL phase error detection	negligible	10 ms

proposed PSRF-PLL method. The proposed PSRF-PLL method presents negligible non-detection zone and high islanding detection efficiency with less detection time.

Table 4.1 shows a comparison of the various islanding detection methods with the proposed PSRF-PLL islanding detection method. The proposed PSRF-PLL method presents negligible non-detection zone and high islanding detection efficiency with less detection time compared with the other methods presented in the literature (Sun et al., 2003), (De Mango et al., 2006)-(Dong et al., 2014), and depicted in Figure 4.12.

In Figure 4.13 (a) and (b), the active powers P_1 , P_2 , P_g , and P_{load} and the reactive powers Q_1 , Q_2 , Q_g , and Q_{load} are shown. At no load, the generated power is exported to the grid, and when the load switches at 0.5 s, the load is supplied by the DGs and the grid. At 2.010 s, the mode switches to the islanded mode, and the power generated by DGs is supplied to the load demand. The power exchange by the DGs, grid, and the load is summarized in Table 4.2, and depicted in Figure 4.15 (a) and (b).

In Figure 4.14, when the disturbance occurs, the $\sin(\gamma - \theta)$ exceeds the threshold value, and within 10 ms, the PLL detects the islanding and switches to islanded mode. The fault is introduced between 2.0 s to 2.5 s, but the system continues in the islanded operation mode up to 3.004 s, after fault clearance. At 3.004 s, the grid voltage settles down to normal value, and the mode switches the operating mode to the grid-connected mode. The variations of the PCC frequency are (50.4 to 49.6) during the mode switching operation and are within the IEEE standard limits.

In the grid-connected operation mode, the PLL phase error and the PLL phase

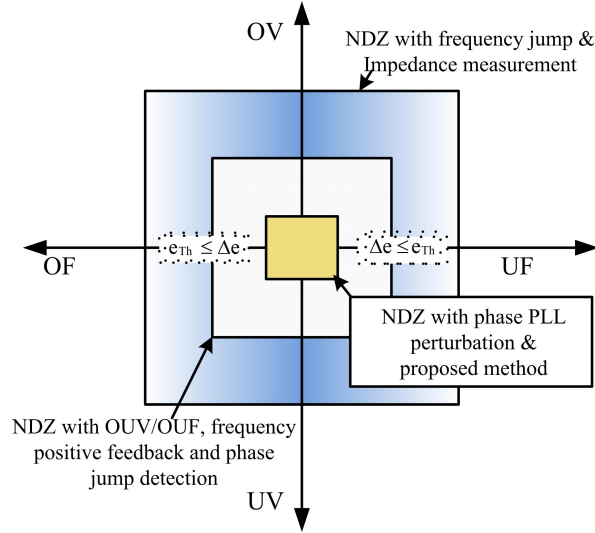


Figure 4.12: NDZ of proposed islanding detection method with other active and passive islanding detection methods.

Table 4.2: Test results for transition between grid-connected-islanded-grid-connected modes

	0.0-0.5 sec		0.5-1.5 sec		1.5-2.0 sec		2.0-3.0 sec		3.0-5.0 sec	
Power	P	Q	P	Q	P	Q	P	Q	P	Q
	(kW)	(kVAr)	(kW)	(kVAr)	(kW)	(kVAr)	(kW)	(kVAr)	(kW)	(kVAr)
Load	-	-	8.0	0.2	20.0	0.7	15.0	0.5	20.0	0.7
Grid	-6.0	-	1.0	-	12.5	-0.3	-	-	12.5	-0.3
		0.75		0.02						
DG1	4.0	0.5	4.6	0.15	5.0	0.25	9.8	0.3	5.0	0.25
DG2	2.0	0.25	2.3	0.07	2.5	0.12	4.9	0.12	2.5	0.12

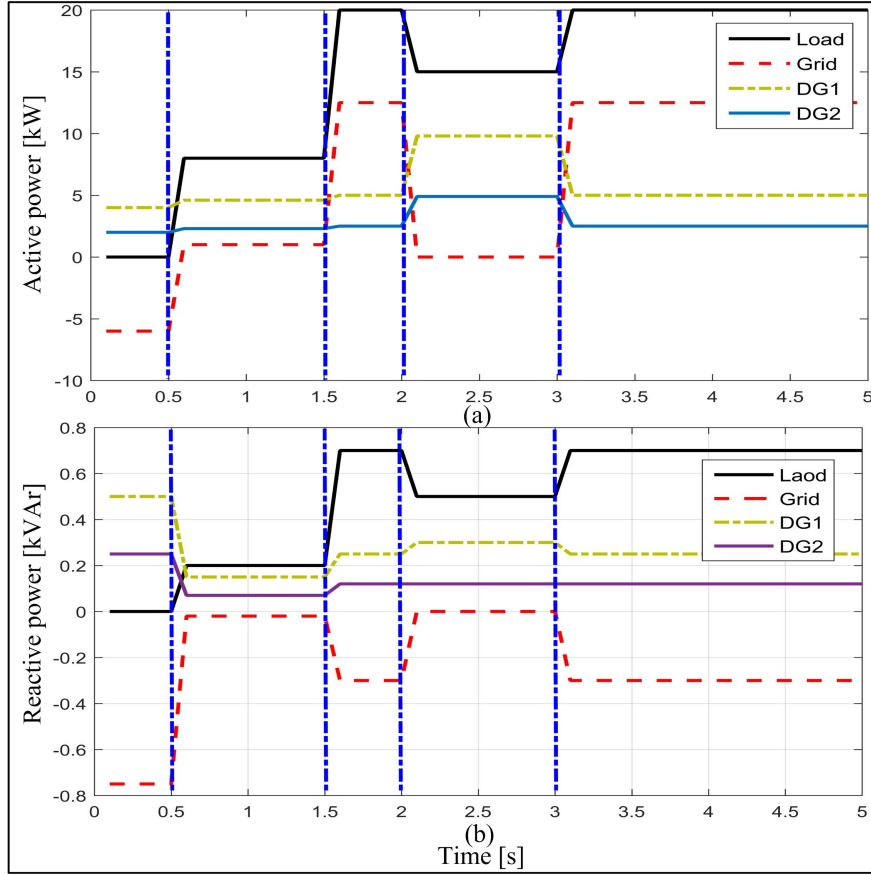


Figure 4.13: Performance of microgrid system model in grid-connected to islanded and islanded to grid-connected mode transition: (a) Active powers of DGs, grid, and load, (b) Reactive powers of DGs, grid, and load.

angle responses for the proposed PSRF-PLL and popular PLLs in the literature (Yang et al., 2015) shown in Figure 4.16. The analysis of the proposed PSRF-PLL controller for its effectiveness under various power quality test cases such as voltage unbalance, harmonics, voltage sag, and voltage swell (10% to 20%) and faults (1ϕ , 1ϕ -G, L-L, L-L-G, 3ϕ , and 3ϕ -G) is shown in Figure 4.17. The disturbance is introduced at 2.0 s, so the window of 2.0 s to 2.05 s is considered for an unobstructed view of the variations. In Figure 4.17 (a), V_{abc} of 260V, 210V, and 230V were considered as a unbalance in the grid voltages, and it was observed that the grid voltage unbalance did not affect the phase-locking between the DGs and the grid. Both the grid and the DG angles had interlocked perfectly in the case of the proposed PSRF-PLL compared with the other PLL controllers. In Figure 4.17 (b), the 2nd, 5th, and 11th harmonics were added to the grid voltages at 2.0 s; there was harmonic content in the phase error and phase

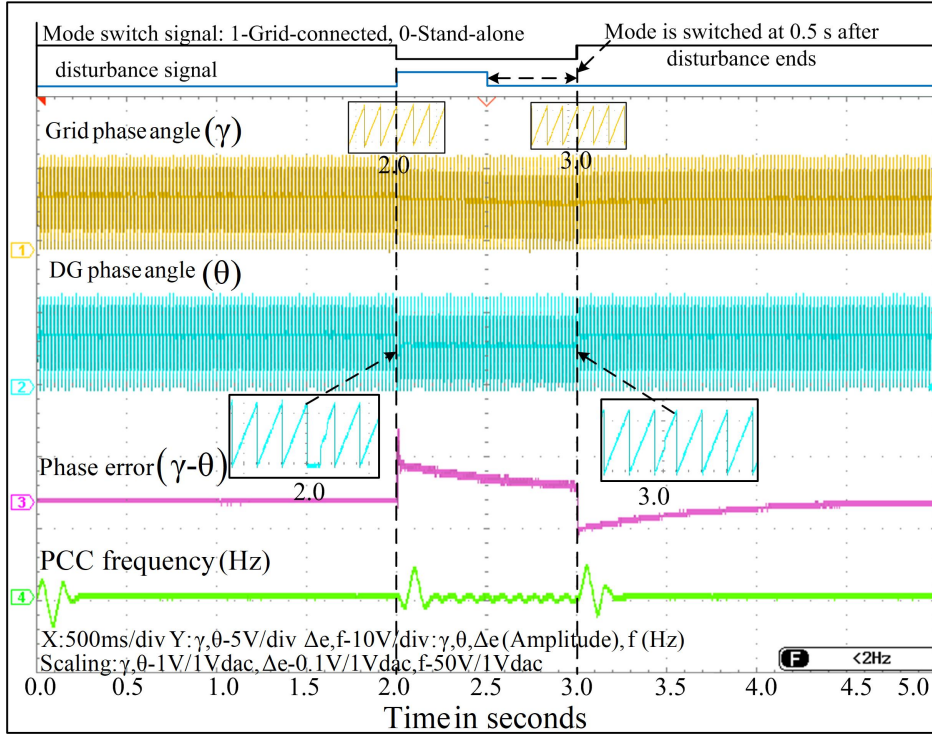
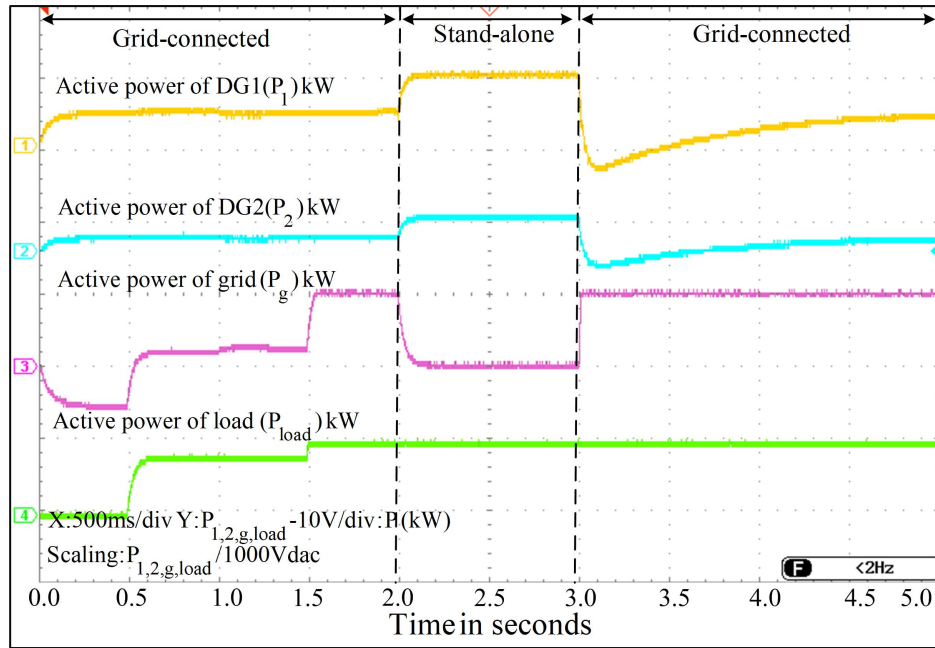


Figure 4.14: Performance of microgrid system model in grid-connected to islanded and islanded to grid-connected mode transition: Grid phase angle γ , DG phase angle θ , phase error Δe , and frequency at the PCC during transition.

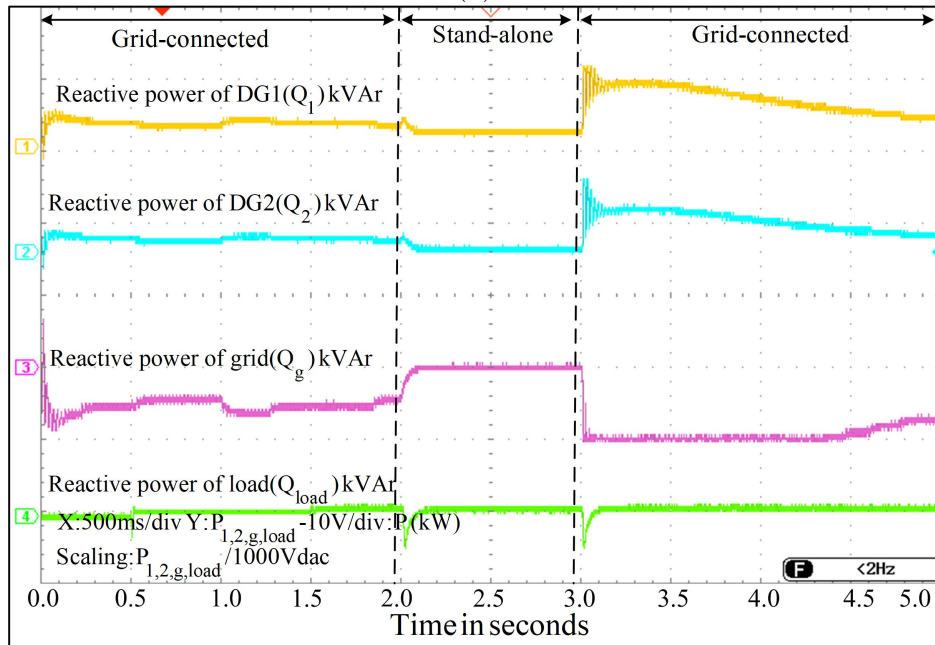
angles, but the zero crossing of the proposed PSRF-PLL was not affected and showed better harmonic immunity. However, the IPT and SOGI PLL subjected to harmonics in the grid voltages and zero-crossing were affected.

Figure 4.17 (c) and (d) shows the variations in phase error and phase angles for the grid voltage sag and swell. When compared with the other PLL controllers, the proposed PSRF-PLL shows better dynamics. In Figure 4.17 (e), the three-phase to ground fault was introduced at 2.0 s at the grid side, and the grid phase angle is no more in phase with the DG phase angle. All the PLL controllers show variations in the phase error response when there is a three-phase fault at the grid side. However, less distortion was observed in the proposed PSRF-PLL and E-PLL. These three-phase faults directly propagate to the inverters connected to the grid and cause permanent damage. To avoid this, the detection of the islanding should be fast and the modes switched accordingly.

To show the power transfer capability, reliability, and stability of the microgrid with the proposed control scheme, we have considered the pole tripping and close-in



(a)



(b)

Figure 4.15: Performance of microgrid system model in grid-connected to islanded and islanded to grid-connected mode transition: (a) Active powers of DGs, grid, and load, (b) Reactive powers of DGs, grid, and load.

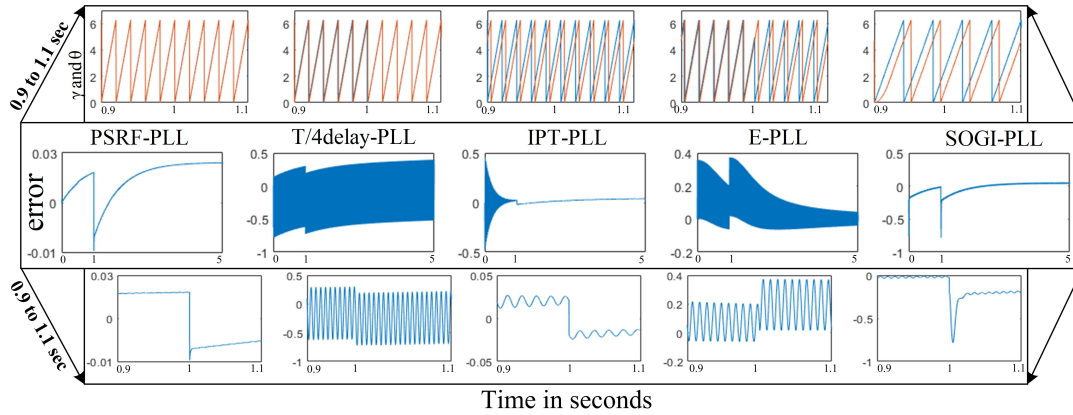


Figure 4.16: Grid-connected operation mode-PLL phase error and phase angle responses for the proposed PSRF-PLL and popular PLLs in the literature (Yang et al., 2015).

fault in the distribution system. The Figure 4.18 (a) and (b) shows the responses for grid-connected microgrid system for pole trip and close-in fault conditions. We can observe from Figure 4.18 (a) that the CB control signal is in position '0' and the mode switch signal in position '1', which means the proposed PLL will not send the command signals to the CB for that if any unbalance due to the pole trip in the grid-connected microgrid system, the CB remains in the closed position. This situation can be overcome by including the gain in the closed-loop of PLL to reach the threshold during the pole trip.

The Figure 4.18 (b) shows the responses for close-in fault, The CB control signal is in position '0' and the mode switch signal in position '1' up to 0.01 sec. The proposed PLL will sense the close-in fault within 0.01 sec and sends the command signal to the CB to operate.

4.5 Islanding detection with piezoelectric acoustic sensor

There has been an increase in demand for smart appliances (SA) due to the numerous advantages that grid-integrated renewable energy sources have to offer. Sensors are a subcategory of SA. A diaphragm converts acoustic signals into corresponding voltage signals in these sensors. The piezoelectric acoustic sensors make it possible to detect islands in the case of a grid failure, and this is one of the endless possibilities for self-healing. Sensors based on piezoelectric materials can be used in conjunction with

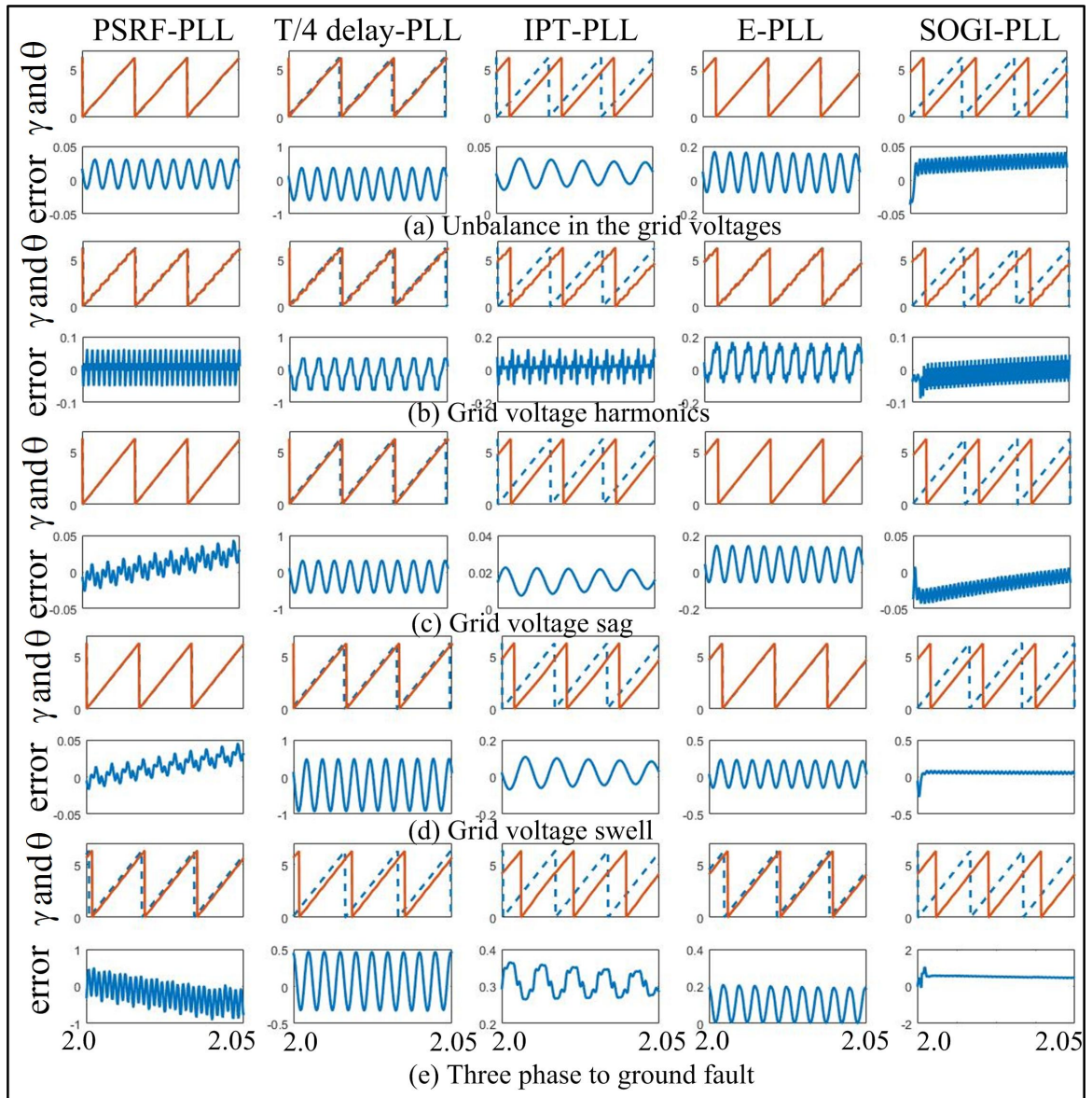
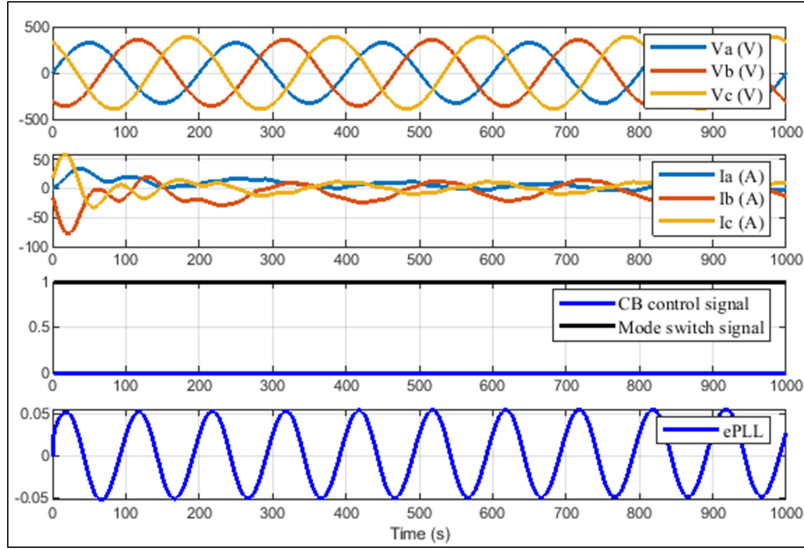
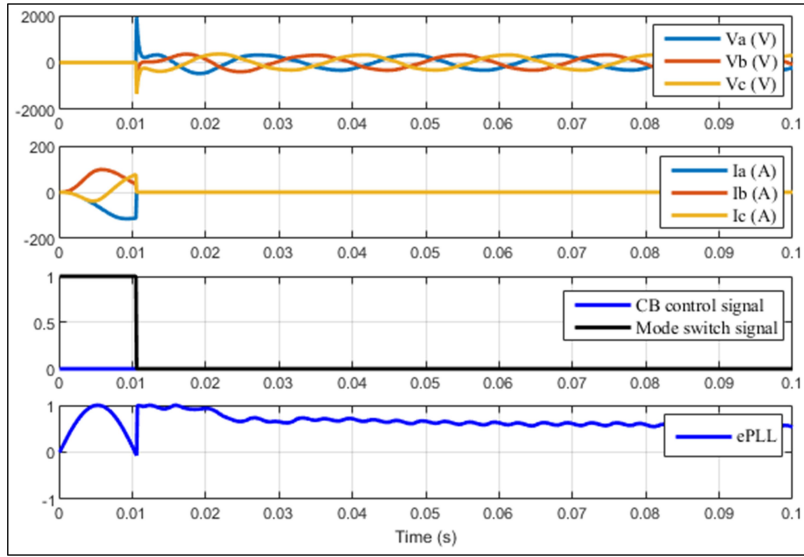


Figure 4.17: Grid-connected operation mode-PLL phase error and phase angle responses for the proposed PSRF-PLL and popular PLLs in the literature. For various case studies- (a) unbalance, (b) harmonics, (c) sag, (d) swell, and (e) faults.



(a)



(b)

Figure 4.18: Performance proposed islanding detection scheme under: (a) pole trip condition, (b) close in fault.

Complementary metal-oxide-semiconductor (CMOS) technology. These structures can also be reduced in size depending on the requirements of the applications (Li et al., 2016).

Piezoelectric sensors usually find applications in automotive, biomedical, and aviation design. These sensors can be scaled down and there will be no need for an external power supply. The piezoelectric sensors are exceptionally sensitive with great

execution and these sensors can be produced on the large scale. For these types of sensors, the diaphragm is an imperative factor so the design should be perfect and reliable. For this reason, we design these sensors with Finite Element Modeling (FEM). The FEM is utilized to look at the sensor boundary parameters in terms of their dynamic performance (stress, deflection, strain distribution, and natural frequency) (Narayanan and Balamurugan, 2003). The layout and its fabrication are of centered exploration to increase the sensitivity and optimize the voltage produced and natural frequency in the required range, and in expanding the transmission capacity by various assembling advancements like mass and surface micromachining (Mohapatra, 2011), (Durani et al., 2020). These piezoelectric sensors operate on the rule of piezoelectricity, in which charge generation happens when the diaphragm deflects because of applied pressure. The more slender the diaphragm, the better deflection, and more sensitivity can be accomplished. In any case, under varying frequencies, the deflection of the sensor diaphragm depends on the shape and the dimensions. Like RLC networks the resonant sensors also work on the principle of resonance. When the device is working under resonance, the pressure is conducted through the neck to the cavity of the sensor and it gets magnified. The magnified pressure or output pressure will be much higher than input pressure (Wang et al., 2017). The diaphragm is formed at the opposite side of the cavity and the deflection is measured. Then with the help of a piezoelectric layer, the deflection of the diaphragm is converted into an equivalent voltage signal.

4.6 Design and dimensions of proposed piezoelectric acoustic sensor

To determine the sensitivity and frequency response of the acoustic sensor, we need to consider the physical property of the material used for the diaphragm. However, with the piezoelectric sensor method, we can sense the acoustic signal's voltage amplitude signal and the natural frequency signal. The sensitivity and the frequency response of the piezoelectric sensor are essentially reliant on the mechanical characteristics and actual physical dimensions of the structure (Qiu et al., 2021). The dynamic response (i.e., natural voltage and frequency of the design) are the fundamental quantities needed for signal sensing for a piezoelectric sensor. To get the maximum output volt-

age during the resonance the frequency shift identification of the piezoelectric sensor has to be considered in the design process. To achieve this, the diaphragm deflection should remain maximum and the strain and stress to be optimized. Likewise, the nominal frequency of the design should be of a similar value as the supply frequency. The open-circuit voltage created by a piezoelectric sensor is given by (4.25),

$$V = \frac{Ed_{33}\epsilon dA}{C} \quad (4.25)$$

Where E is Young's modulus component in Pascals (Pa), dA -space of the terminal electrodes in m^2 , d_{33} - charge coefficient of piezoelectric, ϵ -strain applied, and C -capacitance of piezoelectric material in farad (F). From equation (4.25), the voltage depends upon the property of the component and inversely corresponds to the capacitance of the structure. But the capacitance depends on the dielectric property of the material. Therefore, to optimize the value of strain, the shape of the diaphragm should be proper. Besides, "to ensure maximum deflection of the diaphragm to generate a maximum voltage, the thickness of the diaphragm has to be chosen such that the deflection is linear for the given range of Sound Pressure Level (SPL)". In (Hegde et al., 2020) different dimensions of a square and circular diaphragm have been analyzed using the COMSOL tool for MEMS applications. It was found that the circular diaphragm has better deflection and least fundamental frequency which makes it suitable for applications that should have maximum deflection resulting in more voltage during resonance. Since the device works on the resonance principle, the fundamental frequency of the sensor structure is one of the significant considerations. The undamped fundamental frequency of the diaphragm is given in equation (4.26).

$$f = \frac{0.469t}{R_o^2 \sqrt{\frac{E}{\rho(1-\nu^2)}}} \quad (4.26)$$

Where the thickness of the diaphragm t is given in m, E -Young's Modulus of the elasticity of the material in Pa , ν -Poisson's proportion, R_o -radius of the diaphragm in m, and ρ -material density in kg per m^3 . For applications that require sensing the exact frequency during resonance, the natural frequency should match with that of source frequency resulting in resonance. To maintain the pressure applied constant, the proposed design has a silicon diaphragm with a cavity at the rear of the structure. In-between two aluminum electrodes piezoelectric layer interposed at an upper surface

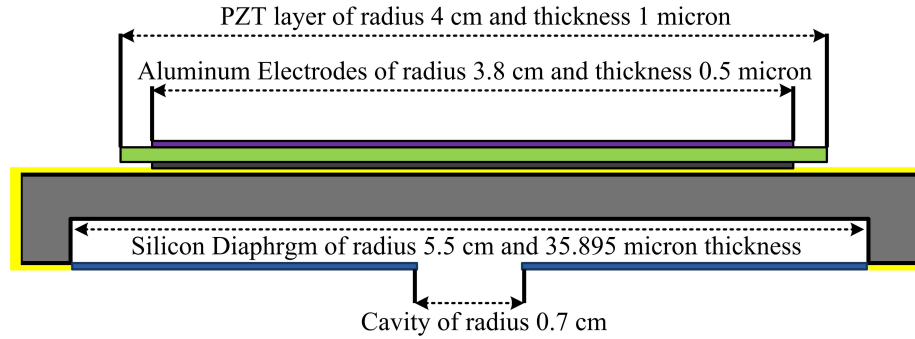


Figure 4.19: Proposed piezoelectric sensor design with requisite dimensions.

of the diaphragm. To form a piezoelectric layer, Lead Zirconate Titanate (PZT) is used, as it has the best piezoelectric features.

The diaphragm is the principal element of the sensor structure, so the design of a diaphragm is the foremost consideration and it has been carried out using the COM-SOL multiphysics platform. The diaphragm is considered to be circular shaped due to the benefits in terms of deflection and natural frequency and formation of silicon. The simulated diaphragm holding a radius of 5.5 cm and thickness of 35.895 microns is having a natural frequency of 49.838 Hz and the diaphragm's natural frequency is close to the system frequency. The dimensions are determined such that the natural frequency is slightly less than 50 Hz considering the structure will have another layer of piezoelectric material which is sandwiched within two electrodes. Taking into account all the above parameters, the final structure to obtain the maximum output voltage at the system frequency is as shown in Figure 4.19.

The variation as a function of space is very less in the acoustic domain so we can model a lumped equivalent circuit model which is analogous in acoustic modeling. Thereby, we can avoid the difficulty in mathematical modeling. Figure 4.20 shows the lumped element model of the acoustic sensor.

It is assumed that the acoustic resistance R_{ad} of the channel is negligible and that the inlet pressure applied P_{in} to the diaphragm is the same as the pressure applied below the diaphragm. Once pressure is applied to the diaphragm, energy will be stored in the M_{ad} and C_{ad} of the diaphragm and converted into the deflection of the diaphragm, and then the electric charge. The transformation ratio $n : 1$ represents the conversation process in terms of transduction. Finally, the C_p will get charged according to the stress and strain of the diaphragm in terms of electric charge. The

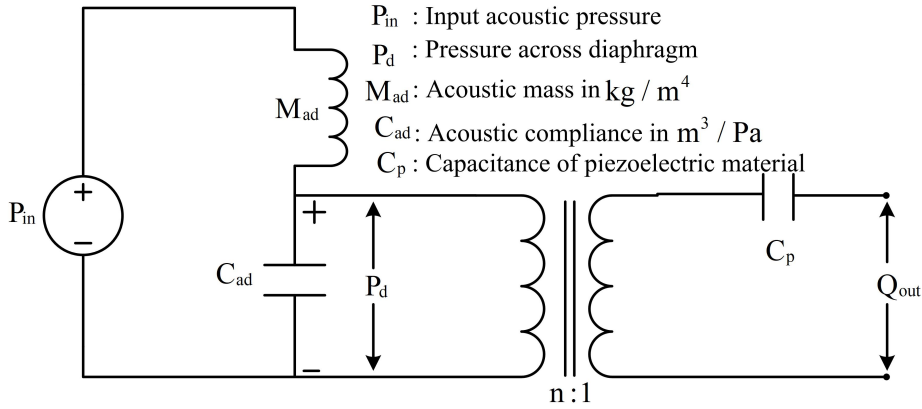


Figure 4.20: Equivalent circuit diagram of the lumped element model of acoustic sensor.

equations (4.27) give the parameter modeling of the lumped element modal of an acoustic sensor

$$M_{ad} = \rho * A * h \quad (4.27)$$

Where, ρ is the density in kg/m^3 and $A * h$ is the area of the circular diaphragm ϕr^2 in m^2 . And to find the Acoustic compliance of the diaphragm the information regarding effective diameter, a moment of inertia, and flexural rigidity of the diaphragm must be known. The values of these mentioned parameters are listed in Table 4.3. With LEM and FEM methods we can calculate the natural frequency of the sensor. The equation (4.28) gives the natural frequency f_0 , at which the acoustic sensor structure resonates.

$$\frac{A}{D} * f_0 = \frac{1}{2\phi * M_{ad} * C_{ad}} \quad (4.28)$$

Where, f_0 is the natural frequency, A is the area of the diaphragm, M_{ad} and C_{ad} are the acoustic mass and compliance respectively. The design of a circular-shaped diaphragm with a 5.5 cm radius and thickness of 35.895 microns with a natural frequency of 49.838 Hz has been carried out using the COMSOL multiphysics platform, shown in Figure 4.19. And the equivalent circuit diagram of the lumped element model of the acoustic sensor is shown in Figure 4.20.

Table 4.3: DG controller and sensor parameters

Parameter	Value	Parameter	Value
V_{DC}	800 V	ω_0	314.2 radians
R_{damp}	0.01	Cavity of radius	0.7 cm
L_f	0.001 H	Aluminium electrodes of radius	308 cm
L_{f1}	0.003 H	Aluminium electrodes of thickness	0.5 microns
C_f	0.5 μ F	k_p	0.02
PZT layer of radius	4 cm	k_1	10
PZT layer of thickness	1 micron	Silicon diaphragm of thickness	35.869 microns
Silicon diaphragm of radius	5.5 cm	-	-

4.7 Islanding detection with piezoelectric acoustic sensor

The output of the piezoelectric sensor is an analog signal i.e., voltage signal, and it is transformed into a digital signal to produce make or break command to the circuit breaker (CB). The signal/command to the CB determines the fault is being sensed and the mode of operation (grid-connected or islanded). The sensor is designed in such a way that it will operate only when the frequency of the system will deviate from the standard IEEE prescribed limit $\pm 1\%$ of the system frequency (49 Hz to 51 Hz). In all other cases, the sensor will produce a high state signal to the breaker to break the contact to isolate the DG from the grid. The piezoelectric sensor is an actual sensing process, it can provide the information from the PLL outer loop to CB input, and is probably designed for a different range of frequencies for distinctive applications. The design of a circular-shaped diaphragm with a 5.5 cm radius and thickness of 35.895 microns with a natural frequency of 49.838 Hz has been carried out using the COMSOL multiphysics platform.

4.8 Simulation and Hardware In Loop Responses

4.8.1 COMSOL Multiphysics Simulation Responses

The sensor structure for islanding detection with respect to the frequency variations is simulated in the COMSOL Multiphysics. The results Figure 4.21 to Figure 4.22 shows the simulated results for our proposed applications. The parameters considered are listed in Table 4.3.

The proposed control scheme is analyzed for under and over frequencies in the grid-integrated mode for islanding detection. The simulated result of the diaphragm in a COMSOL is as shown in Figure 4.21. We can see the deflection of the diaphragm is maximum at the center since the diaphragm is hinged at the center is as shown in Figure 4.22.

Figure 4.23 and Figure 4.24 shows the deflection of the diaphragm for four different modal frequencies is modeled and we can see that the maximum deflection will occur at the center of all the four sections of the diaphragm for frequencies (49.838 Hz, 106.8 Hz, 184.62 Hz, and 202.15 Hz). The structure of the diaphragm will be the same with different dimensions for different modal frequencies. Thereby for a specific application to make or break the contact automatically, we can design the sensors

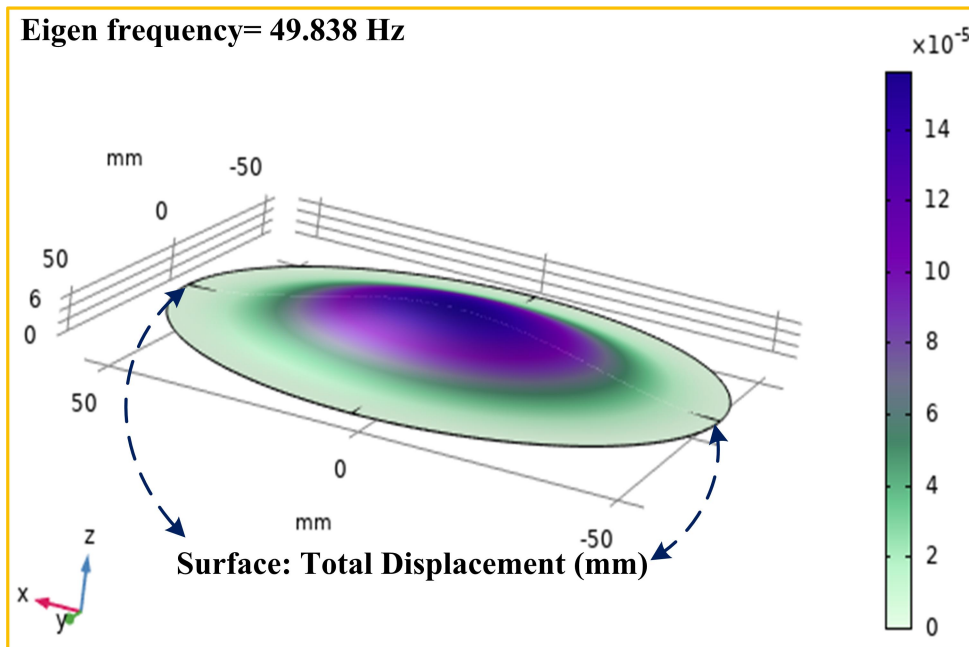


Figure 4.21: Diaphragm simulation of proposed piezoelectric sensor in COMSOL platform.

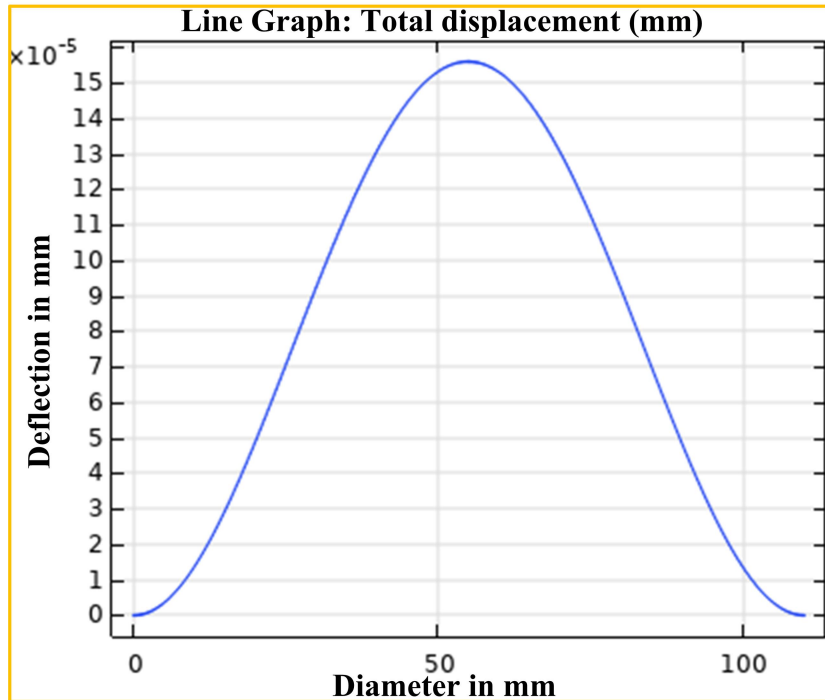


Figure 4.22: Piezoelectric acoustic sensor's diaphragm deflection at natural frequency.

accordingly.

The stress analysis of the diaphragm is as shown in Figure 4.25. It is clear from the figure that the stress endured by the diaphragm is tensile at the periphery due to the hinge and compressive at the center. As the magnitude of the stress changes the value of the voltage changes (voltage generated by the piezoelectric layer). To ensure the unidirectional voltage the deposition of the piezoelectric layer is prepared of these centers covering about 70% of the area of the diaphragm. The aforementioned has resulted in the final structure as shown in Figure 4.19 with a PZT layer of radius 3.8 cm.

Figure 4.26 shows the strain analysis of the diaphragm. The magnitude of the strain experienced by the diaphragm changes in magnitude and direction and it can be seen that the strain is maximum at its center. Therefore to ensure the average voltage across the piezoelectric layer is maximum, the piezoelectric layer has been coated from the center as shown in the proposed sensor design.

The sensor displacement should be maximum at 50 Hz to have a greater selectivity ($\pm, 1\%$). Henceforth it is clear that the sensor will be able to discriminate among the healthy system frequencies ($49 \text{ Hz} < f < 51 \text{ Hz}$) during the grid-connected mode of

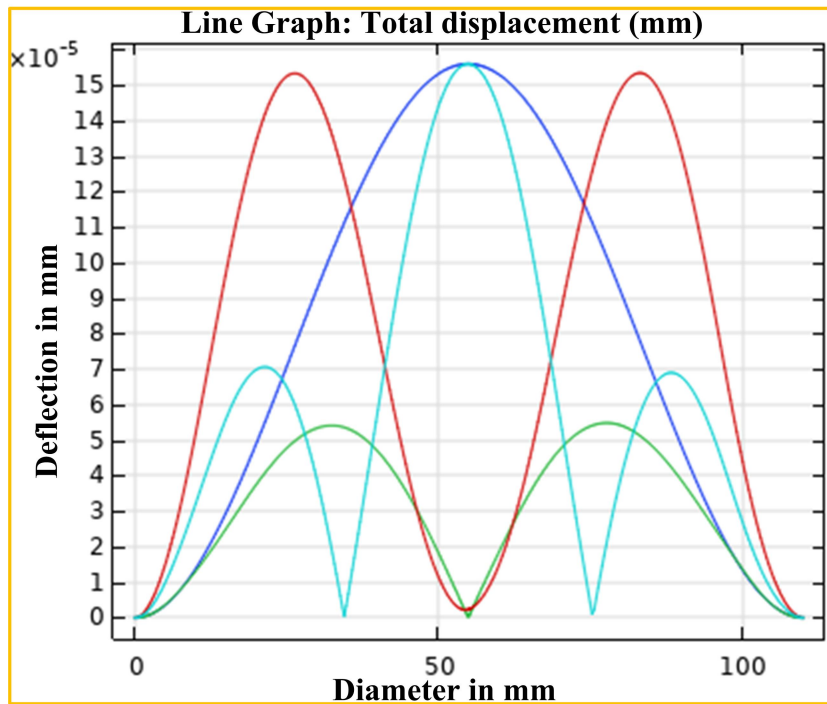


Figure 4.23: Piezoelectric acoustic sensor’s diaphragm deflection at four different modal frequencies.

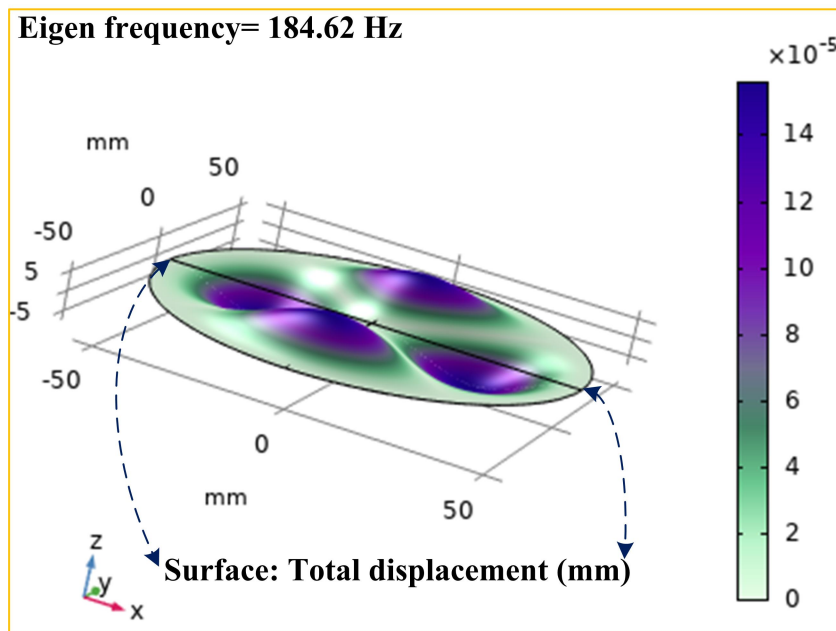


Figure 4.24: Piezoelectric acoustic sensor’s diaphragm simulation at fourth modal frequency.

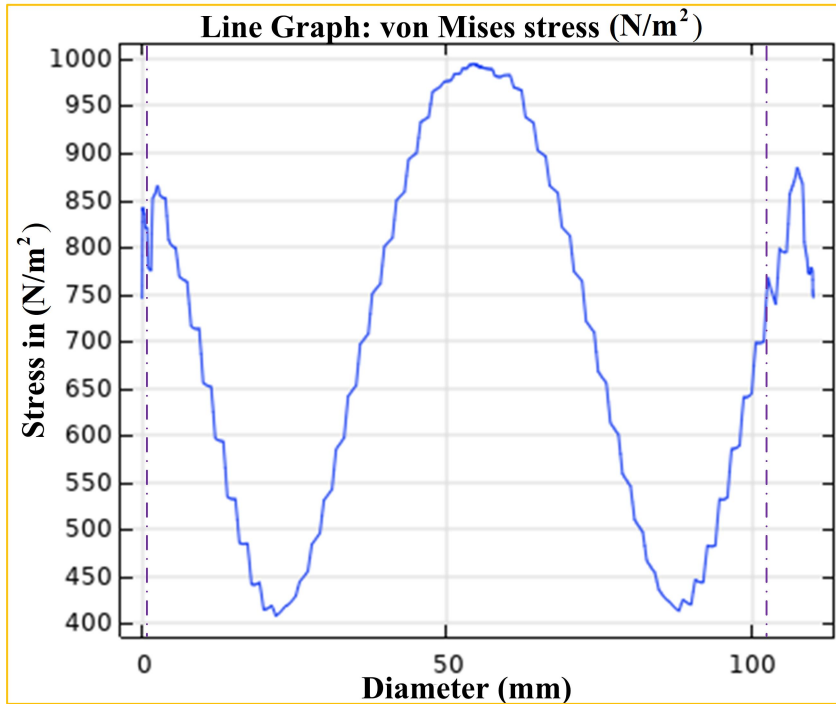


Figure 4.25: Strain analysis of piezoelectric acoustic sensor diaphragm.

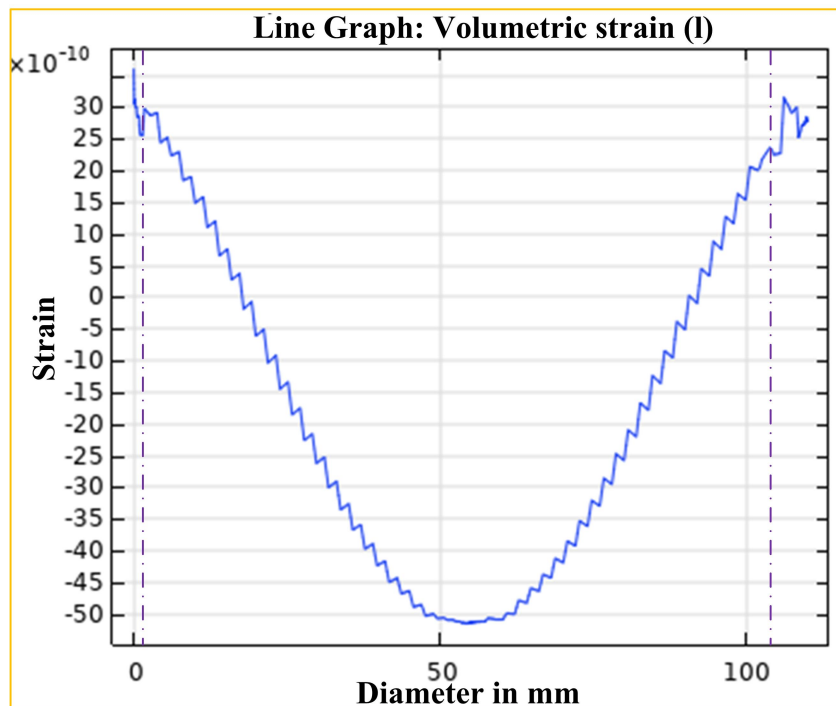


Figure 4.26: Strain analysis of piezoelectric acoustic sensor diaphragm.

Table 4.4: DG controller and sensor parameters

For system frequency (f) upper limit 51 Hz	For system frequency (f) lower limit 48 Hz	Circuit Breaker control signal (o/p: 0 or 1)
1 (f > 51 Hz)	1 (f < 48 Hz)	1 (break contact)
1 (f > 50 Hz)	1 (f = 50 Hz)	1 (make contact)
1 (f > 51 Hz)	1 (f = 50 Hz)	1 (break contact)
1 (f > 50 Hz)	1 (f < 48 Hz)	1 (break contact)

operation. The Sensor output control signal and a circuit breaker switching signal are listed in Table 4.4.

4.8.2 Hardware In the Loop-Virtual Responses

The equivalent lumped network model for the piezoelectric acoustic sensor with the grid-connected DG model is shown in Figure 4.20 and is verified using the hardware in the loop platform. The virtual hardware in loop responses of modeled acoustic piezoelectric sensors for different power quality test cases is discussed below.

The Figure 4.27 depicts the applied input pressure P_{in} in N/m^2 , the pressure across the sensor diaphragm P_d in N/m^2 , the sensor frequency variations in Hz and the sensor output phase angle θ in radians. During the grid's healthy condition (no disturbances/noises) the P_{in} and the P_d will remain constant throughout the operation, due to this the sensor will not receive any signal in terms of circuitual vibration and the frequency will remain constant. In this condition, the control command from the sensor to the circuit breaker remains at a low position (0) and DGs are continued in the grid-integrated operation mode only. We can inspect that the system frequency is in the healthy state thereby the sensor will not sense any kind of maliciousness and the output signal of the sensor will remain in a low state (0) and the circuit breaker switching control command is also in the low state. The frequency ranges from min 49 Hz to max 51 Hz range is considered as a healthy system frequency and the diaphragm of the sensor will be modeled accordingly. And also we can note from Figure 4.27 is that the sensor will not react for the transient at the beginning and these variations are well within the prescribed limits.

In Figure 4.28 the grid voltage sag is created at 0.2 s to 0.3 s and the responses for three-phase grid voltage sag, pressure across the sensor diaphragm, and the sensor

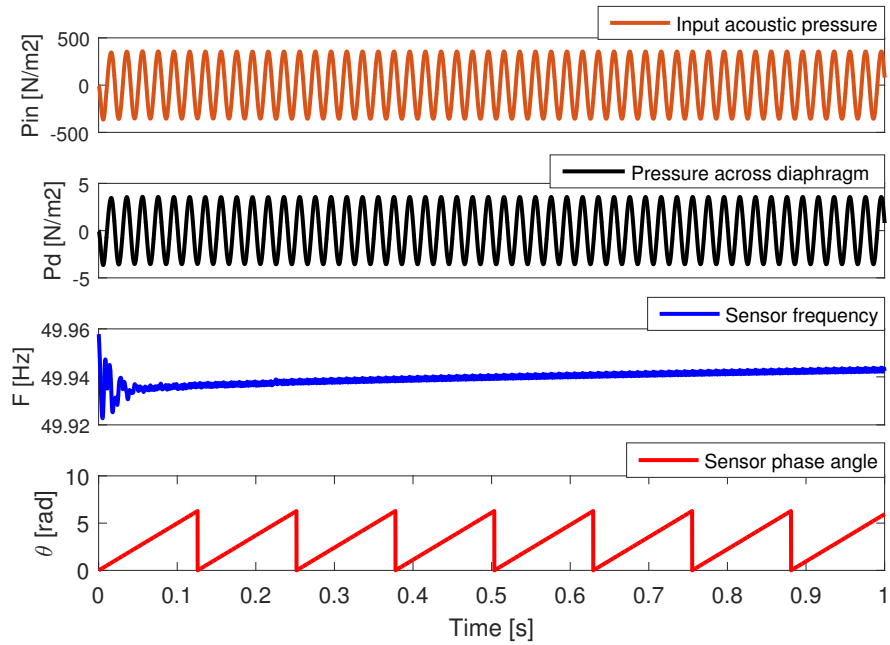


Figure 4.27: Pressure and frequency responses of piezoelectric acoustic sensor under grid healthy condition.

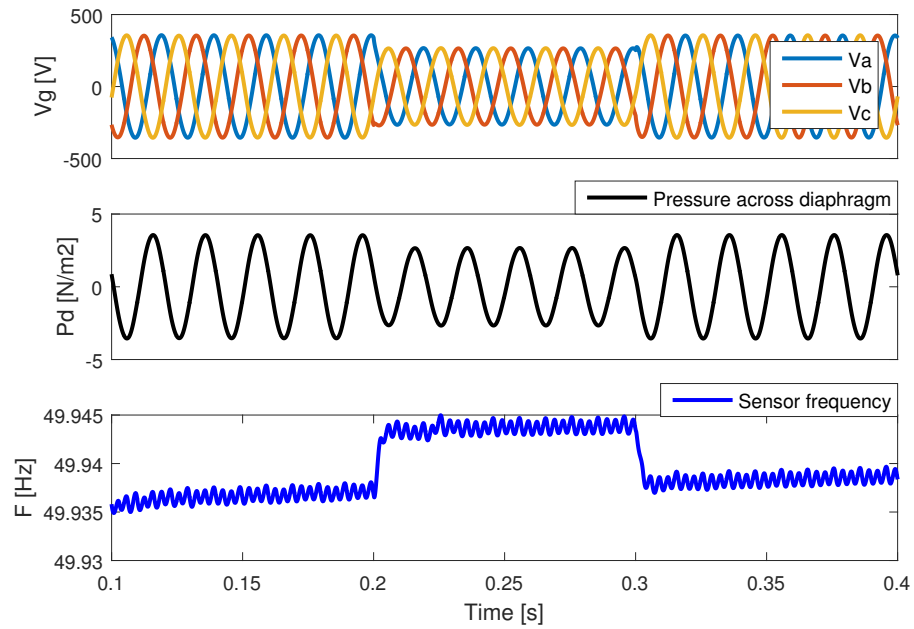


Figure 4.28: Pressure and frequency responses of piezoelectric acoustic sensor under grid voltage Sag condition.

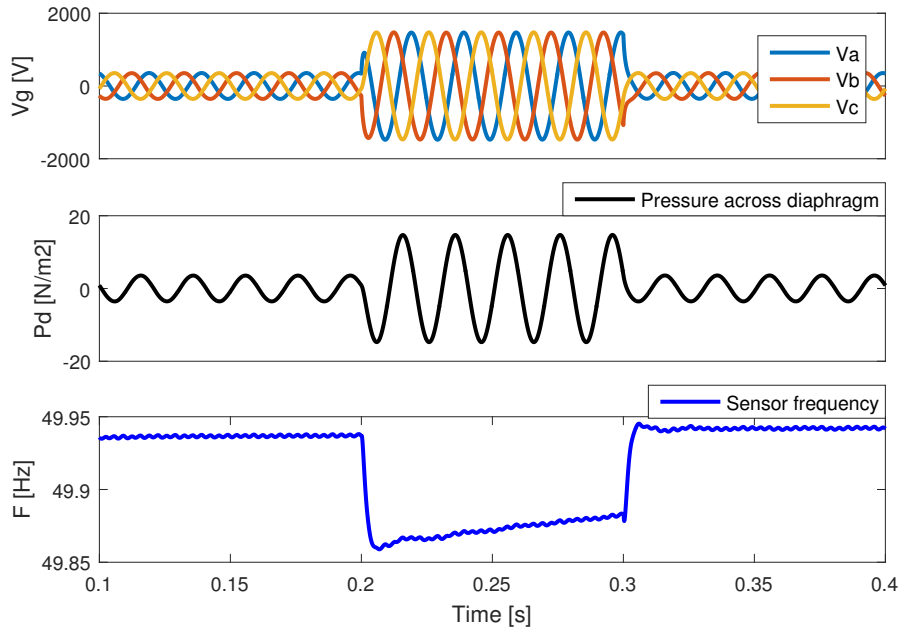


Figure 4.29: Pressure and frequency responses of piezoelectric acoustic sensor under grid voltage Swell condition.

frequency are shown. The variations during the test case can be seen and the sensor frequency will change accordingly. Due to the small change in the frequency during the grid voltage Sag condition, the sensor will not issue a control command to the CB. If the grid working environment is severe to the sag condition, then these sensors can make a big difference in disconnecting the grid for a little variation in the frequency. If not the responses depict that the frequency variations are well within the IEEE 1547 standard limits.

The Figure 4.29 shows the responses for grid voltage swell condition. In all the figures from Figure 4.27 to Figure 4.31 the responses of the pressure across the sensor diaphragm and frequency of the sensor will change in accordance with the nature of the grid voltages. If the pressure changes across the sensor then automatically the sensor will react and so the frequency.

The mode of operation of the DGs whether in the grid-integrated mode or in the islanded mode will be decided by the sensor output control command (either 0 or 1) and circuit breaker switching control command (either 0 or 1). If the system frequency is in-between 49 Hz to 51 Hz the sensor outputs a ‘0’ control command to CB. So that the DGs will remain in the grid-integrated mode only. If the frequency

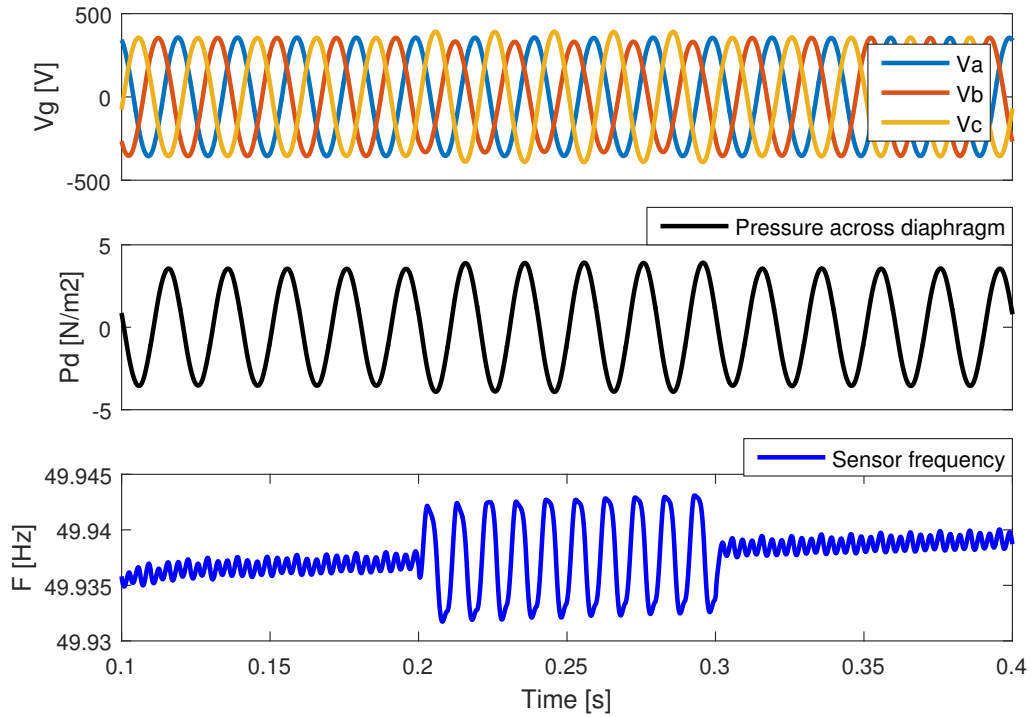


Figure 4.30: Pressure and frequency responses of piezoelectric acoustic sensor under grid voltage Unbalance condition.

had become less than 49 Hz, and greater than 51 Hz then the sensor issues a control command ‘1’ to CB to disconnect the grid from the DGs. Initially, the circuit breaker linking the DG and the grid is in the closed position so that the command signal to the circuit breaker will not be activated by the low state command signal received by the sensor.

In Figure 4.32 the frequency disturbance is injected at 0.3 s to 0.4 s and during this period the disturbance will affect the system frequency (frequency dwindles to 48 Hz). This frequency is less than our prescribed standard limits (49 Hz to 51 Hz). Once the frequency reaches below 49 Hz, the sensor will activate and sense the under-frequency signal and gives the command to the circuit breaker as high state (1) to break the contact and isolate the DG from the grid. At 0.4 s once the disturbance will end and then the sensor will issue a command signal as low state (0) to a circuit breaker to make contact to integrate DG to the grid. In Figure 4.33 the frequency disturbance is injected at 0.3 s to 0.4 s and during this period the disturbance will affect the system frequency (frequency rises to 52 Hz). This frequency is higher than our prescribed

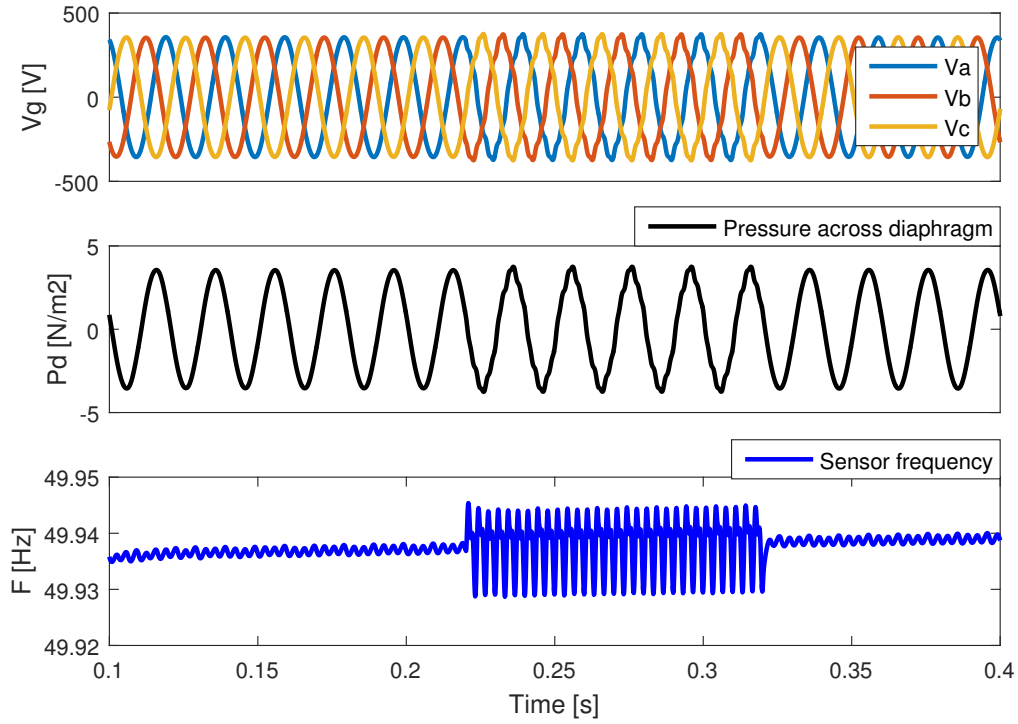


Figure 4.31: Pressure and frequency responses of piezoelectric acoustic sensor under grid voltage Harmonics condition.

standard limits (49 Hz to 51 Hz). Once the frequency reaches above 51 Hz, the sensor will activate and sense the over-frequency signal and gives the command to the circuit breaker as high state (1) to break the contact and isolate the DG from the grid. At 0.4 s once the disturbance will end and then the sensor will issue a command signal as low state (0) to a circuit breaker to make contact to integrate DG to the grid.

Figure 4.35 shows the responses of the active power and the reactive power in kW and in kVAr respectively. The grid frequency disturbance is inserted at 0.3 s and removed at 0.4 s. The frequency variation and the control command signals for this test case are shown in Figure 4.32. We can see the responses during the grid voltage sag condition, the dip in both the active and reactive powers can be seen. The variations in the power-sharing with respect to the load power in the grid-integrated mode in proportion to the DGs power can be noted.

Figure 4.34 shows the comparison of the non-detection zone (NDZ) of the frequency-based islanding detection techniques with the proposed islanding detection. As we can see, the proposed technique will fall under both the regions (region 1 as well

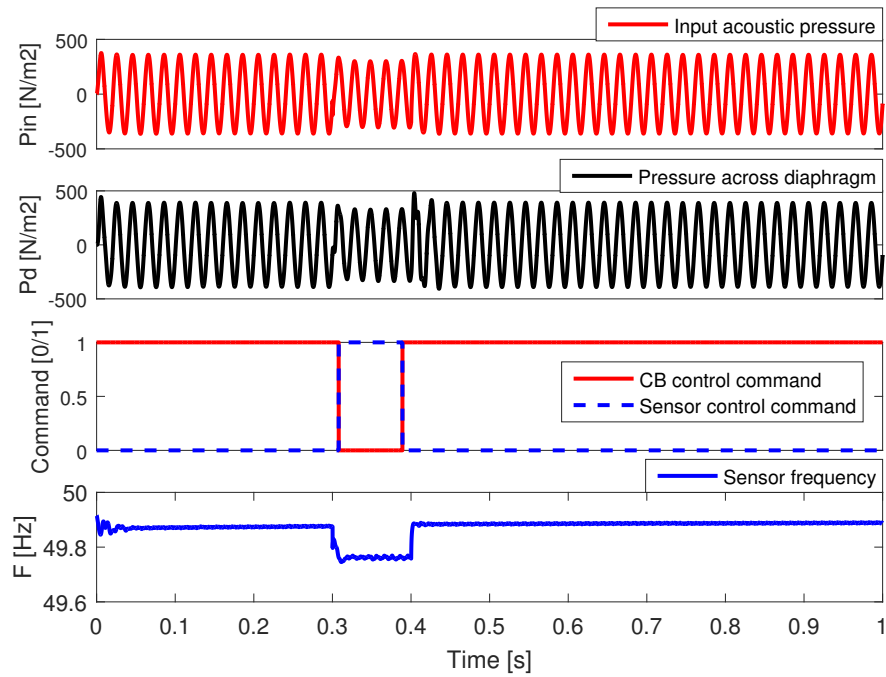


Figure 4.32: Pressure and frequency responses with control commands of piezoelectric acoustic sensor for islanding detection for frequency <49 Hz.

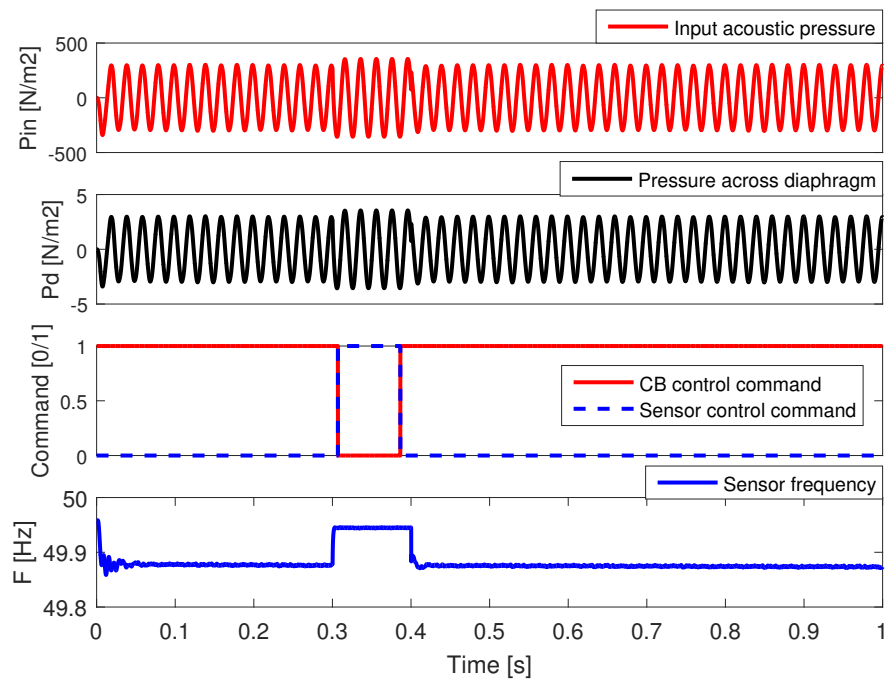


Figure 4.33: Pressure and frequency responses with control commands of piezoelectric acoustic sensor for islanding detection for frequency >51 Hz.

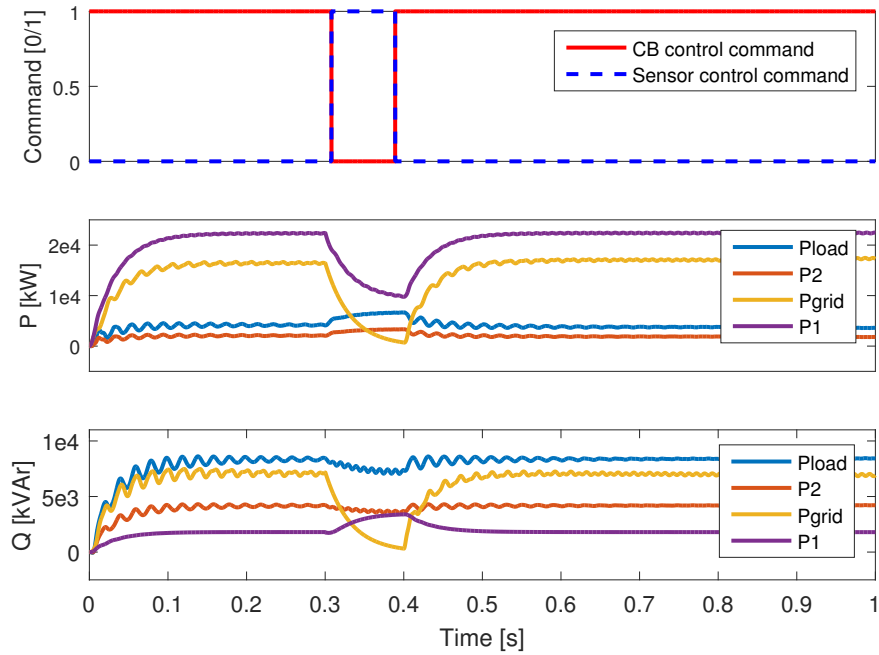


Figure 4.34: Active power in kW and reactive power in kVAR responses with control commands of piezoelectric acoustic sensor during grid voltage sag condition.

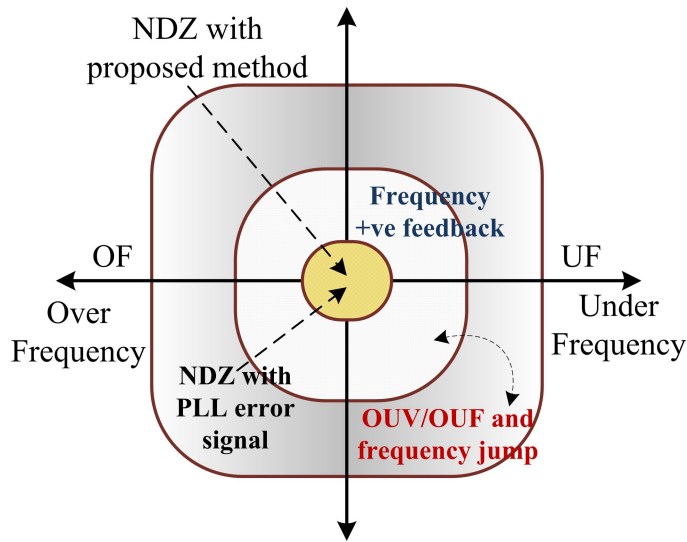


Figure 4.35: NDZ comparison of proposed method with the other active and passive based islanding detection methods.

as region 2). Region 1 for the proposed technique is for power quality test cases like grid voltage sag, swell, unbalance, and harmonics and region 2 is for frequency disturbance injection test cases as shown in Figure 4.32 and in Figure 4.33. The piezoelectric acoustic sensor-based islanding detection will show negligible NDZ and shows moderate or small NDZ for frequency disturbances more than 51 Hz and less than 49 Hz.

4.8.3 Hardware In the Loop-Real-time Responses

In Figure 4.36 the hardware in loop real-time responses for point of common coupling (PCC) frequency, sensor frequency, and the grid frequency variation condition are depicted. The change in the frequencies at 0.3 s and at 0.4 s can be seen during the sag. The PCC frequency must follow the sensor frequency in the grid-integrated mode and we can see that the variations in both the PCC frequency follow the sensor frequency.

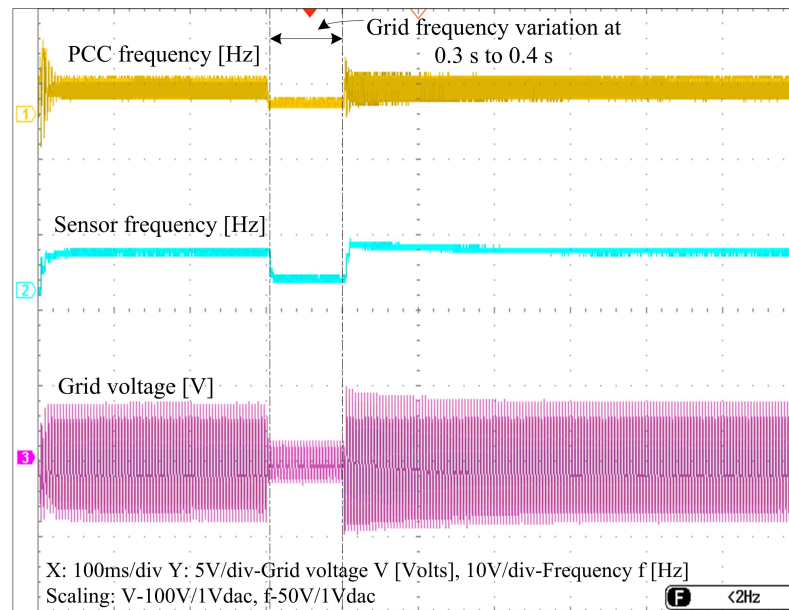


Figure 4.36: HIL real-time responses of PCC frequency in Hz, Sensor frequency in Hz and grid voltage in Volts during the grid frequency variation.

Figure 4.37 and Figure 4.38 show the hardware in loop real-time responses of the active power and the reactive power in kW and in kVAR respectively. We can co-relate the Figure 4.35 with Figure 4.37 and Figure 4.38 for the power-sharing

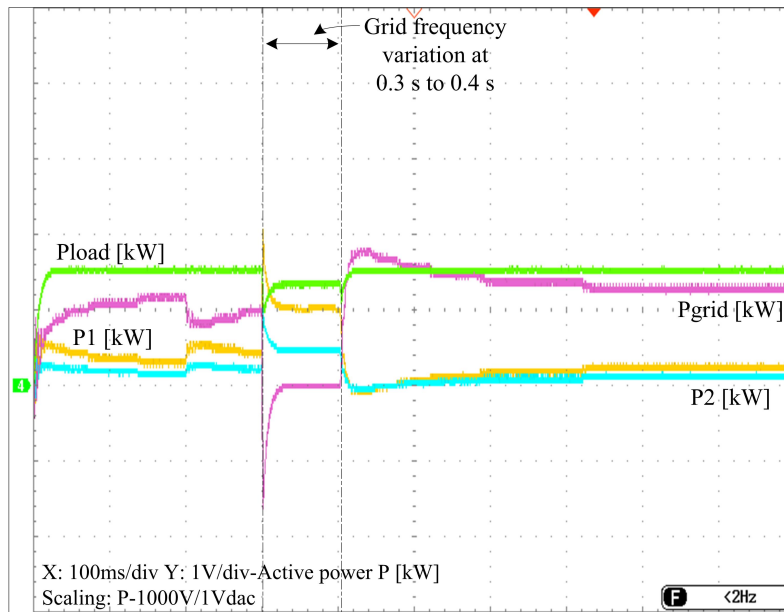


Figure 4.37: HIL real-time responses of active powers of the load, grid, DG1 and DG2 in kW during the grid frequency variation.

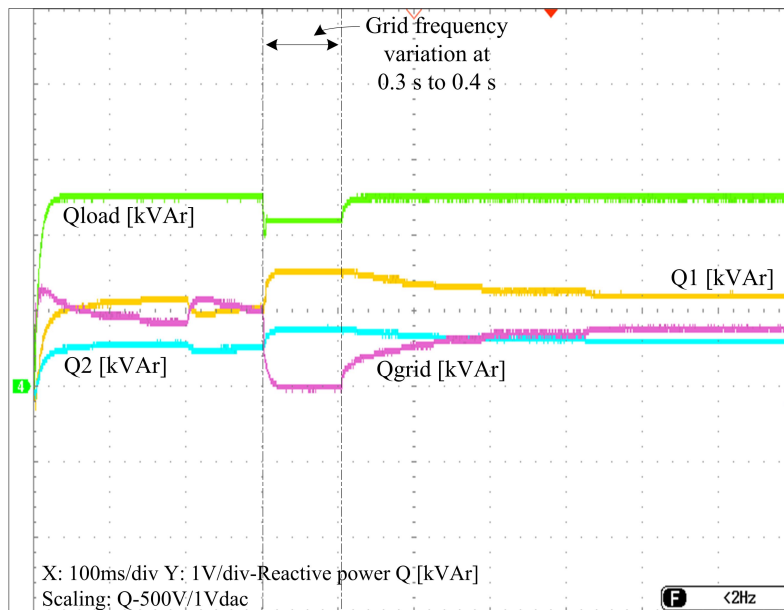


Figure 4.38: HIL real-time responses of reactive powers of the load, grid, DG1 and DG2 in kVAr during the grid frequency variation.

responses in both the virtual platform and in the real-time platform. Though there is a frequency disturbance condition the power will be shared according to the power ratings (proportional power-sharing).

4.9 Summary

The real-time hardware in loop (HIL) tool has been used to verify the islanding detection based on PSRF-PLL and a piezoelectric acoustic sensor. In the presence of grid disturbances, the proposed PSRF-PLL demonstrates good islanding detection and mode switching. The results are presented and examined for a variety of test situations. As compared to previous PLL designs, the suggested PSRF-PLL controller provided good harmonic immunity and achieved approximately 0% phases locking error. The experimental responses for a three-phase fault were presented, and it was discovered that the PSRF-PLL could detect islanding in less than 10 milliseconds. The outcomes of the HIL tool reveal that the proposed control strategies for grid-connected and islanded operation modes for parallel-connected inverter-based DGs in the microgrid performed well. These control approaches can be extended to the microgrid's multiple distributed generation systems. And the circular diaphragm-based piezoelectric sensor has been modeled and tested under various grid disturbances. Thereby, the frequency responses of the modeled sensor are analyzed. The plots of shape and size of the diaphragm, natural frequency, strain, and stress for positioning the piezoelectric layer are detailed. The responses of the piezoelectric acoustic sensor show that the circular diaphragm-based sensor can successfully sense the frequency for selected ranges (49 Hz to 51 Hz). This shows the selectivity and sensitivity of the sensors for special purpose applications. The designed method performs well for the detection of grid disturbances line voltage sag, swell, unbalance, harmonics, and frequency variations. In virtual and real-time HIL, the modeled sensor with a phase-locked loop in the grid-connected operation mode of operation for islanding detection during grid disturbances is examined and verified. The results reveal that the proposed piezoelectric acoustic sensor can detect islanding effectively and efficiently.

Chapter 5

CONCLUSIONS AND SCOPE FOR FUTURE WORK

5.1 Conclusions

An improved droop control technique is given for accurate and proportionate power-sharing between parallel-connected PE-based DGs without circulating currents. Both resistive and inductive output line impedances were taken into account when developing the proposed droop control. As a result, the suggested droop control can be used successfully in both LV and HV networks.

Park synchronous reference frame PLL (PSRF-PLL)-based islanding detection and Piezoelectric Acoustic Sensor-based islanding detection are two innovative approaches for detecting islanding conditions. PSRF-PLL provided good harmonic immunity and had a phase-locking error of approximately 0%. And identify islanding effectively during grid disruptions within 10ms, which is regarded as a relatively short detection period when compared to other approaches. We can even achieve automatic mode switching (grid-connected and islanded) with PSRF-PLL. During grid disturbances, the proposed piezoelectric acoustic sensor with PLL will demonstrate the efficacy of islanding detection.

The contributions in this thesis' concluding remarks are listed below.

Chapter 1 presents the background of the thesis, In both islanded and grid-connected modes of operation, a basic overview of microgrid control and classification is presented. The main principle for the droop control approach in an islanded mode

for parallel-connected PE-based DG systems is described. An overview of islanding detection methods is provided, as well as their significance. The most recent research on droop control strategies and islanding detection techniques are addressed.

Chapter 2 presents the islanded mode of operation of the microgrid, In the islanded mode of operation, modeling and control of parallel-connected power electronics-based distributed generating sources are provided. With the improved droop control technique, effective and proportionate power-sharing across PE-based DGs in an islanded microgrid can be realized. Along with the Eigenvalue spectrum analysis, the mathematical modeling of the improved droop control technique was presented, as well as the small-signal state-space analysis.

In chapter 3, The assessment of three-phase phase-locked loop (PLL) controllers in the grid-connected mode of operation for synchronization is presented. The responses of the PLLs in healthy and unhealthy grid environments were examined and recorded. And, considering their behavior in all of the evaluative situations, conclusions were drawn for the selection of PLL. Then, in both islanded and grid-connected modes of operation, PLL-based islanding detection and automatic mode switching for droop-based microgrids are demonstrated.

In chapter 4, improved islanding detection and an effective automatic mode switching are shown. The usage of a modified Park synchronous reference frame-based phase-locked loop (PSRF-PLL) for islanding detection and automatic mode switching is demonstrated in the grid-connected mode of operation. Through mode switching, the responses in both the grid-connected and islanded modes are provided. The phase error and phase angle responses of the proposed PLL are compared to those of other popular PLLs. During a grid disruption, the proposed PSRF-PLL will detect islanding within 10ms and switch the operating mode to islanded mode automatically. And also an islanding detection method employing piezoelectric acoustic sensors design and development for the specified application was shown with suitable responses. The modeled piezoelectric circular diaphragm tests were performed under various grid disturbances and responses were observed. The sensor-based technique suggested here can properly and efficiently detect islands during grid disturbances.

5.2 Scope for future work

The following recommendations for further research are given based on the research work carried out in this thesis.

1. The employment of artificial intelligence approaches, combined with the suggested improved droop control, may help parallel-connected PE-based DGs operate marginally better.
2. Enhanced droop controller based on intelligent approaches for voltage, frequency, and power stabilities can be used to construct an AC and DC hybrid microgrid with parallel operation of the DC and AC distributed generation sources.
3. In phase-locked loop controllers, islanding detection with machine learning and other intelligent techniques can improve detection visibility and effectiveness.
4. The grid's performance can be improved by using a programming language that uses islanding detection to discover errors. These approaches can be used to detect the islanding, and after the islanding is noticed, the information can be stored in the clouds to construct the data sets for reference in the future.
5. Based on the applications, the fabrication, and packing of the proposed piezoelectric acoustic sensor for islanding detection can be modeled using different modes of frequencies.

PUBLICATIONS

Papers in refereed journals

1. Kulkarni, S. V., Gaonkar, D. N., and Guerrero, J. M. (2021). Operation of the Microgrid with Improved Droop Control Strategy and an Effective Islanding Detection Technique for Automatic Mode Switching. *Electric Power Components and Systems*, 1-15, DOI: 10.1080/15325008.2021.1970289.
2. Kulkarni, S. V., and Gaonkar, D. N. (2021). Improved droop control strategy for parallel connected power electronic converter based distributed generation sources in an Islanded Microgrid. *Electric Power Systems Research*, 201, 107531, DOI: 10.1016/j.epsr.2021.107531.
3. Kulkarni, S. V., and Gaonkar, D. N. (2022). HIL implementation of an islanding detection and an automatic mode switching for droop-based microgrid. *International Journal of Power Electronics*, 15(1), 37-54.
4. Kulkarni, S. V., Hegde, V., and Gaonkar, D. N. (2021). A Novel Islanding Detection Technique Based on Piezoelectric Sensors for Grid-Integrated DG Systems. *IETE Journal of Research*, 1-16.
5. Shreeram V Kulkarni., and Dattatraya N Gaonkar. Phase-Locked Loops for Distributed Generation Sources in the Grid-Connected Mode of Operation: An Investigation on PLL Synchronization Techniques, *Submitted to Electric Power Systems Research*, EPSR-D-22-00121, (Under Review).

Book Chapter

1. Kulkarni, S. V., Gatade, S., Samanvita, N., and Gaonkar, D. N. (2022). Comprehensive Strategy for Power Quality Improvement of Inverter Based Distributed Generation Systems. In *Emerging Research in Computing, Information, Communication and Applications* (pp. 185-195). Springer, Singapore.

Papers published in refereed conference proceedings

1. Kulkarni, S. V., and Gaonkar, D. N. (2020, December). Investigation of PLLs for Distributed Generation Systems in the Grid-connected Mode of Operation. In 2020 International Conference on Power, Instrumentation, Control and Computing (PICC) (pp. 1-6). IEEE, DOI: 10.1109/PICC51425.2020.9362490.
2. Kulkarni, S. V., and Gaonkar, D. N. (2017, December). Operation and control of a microgrid in isolated mode with multiple distributed generation systems. In 2017 International Conference on Technological Advancements in Power and Energy (TAP Energy) (pp. 1-6). IEEE, DOI: 10.1109/TAPENERGY.2017.8397210.
3. Kulkarni, S. V., and Gaonkar, D. N. (2017, November). Performance study of microgrid with multiple distributed generation systems, *IEEE Workshop on Electronics Power Transmission And Distribution (eT&D-2017), 7-9th November 2017, Aalborg , Denmark.*

Bibliography

- Abdelaziz, M. M. A., Shaaban, M. F., Farag, H. E., and El-Saadany, E. F. (2014). A multistage centralized control scheme for islanded microgrids with pevs. *IEEE Transactions on Sustainable Energy*, 5(3):927–937.
- Ackermann, T., Andersson, G., and Söder, L. (2001). Distributed generation: a definition1. *Electric power systems research*, 57(3):195–204.
- Ahmad, K. N. E. K., Selvaraj, J., and Abd Rahim, N. (2013). A review of the islanding detection methods in grid-connected pv inverters. *Renewable and Sustainable Energy Reviews*, 21:756–766.
- Arunan, A., Ravishankar, J., and Ambikairajah, E. (2017). Real time stability enhancement for islanded microgrids. In *2017 IEEE Innovative Smart Grid Technologies-Asia (ISGT-Asia)*, pages 1–5. IEEE.
- Basso, T. (2014). Ieee 1547 and 2030 standards for distributed energy resources interconnection and interoperability with the electricity grid. Technical report, National Renewable Energy Lab.(NREL), Golden, CO (United States).
- Basso, T., Chakraborty, S., Hoke, A., and Coddington, M. (2015). Ieee 1547 standards advancing grid modernization. In *2015 IEEE 42nd Photovoltaic Specialist Conference (PVSC)*, pages 1–5. IEEE.
- Bifaretti, S. (2013). Anti-islanding detector based on a robust pll. In *Energy Conversion Congress and Exposition (ECCE), 2013 IEEE*, pages 2934–2940. IEEE.
- Borup, U., Blaabjerg, F., and Enjeti, P. N. (2001). Sharing of nonlinear load in parallel-connected three-phase converters. *IEEE Transactions on Industry Applications*, 37(6):1817–1823.
- Bower, W. and Ropp, M. (2002). Evaluation of islanding detection methods for utility-interactive inverters in photovoltaic systems. *Sandia report SAND*, 3591:2002.

- Bush, S. F. (2014). *Smart grid: Communication-enabled intelligence for the electric power grid*. John wiley & sons.
- Caldognetto, T. and Tenti, P. (2014). Microgrids operation based on master–slave cooperative control. *IEEE Journal of Emerging and Selected Topics in Power Electronics*, 2(4):1081–1088.
- Carreras, B. A., Newman, D. E., Dobson, I., and Poole, A. B. (2004). Evidence for self-organized criticality in a time series of electric power system blackouts. *IEEE Transactions on Circuits and Systems I: Regular Papers*, 51(9):1733–1740.
- Chandorkar, M. C., Divan, D. M., and Adapa, R. (1993). Control of parallel connected inverters in standalone ac supply systems. *IEEE Transactions on Industry Applications*, 29(1):136–143.
- Chang, W.-Y. (2010). A hybrid islanding detection method for distributed synchronous generators. In *The 2010 International Power Electronics Conference-ECCE ASIA-*, pages 1326–1330. IEEE.
- Ciobotaru, M., Agelidis, V. G., Teodorescu, R., and Blaabjerg, F. (2010). Accurate and less-disturbing active antiislanding method based on pll for grid-connected converters. *IEEE Transactions on Power Electronics*, 25(6):1576–1584.
- Code, G. (2006). High and extra high voltage.
- Collins, I. (2018). Phase-locked loop (pll) fundamentals. *SSB*, 130(140):150.
- D’Arco, S. and Suul, J. A. (2014). Equivalence of virtual synchronous machines and frequency-droops for converter-based microgrids. *IEEE Transactions on Smart Grid*, 5(1):394–395.
- De Brabandere, K., Bolsens, B., Van den Keybus, J., Woyte, A., Driesen, J., and Belmans, R. (2007). A voltage and frequency droop control method for parallel inverters. *IEEE Transactions on power electronics*, 22(4):1107–1115.
- De Mango, F., Liserre, M., Dell’Aquila, A., and Pigazo, A. (2006). Overview of anti-islanding algorithms for pv systems. part i: Passive methods. In *2006 12th International Power Electronics and Motion Control Conference*, pages 1878–1883. IEEE.
- Diaz, G., Gonzalez-Moran, C., Gomez-Aleixandre, J., and Diez, A. (2010). Scheduling of droop coefficients for frequency and voltage regulation in isolated microgrids. *IEEE Transactions on Power Systems*, 25(1):489–496.

- Dong, D., Wen, B., Mattavelli, P., Boroyevich, D., and Xue, Y. (2014). Modeling and design of islanding detection using phase-locked loops in three-phase grid-interface power converters. *IEEE Journal of Emerging and Selected Topics in Power Electronics*, 2(4):1032–1040.
- Dragicevic, T., Wu, D., Shafiee, Q., and Meng, L. (2017). Distributed and decentralized control architectures for converter-interfaced microgrids. *Chinese Journal of Electrical Engineering*, 3(2):41–52.
- Durani, F., Mainuddin, Mittal, U., Kumar, J., and Nimal, A. (2020). Use of surface acoustic wave (saw) for thermal conductivity sensing of gases—a review. *IETE Technical Review*, pages 1–11.
- Eid, B. M., Rahim, N. A., Selvaraj, J., and El Khateb, A. H. (2016). Control methods and objectives for electronically coupled distributed energy resources in microgrids: A review. *IEEE Systems Journal*, 10(2):446–458.
- Freitas, W., Xu, W., Affonso, C. M., and Huang, Z. (2005). Comparative analysis between rocof and vector surge relays for distributed generation applications. *IEEE Transactions on power delivery*, 20(2):1315–1324.
- Gaonkar, D. (2010). Investigation on electromagnetic transients of distributed generation systems in the microgrid. *Electric Power Components and Systems*, 38(13):1486–1497.
- Golestan, S., Guerrero, J. M., Musavi, F., and Vasquez, J. C. (2019). Single-phase frequency-locked loops: A comprehensive review. *IEEE Transactions on Power Electronics*, 34(12):11791–11812.
- Guerrero, J. M., Chandorkar, M., Lee, T.-L., and Loh, P. C. (2013). Advanced control architectures for intelligent microgrids-part i: Decentralized and hierarchical control. *IEEE Transactions on Industrial Electronics*, 60(4):1254–1262.
- Guerrero, J. M., De Vicuna, L. G., Matas, J., Castilla, M., and Miret, J. (2004). A wireless controller to enhance dynamic performance of parallel inverters in distributed generation systems. *IEEE Transactions on power electronics*, 19(5):1205–1213.
- Guerrero, J. M., De Vicuna, L. G., Matas, J., Castilla, M., and Miret, J. (2005). Output impedance design of parallel-connected ups inverters with wireless load-sharing control. *IEEE Transactions on industrial electronics*, 52(4):1126–1135.
- Guerrero, J. M., Hang, L., and Uceda, J. (2008). Control of distributed uninterruptible power supply systems. *IEEE Transactions on Industrial Electronics*, 55(8):2845–2859.

- Guerrero, J. M., Matas, J., de Vicuna, L. G., Castilla, M., and Miret, J. (2007). Decentralized control for parallel operation of distributed generation inverters using resistive output impedance. *IEEE Transactions on industrial electronics*, 54(2):994–1004.
- Guerrero, J. M., Vasquez, J. C., Matas, J., De Vicuña, L. G., and Castilla, M. (2011). Hierarchical control of droop-controlled ac and dc microgrids—a general approach toward standardization. *IEEE Transactions on industrial electronics*, 58(1):158–172.
- Guo, X.-Q., Wu, W.-Y., and Gu, H.-R. (2011). Phase locked loop and synchronization methods for grid-interfaced converters: a review. *Przeglad Elektrotechniczny*, 87(4):182–187.
- Han, H., Hou, X., Yang, J., Wu, J., Su, M., and Guerrero, J. M. (2016). Review of power sharing control strategies for islanding operation of ac microgrids. *IEEE Transactions on Smart Grid*, 7(1):200–215.
- Han, H., Liu, Y., Sun, Y., Su, M., and Guerrero, J. M. (2015). An improved droop control strategy for reactive power sharing in islanded microgrid. *IEEE Transactions on Power Electronics*, 30(6):3133–3141.
- Hanaoka, H., Nagai, M., and Yanagisawa, M. (2003). Development of a novel parallel redundant ups. In *Telecommunications Energy Conference, 2003. INTELEC'03. The 25th International*, pages 493–498. IEEE.
- He, J. and Li, Y. W. (2011). An accurate reactive power sharing control strategy for dg units in a microgrid. In *Power Electronics and ECCE Asia (ICPE & ECCE), 2011 IEEE 8th International Conference on*, pages 551–556. IEEE.
- He, J. and Li, Y. W. (2012). An enhanced microgrid load demand sharing strategy. *IEEE Transactions on Power Electronics*, 27(9):3984–3995.
- He, J., Li, Y. W., Guerrero, J. M., Blaabjerg, F., and Vasquez, J. C. (2013). An islanding microgrid power sharing approach using enhanced virtual impedance control scheme. *IEEE Trans. Power Electron*, 28(11):5272–5282.
- Hegde, V., Yellampalli, S. S., and Ravikumar, H. (2020). Simulation, mathematical modeling, fabrication and experimental analysis of piezoelectric acoustic sensor for energy harvesting applications. *Microsystem Technologies*, 26(5):1613–1623.

- Jang, S.-I. and Kim, K.-H. (2004). An islanding detection method for distributed generations using voltage unbalance and total harmonic distortion of current. *IEEE transactions on power delivery*, 19(2):745–752.
- Karimi-Ghartemani, M. and Iravani, M. R. (2002). A nonlinear adaptive filter for online signal analysis in power systems: applications. *IEEE Transactions on Power Delivery*, 17(2):617–622.
- Karimi-Ghartemani, M., Khajehoddin, S. A., Jain, P. K., and Bakhshai, A. (2011). Derivation and design of in-loop filters in phase-locked loop systems. *IEEE Transactions on Instrumentation and Measurement*, 61(4):930–940.
- Khajehoddin, S. A., Karimi-Ghartemani, M., Bakhshai, A., and Jain, P. (2012). A power control method with simple structure and fast dynamic response for single-phase grid-connected dg systems. *IEEE Transactions on Power Electronics*, 28(1):221–233.
- Kivimäki, J., Kolesnik, S., Sitbon, M., Suntio, T., and Kuperman, A. (2017). Design guidelines for multiloop perturbative maximum power point tracking algorithms. *IEEE Transactions on Power Electronics*, 33(2):1284–1293.
- Kulkarni, S. V. and Gaonkar, D. N. (2017). Operation and control of a microgrid in isolated mode with multiple distributed generation systems. In *2017 International Conference on Technological Advancements in Power and Energy (TAP Energy)*, pages 1–6. IEEE.
- Kulkarni, S. V. and Gaonkar, D. N. (2020). Investigation of plls for distributed generation systems in the grid-connected mode of operation. In *2020 International Conference on Power, Instrumentation, Control and Computing (PICC)*, pages 1–6. IEEE.
- Kulkarni, S. V. and Gaonkar, D. N. (2021). Improved droop control strategy for parallel connected power electronic converter based distributed generation sources in an islanded microgrid. *Electric Power Systems Research*, 201:107531.
- Kulkarni, S. V., Gaonkar, D. N., and Guerrero, J. M. (2021). Operation of the microgrid with improved droop control strategy and an effective islanding detection technique for automatic mode switching. *Electric Power Components and Systems*, pages 1–15.
- Laaksonen, H., Saari, P., and Komulainen, R. (2005). Voltage and frequency control of inverter based weak lv network microgrid. In *2005 International Conference on Future Power Systems*, pages 6–pp. IEEE.

- Langella, R. and Testa, A. (2010). Ieee standard definitions for the measurement of electric power quantities under sinusoidal, nonsinusoidal, balanced, or unbalanced conditions. *Revision of IEEE Std*, pages 1459–2000.
- Lasseter, R. H. (2002). Microgrids. In *2002 IEEE Power Engineering Society Winter Meeting. Conference Proceedings (Cat. No. 02CH37309)*, volume 1, pages 305–308. IEEE.
- Lee, C.-T., Chu, C.-C., and Cheng, P.-T. (2013a). A new droop control method for the autonomous operation of distributed energy resource interface converters. *IEEE Transactions on Power Electronics*, 28(4):1980–1993.
- Lee, C.-T., Chuang, C.-C., Chu, C.-C., and Cheng, P.-T. (2009). Control strategies for distributed energy resources interface converters in the low voltage microgrid. In *Energy Conversion Congress and Exposition, 2009. ECCE 2009. IEEE*, pages 2022–2029. IEEE.
- Lee, C.-T., Jiang, R.-P., and Cheng, P.-T. (2013b). A grid synchronization method for droop-controlled distributed energy resource converters. *IEEE Transactions on Industry Applications*, 49(2):954–962.
- Li, C., Cao, C., Cao, Y., Kuang, Y., Zeng, L., and Fang, B. (2014). A review of islanding detection methods for microgrid. *Renewable and Sustainable Energy Reviews*, 35:211–220.
- Li, Y., Gao, Z., Qin, W., Wen, Q., Jun, M., et al. (2016). Nano size related piezoelectric efficiency in a large zno thin film, potential for self powered medical device application. *Biochem Anal Biochem*, 5(243):2161–1009.
- Li, Y. W. and Kao, C.-N. (2009). An accurate power control strategy for power-electronics-interfaced distributed generation units operating in a low-voltage multibus microgrid. *IEEE Transactions on Power Electronics*, 24(12):2977–2988.
- Lin, L., Ma, H., and Bai, Z. (2016). An improved proportional load-sharing strategy for meshed parallel inverters system with complex impedances. *IEEE Transactions on Power Electronics*, 32(9):7338–7351.
- Liu, F., Kang, Y., Zhang, Y., Duan, S., and Lin, X. (2010). Improved sms islanding detection method for grid-connected converters. *IET renewable power generation*, 4(1):36–42.

- Lopes, L. A. and Sun, H. (2006). Performance assessment of active frequency drifting islanding detection methods. *IEEE Transactions on Energy Conversion*, 21(1):171–180.
- Mahat, P., Chen, Z., and Bak-Jensen, B. (2009). A hybrid islanding detection technique using average rate of voltage change and real power shift. *IEEE Transactions on Power Delivery*, 24(2):764–771.
- Mahmud, K., Sahoo, A. K., Ravishankar, J., and Dong, Z. Y. (2019). Coordinated multilayer control for energy management of grid-connected ac microgrids. *IEEE Transactions on Industry Applications*, 55(6):7071–7081.
- Mahmud, M., Hossain, M., Pota, H., and Oo, A. (2014). Robust nonlinear distributed controller design for active and reactive power sharing in islanded microgrids. *IEEE Transactions on Energy Conversion*, 29(4):893–903.
- Majumder, R., Ghosh, A., Ledwich, G., and Zare, F. (2009). Angle droop versus frequency droop in a voltage source converter based autonomous microgrid. In *Power & Energy Society General Meeting, 2009. PES'09. IEEE*, pages 1–8. IEEE.
- Majumder, R., Ledwich, G., Ghosh, A., Chakrabarti, S., and Zare, F. (2010). Droop control of converter-interfaced microsources in rural distributed generation. *IEEE Transactions on Power Delivery*, 25(4):2768–2778.
- Malik, S. M., Ai, X., Sun, Y., Zhengqi, C., and Shupeng, Z. (2017). Voltage and frequency control strategies of hybrid ac/dc microgrid: a review. *IET Generation, Transmission & Distribution*, 11(2):303–313.
- Menon, V. and Nehrir, M. H. (2007). A hybrid islanding detection technique using voltage unbalance and frequency set point. *IEEE Transactions on Power Systems*, 22(1):442–448.
- Moawwad, A., Khadkikar, V., and Kirtley, J. L. (2013). A new p-q-v droop control method for an interline photovoltaic (i-pv) power system. *IEEE transactions on power delivery*, 28(2):658–668.
- Mohapatra, G. (2011). Design and implementation of diaphragm type pressure sensor in a direct tire pressure monitoring system (tpms) for automotive safety applications. *International Journal of Engineering Science and Technology (IJEST)*, 3(8):6514–6524.

- Mohd, A., Ortjohann, E., Morton, D., and Omari, O. (2010). Review of control techniques for inverters parallel operation. *Electric Power Systems Research*, 80(12):1477–1487.
- Narayanan, S. and Balamurugan, V. (2003). Finite element modelling of piezolaminated smart structures for active vibration control with distributed sensors and actuators. *Journal of sound and vibration*, 262(3):529–562.
- Ndjountche, T. (2018). *Data Converters, Phase-Locked Loops, and Their Applications*. CRC Press.
- Nichols, D. K., Stevens, J., Lasseter, R. H., Eto, J. H., and Vollkommer, H. T. (2006). Validation of the certs microgrid concept the cec/certs microgrid testbed. In *2006 IEEE Power Engineering Society General Meeting*, pages 3–pp. IEEE.
- O’kane, P. and Fox, B. (1997). Loss of mains detection for embedded generation by system impedance monitoring. In *Sixth International Conference on Developments in Power System Protection (Conf. Publ. No. 434)*, pages 95–98. IET.
- Pai, F.-S. and Huang, S.-J. (2001). A detection algorithm for islanding-prevention of dispersed consumer-owned storage and generating units. *IEEE Transactions on Energy Conversion*, 16(4):346–351.
- Pawar, S. N. and Mane, P. B. (2017). Wide band pll frequency synthesizer: A survey. In *2017 International Conference on Advances in Computing, Communication and Control (ICAC3)*, pages 1–6. IEEE.
- Pei, Y., Jiang, G., Yang, X., and Wang, Z. (2004). Auto-master-slave control technique of parallel inverters in distributed ac power systems and ups. In *Power Electronics Specialists Conference, 2004. PESC 04. 2004 IEEE 35th Annual*, volume 3, pages 2050–2053. IEEE.
- Perreault, D. J., Selders, R. L., and Kassakian, J. G. (1998). Frequency-based current-sharing techniques for paralleled power converters. *IEEE transactions on Power Electronics*, 13(4):626–634.
- Petrone, G., Spagnuolo, G., Teodorescu, R., Veerachary, M., and Vitelli, M. (2008). Reliability issues in photovoltaic power processing systems. *IEEE transactions on Industrial Electronics*, 55(7):2569–2580.
- Pogaku, N., Prodanovic, M., and Green, T. C. (2007). Modeling, analysis and testing of autonomous operation of an inverter-based microgrid. *IEEE Transactions on power electronics*, 22(2):613–625.

- Pouresmaeil, E., Miguel-Espinar, C., Massot-Campos, M., Montesinos-Miracle, D., and Gomis-Bellmunt, O. (2012). A control technique for integration of dg units to the electrical networks. *IEEE transactions on Industrial Electronics*, 60(7):2881–2893.
- Pouresmaeil, E., Miguel-Espinar, C., Massot-Campos, M., Montesinos-Miracle, D., and Gomis-Bellmunt, O. (2013). A control technique for integration of dg units to the electrical networks. *IEEE transactions on Industrial Electronics*, 60(7):2881–2893.
- Prodanovic, M., Green, T., and Mansir, H. (2000). A survey of control methods for three-phase inverters in parallel connection. In *2000 Eighth International Conference on Power Electronics and Variable Speed Drives (IEE Conf. Publ. No. 475)*, pages 472–477. IET.
- Qiu, Y., Sun, S., Xu, C., Wang, Y., Tian, Y., Liu, A., Hou, X., Chai, H., Zhang, Z., and Wu, H. (2021). The frequency-response behaviour of flexible piezoelectric devices for detecting the magnitude and loading rate of stimuli. *Journal of Materials Chemistry C*, 9(2):584–594.
- Ray, S., Gupta, N., and Gupta, R. A. (2017). A comprehensive review on cascaded h-bridge inverter-based large-scale grid-connected photovoltaic. *IETE Technical review*, 34(5):463–477.
- Redfern, M., Usta, O., and Fielding, G. (1993). Protection against loss of utility grid supply for a dispersed storage and generation unit. *IEEE transactions on power delivery*, 8(3):948–954.
- Rezaei, M. M. and Soltani, J. (2015). Robust control of an islanded multi-bus microgrid based on input–output feedback linearisation and sliding mode control. *IET Generation, Transmission & Distribution*, 9(15):2447–2454.
- Rodriguez, P., Luna, A., Munoz-Aguilar, R. S., Etxeberria-Otadui, I., Teodorescu, R., and Blaabjerg, F. (2011). A stationary reference frame grid synchronization system for three-phase grid-connected power converters under adverse grid conditions. *IEEE transactions on power electronics*, 27(1):99–112.
- Rokrok, E. and Golshan, M. E. H. (2010). Adaptive voltage droop scheme for voltage source converters in an islanded multibus microgrid. *IET generation, transmission & distribution*, 4(5):562–578.
- Rolim, L. G. B., da Costa, D. R., and Aredes, M. (2006). Analysis and software

- implementation of a robust synchronizing pll circuit based on the pq theory. *IEEE Transactions on Industrial Electronics*, 53(6):1919–1926.
- Ropp, M., Begovic, M., and Rohatgi, A. (1999). Analysis and performance assessment of the active frequency drift method of islanding prevention. *IEEE Transactions on Energy conversion*, 14(3):810–816.
- Saha, A., Chowdhury, S., Chowdhury, S., and Crossley, P. (2008). Modelling and simulation of microturbine in islanded and grid-connected mode as distributed energy resource. In *2008 IEEE Power and Energy Society General Meeting-Conversion and Delivery of Electrical Energy in the 21st Century*, pages 1–7. IEEE.
- Sao, C. K. and Lehn, P. W. (2005). Autonomous load sharing of voltage source converters. *IEEE Transactions on Power Delivery*, 20(2):1009–1016.
- Sao, C. K. and Lehn, P. W. (2008). Control and power management of converter fed microgrids. *IEEE Transactions on Power Systems*, 23(3):1088–1098.
- Shanxu, D., Yu, M., Jian, X., Yong, K., and Jian, C. (1999). Parallel operation control technique of voltage source inverters in ups. In *Power Electronics and Drive Systems, 1999. PEDS'99. Proceedings of the IEEE 1999 International Conference on*, volume 2, pages 883–887. IEEE.
- Singam, B. and Hui, L. Y. (2006). Assessing sms and pjd schemes of anti-islanding with varying quality factor. In *2006 IEEE International Power and Energy Conference*, pages 196–201. IEEE.
- Siri, K., Lee, C., and Wu, T.-E. (1992). Current distribution control for parallel connected converters. i. *IEEE Transactions on Aerospace and Electronic Systems*, 28(3):829–840.
- Sun, X., Lee, Y.-S., and Xu, D. (2003). Modeling, analysis, and implementation of parallel multi-inverter systems with instantaneous average-current-sharing scheme. *IEEE Transactions on Power Electronics*, 18(3):844–856.
- Tang, X., Hu, X., Li, N., Deng, W., and Zhang, G. (2016). A novel frequency and voltage control method for islanded microgrid based on multienergy storages. *IEEE Transactions on Smart Grid*, 7(1):410–419.
- Teodorescu, R. and Blaabjerg, F. (2004). Flexible control of small wind turbines with grid failure detection operating in stand-alone and grid-connected mode. *IEEE transactions on power electronics*, 19(5):1323–1332.

- Teodorescu, R., Liserre, M., and Rodriguez, P. (2011). *Grid converters for photovoltaic and wind power systems*, volume 29. John Wiley & Sons.
- Tuladhar, A., Jin, H., Unger, T., and Mauch, K. (2000). Control of parallel inverters in distributed ac power systems with consideration of line impedance effect. *IEEE Transactions on Industry Applications*, 36(1):131–138.
- Vahedi, H., Noroozian, R., Jalilvand, A., and Gharehpetian, G. (2010). Hybrid sfs and qf islanding detection method for inverter-based dg. In *2010 IEEE International Conference on Power and Energy*, pages 672–676. IEEE.
- Vasquez, J. C., Guerrero, J. M., Luna, A., Rodríguez, P., and Teodorescu, R. (2009). Adaptive droop control applied to voltage-source inverters operating in grid-connected and islanded modes. *IEEE Transactions on Industrial Electronics*, 56(10):4088–4096.
- Velasco, D., Trujillo, C., Garcera, G., and Figueres, E. (2010). An active anti-islanding method based on phase-pll perturbation. *IEEE Transactions on Power Electronics*, 26(4):1056–1066.
- Vijay, A., Doolla, S., and Chandorkar, M. C. (2017). Real-time testing approaches for microgrids. *IEEE Journal of Emerging and Selected Topics in Power Electronics*, 5(3):1356–1376.
- Vijay, A., Parth, N., Doolla, S., and Chandorkar, M. C. (2021). An adaptive virtual impedance control for improving power sharing among inverters in islanded ac microgrids. *IEEE Transactions on Smart Grid*.
- Vrdoljak, K., Perić, N., and Petrović, I. (2010). Sliding mode based load-frequency control in power systems. *Electric Power Systems Research*, 80(5):514–527.
- Wang, X., Guerrero, J. M., Blaabjerg, F., and Chen, Z. (2012). A review of power electronics based microgrids. *Journal of Power Electronics*, 12(1):181–192.
- Wang, X., Li, Y. W., Blaabjerg, F., and Loh, P. C. (2015). Virtual-impedance-based control for voltage-source and current-source converters. *IEEE Trans. Power Electron*, 30(12):7019–7037.
- Wang, Z., Tan, L., Pan, X., Liu, G., He, Y., Jin, W., Li, M., Hu, Y., and Gu, H. (2017). Self-powered viscosity and pressure sensing in microfluidic systems based on the piezoelectric energy harvesting of flowing droplets. *ACS applied materials & interfaces*, 9(34):28586–28595.

- Weedy, B. M., Cory, B. J., Jenkins, N., Ekanayake, J. B., and Strbac, G. (2012). *Electric power systems*. John Wiley & Sons.
- Wu, T., Siri, K., and Banda, J. (1994). The central-limit control and impact of cable resistance in current distribution for parallel-connected dc-dc converters. In *Power Electronics Specialists Conference, PESC'94 Record., 25th Annual IEEE*, volume 1, pages 694–702. IEEE.
- Xiang, Q., Liao, Z., and Li, T. (2021). A novel control strategy of the seamless transitions between grid-connected and islanding operation modes for the multiple complementary power microgrid. *International Journal of Electronics*, pages 1–20.
- Xiao, F., Dong, L., Li, L., and Liao, X. (2016). A frequency-fixed sogi-based pll for single-phase grid-connected converters. *IEEE Transactions on Power Electronics*, 32(3):1713–1719.
- Xin, H., Zhang, L., Wang, Z., Gan, D., and Wong, K. P. (2015). Control of island ac microgrids using a fully distributed approach. *IEEE Transactions on Smart Grid*, 6(2):943–945.
- Yang, Y., Hadjidemetriou, L., Blaabjerg, F., and Kyriakides, E. (2015). Benchmarking of phase locked loop based synchronization techniques for grid-connected inverter systems. *Proc. ICPE ECCE Asia*, pages 2517–2524.
- Zhang, Q., Liu, Y., Zhao, Y., and Wang, N. (2016). A multi-mode operation control strategy for flexible microgrid based on sliding-mode direct voltage and hierarchical controls. *ISA transactions*, 61:188–198.
- Zhong, Q.-C. (2013a). Harmonic droop controller to reduce the voltage harmonics of inverters. *IEEE Transactions on Industrial Electronics*, 60(3):936–945.
- Zhong, Q.-C. (2013b). Robust droop controller for accurate proportional load sharing among inverters operated in parallel. *IEEE Transactions on Industrial Electronics*, 60(4):1281–1290.
- Zhou, Y., Qin, P., and Chen, D. (2014). Fast and high-precision vco frequency calibration technique for wide-band frequency synthesizer. In *2014 12th IEEE International Conference on Solid-State and Integrated Circuit Technology (ICSICT)*, pages 1–3. IEEE.

Appendix A

Typhoon Model initialization script parameters

Numpy module is imported as 'np'

Scipy module is imported as 'sp'

V_{DC}	800 V
R_{DC}	0.01 Ω
C_{DC}	$8e - 4$ F
L_{finv}	$5.082e - 3$ H
R_{finv}	0.1 Ω
C_f	$2.104e - 4$ F
L_g	$0.10164e - 3$ H
R_g	0.1 Ω
m_{pi}	$2.5e - 4$
n_{qi}	$1.33e - 3$
R_v, L_v	$1.2e - 3 \Omega, 0.55e - 3$ H
k_{pv}, k_{iv}	0.0263, 2.893
k_{pi}, k_{ii}	13, 1430
τ_i, τ_v	$1e - 3$ s, $10e - 3$ s
V_{dn}	400 Volts
ω_n	314.2 radians
ω_c	0.1 * ω_n radians
f	50 Hz
PZT layer of radius	4 cm
PZT layer of thickness	1 micron
Si diaphragm of thickness	35.869 microns
Si diaphragm of radius	5.5 cm
Effective diameter of diaphragm	4000 μm
Mass of the diaphragm	2 μkg
Moment of Inertia	4 kg m ²
Flexural rigidity	0.63 N kg

Appendix B

```
#Grid Simulator Data for Grid Healthy Condition
# NOTE: The code specified in this handler will be executed on simulation start.
# NOTE: Variables specified here will be available in other two handlers.
# HIL API
#----- MANDATORY IMPORTS -----
# HIL Control Panel API
# Function
Va = 'Grid Simulator1.V_source_phase_A'
Vb = 'Grid Simulator1.V_source_phase_B'
Vc = 'Grid Simulator1.V_source_phase_C'
hil.prepare_source_sine_waveform(Va, rms = 230.0, frequency = 50.0, phase =
0.0,harmonics_pu = ())
hil.prepare_source_sine_waveform(Vb, rms = 230.0, frequency = 50.0, phase =
-120.0,harmonics_pu = ())
hil.prepare_source_sine_waveform(Vc, rms = 230.0, frequency = 50.0, phase =
120.0,harmonics_pu = ())
hil.update_sources([Va,Vb,Vc])
```

Appendix C

```
#Grid Simulator Data for Grid Unhealthy Condition (Grid Voltage Sag)
# NOTE: The code specified in this handler will be executed on simulation start.
# NOTE: Variables specified here will be available in other two handlers.
# HIL API
#----- MANDATORY IMPORTS -----
# HIL Control Panel API
simulationStep = hil.get_sim_step()
executeAt1 = simulationStep * 2000 # execute after 2000 simulation cycles
executeAt2 = simulationStep * 4000 # execute after 4000 simulation cycles
# Function
Va_sag = Grid Simulator1.V_source_phase_A
Vb_sag = Grid Simulator1.V_source_phase_B
Vc_sag = Grid Simulator1.V_source_phase_C
hil.prepare_source_sine_waveform(Va_sag, rms = 156.4)
hil.prepare_source_sine_waveform(Vb_sag, rms = 156.4)
hil.prepare_source_sine_waveform(Vc_sag, rms = 156.4)
hil.update_sources([Va_sag, Vb_sag, Vc_sag], executeAt = executeAt1)
#-----#
hil.prepare_source_sine_waveform(Va, rms = 230.0)
hil.prepare_source_sine_waveform(Vb, rms = 230.0)
hil.prepare_source_sine_waveform(Vc, rms = 230.0)
hil.update_sources([Va, Vb, Vc], executeAt = executeAt2)
```

Appendix D

```
#Grid Simulator Data for Grid Unhealthy Condition (Grid Voltage Swell)
# NOTE: The code specified in this handler will be executed on simulation start.
# NOTE: Variables specified here will be available in other two handlers.
# HIL API
#----- MANDATORY IMPORTS -----
# HIL Control Panel API
simulationStep = hil.get_sim_step()
executeAt1 = simulationStep * 2000 # execute after 2000 simulation cycles
executeAt2 = simulationStep * 4000 # execute after 4000 simulation cycles
# Function
Va_sag = Grid Simulator1.V_source_phase_A
Vb_sag = Grid Simulator1.V_source_phase_B
Vc_sag = Grid Simulator1.V_source_phase_C
hil.prepare_source_sine_waveform(Va_swell, rms = 1150.0)
hil.prepare_source_sine_waveform(Vb_swell, rms = 1150.0)
hil.prepare_source_sine_waveform(Vc_swell, rms = 1150.0)
hil.update_sources([Va_swell, Vb_swell, Vc_swell], executeAt = executeAt1)
#-----#
hil.prepare_source_sine_waveform(Va, rms = 230.0)
hil.prepare_source_sine_waveform(Vb, rms = 230.0)
hil.prepare_source_sine_waveform(Vc, rms = 230.0)
hil.update_sources([Va, Vb, Vc], executeAt = executeAt2)
```

Appendix E

```
#Grid Simulator Data for Grid Unhealthy Condition (Grid Voltage Unbalance)
# NOTE: The code specified in this handler will be executed on simulation start.
# NOTE: Variables specified here will be available in other two handlers.
# HIL API
#----- MANDATORY IMPORTS -----
# HIL Control Panel API
simulationStep = hil.get_sim_step()
executeAt1 = simulationStep * 2000 # execute after 2000 simulation cycles
executeAt2 = simulationStep * 4000 # execute after 4000 simulation cycles
# Function
Va_sag = Grid Simulator1.V_source_phase_A
Vb_sag = Grid Simulator1.V_source_phase_B
Vc_sag = Grid Simulator1.V_source_phase_C
hil.prepare_source_sine_waveform(Va_unbalance, rms = 260.0)
hil.prepare_source_sine_waveform(Vb_unbalance, rms = 210.0)
hil.prepare_source_sine_waveform(Vc_unbalance, rms = 230.0)
hil.update_sources([Va_unbalance, Vb_unbalance, Vc_unbalance], executeAt = executeAt1)
#-----#
hil.prepare_source_sine_waveform(Va, rms = 230.0)
hil.prepare_source_sine_waveform(Vb, rms = 230.0)
hil.prepare_source_sine_waveform(Vc, rms = 230.0)
hil.update_sources([Va, Vb, Vc], executeAt = executeAt2)
```

Appendix F

```
#Grid Simulator Data for Grid Unhealthy Condition (Grid Voltage Harmonics)
# NOTE: The code specified in this handler will be executed on simulation start.
# NOTE: Variables specified here will be available in other two handlers.
# HIL API
#----- MANDATORY IMPORTS -----
# HIL Control Panel API
simulationStep = hil.get_sim_step()
executeAt1 = simulationStep * 2000 # execute after 2000 simulation cycles
executeAt2 = simulationStep * 4000 # execute after 4000 simulation cycles
# Function
Va = 'Grid Simulator1.V_source_phase_A'
Vb = 'Grid Simulator1.V_source_phase_B'
Vc = 'Grid Simulator1.V_source_phase_C'
harmonics = [ (5,0.1,0.0), (11,0.1,0.0), (2,0.0,0.0), (2,0.0,0.0), (2,0.0,0.0), (2,0.0,0.0),
(2,0.0,0.0), (2,0.0,0.0), (2,0.0,0.0), (2,0.0,0.0), ]
hil.prepare_source_sine_waveform(Va, harmonics_pu = harmonics)
hil.prepare_source_sine_waveform(Vb, harmonics_pu = harmonics)
hil.prepare_source_sine_waveform(Vc, harmonics_pu = harmonics)
hil.update_sources([Va,Vb,Vc])
hil.update_sources([Va, Vb, Vc,], executeAt = executeAt1)
#-----#
hil.prepare_source_sine_waveform(Va, rms = 230.0, frequency = 50.0, phase =
0.0,harmonics_pu = ()) hil.prepare_source_sine_waveform(Vb, rms = 230.0, frequency =
50.0, phase = -120.0,harmonics_pu = ()) hil.prepare_source_sine_waveform(Vc, rms =
230.0, frequency = 50.0, phase = 120.0,harmonics_pu = ())
hil.update_sources([Va, Vb, Vc,], executeAt = executeAt2)
```


Bio-data

Name : Shreeram Vishwanath Kulkarni

Date of birth: 02-07-1991

E-mail: vshreeramk@gmail.com

Mobile: +91-8123683011

Education

- **M.Tech.**, Master of Technology in Power System Engineering, Shri Dharmasthala Manjunatheshwara College of Engineering and Technology (SDMCET), Dharwad, Karnataka–Visvesvaraya Technological University (VTU), Belagavi, Karnataka, 2016.
- **B.E.**, Electrical & Electronics Engineering, Guru Nanak Dev Engineering College (GNDEC), Bidar, Karnataka–Visvesvaraya Technological University (VTU), Belagavi, Karnataka, 2013.

Experience

- **Project Assistant** in National Institute of Technology Karnataka (NITK), Surathkal, India from December 2016 to March 2019.
- **Assistant Professor** in Nitte Meenakshi Institute of Technology (NMIT), Bengaluru, Karnataka, India from July 2019 to Till Date.

Address

H.No 506, Market Road

Near Basava Temple,

Mugalkhod -591235, Belagavi, Karnataka, India.